Improving Reduced Order Models of Soil-Structure Interaction Using an Ensemble Kalman Inversion Finite Element Model Updating Framework

Thesis by
Danilo Smiljan Kusanovic

In Partial Fulfillment of the Requirements for the
Degree of
Doctor of Philosophy in Civil Engineering

CALIFORNIA INSTITUTE OF TECHNOLOGY
Pasadena, California

2021
Defended September 18th, 2020

Danilo Smiljan Kusanovic
ORCID: 0000-0002-0935-2577

ACKNOWLEDGEMENTS

First and foremost, I offer my sincerest gratitude to my supervisor *Domniki Asimaki*, who has supported me throughout my graduate studies with wisdom, patience, and kindness. Domniki, a student cannot simply wish for a better and friendlier supervisor. I attribute the level of my doctorate thesis to your encouragement and knowledge; without them, this thesis would not have been completed or written. Also, during my professional career and at my early stage as a researcher, I was aided by *Hector Jensen*, a fine professor who not only kept me interested in the computational and stochastic mechanics field, but also encouraged me to pursuit graduate studies at Caltech. The fulfillment of this work is much more a testament to his efforts than my own.

During my stay at Caltech, two exceptional professors have left a deep impression on my education. First, *Dennis Kochmann* who not only gave me useful guidance in understanding computational solid mechanics, but also a friendly conversation every time we met. Dennis, your friendship, respect, and patience towards your graduates will be my personal hallmark to be transmitted to my future colleagues and students. Second, *Andrew Stuart* who taught me throughout his lectures and books how an inverse problem can been applied in a general finite element setting, and how fundamental is understanding mathematics in conducting novel research in the applied engineering field. Andrew, as an outsider of the applied mathematics world, I can say you are an excellent instructor for engineers, your passion during lectures and interest of understanding the real-engineering world will never be forgotten.

A special place in my heart and mind will be always occupied by my dear friend, partner, and companion *Ying Shi Teh*. Thanks very much for your friendship, devotion, and unconditional support, especially in the moments I needed them the most. Ying Shi, thanks for a friendly smile, invitation for dinner, and coffee-breaks every day in the morning. Your presence in Gate-Thomas was my reason for going to the office every morning. I believe God has blessed me in several ways, but knowing you, and being with you, is for sure the best that has ever happen to me. Thanks to you, my life and experiences at Caltech changed.

As a member of Asimaki's lab, I have to recognize several people that have contributed to my personal and scientific development. *Elnaz Seylabi* and *Joaquín*

García, both of you have been the inspiration for the completion of my thesis. Without any of you, none of this could have been even possible. A considerable part of my work is due to your engagement during our countless discussions over research in Gate-Thomas. Thank you Elnaz and Joaquín for always having time to answer my questions and for enlightening my path during those darkest hours. Also, I cannot leave out my counter-strike fellows *Peyman Ayoubi* and *Kien Nguyen*, who have always provided me with useful comments during group presentations. Thank you all for your guidance as friends, groupmates, and researchers.

In my daily work, I have been blessed with a friendly and cheerful group of fellow students. I would like to thank my best friend during my stay at Caltech, *Guillaume Beardsell*, for always having time to waste during those infinitely many coffee-breaks, and for sharing your opinion every time I needed it. *Don Caballero*, I do not have enough words to say how thankful I am. On the same track, I need to highlight my dear friend *Ke Yu*, whose sense of humor and hardwork have been inspirational. Ke, thanks for showing me that a brilliant student like you can be humble and hardworking. You are certainly one of the students I was expecting to find at Caltech. Thanks for always being available to share a coffee, a coke, a beer, a margarita, a cadillac, a cigarette at T-Boyles, Amigos, and Gate-Thomas. My group of friends would not be complete without an honest and direct friend. Tough words such as "You are hoping, not thinking!" are sometimes needed to bring you back on Earth. With that being said, I would like to thank *Florian Schäfer* who not only helped me with my math classes, but also shared an interesting conversation about computer science and applied mathematics. Florian, you were an important pillar during my learning process, and the secret of my success at Caltech, for which I am very grateful for it. Last, but not least *Daniel Pastor* for always sharing a fun conversation and helped me to discover new techniques and packages for software development, and *John Harmon* and *Joseph Ruan* for being my T-Boyles friends; those beers and conversations were always a nice break from work. *Amanda Bouman* for being an inconditional friend throughout my five years at Caltech. *Lucía De Rose* for always being available to share a mate and a friendly conversation. El garoto *Francisco Lajus* who I had the opportunity to have some unforgettable experiences. Francisco thanks very much for all those beers at T-Boyles, and for teaching me some cool stuff in the fluid mechanic world. *Tomoyuki Oniyama* and *Tung Phan-Minh* who were very helpful during my first year, and latter showed me how to be able to do ordinary things extraordinarily well. As Chuck Palahniuk said: “Nothing of me is original. I am the combined effort of everybody I’ve ever known.”

Finally, none of this work, experiences, and memories could have been possible without financial support, thus I would like to acknowledge both *CONICYT - Becas Chile* for the financial support to conduct doctoral studies at The California Institute of Technology, and *PG&E* for the financial support in developing the Seismo-VLAB software in its serial and parallel versions.

Danilo S. Kusanovic
December 9, 2020

ABSTRACT

In civil engineering, almost all structures are somehow in contact with soil–i.e., have foundations or support elements that either rest on or are embedded in soil. Thus, their seismic response is governed by the interaction between the structure, the non-structural components, the foundation, and the surrounding soil. Predicting such interaction becomes increasingly complex when uncertainties of soil and structural material, ground motion variability, and dissipation mechanisms are considered. The accuracy of numerical models to predict the linear or nonlinear responses of structures depends not only on how well the uncertainties in the material properties and input motion are estimated, but also on how well the various sources of energy dissipation and their interaction are modeled. Therefore, high-fidelity simulation of soil-structure interaction (SSI) problems require advanced models that can capture the nonlinear behavior of soils and structures, and parallel computing capabilities to optimize the cost associated with large scale problems. In spite of this fact, SSI in practice is widely accounted for using fixed-base building and reduced-order-models (ROM) which usually trade accurate solution for fast ones. Unfortunately, if SSI effects are neglected or poorly estimated, then critical response measures of a structure can be over- or under-estimated, which in turn can lead to unsafe or overly conservative designs.

Motivated by the previous challenge, in this thesis work we present a robust and efficient framework for finite element model (FEM) updating based on ensemble-Kalman inversion (EnKI). The EnKI-FEM updating framework is used to obtain suitable parameters to inform a ROM from data generated using high-fidelity FEM simulations. Since high-fidelity SSI simulations call for accurate and computationally efficient capabilities, as a part of this work, we developed Seismo-VLAB, a simple, fast, and extendable C++ finite element software to optimize large-scale simulations of dynamic and nonlinear SSI problems. The EnKI-FEM updating framework is thus integrated in Seismo-VLAB allowing to identify any parameter of the ROM without compromising accuracy. The so-generated ROM are finally employed to propose a new dimensionless frequency mapping to estimate the soil impedance for time domain analysis and to investigate soil-structure-interaction effects at a regional-scale. The presented methodology is general enough and it can be extended to more complex structural and/or geotechnical systems, allowing to construct highly-accurate ROM in a simple manner.

PUBLISHED CONTENT AND CONTRIBUTIONS

Danilo S. Kusanovic, Elnaz Seylabi, and Domniki Asimaki. (2021). "Seismo-VLAB: An open-source finite element software for meso-scale simulations." In preparation to be submitted to *The Journal of Open Source Software*.

D.S.K participated in the conception of the project, performed data analysis, model development, numerical simulations, produced figures, and wrote most of the manuscript.

Danilo S. Kusanovic, Elnaz Seylabi, Albert Kottke, and Domniki Asimaki. (2020). "Seismo-VLAB: A parallel object-oriented platform for reliable nonlinear seismic wave propagation and soil-structure interaction simulation." In preparation to be submitted to *Computers and Geotechnics*.

D.S.K participated in the conception of the project, performed data analysis, model development, numerical simulations, produced figures, and wrote most of the manuscript.

Danilo S. Kusanovic, Elnaz Seylabi, and Domniki Asimaki. (2020). "Optimization of frequency domain impedances for time domain response analyses of building structures with rigid shallow foundations." Accepted to *Earthquake Spectra*.

D.S.K performed all data analysis, model development, numerical simulations, produced all figures, and wrote most of the manuscript.

Domniki Asimaki, Joaquín Garcia-Suarez, **Danilo S. Kusanovic**, Kien T. Nguyen and Elnaz Seylabi. (2019). "Next generation reduced order models for soil-structure interaction." *Proceedings of the 7th International Conference on Earthquake Geotechnical Engineering, Rome, Italy*, pp. 138–152. DOI: 10.1201/9780429031274.

D.S.K participated in the conception of the project, solved and analyzed the building structures, and wrote Section 3 of the manuscript.

TABLE OF CONTENTS

Acknowledgements . . . iii
Abstract . . . vi
Published Content and Contributions . . . vii
Table of Contents . . . viii
List of Illustrations . . . x
List of Tables . . . xviii
Chapter I: Introduction . . . 1
1.1 How to model soil-structure interaction effects? . . . 2
1.2 Next generation reduced order models for soil-structure interaction . . . 5
1.3 Objectives of the thesis . . . 6
1.4 Organization of the thesis . . . 7
Chapter II: Seismo-VLAB: A parallel object-oriented platform for reliable nonlinear seismic wave propagation and soil-structure interaction simulation 10
2.1 The finite element analysis . . . 12
2.2 The object-oriented analysis . . . 21
2.3 Seismo-VLAB: Style, performance and extensions . . . 25
Chapter III: Simulation of wave propagation in heterogeneous half-space . . . 35
3.1 The domain reduction method . . . 36
3.2 Hybrid formulation of perfectly matched layer for truncated domain . . . 40
3.3 Domain reduction method formulated in a perfectly matched layer for truncated domain . . . 43
3.4 Examples of wave propagation using DRM and PML . . . 46
3.5 Conclusions . . . 50
Chapter IV: The direct modeling method for soil-structure interaction problems 52
4.1 The continuum formulation of the soil-structure interaction problems 52
4.2 The finite element method applied to soil-structure interaction . . . 55
4.3 Some numerical modeling considerations . . . 57
4.4 Demonstration of the finite element applied to soil-structure-interaction 61
4.5 Conclusions . . . 64
Chapter V: The reduced order model for soil-structure interaction problems . . . 66
5.1 Effects of shallow foundation embedment . . . 67
5.2 Static condensation of building structures . . . 70
5.3 Equation of motion for soil-structure interaction . . . 72
5.4 The effects of soil-structure interaction . . . 74
5.5 Comparison of reduced order model and finite element analysis . . . 77
5.6 Conclusions . . . 81
Chapter VI: Finite element updating for parameter estimation via ensemble Kalman inversion . . . 82
6.1 The forward model . . . 83

6.2 The inverse problem . . . 85
6.3 The ensemble Kalman inversion for parameter estimation . . . 86
6.4 Properties of the iterative ensemble Kalman inversion method . . . 90
6.5 Ensemble-Kalman inversion finite element model updating framework 91
6.6 Conclusions . . . 96
Chapter VII: Application: Improving the state-of-practice dimensionless frequency estimation . . . 98
7.1 Motivation . . . 98
7.2 The problem statement and method of analysis . . . 99
7.3 Computing dimensionless frequencies using Random Forest . . . 114
7.4 Validation of proposed dimensionless frequency mapping . . . 118
7.5 Summary and conclusions . . . 124
Chapter VIII: Application: Simplified regional soil-structure interaction assessment applied to Southern California . . . 126
8.1 Motivation . . . 126
8.2 The problem statement and method of analysis . . . 127
8.3 Verification of the reduced order model for SSI assessment . . . 134
8.4 Evaluation of SSI effects on regional scale . . . 138
8.5 Summary and conclusions . . . 143
Chapter IX: Summary and Conclusions . . . 145
9.1 Limitations and major findings of the research work . . . 146
9.2 Recommendations for future research work . . . 148
9.3 Concluding remarks . . . 149
Bibliography . . . 150

LIST OF ILLUSTRATIONS

Number *Page*

1.1 NIST iterative procedure to compute frequency independent foundation soil spring and dashpot coefficients. (a) Simplified SSI model using lumped translational and rotational spring and dashpots and the fixed first modal information. (b) Frequency dependent impedance function. 3

1.2 NIST procedure to compute foundation input motion. (a) Free field motion time series, here a Ricker pulse is considered. (b) Transfer function in black-solid line and FFM Fourier transform function of the Ricker pulse in dashed-blue line. (c) Translational and rotational foundation input motion. 4

2.1 The general three-dimensional boundary value problem to be solved using finite element analysis (adopted from Bathe [16]). 12

2.2 The isoparametric coordinate transformation. 17

2.3 Seismo-VLAB global software structure. The Pre-Analysis is an interface that provides the files to be executed, and the Run-Analysis is the main core that performs the finite element analysis. 22

2.4 Seismo-VLAB software packages for finite element analysis. Classes represented in boxes are abstract classes. Developers can provide their own sub-classes to personalize applications. 23

2.5 The classes required to be partitioned for a parallel execution of Seismo-VLAB. The classes represented correspond to the objects required to be sent to the k-th processor. 24

2.6 The earth dam problem geometry considered to validate Seismo-VLAB against OpenSEES. The red dashed-line represents where Lysmer-Kuhlemeyer dashpots are added. 29

2.7 Seismo-VLAB strong scaling performance (up to 16 processors) obtained for the earth dam problem. 30

2.8 A real three-dimensional SSI problem using DRM and PML to study strong scaling performance. (Left) the finite element mesh used in this analysis, and (Right) example of the domain partition in eight processors. 31

2.9 Seismo-VLAB strong scaling performance for MUMPS and PETSc (up to 16 processors) obtained for the full fidelity SSI problem. . . . 33
3.1 Truncated seismic region partitioned explicitly into two sub-domains across interface Γ_{NF} where P_b^R are nodal forces transmitted from Ω_F onto Ω_N. (a) The domain Ω_N contains the features (near-field), and (b) the domain Ω_F the semi-infinite exterior sub-domain which includes the fault (far-field). 36
3.2 Auxiliary truncated seismic region partitioned explicitly into two sub-structures across interface Γ_{BF} where P_b^B are nodal forces transmitted from Ω_F onto Ω_B. (a) Localized features of the actual problem in Ω_N have been replaced by a simpler background model over domain Ω_B, and (b) the domain Ω_F is the semi-infinite exterior sub-domain which includes the fault defined identical to Ω_F. 38
3.3 Seismic region with two neighboring surfaces Γ_{NL} and Γ_e on which effective nodal forces P_{eff} defined by Equation (3.9) are to be applied. These forces are equivalent to and replace the original seismic forces P_e^R , which act in the vicinity of the causative fault. 39
3.4 The problem geometry and boundary conditions of a perfectly matched layer for truncated domain in a plane-strain setting. 40
3.5 Domain reduction method formulated in a perfectly matched layer. (a) The total-field displacement $\mathbf{u}^t = \mathbf{u}^f + \mathbf{u}^s$ around structures due to the soil-structure interaction induced by the remote seismic excitation in a semi-infinite domain; (b) the free-field displacement $\mathbf{u}_{free}$ due to remote seismic excitation in a semi-infinite domain; (c) the DRM modeling approach for a domain truncated by ABCs (adopted from Bielak et al. [24]). 43
3.6 Velocity field amplitude at time (a) $t = 1.10\,[s]$, (b) $t = 1.65\,[s]$, (c) $t = 1.95\,[s]$, and (d) $t = 2.25\,[s]$ for testing the DRM elements. The blue color represents a velocity amplitude of $0.0\,[m/s]$, while the red color represents a velocity amplitude of $0.2\,[m/s]$. 47
3.7 Synthetic seismogram (a) horizontal component $v_x(t)$, and (b) vertical component $v_z(t)$ of the velocity, recorded on the soil surface for the soil-structure interaction problem. 48

3.8 Velocity field amplitude and deformed configuration at time (a) $t = 1.05\,[s]$, (b) $t = 1.65\,[s]$, (c) $t = 1.95\,[s]$, and (d) $t = 2.25\,[s]$ for the dam problem. The blue color represents a velocity amplitude of $0.0\,[m/s]$, while the red color represents a velocity amplitude of $0.2\,[m/s]$. 49
3.9 Synthetic seismogram (a) horizontal component $v_x(t)$, and (b) vertical component $v_z(t)$ of the velocity, recorded on the soil surface for the dam problem. 50
4.1 The continuum soil-structure interaction layout. 53
4.2 Degrees of freedom for the soil element and structural elements. . . . 58
4.3 Frame and soil element connection through kinematic constraints. . . 59
4.4 Displacement time history signals at (a) first-modal height at coordinates $(x, z) = (-9, 28)\,[m]$, (b) the roof at coordinates $(x, z) = (-9, 42)\,[m]$, and (c) the foundation at coordinates $(x, z) = (0, -2.5)\,[m]$ of the building. 63
4.5 Velocity field amplitude and deformed configuration at time (a) $t = 1.05\,[s]$, (b) $t = 1.65\,[s]$, (c) $t = 1.95\,[s]$, and (d) $t = 2.25\,[s]$ for the soil-structure interaction problem. The blue color represents a velocity amplitude of $0.0\,[m/s]$, while the red color represents a velocity amplitude of $0.2\,[m/s]$. 63
4.6 Synthetic seismogram (a) horizontal component $v_x(t)$, and (b) vertical component $v_z(t)$ of the velocity, recorded on the soil surface for the soil-structure interaction problem. 64
5.1 The soil-foundation system. (a) Geometry of the foundation system, (b) modeling of the soil continuum as distributed springs, and (c) free-body diagram of the foundation. 68
5.2 The fixed-base building structure in which $x_1, \ldots, x_n$ represents the relative displacement of each floor on the horizontal axis and $\ddot{u}_g(t)$ the free-field acceleration. The i, j, k are nodes in the finite element model and the blue arrows the degree of freedom in each node. 70
5.3 The flexible-base soil-structure interaction system in which $x = (x_1, \ldots, x_n)$ represents the relative displacement of each floor, u represents the relative deformation of the soil, and θ the rigid rotation of the foundation, and $\ddot{u}_g(t)$ the free-field acceleration. 72
5.4 Model reduction from (a) the simplified flexible-base system into (b) the equivalent fixed-base system. 75

5.5 Displacement time history responses evaluated at the roof at coordinates $(x, z) = (-9, 42)\,[m]$, first-modal height at coordinates $(x, z) = (-9, 28)\,[m]$, and the foundation base at coordinates $(x, z) = (0, -2.5)\,[m]$ of the building. The finite element model responses are shown in solid-blue line, and the ROM using NIST recommendations are displayed in dashed-red lines. 80

5.6 Displacement time history responses evaluated at the roof at coordinates $(x, z) = (-9, 42)\,[m]$, first-modal height at coordinates $(x, z) = (-9, 28)\,[m]$, and the foundation base at coordinates $(x, z) = (0, -2.5)\,[m]$ of the building. The finite element model responses are shown in solid-blue line, and the ROM using a judiciously chosen set of spring/dashpot values is displayed in dashed-red lines. 80

6.1 The flexible-base soil-structure interaction system in which $x_1, \ldots, x_{N-2}$ represents the relative displacement of each floor, x_{N-1} represents the relative deformation of the soil, and x_N the rigid rotation of the foundation. 84

6.2 Ensemble-Kalman inversion finite element model updating framework applied to SSI. (a) Full finite element model from which the "true" responses are computed (observations), and (b) reduced order method from which the spring and dashpot coefficients are estimated. Note how each iteration of the ensemble Kalman inversion algorithm breaks into two parts: a prediction step and an update step. 89

6.3 ℓ_2-norm misfit error between the finite element model (FEM) and the reduced order model (ROM) for different percentage of artificially perturbed data, initial ensemble estimation, and number of ensemble. 92

6.4 Normalized soil spring and dashpot coefficients using a 1% of artificially perturbed data, different initial ensemble estimation, and different number of ensemble. 93

6.5 Displacement time history signals at first-modal height $u_X^h(t)$ at coordinates $(x, z) = (-9, 28)\,[m]$, the roof $u_r^h(t)$ at coordinates $(x, z) = (-9, 42)\,[m]$, and the foundation $u_{X,\theta}^g(t)$ at coordinates $(x, z) = (0, -2.5)\,[m]$ of the building. The high-fidelity finite element model responses are shown in solid-blue lines, and the ROM responses are displayed in dashed-red lines. 95

6.6 Ensemble Kalman inversion finite element updating algorithm evolution. On the left, the evolution of the soil parameters, and on the right the normalized misfit ℓ_2-error obtained for each j-iteration between the FEM and ROM. 96
7.1 Rigid foundation kinematics for the numerical estimation of soil impedance-functions. (a) Infinite half-space finite element model, and (b) truncated half-space finite element model using PML elements. 103
7.2 Real and imaginary components for the normalized soil impedance function. The soil impedances are computed considering a Poisson's ratio of 0.25 and embedments ratios $D/B = 0.1, 0.25, 0.5, 1.0, 2.0$ from left to right. The blue solid line represents the translational impedance with $\tilde{B} = 1$, the yellow solid line represents the rotational impedance with $\tilde{B} = B^2$, and the red solid line represents the coupled impedance with $\tilde{B} = B$. 105
7.3 Real and imaginary components for the normalized soil impedance function. The soil impedances are computed considering a Poisson's ratio of 0.35 and embedments ratios $D/B = 0.1, 0.25, 0.5, 1.0, 2.0$ from left to right. The blue solid line represents the translational impedance with $\tilde{B} = 1$, the yellow solid line represents the rotational impedance with $\tilde{B} = B^2$, and the red solid line represents the coupled impedance with $\tilde{B} = B$. 105
7.4 Real and imaginary components for the normalized soil impedance function. The soil impedances are computed considering a Poisson's ratio of 0.45 and embedments ratios $D/B = 0.1, 0.25, 0.5, 1.0, 2.0$ from left to right. The blue solid line represents the translational impedance with $\tilde{B} = 1$, the yellow solid line represents the rotational impedance with $\tilde{B} = B^2$, and the red solid line represents the coupled impedance with $\tilde{B} = B$. 106
7.5 Rigid foundation kinematics for the numerical estimation of soil impedance-functions. 106

7.6 Normalized magnitude for the foundation input motion transfer function. The transfer function is computed considering different embedments ratios $D/B = 0.1, 0.25, 0.5, 1.0, 2.0$. The blue solid line represents the translational transfer function for a Poisson's ratio of $\nu = 0.25$, the yellow solid line represents the translational transfer function for a Poisson's ratio of $\nu = 0.35$, and the red solid line represents the translational transfer function for a Poisson's ratio of $\nu = 0.45$. 108

7.7 Normalized magnitude for the foundation input motion transfer function. The transfer function is computed considering different embedments ratios $D/B = 0.1, 0.25, 0.5, 1.0, 2.0$. The blue solid line represents the rotational transfer function for a Poisson's ratio of $\nu = 0.25$, the yellow solid line represents the rotational transfer function for a Poisson's ratio of $\nu = 0.35$, and the red solid line represents the rotational transfer function for a Poisson's ratio of $\nu = 0.45$. . . . 108

7.8 Reduced infinite half-space model using DRM and absorbing PML elements. 109

7.9 Building configurations employed in the dimensional analysis for the SSI problem. 110

7.10 The reduced order model. (a) The column and beam element used to construct the fixed base FEM. (b) The fixed base FEM building model where $\mathbf{M}_s, \mathbf{C}_s, \mathbf{K}_s$ are obtained using static condensation. (c) The flexible-base soil-structure interaction system in which $x = (x_1, \ldots, x_n)$ represents the relative displacement of each floor, u represents the relative deformation of the soil, and θ the rigid rotation of the foundation. 112

7.11 Distribution of a_0^* values in training (left) and test (right) data sets. . 115

7.12 A comparison between true values (FE analysis) and RF predictions for training set (left) and test set (right). 116

7.13 Feature importance (left) and correlation of features (right). 116

7.14 The parameters considered in the validation are for the building a fixed-fundamental period $T_b = 1.0\,[s]$ and a fixed-first modal height $h_b = 30.0\,[m]$. The foundation dimensions are a half-width $B = 10\,[m]$ and a foundation depth $D = 20.0\,[m]$. The soil shear velocity is $V_s = 100\,[m/s]$. 120

7.15 The parameters considered in the analysis are for the building a fixed-fundamental period $T_b = 2.25\,[s]$ and a fixed-first modal height $h_b = 64.0\,[m]$. The foundation dimensions are a half-width $B = 15\,[m]$ and a foundation depth $D = 10.0\,[m]$. The soil shear velocity is $V_s = 250\,[m/s]$. 120
7.16 Earthquake signals and frequency content used for the dimensionless flexible-base frequency mapping validation. 121
7.17 The parameters considered in the analysis are for the building a fixed-fundamental period $T_b = 0.5\,[s]$ and a fixed-first modal height $h_b = 15\,[m]$. The foundation dimensions are a half-length $B = 10\,[m]$ and a foundation depth $D = 1.0\,[m]$. The soil shear velocity is $V_s = 200\,[m/s]$ and subjected to Berkeley earthquake. 123
7.18 The parameters considered in the analysis are for the building a fixed-fundamental period $T_b = 1.0\,[s]$ and a fixed-first modal height $h_b = 30\,[m]$. The foundation dimensions are a half-length $B = 10\,[m]$ and a foundation depth $D = 2.5\,[m]$. The soil shear velocity is $V_s = 200\,[m/s]$ and subjected to Chino Hills earthquake. 123
7.19 The parameters considered in the analysis are for the building a fixed-fundamental period $T_b = 1.5\,[s]$ and a fixed-first modal height $h_b = 40.0\,[m]$. The foundation dimensions are a half-length $B = 10\,[m]$ and a foundation depth $D = 5.0\,[m]$. The soil shear velocity is $V_s = 200\,[m/s]$ and subjected to Northridge earthquake. 124
8.1 A truncated view of the building configurations employed for the 2D Southern California SSI problem. 128
8.2 The reduced order model. (a) The column and beam element used to construct the fixed base FEM. (b) The fixed base FEM building model where $\mathbf{M}_s, \mathbf{C}_s, \mathbf{K}_s$ are obtained using static condensation. (c) The flexible-base soil-structure interaction system in which $x = (x_1, \ldots, x_n)$ represents the relative displacement of each floor, u represents the relative deformation of the soil, and θ the rigid rotation of the foundation. 131
8.3 Non-linear curve fitting for the soil-structure interaction function to the generated data provided with the identified parameters of the 30 analyses. 134
8.4 Earthquake signals and frequency content used for the ROM validation. 135

8.5 The parameters considered in the analysis for the building are a fixed-fundamental period $T = 0.5\,[s]$ and a fixed-first modal height $h = 15\,[m]$. The foundation dimensions are a half-length $B = 10\,[m]$ and a foundation depth $D = 1.0\,[m]$. The soil shear velocity is $V_s = 200\,[m/s]$ and subjected to Northridge earthquake. 136
8.6 The parameters considered in the analysis for the building are a fixed-fundamental period $T = 1.0\,[s]$ and a fixed-first modal height $h = 30\,[m]$. The foundation dimensions are a half-length $B = 10\,[m]$ and a foundation depth $D = 2.5\,[m]$. The soil shear velocity is $V_s = 200\,[m/s]$ and subjected to Chino Hills earthquake. 136
8.7 The parameters considered in the analysis for the building are a fixed-fundamental period $T = 1.5\,[s]$ and a fixed-first modal height $h = 40.0\,[m]$. The foundation dimensions are a half-length $B = 10\,[m]$ and a foundation depth $D = 5.0\,[m]$. The soil shear velocity is $V_s = 200\,[m/s]$ and subjected to Berkeley earthquake. 137
8.8 The period lenghtening and radiation damping distribution in the Southern California area. 139
8.9 The urban-scale effects of SSI on seismic demands (rows) in the Southern California area for the three buildings (columns). 141

LIST OF TABLES

Number *Page*

2.1 Hardware description used in all analyses throughout this thesis. . . . 28

2.2 Performance comparison between Seismo-VLAB and OpenSEES. Speed-up, maximum memory usage, and memory leaks for a single core execution. . . . 29

2.3 MUMPS' elapsed time during the `Assembler`, `Solver`, and `Recorder` for one step for the solution of $\mathbf{K}_{\text{eff}}\,\Delta\mathbf{U} = \mathbf{F}_{\text{eff}}$ using different number of processors. . . . 31

2.4 PETSc's elapsed time during the `Assembler`, `Solver`, and `Recorder` for one step for the solution of $\mathbf{K}_{\text{eff}}\,\Delta\mathbf{U} = \mathbf{F}_{\text{eff}}$ using different number of processors. . . . 32

2.5 Performance comparison between MUMPS and PETSc for multiple core execution. Speed-up and parallel efficiency are measured for one time step. . . . 32

7.1 The n-physical parameters of the SSI problem to be considered in the dimensional analysis. . . . 101

7.2 Building's first fixed-modal parameters using eigen-analysis. . . . 110

7.3 Improvement of the proposed dimensionless frequency compared to the state-of-the-art for different soil, foundation, and building configurations. . . . 119

7.4 Errors associated to building's responses for the validation of real-earthquake motion. . . . 124

8.1 Summary of geometry and first fixed-modal parameters for three buildings considered in Southern California. . . . 129

8.2 Errors associated with displacement responses and period elongation for the buildings described in § 8.2 to a transient analysis. . . . 137

Chapter 1

INTRODUCTION

In civil engineering, almost all structures (buildings, dams, bridges, tunnels, and retaining walls to name a few) are somehow in contact with soil–i.e., have foundations or support elements that either rest on or are embedded in soil. Therefore, their seismic response is governed by the interaction between the structure, the non-structural components, the foundation, and the surrounding soil [157–159]. However, predicting such interaction becomes increasingly complex when uncertainties of soil and structural material, ground motion variability, and dissipation mechanisms are taken into consideration. Thus, the accuracy of numerical models to predict the linear or nonlinear responses of structures depends not only on how well the uncertainties in the material properties and input motion are estimated, but also on how well the various sources of energy dissipation and their interaction are modeled.

The inherent challenges and difficulties in modeling soil-structure interaction (SSI) have lead researchers to focus on the design of a series of simplified models: for instance, energy dissipation in buildings has been represented for decades using mathematical models based on viscous damping. The basic idea is to combine all the sources of energy dissipation (especially those which may be impractical, too complex, or not fully understood) into a simple set of viscous parameters. Although it has been well established that some of the dissipation mechanisms do not behave in a viscous manner [20, 63] (for example, material damping of soil and structural elements), this inconsistency is frequently ignored in engineering practice because it simplifies the analysis [74] and produces reasonable results [19]. In a similar fashion, SSI is in practice simplified using fixed-base building models, where properties such as damping ratios are modified to appropriately account for mechanisms such as radiation damping. This approach is once again used because SSI problems are complex and computationally expensive.

Nevertheless, accurate quantification of SSI effects (or other source or interactions) is critical in the design of earthquake resistant structures. If SSI effects are neglected or poorly estimated, then critical response measures of a structure can be over- or under-estimated, which in turn can lead not only to unsafe or overly conservative designs [116, 125], but also to large economic losses.

1.1 How to model soil-structure interaction effects?

Soil-Structure Interaction effects can be considered in numerical analyses using one of two methods: the *direct method* and the *substructure method*.

In the direct method, the super-structure, the foundation, and the surrounding soil are explicitly taken into account, using in general the finite element method [16, 70]. However, in this method is impossible to model the semi-infinite extent of the soil with a finite number of the elements; therefore, appropriate boundary conditions [15, 51, 95, 106] have to be applied to the finite element model, such that the radiated energy away from the truncated boundary is perfectly emulated. Although domain truncation together with the insertion of an appropriate boundary condition reduces the order of the original problem, the direct method is still computationally expensive and is rarely used in engineering practice.

As a consequence of the latter constraint, the state-of-the-practice has adopted the substructure method [157–159]. In this method, the problem is divided into two systems: the superstructure and the soil-foundation sub-systems. The soil-foundation system is first represented as force-deformation relationships, known as impedance functions, which are then applied to the nodes along the soil-foundation interface to model the dynamic interaction between soil-foundation and superstructure. These impedance functions have been developed in the last 50 years (e.g., [104, 105, 119, 154]) assuming linear elastic soil behavior. In particular, for linear SSI analyses, it is convenient to solve the problem in the frequency domain, using the soil impedance functions and the modified input motion, together with dynamic characteristic of the structure. While the use of impedance functions in linear SSI analyses are quite straightforward, they cannot be used—at least, directly—in non-linear SSI analyses. This is because it is not nominally possible to solve nonlinear problems in the frequency domain.

In order to make the use of the substructure method practical in time domain analysis, researchers and practitioners have proposed different models to approximate the soil impedance functions [138–140]. Among them, and for building structures with shallow foundation, the National Institute of Standards and Technology (NIST) under the project entitled *Improved Procedures for Characterizing and Modeling Soil-Structure Interaction for Performance-Based Seismic Engineering* recommends using single-valued functions at a representative frequency, which can be modeled as constant-valued springs and dashpots along the soil-structure interface. The frequency at which the soil impedance is read is computed using an iterative method

proposed by Bielak and Veletsos [21, 125]. In this method, one starts assuming that the period of the interaction is the fixed-base building period (i.e., T). This value and geometry of the foundation allow to compute the dimensionless frequency $a_0 = \frac{\omega B}{V_s}$ as shown in Figure 1.1a. Such frequency enables computing the values of the lumped translational and rotational spring and dashpot coefficients as represented in Figure 1.1b.

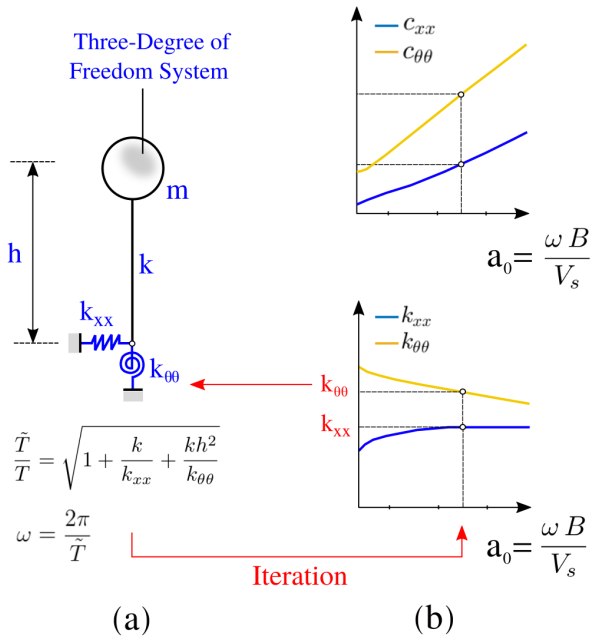

Figure 1.1: NIST iterative procedure to compute frequency independent foundation soil spring and dashpot coefficients. (a) Simplified SSI model using lumped translational and rotational spring and dashpots and the fixed first modal information. (b) Frequency dependent impedance function.

Provided with the lumped soil impedance coefficients, one can compute the period elongation of the system using

$$\frac{\tilde{T}}{T} = \sqrt{1 + \frac{k}{k_{xx}} + \frac{kh^2}{k_{\theta\theta}}}, \tag{1.1}$$

where the variable $\tilde{T}$ is the flexible-base period, T is the fixed-base period, h is the first-modal height, k is the fixed building stiffness, k_{xx} and $k_{\theta\theta}$ are the lumped translational and rotational springs coefficients that account for the flexibility of the surrounding soil. The process is repeated until there is no variation of the period elongation. Finally, provided with the flexible-base period, one can read from the impedance function the lumped soil spring $k_{xx}, k_{\theta\theta}$ as well as the lumped soil

dashpots c_{xx}, $c_{\theta\theta}$ and – if necessary – distribute them along the foundation perimeter.

Furthermore, for modifying the free field motion (FFM) due to the foundation embedment, NIST recommends using zero-phase transfer functions $\mathcal{H}_u$ and $\mathcal{H}_\theta$, which reduce the translational and introduce the rotational motion, respectively.

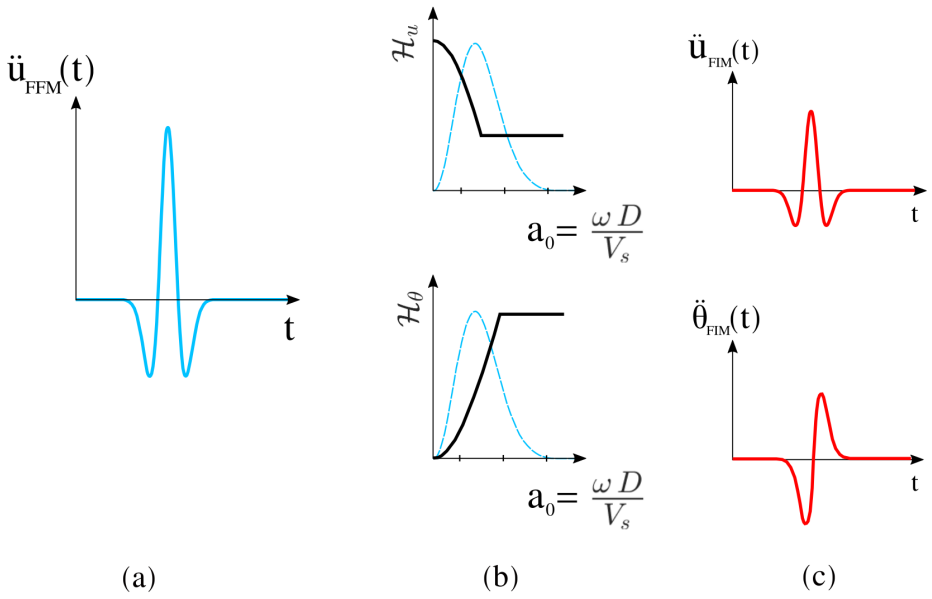

Figure 1.2: NIST procedure to compute foundation input motion. (a) Free field motion time series, here a Ricker pulse is considered. (b) Transfer function in black-solid line and FFM Fourier transform function of the Ricker pulse in dashed-blue line. (c) Translational and rotational foundation input motion.

$$\mathcal{H}_u = \begin{cases} \cos\left(\frac{D\,\omega}{V_s}\right), \text{ if } \frac{D\,\omega}{V_s} < 1.1 \\ 0.45, \text{ otherwise} \end{cases}, \tag{1.2}$$

$$\mathcal{H}_\theta = \begin{cases} 0.26\left[1 - \cos\left(\frac{D\,\omega}{V_s}\right)\right], \text{ if } \frac{D\,\omega}{V_s} < \frac{\pi}{2} \\ 0.26, \text{ otherwise} \end{cases}. \tag{1.3}$$

In Equations (1.2) and (1.3) the variable D represents the foundation embedment, V_s the shear wave velocity, and ω the frequency. This mapping to determine the Foundation Input Motions (FIMs) is shown schematically in Figure 1.2 where the FFM signal in Figure 1.2a is first transformed in Fourier space (dashed blue line), then the Fourier coefficients are scaled by the translational and rotational transfer

functions as shown in Figure 1.2b (in solid black line), and the results are transformed back to the real space (using the inverse Fourier transform) to obtain the FIM as shown in Figure 1.2c in red solid lines.

Unfortunately, the NIST recommendations make two important simplifications for using the substructure method in time domain analysis: (a) the frequency at which the impedance value should be read is the flexible-base frequency, and (b) it assumes that the FIM preserves the phase of the FFM and it does not change as a function of foundation embedment ratio D/B.

1.2 Next generation reduced order models for soil-structure interaction

Nowadays, computer capabilities allow to perform high-fidelity simulations for analysis of complex SSI problems, e.g. [153]. In addition, data from small to large scale experiments, intended to inform high-fidelity numerical models, e.g. [101], can be used to achieve a better understanding of the system behavior. Nonetheless, the computational cost of high fidelity SSI simulations continues to loom large, particularly for nonlinear fully coupled models, an obstacle which, combined with the large number of analyses needed to make fully probabilistic risk predictions, can render the problem intractable. Therefore, lower (or equivalent) fidelity predictive models, namely models that can capture the main features of high-fidelity simulations at reduced computational cost, are essential in probabilistic engineering and resilient design of interconnected civil infrastructure systems [26, 34].

Developing lower fidelity predictive models for SSI problems usually relies on replacing the surrounding soil by reduced order models (ROM) while keeping the structure intact. The soil ROM is a nonlinear spatio-temporal map that translates the transient ground deformations to the traction resultants along the soil-structure interface. Although a large number of ROMs have been previously proposed to quantify SSI effects, most have been formulated in the frequency-domain, and are restricted either by oversimplifying assumptions, e.g. [21, 154] or by relying on superposition, e.g. [57, 138, 139] to a limited class of linear elastic problems. ROMs for quantifying SSI effects in building structures are usually developed based solely on (semi-)analytical impedance functions (or dynamic springs) available for rigid foundations with simplified configurations, e.g. [56, 119]. Among other drawbacks associated with the existing models, their distribution along the building foundation is cumbersome, and by extension, so is their use for buildings with large, complex footprints that do not conform to the original simplified configurations. Moreover, as

pointed out previously, integrating the impedance values in time-domain analyses of soil-foundation-structure interaction by selecting a representative, frequency-independent value, is not clear.

Therefore, a new generation of ROMs that enables users

(a) to estimate the dimensionless frequency of the the combined system (i.e. the foundation, structure and the surrounding soil) to read the impedance functions, and

(b) to extend computer simulations to the nonlinear regime and time-domain structural analysis solutions,

becomes indispensable at the present time. All the above phenomena can be addressed using for instance a series of uniformly distributed springs and dashpots elements[1], in which the element coefficients are learn using data (real or synthetic) that incorporate all the above mechanisms of interaction. The focus is then directed towards developing an efficient and reliable system identification framework that can be used to estimate ROM parameters for SSI problems in a rigorous manner. In particular, ROMs based on rigorous mechanics, intended to expand the range of their applicability and understanding of SSI effects, in both a local and a regional scale can be of a great use. Thus, ROMs developed using a system identification framework will allow not only to produce high fidelity SSI simulations, but also to reduce the enormously computational cost associated with the analysis, and then allow their usage for instance in probabilistic engineering and resilient design.

1.3 Objectives of the thesis

The main objective of this thesis is to propose a general framework for improving reduced-order modeling of SSI problems. In particular, two-dimensional wave propagation in homogeneous-media is considered, and system identification techniques based on ensemble Kalman inversion are employed. The framework presented in this thesis is general enough that can be extended to three-dimensional wave-propagation problems, fully-coupled nonlinear interaction between soil and foundation, and nonlinear building behavior.

In addition, Seismo-VLAB, a parallel object-oriented platform for reliable nonlinear seismic wave propagation and soil-structure interaction simulation, is developed as

[1] These elements reflect the aggregate stiffness and energy dissipation characteristics of the soil system as seen from the building foundation

an important part of this thesis. Seismo-VLAB is thus employed to carry out all numerical analyses to generate the synthetic data for the ROM's development.

The main steps toward achieving the previous goals, along with the tools developed in that process, are listed below:

I. Implement a fully-parallel MPI-based finite element code in C++ that handles direct modeling of SSI problems. In other words, features such as perfectly matched layers (PMLs) to absorb the radiation energy thoroughly, and the domain reduction method (DRM) to consistently prescribe the input motions within the PML-truncated domain are required.

II. Compute the impedance functions for arbitrary foundation geometry resting on soil. In this regard, Seismo-VLAB is used to numerically compute the impedance functions for rigid interfaces using time domain solvers.

III. Compute the foundation input motion transfer functions for different types of soil-structure interfaces. The method is here employed under vertically propagating shear waves, but it can be used for inclined waves as well.

IV. Propose a new dimensionless frequency (a_0) mapping to estimate the soil impedance for time domain analysis. The analysis is carried out in three steps: First, generate time history responses using the direct modeling method for different configuration of building, soil, and foundation. Second, estimate the best dimensionless frequency that minimizes the misfit between the generated data and the reduced order model using ensemble Kalman inversion (EnKI). Third, find a mapping between the different configuration of building, soil, and foundation and the dimensionless frequency.

V. Investigate soil-structure interaction effects of simplified two-dimensional symmetric buildings at a regional-scale. The analysis is focused on the evaluation of SSI effects in southern California combining different building topology, a simulated real earthquake, geothecnical data, and local site effects. The analysis is carried out constructing a reduced order model where soil spring and solid dashpots are estimated using ensemble Kalman inversion (EnKI) as a function of a dimensionless parameters.

1.4 Organization of the thesis

The remainder of this dissertation is organized as follows:

In Chapter 2, we present Seismo-VLAB, a C++ multi-platform finite element software designed to optimize meso-scale simulations of dynamic soil-structure interaction (SSI) problems. In particular, the object-oriented approach adopted in Seismo-VLAB for finite element analysis is illustrated. This chapter constitutes the base of the object-oriented design framework, and provides details on the implementation as well as the interaction between classes such that a highly modular, easily understandable and extendable code is generated. Finally, features presented in Seismo-VLAB are tested using a range of simple to sophisticated examples. A comparison of software performance in terms of speedup, memory management (leaks), and code structure will be provided against widely used alternatives such as OpenSEES.

In Chapter 3, the finite element formulation used for the simulation of wave propagation in homogeneous half-space is presented. In this regard, the domain reduction method (DRM) is introduced, and then a perfectly matched layer formulation for absorbing boundaries is presented. These two sections are next employed in order to derive a coupled formulation for domain reduction and perfectly matched layer to be integrated in Seismo-VLAB. Some illustrative examples are presented to show Seismo-VLAB's correct and robust implementation of DRM and PML.

In Chapter 4, the continuum formulation for a general linear soil-structure interaction problem is presented. The discretized version or weak-form of the continuum problem is formulated using the finite element method to approximate the semi-infinite domain. Some examples are presented to show the robustness of Seismo-VLAB for handling soil-structure interaction problems.

In Chapter 5, a better suited simplified reduced order model (ROM) in time domain is presented. The ROM constructed in this manner reduces soil-structure interaction complexity using three steps. First, the effects of foundation embedment on elastic media of the foundation alone is studied. Second, the building (superstructure) system is simplified using substructure (condensation) method. Third, the latter results are integrated to generate the reduced order model for the soil-structure-interaction. Likewise, the effectiveness of the reduced order model is shown by comparing time history results against the finite element model presented in Chapter 4.

In Chapter 6, the system identification method based on Ensemble Kalman inversion (EnKI) is formulated. In particular, a framework that uses Seismo-VLAB as a forward model for parameter estimation for the soil-structure interaction problem is addressed. The integration of Seismo-VLAB as an engine for parameter estimation is

discussed, and the robustness of the proposed identification framework are presented using some illustrative examples.

Finally, in Chapter 7 and 8, two applications of the presented EnKI-FEM framework for estimating parameters of reduced order models in SSI problems are presented. In particular, a much better dimensionless frequency to read the frequency-independent soil impedance in a homogeneous media is proposed, and maps where a certain building configuration is more prone to experience detrimental SSI effects in southern California are developed. The applications studied in these chapters have the purpose of demonstrating that reliable reduced order models based on rigorous mechanics, intended to expand the range of their applicability to conditions outside the range of numerical and physical experiments, can be generated if data is available.

Chapter 2

SEISMO-VLAB: A PARALLEL OBJECT-ORIENTED PLATFORM FOR RELIABLE NONLINEAR SEISMIC WAVE PROPAGATION AND SOIL-STRUCTURE INTERACTION SIMULATION

In structural and geotechnical engineering, the finite element method (FEM) [16, 70, 123, 141] is the preferred methodology to approximate the linear or nonlinear responses of structures [112]. The literature has constantly shown that software that uses the FEM can capture the responses shown in physical experiments [127, 136, 147] and real-world monitored structures [33, 115, 151] with enough accuracy. Not surprisingly, the most powerful commercial softwares such as MSC Nastran [111], ANSYS [46], ABAQUS [66], LS-DYNA [103] are frequently used in industry since they offer several sophisticated material and elements for modeling structure and multi-phase soil systems. However, in civil engineering practice, simpler commercial softwares such as SAP2000 [39], ETABS [37], Perform3D [38] are usually preferred to deal with this task. These softwares typically allow for modeling only the structure itself, with limited (usually elastic) soils modeling, if they offer any at all. Unfortunately, these softwares lack the capabilities to properly account for soil-structure interaction [21–23, 116, 157–159]. For example, none of them implements the well-celebrated domain reduction method (DRM) proposed by Bielak et all [24]. This method is required in SSI analyses since it allows to transmit ground motion in heterogeneous media and to reduce the size of the near-field region. Another example is the absorbing boundaries conditions required to limit the occurrence of spurious waves that are reflected from the far-field boundaries. In general, the absorption of scattered waves is achieved efficiently through a perfectly-matched-layer (PML), which is barely found in commercial packages, even though the formulation proposed by Kucukcoban and Kallivokas [51, 95] is suitable for being incorporated in already existing FEM codes [160]. In light of this, an efficient, reliable, and robust numerical platform for high-fidelity simulation of wave propagation in homogeneous and heterogeneous half-spaces must consider at least the latter two features.

As a consequence of the strong need to perform SSI in meso-scale (~km) simulations, Seismo-VLAB is created to provide a simple platform for reliable SSI analysis

and nonlinear wave propagation in shallow crust. Seismo-VLAB is a simple, fast, and extendable C++ [143] multi-platform finite element software designed to optimize meso-scale simulations of dynamic, nonlinear soil-structure interaction (SSI) problems. High-fidelity simulation of SSI problems calls for both advanced methods for modeling the structure and the soil and parallel computing. These features are not generally available in a single open-source software package, making the SSI modeling a complicated and sometimes tedious process. In Seismo-VLAB, we have implemented state-of-the-art tools to achieve optimal robustness and efficiency for solving SSI problems. The most important features of the software include dynamic nonlinear solvers for time-domain analyses of inelastic problems, cutting-edge direct and iterative parallel linear system solvers, interfaces with Message Passing Interface (MPI) [35] and Open Multi-Processing (OpenMP) [44] parallelization, domain decomposition for optimal parallel computing [86], perfectly matched layers as robust absorbing boundaries [51, 95], domain reduction for modeling wave-field incoherence in truncated domains [24], and a number of plasticity models. The highlighted features make Seismo-VLAB an ideal software to solve efficiently nonlinear wave propagation problems in presence of infrastructure systems such as building clusters and lifelines.

Since Seismo-VLAB is not intended to be a commercial software, it lacks some of the sophisticated element and material routines found in the most powerful commercial applications. The purpose of Seismo-VLAB is to provide a common open source framework in which researchers as well as engineers can quickly test, experiment with, and share/implement not only new material and element routines, but also new solvers, integration schemes, and nonlinear solution algorithms. Such features, not provided by most commercial applications, are necessary for researchers to improve the modeling capabilities of the software and to use state-of-the-art nonlinear structural analyses. Currently, Seismo-VLAB is developed to meet two important functionalities that we believe will become important in the near future: (a) can perform spatial variability of soil properties for uncertainty quantification in linear and nonlinear models of civil structures, and (b) can be coupled to high-level languages such as MatLab [109] and Python [152] to perform system identification for parameter estimation in nonlinear structural finite element models of civil structures.

In this chapter, the primary goal is to illustrate the practical application of the object-oriented approach adopted in Seismo-VLAB for finite element analysis. This broad objective is organized into three parts. In § 2.1, we present a brief introduction to the

finite element method. This section allows to identify the main classes required to develop Seismo-VLAB, and provides insight about how the main methods are implemented. Thus, in § 2.2, we present a brief introduction to object-oriented concepts and terminology. This section constitutes the base of the object-oriented design framework, and provides details on the implementation as well as the interaction between classes such that a highly modular, easily understandable, and extendable code can be developed. Finally, in § 2.3, features presented in Seismo-VLAB are tested using a range of simple to sophisticated examples. A comparison of software performance in terms of speedup, memory management (leaks), and code structure will be provided against widely used alternatives such as OpenSEES [112–114].

2.1 The finite element analysis

In this section, we briefly describe the theoretical foundations of the finite element method. This process is needed in order to identify the main classes required to represent the main components of the object-oriented finite element analysis (OOFEM). Although the latter has been addressed in the past [47, 53, 107, 113], we believe a closer review may help not only to understand the main member functions that each class must possess, but also their interaction.

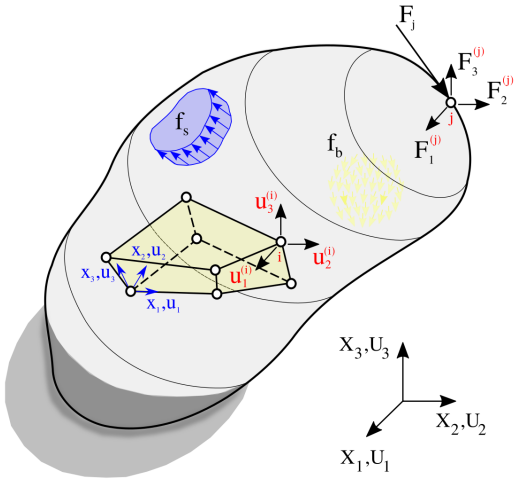

Figure 2.1: The general three-dimensional boundary value problem to be solved using finite element analysis (adopted from Bathe [16]).

Consider the equilibrium of a general three-dimensional body such as that shown in Figure 2.1. The body is located in a stationary coordinate system X_1, X_2, X_3, and it is subjected to body forces $\mathbf{f}_b \in \mathbb{R}^3$, surface traction $\mathbf{f}_s \in \mathbb{R}^3$, and concentrated forces $\mathbf{F}_j \in \mathbb{R}^3$ applied at the j-th node. In general, the externally applied forces can

be represented as vector objects

$$\mathbf{f}_b = \begin{bmatrix} f_1^b \\ f_2^b \\ f_3^b \end{bmatrix}, \quad \mathbf{f}_s = \begin{bmatrix} f_1^s \\ f_2^s \\ f_3^s \end{bmatrix}, \quad \mathbf{F}_{\mathrm{j}} = \begin{bmatrix} F_1^{(\mathrm{j})} \\ F_2^{(\mathrm{j})} \\ F_3^{(\mathrm{j})} \end{bmatrix}. \tag{2.1}$$

The displacements of the body–i.e., $\mathbf{U} \in \mathcal{U} \subset \mathbb{R}^3$ with $\mathbf{U} : \mathcal{U} \to \mathbb{R}^3$, is represented as a vector field:

$$\mathbf{U}(\mathrm{X}_1, \mathrm{X}_2, \mathrm{X}_3) = \begin{bmatrix} \mathrm{U}_1 \\ \mathrm{U}_2 \\ \mathrm{U}_3 \end{bmatrix}. \tag{2.2}$$

The strain vector $\boldsymbol{\epsilon} \in \mathbb{R}^6$ written in Voigt notation is

$$\boldsymbol{\epsilon} = [\epsilon_{11}, \epsilon_{22}, \epsilon_{33}, \epsilon_{12}, \epsilon_{23}, \epsilon_{31}]^\top, \tag{2.3}$$

where each strain component in linear-elasticity is related to the displacement field in the following manner,

$$\epsilon_{\mathrm{ij}} = \frac{1}{2}\left(\frac{\partial \mathrm{U_i}}{\partial \mathrm{X_j}} + \frac{\partial \mathrm{U_j}}{\partial \mathrm{U_i}}\right). \tag{2.4}$$

Similarly, the stress vector $\boldsymbol{\tau} \in \mathbb{R}^6$ written in Voigt notation is

$$\boldsymbol{\tau} = [\tau_{11}, \tau_{22}, \tau_{33}, \tau_{12}, \tau_{23}, \tau_{31}]^\top. \tag{2.5}$$

Assuming linear-elastic behavior of the material, the stresses and strains are related through the material constitutive law: $\boldsymbol{\tau} = \mathbb{C}\,\boldsymbol{\epsilon}$, where $\mathbb{C} : \mathbb{R}^6 \to \mathbb{R}^6$ maps strains into stresses.

The latter equations all contain references to entities which could be considered as objects. In particular, a natural class with which to begin the description of finite elements is `Node` (point in space), since forces, displacements, boundary conditions, and even the domain geometry rely on nodes.

The `Node` class is defined by a unique number identifier from $\mathrm{n} = 1, \ldots, \mathrm{N_n}$, and the private member variables `Coordinates`, `Displacements`, `Velocity`, `Acceleration`, and `IncrementalDisplacements`, are employed to keep track on the node's motion. Public member functions, such as `GetCoordinates` and `GetDisplacements`, return the nodal vector with such quantities. As it is discussed later on, these vectors are employed in the `Element` class to update properties such as stiffness matrix, local coordinates, Jacobian matrix and so on. Also, a

public member function `SetFreeDegreeOfFreedom` is required to map the equation numbers to the degree of freedom in the `Solver` class, and a member function `SetIncrementalDisplacement` is responsible to update the incremental displacements that come from solving the linear system at each node.

The `Load` class can be defined in a similar manner. We identify each `Load` object by a unique number identifier $\mathrm{l} = 1, \ldots, \mathrm{N_l}$, and a list of `Node` or `Element` objects is provided to identify where the `Load` object is applied. Thus, public member functions such as `AddNode`, and `AddElement` allow the class to incorporate forces to these objects, and methods such as `GetNode`, `GetElement`, and `GetLoadVector` allow the class to construct the load vector at the applied `Node` or `Element` class.

Principle of virtual work

The displacement-based finite element solution is based on the principle of virtual displacements, see Bathe [16]. The principle of virtual displacements is a functional[1] $\mathcal{F}[\mathbf{U}, \overline{\mathbf{U}}] : \mathcal{U} \times \mathcal{V} \to \mathbb{R}$ that represents the first variation of the total potential energy, and in our case for linear elasticity reads,

$$\int_{\mathrm{V}} \overline{\boldsymbol{\epsilon}}^{\top} \mathbb{C}\, \boldsymbol{\epsilon}\, d\mathrm{V} = \int_{\mathrm{V}} \overline{\mathbf{U}}^{\top} \mathbf{f}_b\, d\mathrm{V} + \int_{\mathrm{S}} \overline{\mathbf{U}}^{\top} \mathbf{f}_s\, d\mathrm{S} + \sum_{\mathrm{i}=1}^{\mathrm{N}} \overline{\mathbf{U}}^{\top} \mathbf{F}_{\mathrm{i}}\,, \tag{2.6}$$

where $\overline{\mathbf{U}} \in \mathcal{V} \subset \mathbb{R}^3$ are the virtual displacements and $\overline{\boldsymbol{\epsilon}}$ the corresponding virtual strains. See for instance Bathe [16] for further details on how the functional in (2.6) is obtained.

However, in the finite element analysis we approximate the continuum body in Figure 2.1 as an assemblage of discrete finite elements interconnected at nodal points. The displacements within each element are assumed to be related to the global displacement vector by a displacement interpolation matrix in local coordinates. In this regard, the approximate displacement field at e-th element is

$$\mathbf{u}^{\mathrm{e}}(x_1, x_2, x_3) = \mathbf{N}^{\mathrm{e}}(x_1, x_2, x_3)\, \hat{\mathbf{U}}\,, \tag{2.7}$$

where $\mathbf{N}^{\mathrm{e}} : \mathbb{R}^{\mathrm{N}^{\mathrm{e}}_{\mathrm{dof}}} \to \mathbb{R}^3$ is the displacement interpolation matrix of the e-th element, $\hat{\mathbf{U}} \in \mathbb{R}^{\mathrm{N}^{\mathrm{e}}_{\mathrm{dof}}}$ is a vector of the three global displacement components of the nodal points of the element, and $\mathrm{N}^{\mathrm{e}}_{\mathrm{dof}}$ is the number of degree-of-freedom for the e-th element.

[1] A functional is a special type of mapping which maps from a function space $\mathcal{U}$ to $\mathbb{R}$, in other words $I : u \in \mathcal{U} \to I[u] \in \mathbb{R}$.

Provided with Equation (2.7), the strains within each element can be evaluated as

$$\boldsymbol{\epsilon}^{\mathrm{e}}(x_1, x_2, x_3) = \mathbf{B}^{\mathrm{e}}(x_1, x_2, x_3)\,\hat{\mathbf{U}}, \tag{2.8}$$

where $\mathbf{B}^{\mathrm{e}} : \mathbb{R}^{\mathrm{N}^{\mathrm{e}}_{\mathrm{dof}}} \longrightarrow \mathbb{R}^6$ is the strain-displacement matrix obtained using differentiation as in Equation (2.4).

Lastly, the principle of virtual displacement in Equation (2.6) can be approximated as a summation over all elements

$$\sum_{\mathrm{e}=1}^{\mathrm{N_e}} \int_{\mathrm{V}^{\mathrm{e}}} \overline{\boldsymbol{\epsilon}^{\mathrm{e}}}^{\top} \mathbb{C}^{\mathrm{e}} \boldsymbol{\epsilon}^{\mathrm{e}}\, d\mathrm{V}^{\mathrm{e}} = \sum_{\mathrm{e}=1}^{\mathrm{N_e}} \int_{\mathrm{V}^{\mathrm{e}}} \overline{\mathbf{U}^{\mathrm{e}}}^{\top} \mathbf{f}_b^{\mathrm{e}}\, d\mathrm{V}^{\mathrm{e}} + \sum_{\mathrm{e}=1}^{\mathrm{N_e}} \int_{\mathrm{S}^{\mathrm{e}}} \overline{\mathbf{U}^{\mathrm{e}}}^{\top} \mathbf{f}_s^{\mathrm{e}}\, d\mathrm{S}^{\mathrm{e}} + \sum_{\mathrm{i}=1}^{N} \overline{\mathbf{U}^{\mathrm{e}}}^{\top} \mathbf{F}_{\mathrm{i}}^{\mathrm{e}}. \tag{2.9}$$

In defining the principle of virtual displacement, we note that a new object is introduced. The `Material` class is then required to estimate the strain energy associated within an element. Moreover, internal properties such as strains and tangent stiffness matrix must be obtained from this class.

The `Material` class is defined by a unique number identifier $\mathrm{m} = 1, \ldots, \mathrm{N_m}$, and elastic properties such as elasticity modulus, Poisson's ratio, density are specified at each derived class. The member functions `CopyMaterial` are employed to establish a link between the `Element` class and the `QuadratureRule` class for the numerical integration. Other public member functions such as `GetStress` and `GetTangentStiffness` are required to compute the `Element` internal energy, and for nonlinear analyses, member functions, such as `UpdateState` to store the strain at the material level for the current analysis step, and `CommitState` to save the last strain as the final value (usually when converge is reached), are required as well.

Equilibrium equations

The inertial terms can be easily incorporated in Equation (2.6), and after substitution of the approximated displacement field (2.7) and strain-displacement relationships (2.8), the dynamic linear equilibrium equations become,

$$\mathbf{M}\ddot{\mathbf{U}} + \mathbf{K}\mathbf{U} = \mathbf{F}, \tag{2.10}$$

where the stiffness and mass matrices $\mathbf{K}, \mathbf{M} \in \mathbb{R}^{\mathrm{N_{free}} \times \mathrm{N_{free}}}$ are defined as

$$\mathbf{K} = \sum_{\mathrm{e}=1}^{\mathrm{N_e}} \int_{\mathrm{V}^{\mathrm{e}}} \mathbf{B}^{\mathrm{e}}(x_1, x_2, x_3)^{\top} \mathbb{C}^{\mathrm{e}}\, \mathbf{B}^{\mathrm{e}}(x_1, x_2, x_3)\, d\mathrm{V}^{\mathrm{e}}, \tag{2.11}$$

$$\mathbf{M} = \sum_{e=1}^{N_e} \int_{V^e} \mathbf{N}^e(x_1, x_2, x_3)^\top \rho^e \, \mathbf{N}^e(x_1, x_2, x_3) \, dV^e \,, \tag{2.12}$$

and the force vector $\mathbf{F} \in \mathbb{R}^{N_{free}}$ is defined as

$$\begin{aligned} \mathbf{F} = & \sum_{e=1}^{N_e} \int_{V^e} \mathbf{N}^e(x_1, x_2, x_3)^\top \mathbf{f}_b^e \, dV^e + \quad \text{(body force in } V \subset \mathbb{R}^3) \\ & \sum_{e=1}^{N_e} \int_{S^e} \mathbf{N}^e(x_1, x_2, x_3)^\top \mathbf{f}_s^e \, dS^e + \quad \text{(surface traction on } S \subset \mathbb{R}^2) \\ & \sum_{i=1}^{N} \mathbf{N}^e(x_1^{(i)}, x_2^{(i)}, x_3^{(i)})^\top \mathbf{F}_i^e \qquad \text{(point force at } \mathbf{x}^{(i)} \in \mathbb{R}^3), \end{aligned} \tag{2.13}$$

and $\mathbf{U}, \ddot{\mathbf{U}} \in \mathbb{R}^{N_{free}}$ represents the nodal displacement and acceleration vectors respectively, and N_{free} the number of free degree of freedom–i.e., after applying restraints/constraints.

We now see that each element contributes to the generation of the dynamic equilibrium equation in (2.10); then, the definition of the `Element` class is here required. The `Element` class is defined by a unique number identifier from $e = 1, \ldots, N_e$, and it must provide functions such as `ComputeStiffnessMatrix`, `ComputeInternalForces`, and `ComputeDomainReductionForces` to evaluate at the element level the desired quantities. Additionally, the natural binding between `Material`, `Node`, and `Element` classes is achieved through the public member function `SetDomain` that establishes the link between the `Nodes` objects that forms the `Element`, and the dependence of the `Element` and `Material` is achieved through the public member function `UpdateState` to provide the material with the strains computed in one iteration, and `CommitState` to set the converged material strains at the final iteration step.

Isoparametric elements

The geometrical transformation of an element into its reference coordinate system is shown in Figure 2.2. This transformation is based on the description of the coordinates of any point x_1, x_2, x_3 inside the element in terms of shape functions $\mathbf{N}_i(\xi, \eta, \zeta)$ written in reference coordinates. The values of the j-th element nodal coordinates $x_j^{(i)}$ is written in natural coordinates as:

$$x_j^e(\xi, \eta, \zeta) = \sum_{i=1}^{N_n} x_j^{(i)} \, \mathbf{N}_i^e(\xi, \eta, \zeta) \,. \tag{2.14}$$

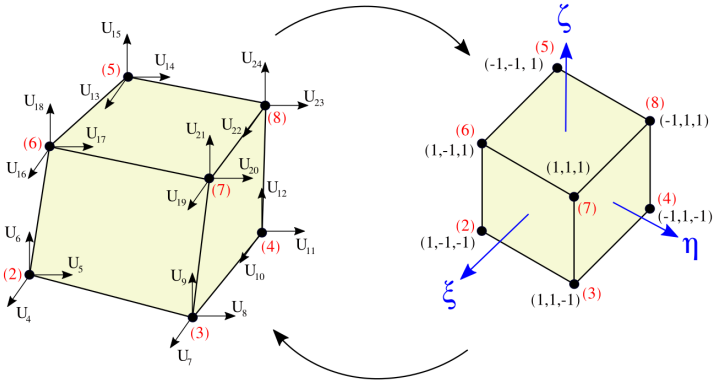

Figure 2.2: The isoparametric coordinate transformation.

If the same transformation is used to evaluate the displacements within the element, the same shape function routines may be applied to obtain $u_j^e(\xi, \eta, \zeta)$. Then, the design of an element class could take advantage of this simplification, and then approximate the displacement field as

$$u_j^e(\xi, \eta, \zeta) = \sum_{i=1}^{N_n} u_j^{(i)} \mathbf{N}_i^e(\xi, \eta, \zeta)\,. \tag{2.15}$$

Since both the displacement field and the point element coordinates are approximated using the same shape function, this formulation is commonly known as isoparametric transformation.

Computation of the strain-displacement matrix $\mathbf{B}^e(x_1, x_2, x_3)$ now requires to be mapped into the reference coordinate systems. Application of the chain rule for differentiation to the shape functions yields

$$\begin{bmatrix} \frac{\partial N_i}{\partial \xi} \\ \frac{\partial N_i}{\partial \eta} \\ \frac{\partial N_i}{\partial \zeta} \end{bmatrix} = \begin{bmatrix} \frac{\partial x}{\partial \xi} & \frac{\partial y}{\partial \xi} & \frac{\partial z}{\partial \xi} \\ \frac{\partial x}{\partial \eta} & \frac{\partial y}{\partial \eta} & \frac{\partial z}{\partial \eta} \\ \frac{\partial x}{\partial \zeta} & \frac{\partial y}{\partial \zeta} & \frac{\partial z}{\partial \zeta} \end{bmatrix} \begin{bmatrix} \frac{\partial N_i}{\partial x} \\ \frac{\partial N_i}{\partial y} \\ \frac{\partial N_i}{\partial z} \end{bmatrix} = \mathbf{J} \begin{bmatrix} \frac{\partial N_i}{\partial x} \\ \frac{\partial N_i}{\partial y} \\ \frac{\partial N_i}{\partial z} \end{bmatrix}, \tag{2.16}$$

where $\mathbf{J} : \mathbb{R}^3 \rightarrow \mathbb{R}^3$ is called the Jacobian matrix. Hence, derivatives in Equation (2.4) can be used to evaluate $\mathbf{B}^e(\xi, \eta, \zeta)$ in the reference coordinates.

The isoparametric transformation has the advantage that every element is treated in the same manner. In this regard, mass and stiffness matrices as well as force vector

are evaluated using the same reference coordinates as follows

$$\mathbf{M}^{\mathrm{e}} = \int_{-1}^{1}\int_{-1}^{1}\int_{-1}^{1} \mathbf{N}^{\mathrm{e}}(\xi,\eta,\zeta)^{\top}\, \rho^{\mathrm{e}}\, \mathbf{N}^{\mathrm{e}}(\xi,\eta,\zeta) \det \mathbf{J}^{\mathrm{e}}\, d\xi\, d\eta\, d\zeta\,, \tag{2.17}$$

$$\mathbf{K}^{\mathrm{e}} = \int_{-1}^{1}\int_{-1}^{1}\int_{-1}^{1} \mathbf{B}^{\mathrm{e}}(\xi,\eta,\zeta)^{\top}\, \mathbb{C}^{\mathrm{e}}\, \mathbf{B}^{\mathrm{e}}(\xi,\eta,\zeta) \det \mathbf{J}^{\mathrm{e}}\, d\xi\, d\eta\, d\zeta\,, \tag{2.18}$$

$$\mathbf{F}^{\mathrm{e}} = \int_{-1}^{1}\int_{-1}^{1}\int_{-1}^{1} \mathbf{N}^{\mathrm{e}}(\xi,\eta,\zeta)^{\top}\, \mathbf{F}^{\mathrm{e}}_{b} \det \mathbf{J}^{\mathrm{e}}\, d\xi\, d\eta\, d\zeta\,, \tag{2.19}$$

where $\mathbf{M}^{\mathrm{e}}, \mathbf{K}^{\mathrm{e}} \in \mathbb{R}^{\mathrm{N}^{\mathrm{e}}_{\mathrm{dof}} \times \mathrm{N}^{\mathrm{e}}_{\mathrm{dof}}}$, and $\mathbf{F}^{\mathrm{e}} \in \mathbb{R}^{\mathrm{N}^{\mathrm{e}}_{\mathrm{dof}}}$.

Note that an isoparametric element requires the `Element` class to be provided with additional private member functions. In this regard, `ComputeJacobianMatrix`, `ComputeShapeFunctionMatrix`, and `ComputeStrainDisplacementMatrix` are implemented such that the requested quantities at a given integration point in the reference coordinate system are evaluated. These private functions are used internally, and their implementation may change depending on the derived isoparametric `Element` class that is defined.

Numerical integration

In § 2.1, mass and stiffness matrices as well as force vectors are evaluated using numerical integration. These integrals for each element can be approximated as

$$\int_{-1}^{1}\int_{-1}^{1}\int_{-1}^{1} \mathbf{\Phi}(\xi,\eta,\zeta)\, d\xi\, d\eta\, d\zeta = \sum_{\mathrm{k}=1}^{\mathrm{N_p}}\sum_{\mathrm{j}=1}^{\mathrm{N_p}}\sum_{\mathrm{i}=1}^{\mathrm{N_p}} \omega_{\mathrm{i}}\, \omega_{\mathrm{j}}\, \omega_{\mathrm{k}}\, \mathbf{\Phi}(\xi_{\mathrm{i}},\eta_{\mathrm{j}},\zeta_{\mathrm{k}})\,, \tag{2.20}$$

where $\mathbf{\Phi}(\xi,\eta,\zeta) : \mathbb{R}^3 \to \mathbb{R}$ represents the function in isoparametric coordinates to be integrated, $\omega_{\mathrm{i}}, \omega_{\mathrm{j}}, \omega_{\mathrm{k}} \in \mathbb{R}$ are the integration weights, $\xi_{\mathrm{i}}, \eta_{\mathrm{j}}, \zeta_{\mathrm{k}} \in \mathbb{R}^3$ the integration point coordinates, and $\mathrm{N_p}$ the number of integration points.

The `QuadratureRule` class contains references to the total number of integration points (used to decide how much storage to allocate), as well as to the actual points and weights. These quantities are obtained using the public member function `GetQuadraturePoints`. This information is used inside the `Element` class to compute the stiffness/mass/damping matrices as well as force vector using numerical integration as described above.

Matrices assembly

Once mass and stiffness matrices and the force vector has been computed for each element, Equation (2.10) can be constructed using an assembler operator in a two-

steps procedure:

$$\mathbf{M} = \mathbf{T}^\top \left[\sum_{e=1}^{N_e} \mathbf{A}^{e\top} \mathbf{M}^e \mathbf{A}^e \right] \mathbf{T} = \mathbf{T}^\top \mathcal{M} \mathbf{T},$$
$$\mathbf{K} = \mathbf{T}^\top \left[\sum_{e=1}^{N_e} \mathbf{A}^{e\top} \mathbf{K}^e \mathbf{A}^e \right] \mathbf{T} = \mathbf{T}^\top \mathcal{K} \mathbf{T},$$
$$\mathbf{F} = \mathbf{T}^\top \left[\sum_{e=1}^{N_e} \mathbf{A}^{e\top} \mathbf{F}^e \right] = \mathbf{T}^\top \mathcal{F}. \tag{2.21}$$

First, the assembly operator $\mathbf{A}^e : \mathbb{R}^{N^e_{dof}} \longrightarrow \mathbb{R}^{N_{total}}$ assembles the element matrix/vector to the total matrix/vector. Then, the transformation operator $\mathbf{T} : \mathbb{R}^{N_{total}} \longrightarrow \mathbb{R}^{N_{free}}$ enforces the displacement boundary condition as well as kinematic constraints applied to some number of degree of freedom.

The contribution of each `Element` object in Equation (2.9) is performed in the `Assembler` class. The `Assembler` class provides the public member functions: `ComputeMassMatrix`, `ComputeStiffnessMatrix`, `ComputeInternalForceVector`, and `ComputeExternalForceVector` which are in charge of assembling the global matrices/vectors, respectively. This process requires information regarding the degree of freedom of each `Node` and the list of `Elements`. Both lists are provided by the `Mesh` class, which also provides the transformation operator from total-degree-of-freedom numbering to free-degree-of-freedom numbering. This operator enforces `Node` displacement restraints and kinematic constraints specified by the user.

Solution of equilibrium equations

In general, Equation (2.10) is solved using some discrete integration schemes. Popular time integration schemes, such as central difference [16], Newmark constant acceleration [117], Bathe two-step implicit method [17], can be used in their incremental form to yield,

$$\mathbf{K}_{\text{eff}} \, \Delta\mathbf{U} = \mathbf{F}_{\text{eff}} \tag{2.22}$$

where $\mathbf{K}_{\text{eff}} \in \mathbb{R}^{N_{free} \times N_{free}}$ is the effective stiffness matrix, and $\mathbf{F}_{\text{eff}} \in \mathbb{R}^{N_{free}}$ is the effective force vercor. The structure of $\mathbf{K}_{\text{eff}}$ and $\mathbf{F}_{\text{eff}}$ depends on the incremental integration scheme.

Note that solving Equation (2.10) is reduced to solving a linear system for each time step. However, depending on the nonlinearities encountered (material, large

deformation), the solution of Equation (2.22) may require iterations. Then, a suitable nonlinear fixed-point algorithm such as Newton-Raphson may be required.

The solution of the equilibrium equations requires three different classes to handle very specific tasks:

(a) The `Algorithm` class handles the solution of the linear/nonlinear system incrementally. The private member variable `ConvergenceTest` provides the criterion to be performed to accept a solution. This variable requests the private member function `ReduceParallelResidual` to gather all the information across and reconstruct the residual vector, so that `ComputeConvergence` evaluates the norm of the residual vector. The solution algorithm uses the `ComputeNewIncrement` member function to solve the linearized problem at that step, while `UpdateStateIncrement` accumulates the incremental displacements obtained at each iteration.

(b) The `Integrator` class is defined to evolve the solution in time. If the solution is nonlinear, moving from one time step to another may require several iterations at the `Algorithm` level. Therefore, the function `ComputeNewStep` evolves the solution just one time step, and `ComputeEffectiveStiffness` and `ComputeEffectiveForce` construct the effective stiffness matrix and effective force vector to be transferred to the `Algorithm` class at each iteration. Member function such as `GetDisplacements`, `GetVelocities`, and `GetAcceleration` are required to compute and return the desired solution vector using the specific time integration of each method.

(c) The `LinearSystem` class is defined to solve the linear system provided with the effective stiffness matrix and effective force vector evaluated using the `Integrator` object. The private member variables are the solution and the effective force vector, while the member function `GetSolution` returns the solution of the linear system.

The definition of the previous classes allows enough modularity to further define the `Analysis` class, whose derived class will be in charge of performing the static or dynamic analysis. Note that both analyses only differ on the `Integrator` that is employed, since inertial forces are not considered in static analysis.

2.2 The object-oriented analysis

Several object-oriented programming (OOP) designs have been proposed for the finite element method [47, 53, 107, 114]. Most of them use the same class names (`Node`, `Material`, `Element`, `Solver` to name a few) and the interactions between them are similar. However, the structures in which the `Analysis` is performed varies from case to case. It is not our intention in this work to describe each one of them. However, we consider the widely used open system for earthquake engineering simulation (OpenSEES) software [114] as a reference, and we try to improve features that we consider are bottle-neck in the maintainability and extendability of OpenSEES. The reader may consider for instance:

(a) The OOP framework of OpenSEES employs roughly 1100 different classes that makes difficult to add new features, since several files must be updated.

(b) Provides built-in classes to handle collection of nodes and elements instead of using the fully optimized Standard Template Library (STL) [137], in particular `std::vector<>` and `std::map<>` that achieve the same objective.

(c) Provides built-in `Vector` and `Matrix` classes which are not optimized, instead of taking advantage of well-developed and optimized free-libraries such as the Eigen C++ Template Library [60].

(d) The provided Makefile is not very intuitive and in general the installation on Linux and MacOSX machines is cumbersome, in particular the SP and MP versions.

Therefore, in order to provide a software design that actually promotes the maintainability and extendability of Seismo-VLAB, we have employed a fewer number of classes avoiding the overuse of sub-classes definitions and inheritance that are actually not needed. Until now, Seismo-VLAB has 78 classes divided as follows:

(a) 12 Materials

(b) 18 Sections

(c) 24 Elements

(d) 2 Analysis

(e) 2 Algorithms

(f) 4 Integrators

(g) 4 Solvers

We use the fully optimized STL [137] to handle containers of data and operations over it. We employ the fully-optimized Eigen C++ Template Library [60] to carry out linear algebra manipulations. This library offers a great interface that allows the user to create, operate, and transform `Eigen::VectorXd` and `Eigen::MatrixXd` objects as it were using Matlab [109] or Python [152] languages, incentivizing the modification and creation of other classes in a very simple manner. In addition, we are aware that manipulation of data in a Pre-Analysis level can become complicated in a low-level language, thus we provide a Python interface so that model's input file, spatial variability analysis, as well as parameter identification can be generated externally in a much cleaner and straightforward manner.

In order to optimize all the previous requirements, we have divided the structure of Seismo-VLAB into two main processes: the Pre-Analysis and the Run-Analysis that are shown schematically in Figure 2.3.

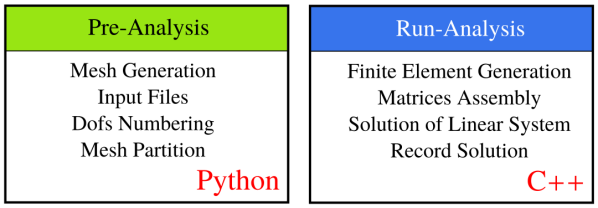

Figure 2.3: Seismo-VLAB global software structure. The Pre-Analysis is an interface that provides the files to be executed, and the Run-Analysis is the main core that performs the finite element analysis.

Because flexibility is needed to generate input files, domain (mesh) partition, degree of freedom numbering, spatial variability of soil/structure properties, and parameter identification, we have used a high-level language such as Python [152] to handle the Pre-Analysis main tasks. Python offers the possibility to manipulate externally the Run-Analysis in a very straightforward manner, and thus abstracting the user from complicated manipulation in a low-level language. The popular and user-friendly features that Python provides makes it the perfect choice.

On the other hand, the Run-Analysis is the core of Seismo-VLAB and needs to be fast and efficient; therefore, we have used a low-level language such as C++ [143] to

handle these requirements. The Run-Analysis performs the finite element analysis– i.e., generates the element matrices, assembles them together, solves the linear system, and stores the solution according to the user's specifications. Figure 2.4 shows the main abstract classes employed to develop the Run-Analysis.

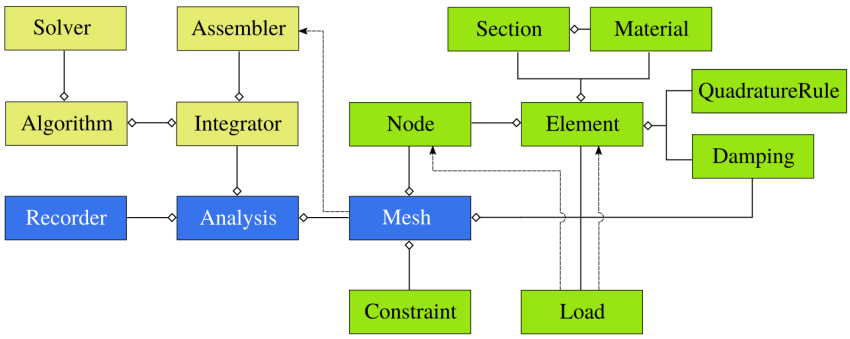

Figure 2.4: Seismo-VLAB software packages for finite element analysis. Classes represented in boxes are abstract classes. Developers can provide their own subclasses to personalize applications.

In this diagram, the diamond arrow that arrives at an abstract class represents an internal relation between them, for example the `Element` class is formed by `Node` and `Material`. The point arrow that arrives at an abstract class represents a dependency between them, for example a `Load` is given to an `Element` to compute external forces. The diagram also represents in blue boxes the main classes (core) of Seismo-VLAB. These components are divided into the `Mesh`, `Analysis`, and `Recorder` classes. The `Mesh` class contains the finite element model, and as one can see, the FE components are represented by the group of green boxes. These components are: `Node`, `Material`, `Section`, `Element`, `Load`, and `Constraint`. In general, a set of `Node` and a `Material` forms an `Element`. The stiffness/mass/damping matrices of the element are computed using numerical integration, i.e.`QuadratureRule`. The `Analysis` class contains the instructions or modifications to be performed in the finite element model, thus the group of yellow boxes represents the components of the `Analysis` class of Seismo-VLAB, i.e. the `Solver`, `Algorithm`, and `Integrator` are employed to carry out an analysis.

However, the structure represented in Figure 2.4 is only well-suited for single core machines, but its extension to parallel machines is straight forward using OpenMPI [30, 35, 54, 71]. This process is achieved at the Pre-Analysis using Metis [86]. Metis allows to partition the finite element mesh in an almost equal number of elements–

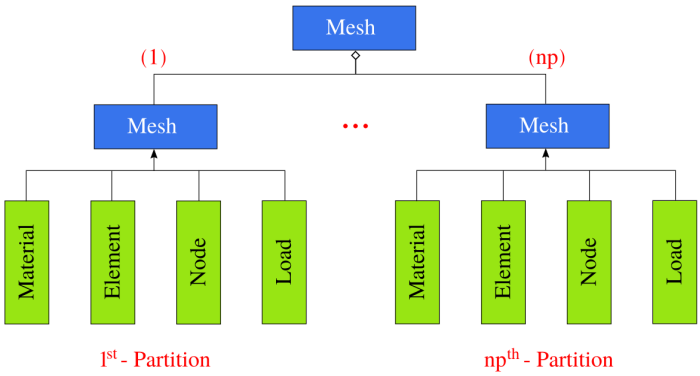

Figure 2.5: The classes required to be partitioned for a parallel execution of Seismo-VLAB. The classes represented correspond to the objects required to be sent to the k-th processor.

i.e., minimizing the load imbalance[2]. Then, each partition is sent to a different processor using openMPI. Since in OpenMPI each process will act independently, all the information required to generate the mesh partition in the k-th processor must be provided. Figure 2.5 provides a conceptual representation of the main classes required to be partitioned. We have decided to generate the `Mesh` partitions and the degree of freedom numbering off-line, using once again the Pre-Analysis implemented in Python. This allows Seismo-VLAB to be run almost fully parallel, avoiding the user to make mistakes by partitioning the domain manually. The `Mesh` partition can be easily checked using Paraview [10] after executing the Pre-Analysis.

Software external packages

In order to obtain good performance at the `Element` level, specifically in tasks involving numerical integration, the well-developed and optimized open-source library Eigen C++ Template Library [60] is employed throughout the Run-Analysis in Seismo-VLAB. The advantage of using Eigen C++ is two-fold: (a) It minimizes the debugging process since the structure of matrices and vector operations are similar to those in Matlab and Python, see § 2.3 for details. (b) It is already optimized – comparison against the Intel Math Kernel Library (MKL) are simply outstanding – especially in ranges where matrices $\mathbb{R}^{n\times n}$ and vectors $\mathbb{R}^n$ are not too large, i.e., $n \leq 500$. This is indeed the main usage of Eigen C++ in Seismo-VLAB.

In addition, scalability of parallel implementation for large simulations is usually

[2] A load imbalance is the uneven distribution of work across processors. The load imbalance can impact scalability if it is not taken into consideration.

subjected to the solver–i.e., solving the linear system, which in general is performed using a direct solver that exploits LDL decomposition. A very optimized library that solves linear systems using LDL-decomposition is the **MU**ltifrontal **M**assively **P**arallel sparse direct **S**olver (MUMPS) [4, 5]. The structure in which MUMPS solves a linear system is well-suited with the domain decomposition structure presented in Figure 2.5. Thus, if parallel simulations are run in Seismo-VLAB, the MUMPS solver is chosen to deal with this task. Unfortunately, MUMPS is optimal only for medium to large problems, since very large problems will not only require a large number of processors, but also a long time of execution.

Nevertheless, very large problems can be approached using iterative solvers. The Krylov space methods [133, 134] for solving linear systems turn out to be very efficient at the expense of accuracy. In particular, a conjugate gradient method [45] is the best option when using symmetric and positive definite matrices. In this regard, a very optimized library that solves linear systems using Krylov space methods is the **P**ortable and **E**xtensible **T**oolkit for **S**cientific **c**omputation (PETSc) [11–13]. Once again, the structure in which PETSc solves a linear system is well-suited with the domain decomposition structure presented in Figure 2.5. Thus, the PETSc solver for parallel simulation in Seismo-VLAB is ideal to deal with this task. Therefore, the preconditioned conjugate gradient (PCG), stabilized version of Bi-Conjugate gradient (BiCGStab), conjugate Gradient Squared (CGS), and Bi-Conjugate gradient iterative method (BiCG) are available in Seismo-VLAB. These versions are very optimized, and it provides good-agreement and speedups for a given tolerance.

2.3 Seismo-VLAB: Style, performance and extensions

In this section, features presented in Seismo-VLAB are tested using a range of simple to sophisticated examples. A comparison of the software performance in terms of speedup, memory management (leaks), and code style are also provided and compared against widely used OpenSEES. Furthermore, strong scaling performance is measured for a 2D wave propagation problem, and performance of MUMPS and PETSc are measured for a 3D soil-structure interaction problem.

Code structure and style

For an open source code to be extendable, the programming style must be simple to read and simple to write. Thus, good-coding practice–i.e., appropriate commenting, well-formatted code, self-explanatory variable names, and simple class definition,

are essential to promote modifications in any open source code. In Seismo-VLAB, the Eigen C++ Template library provides structures of matrices and vector operations that are similar to those in Matlab [110] and Python [152]. This Eigen's feature encourages users to perform modifications. Also, classes are implemented in Seismo-VLAB so that they avoid methods that are too complex (too long), with too many parameters (or local variables), and abuse of multiple inheritances.

Code 2.1: Isoparametric element stiffness matrix computation in Seismo-VLAB.

```
1  //Compute the stiffness matrix of the element using Gauss-integration.
2  Eigen::MatrixXd lin3DHexa8::ComputeStiffnessMatrix(void){
3    //Element stiffness matrix definition:
4    Eigen::MatrixXd StiffnessMatrix(24,24);
5    StiffnessMatrix.fill(0.0);
6
7    //Gets the quadrature information.
8     Eigen::VectorXd wi;
9     Eigen::MatrixXd xi;
10    QuadraturePoints->GetQuadraturePoints("Hexa", wi, xi);
11
12   //Compute element stiffness matrix as in Equation (2.18).
13   for(unsigned int i = 0; i < nPoints; i++){
14     //Jacobian matrix.
15     Eigen::MatrixXd Jij = ComputeJacobianMatrix(xi(i,0), xi(i,1), xi(i,2));
16
17     //Compute Strain-Displacement Matrix at Gauss Point.
18     Eigen::MatrixXd Bij = ComputeStrainDisplacementMatrix(xi(i,0), xi(i,1), xi(i,2), Jij);
19
20     //Gets material tangent matrix at Gauss point.
21     Eigen::MatrixXd Cij = theMaterial[i]->GetTangentStiffness();
22
23     //Numerical integration in Equation (2.20).
24     StiffnessMatrix += wi(i)*fabs(Jij.determinant())*Bij.transpose()*Cij*Bij;
25   }
26
27   return StiffnessMatrix;
28 }
```

The latter statement is clearer when the `Brick.cpp` implementation in OpenSEES, for computing the element stiffness matrix, is for instance analyzed. This task is performed in the public member function `Brick::getTangentStiff`, which internally calls a private function `Brick::formResidAndTangent` to compute the element stiffness matrix. A close inspection of the latter function reveals a poorly indented code, written in 216 lines, that only works for 8 Gauss integration points, in which multiple nested for-loops are required to perform the task. In addition, private member variable and public member function names are not very meaningful, and sometimes confusing, making even harder to understand the class.

A user tempted to modify this code may spend a few hours understanding the member function, variables, and their relation. In Seismo-VLAB, the same task is performed in the public member function `lin3DHexa8::ComputeStiffnessMatrix`. This function is provided in Code 1, and essentially translates Equation (2.18) and (2.20) into C++ Code. Note how the stiffness matrix process in Code 1 shows a short, well-indented, and self-explanatory member function, where local variable names are chosen such that it helps the understanding of the task being developed.

Code 2.2: Stiffness matrix assembly process used in Seismo-VLAB.

```
1  //Assemble stiffness matrix.
2  Eigen::SparseMatrix<double> Assembler::ComputeStiffnessMatrix(Mesh *mesh){
3    //Global stiffness matrix.
4    Eigen::SparseMatrix<double> StiffnessMatrix(numberOfTotalDofs,numberOfTotalDofs);
5
6    //Gets element information from the mesh.
7    std::map<unsigned int, Element*> Elements = mesh->GetElements();
8
9    //Assemblage stiffness matrix process:
10   unsigned int sum = 0;
11   for(std::map<int, Element*>::iterator it = Elements.begin(); it != Elements.end(); ++it){
12     unsigned int Tag = it->first;
13
14     //Gets the element degree-of-freedom connectivity.
15     std::vector<unsigned int> dofs = Elements[Tag]->GetTotalDegreeOfFreedom();
16
17     //Assemble contribution of each element in mesh (apply 'A' operator in Equation (2.21)).
18     Eigen::MatrixXd Ke = Elements[Tag]->ComputeStiffnessMatrix();
19     for(unsigned int j = 0; j < dofs.size(); j++){
20       for(unsigned int i = 0; i < dofs.size(); i++){
21         if(fabs(Ke(i,j)) > StiffnessTolerance){
22           tripletList[sum] = T(dofs[i], dofs[j], Ke(i,j));
23           sum++;
24         }
25       }
26     }
27   }
28
29   //Builds the total sparse stiffness sparse matrix in Equation (2.10).
30   StiffnessMatrix.setFromTriplets(tripletList.begin(), tripletList.begin() + sum);
31
32   //Impose boundary conditions on stiffness matrix (apply 'T' operator in Equation (2.21)).
33   StiffnessMatrix = Total2FreeMatrix.transpose()*StiffnessMatrix*Total2FreeMatrix;
34
35   return StiffnessMatrix;
36 }
```

Additionally, and in order to stress the importance of code readability, in Code 2 we examine the `Assembler` class, and in particular the `ComputeStiffnessMatrix` member function. This member function essentially translates Equations (2.10)

and (2.21) into C++ code. Here, we easily observe that the stiffness matrix $\mathbf{K} \in \mathbb{R}^{N_{total} \times N_{total}}$ is allocated, element information is obtained from the mesh, and a loop over the elements is performed. Each element is required to return its stiffness matrix $\mathbf{K}^e \in \mathbb{R}^{N^e_{dof} \times N^e_{dof}}$, and the element matrix coefficients that are larger than some tolerance are stored in a triplet, to be used to form the stiffness matrix. Finally, restraints and constraints are applied to generate $\mathbf{K} \in \mathbb{R}^{N_{free} \times N_{free}}$ as in Equation (2.10).

Hardware description for numerical analyses

In this sub-section, we provide the CPU specifications in which all numerical analyses are performed. The Intel Xeon CPU E5-2687 is a normal workstation that has GPU enable capabilities that are not specified. Further details can be found at www.intel.com/content/www/us/en/products/processors/xeon.html.

Architecture	:	x86_64
CPU op-mode(s)	:	64-bit
CPU(s)	:	40
On-line CPU(s) list	:	0-39
Thread(s) per core	:	2
Core(s) per socket	:	10
Socket(s)	:	2
NUMA node(s)	:	2
Vendor ID	:	GenuineIntel
Model name	:	Intel(R) Xeon(R) CPU E5-2687W v3 @ 3.10GHz
CPU MHz	:	1269.062
BogoMIPS	:	6191.42

Table 2.1: Hardware description used in all analyses throughout this thesis.

Performance, memory management, and leaks

We first study the performance of Seismo-VLAB in solving wave equations for analysis of an earth dam problem shown schematically in Figure 2.6 (a). To this end, we solve the same problem in OpenSEES, and to make the comparisons rational, we use a conventional approach for defining transmitting boundaries – i.e., using Lysmer-Kuhlemeyer dashpots [106] with prescribed nodal forces in terms of the incident wave velocity along the far-field boundary [8].

The finite element mesh in Figure 2.6 (b) has 57770 degrees of freedom in total, 28885 nodes are used to generate the mesh discretization, thus 28847 elements, 203

boundary nodal forces are applied, and 1501 time steps are required for the simulation. The maximum absolute displacement, velocity, and acceleration throughout the simulation are $(0.0095, 0.0046)$ m, $(0.2323, 0.1206)$ m/s, and $(5.0887, 3.3455)$ m/s^2. The maximum absolute[3] displacement, velocity, and acceleration errors are: 5.0E-11, 5.0E-9, 7.0E-8, respectively.

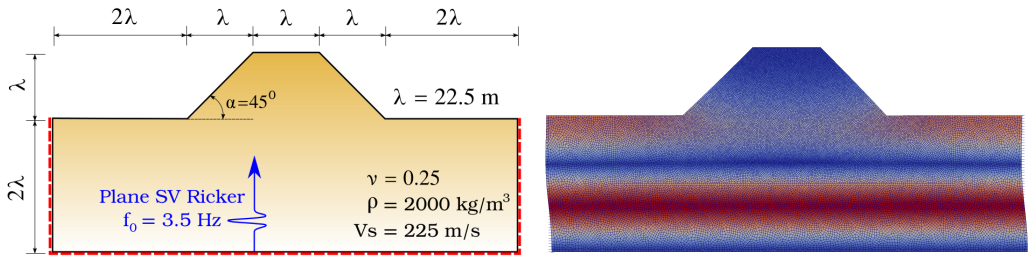

Figure 2.6: The earth dam problem geometry considered to validate Seismo-VLAB against OpenSEES. The red dashed-line represents where Lysmer-Kuhlemeyer dashpots are added.

In addition, Table 2.2 shows the statistics of each code in solving this problem.

Software	**Time** [min]	**RAM** [MB]	**Leaks** [MB]
Seismo-VLAB	23.0	220.1	0.0
OpenSEES	283.5	825.1	0.9
Performance	~ 12×	~ 4×	–

Table 2.2: Performance comparison between Seismo-VLAB and OpenSEES. Speed-up, maximum memory usage, and memory leaks for a single core execution.

We see in Table 2.2 that Seismo-VLAB is not only 10 times faster, but also uses almost 4 times less RAM memory during the program execution when is compared to OpenSEES. In addition, to test parallel capabilities of Seismo-VLAB, we solve the same problem using different number of processors. Figure 2.7 shows the strong scaling analysis where the horizontal axis shows the number of processors while the vertical axis is the speedup obtained compared to the best single core case. Figure 2.7 shows that Seismo-VLAB also scales linearly for a number of processors less than 8. This behavior is indeed expected since the earth dam problem is not large

[3]The maximum absolute error between two vectors $\mathbf{x}, \hat{\mathbf{x}} \in \mathbb{R}^n$ is defined in the following manner: $\mathsf{e} = \max_j \|\mathbf{x}^j - \hat{\mathbf{x}}^j\|_{\ell^\infty} = \max_{i,j} \|x_i^j - \hat{x}_i^j\|$, where $j = 1, \ldots, n_t$ is the time step, and $i = 1, \ldots, n$ the vector component.

enough to be solved using a larger number of domain partitions. The increase in the number of partitions causes overhead in the communication between processors at the linear system solution, generating a decrease in the speedup. However, a speedup of 13× is still reached for 16 processors, which correspond to 80% of the optimal parallel efficiency.

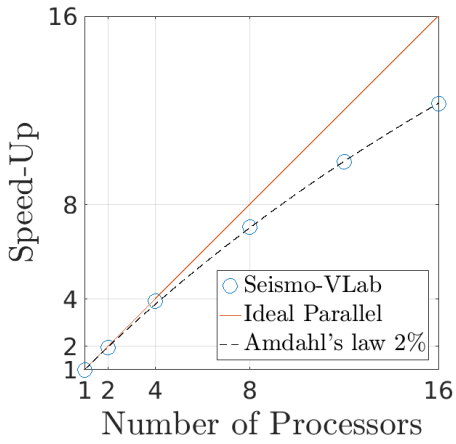

Figure 2.7: Seismo-VLAB strong scaling performance (up to 16 processors) obtained for the earth dam problem.

As a second example, we study the performance of Seismo-VLAB for solving a full-fidelity linear soil-structure interaction problem. The finite element mesh considered in this analysis is shown schematically in Figure 2.8 (a), and in Figure 2.8 (b) we represent the domain partitioning performed for 8 processors.

The mesh has 121944 nodes in total, 105825 elements divided as follows: 2164 `lin3DFrame2`, 7388 `lin3DShell4`, and 96273 `lin3DHexa8` and `PML3DHexa8` elements. In addition, 7 different materials and 19 different sections are employed to define both soil and building domain. The connections between shell/frame and solid as well as PML and soil elements are performed through kinematics constraints [42, 80]. Then, 26247 `Constraints` are used in order to tie the model together. The SSI problem has around 380000 degrees of freedom in total, thus can be considered as a large model[4] according to McKenna [112] that requires HPC[5]. However, we

[4]Our strong desire is to achieve solving finite element models greater than 1000000 degree of freedom, so that structure-soil-structure interaction problems can be solved in a reasonable amount of time on a workstation.

[5]High Performance Computing refers to combine computing power in a way that delivers much higher performance than typical desktop computer or workstation in order to solve large problems in science and engineering.

perform the analysis in a workstation, and we solve the same problem using different numbers of processors.

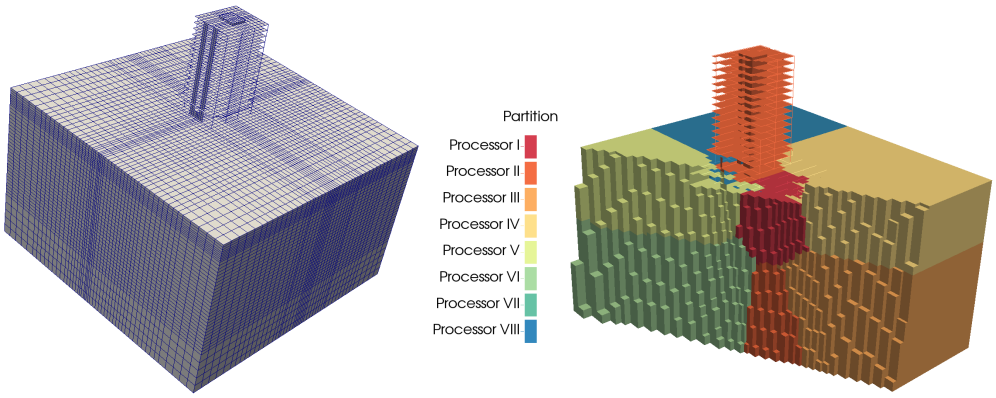

Figure 2.8: A real three-dimensional SSI problem using DRM and PML to study strong scaling performance. (Left) the finite element mesh used in this analysis, and (Right) example of the domain partition in eight processors.

We compare the performance between MUMPS (direct LDL-decomposition) and PETSc (iterative conjugate gradient with Jacobi preconditioner) solvers. We assess the time used for the `Assembler`, `Solver`, and `Recorder` in one time step. The results for MUMPS and PETSc are shown in Table 2.3 and 2.4, respectively.

	MUMPS			Total
	Assembler	Solver	Recorder	Time
n_p	[s]	[s]	[s]	[s]
1	9.78	348.75	0.95	360.05
2	5.08	184.59	0.50	196.17
4	2.62	112.22	0.25	120.02
8	1.45	78.98	0.13	81.57
16	0.78	56.98	0.07	58.78

Table 2.3: MUMPS' elapsed time during the `Assembler`, `Solver`, and `Recorder` for one step for the solution of $\mathbf{K}_{\text{eff}}\,\Delta\mathbf{U} = \mathbf{F}_{\text{eff}}$ using different number of processors.

Both Table 2.3 and 2.4 show that the `Assembler` and `Recorder` scales linearly. This should not be surprising since METIS partition minimizes the load-imbalance. Thus, the generation of element matrices, and then their assemblage is almost uniform across processors. The same can be inferred from the `Recorder` since almost the same amount of data is being written in each processor. Unfortunately, as

	PETSc			Total
	Assembler	Solver	Recorder	Time
n_p	[s]	[s]	[s]	[s]
1	9.72	43.23	0.95	60.02
2	5.03	22.19	0.56	30.81
4	2.41	14.40	0.25	18.40
8	1.43	9.31	0.13	11.55
16	0.76	7.45	0.08	8.35

Table 2.4: PETSc's elapsed time during the `Assembler`, `Solver`, and `Recorder` for one step for the solution of $\mathbf{K}_{\text{eff}}\,\Delta\mathbf{U} = \mathbf{F}_{\text{eff}}$ using different number of processors.

it can be seen in Table 2.3 and 2.4, the `Solver` becomes the bottle-neck in Seismo-VLAB. Notice for the MUMPS solver, performance deteriorates as the number of processors increases. It is known that direct solvers do not perform well in 3D problems, since the complexity is $O(n^2)$. For 16 processors, Seismo-VLAB only reaches 38% of the parallel efficiency. Nevertheless, the PETSc solver performance improves as the number of processors increases. Again, it is known that iterative solvers perform better in 3D problems, since the complexity is $O(\kappa n)$, where κ is the condition number. Thus, for 16 processors, Seismo-VLAB reaches 45% of the parallel efficiency. The important idea to get from Table 2.3 and 2.4 is that one-full iteration takes around 8.0 seconds with 16 processors, which for a full dynamic analysis using 1500 time steps requires 3 hours and 30 minutes, which is a reasonable time for a large model as the one presented here.

The results in term of speed-up are shown in Table 2.5. Note in this table how iterative solvers show a better performance compared against direct solvers.

	MUMPS			PETSc		
	Time	Speed-Up	Efficiency	Time	Speed-Up	Efficiency
n_p	[s]	×	%	[s]	×	%
1	360.05	1.00	100	60.02	1.00	100
2	196.17	1.84	92	30.81	1.95	97
4	120.02	3.00	75	18.04	3.33	83
8	81.57	4.41	55	11.55	5.20	65
16	58.78	6.13	38	8.35	7.19	45

Table 2.5: Performance comparison between MUMPS and PETSc for multiple core execution. Speed-up and parallel efficiency are measured for one time step.

The strong scaling analysis is shown in Figure 2.9 for both MUMPS and PETSc.

The horizontal axis shows the number of processors, while the vertical axis is the speedup obtained compared to the best single core case.

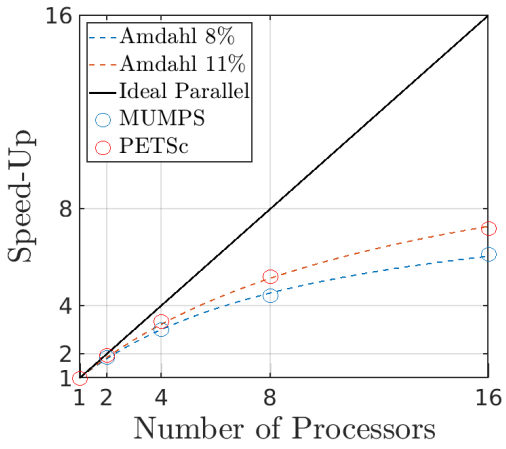

Figure 2.9: Seismo-VLAB strong scaling performance for MUMPS and PETSc (up to 16 processors) obtained for the full fidelity SSI problem.

Lastly, both solvers require different amounts of RAM. The model solved using MUMPS experiences a maximum RAM usage of 4.9 GB[6] during the LDL factorization, while the CG experiences a maximum RAM usage of 2.8 GB during the vector parallel reduction. The latter result is not surprising since the CG only requires matrix-vector multiplications, and LDL requires to store half of the full matrix while performing the Cholesky decomposition. Finally, scalability is strongly subjected to the solver phase rather than assembly, finite element generation, or writing output files. In Seismo-VLAB, 95%[7] of the computation time is spent during MUMPS solution, while 86% of the computation time is spent during PETSc CG solution. The latter behavior is often found in implicit integration schemes using direct solvers. However, explicit schemes provide an alternative to avoid solving a linear system at the expense of small time steps. This feature can be exploit for wave-propagation problems, but it may not be well suited when complex buildings are considered due to absence of mass for some degrees of freedom, ill-conditioning from stiff-spring constraints, etc. This is a feature that has not been implemented in Seismo-VLAB, but it will be considered in the near future.

[6]Memory obtained using valgrind –tool=massif as explained in [130].
[7]Percentages obtained using valgrind –tool=callgrind as explained in [130].

Conclusions

In this chapter, Seismo-VLAB, a simple, fast, and extendable C++ FEM for solving mesoscale soil-structure interaction problems was introduced. Seismo-VLAB allows new elements, materials, integrators, and algorithms to be incorporated in a simple manner. The object-oriented framework allows to add new features as a derived class inside the folder where the parent class is located.

Since the Eigen C++ library resembles languages such as Matlab and Python, any user can add, modify, and create functions or routines in Seismo-VLAB in a simple manner. In this regard, the Eigen C++ library allows simple manipulations at the element, material, quadrature integration level, and therefore, contributes to Seismo-VLAB's extendability.

Comparison against the OpenSEES reveals that Seismo-VLAB is not only faster, but also manages memory better, and has no leaks. Also, the model's manipulation through the Python Pre-Analysis is simple, and allows any user to create, import, modify, and manipulate any finite element model, incentivizing large FE model generations. In our experience, the Python Pre-Analysis can easily manipulate about 1000000 elements in a couple of minutes.

Lastly, Seismo-VLAB scales well as long as the solver does. It is important to keep in mind that direct solvers are well-suited for 2D problems and 3D problems only if the Cholesky decomposition needs to be performed once. On the other hand, iterative solvers (based on Krylov-subspace) are better-suited for 3D problems, and therefore are faster than direct solvers.

Chapter 3

SIMULATION OF WAVE PROPAGATION IN HETEROGENEOUS HALF-SPACE

In geotechnical engineering, the finite element method (FEM) [16, 70, 123, 141] is one of the preferred methodology to approximate the linear and nonlinear response in wave propagation problems. The literature has constantly shown that software that uses the FEM can capture, with enough accuracy, the responses shown in physical experiments [127, 132, 136]. In particular, high-accurate wave propagation simulations are obtained when both spatially variable ground motion and complex velocity field patterns are properly replicated [2, 80]. The latter can be achieved for instance by adding appropriate absorbing boundary conditions around the near-field and appropriate forcing stress fields able to transmit the ground motion of an incident propagating wave inside the near-field domain. In particular, the domain reduction method (DRM) proposed by Bielak et all [24] is a modular two-step finite element methodology used for transmitting ground motion in heterogeneous media. This method allows to reduce the size of the near-field region drastically and thus focus the analysis only on the motion near the features. However, suitable absorbing boundaries conditions must be provided to limit the occurrence of spurious waves that are reflected from the far-field boundaries. The absorption of scattered waves is achieved through perfectly matched layer (PML) elements. In this formulation, a finite-sized layer that surrounds the near-field and stretched internal spatial coordinates are employed in order to mimic the effects of the semi-infinite domain it replaces. Specifically, the absorbing boundaries proposed by Kucukcoban and Kallivokas [51, 95] for plane-strain in two and three dimensions are formulated in such a way that can be included in a finite element framework in a straightforward manner. Therefore, an efficient, reliable and robust numerical platform for high-fidelity simulation of wave propagation in heterogeneous half-spaces must consider these two features.

In this chapter, a brief review on the domain reduction method and a perfectly matched layer formulation for absorbing boundaries are first presented. These two sections are next used in order to derive a coupled formulation for domain reduction and perfectly matched layer to be integrated in a finite element framework. Lastly, some examples using the coupled finite element framework for high-fidelity

simulation of wave propagation in heterogeneous half-spaces are discussed.

3.1 The domain reduction method

The domain reduction method (DRM) proposed by Bielak et all [24] is a modular two-step finite element methodology for transmitting ground motion in heterogeneous media. In this method, the model is first divided into an auxiliary problem that simulates the source and propagation without the localized features. The outputs of such problem are then used in order to derive effective forces and then applied to a second model which now contains the localized features. In other words, the domain reduction method allows to define a new problem in which the excitation (far-field) is brought closer to the region of interest (near-field).

Suppose an effective excitation, as shown in Figure 3.1b, is to be applied on the fictitious interface Γ_{NF} in a finite element domain. This interface divides the domain into two parts: Ω_N which contains the features (near-field), and Ω_F the semi-infinite exterior sub-domain, which includes the fault (far-field). Let the vector field of nodal displacements $\mathbf{u}^s(\mathbf{x}, t) = [u_i^R, u_b^R, u_e^R]^\top$ in the complete domain–i.e., $\Omega_S = \Omega_N \cup \Omega_F$ be ordered as u_i^R (interior), u_e^R (exterior), and u_b^R (boundary), where the superscript "R" stands for real domain. Note that, as shown in Figure 3.1, the displacements u_b^R are continuous across Γ_{NF}, and P_b^R are the nodal forces transmitted by Ω_F onto Ω_N.

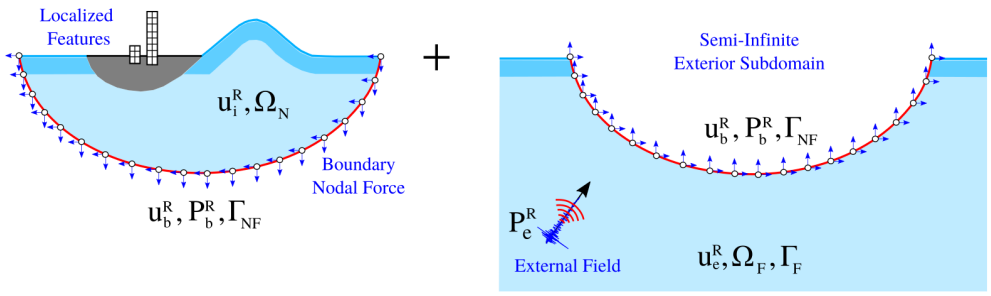

Figure 3.1: Truncated seismic region partitioned explicitly into two sub-domains across interface Γ_{NF} where P_b^R are nodal forces transmitted from Ω_F onto Ω_N. (a) The domain Ω_N contains the features (near-field), and (b) the domain Ω_F the semi-infinite exterior sub-domain which includes the fault (far-field).

In § 4.1 and § 4.2, we present the Navier's equation for wave propagating in soil, and a proper treatment for discretizing the partial differential equation (PDE) is provided through finite element analysis (FEA). For now, assume that in Ω_N the

Navier's equation of wave propagation can be discretized as:

$$\begin{bmatrix} \mathbf{M}_{ii}^{\Omega_N} & \mathbf{M}_{ib}^{\Omega_N} \\ \mathbf{M}_{bi}^{\Omega_N} & \mathbf{M}_{bb}^{\Omega_N} \end{bmatrix} \begin{bmatrix} \ddot{u}_{\mathrm{i}}^{\mathrm{R}} \\ \ddot{u}_{\mathrm{b}}^{\mathrm{R}} \end{bmatrix} + \begin{bmatrix} \mathbf{C}_{ii}^{\Omega_N} & \mathbf{C}_{ib}^{\Omega_N} \\ \mathbf{C}_{bi}^{\Omega_N} & \mathbf{M}_{bb}^{\Omega_N} \end{bmatrix} \begin{bmatrix} \dot{u}_{\mathrm{i}}^{\mathrm{R}} \\ \dot{u}_{\mathrm{b}}^{\mathrm{R}} \end{bmatrix} + \begin{bmatrix} \mathbf{K}_{ii}^{\Omega_N} & \mathbf{K}_{ib}^{\Omega_N} \\ \mathbf{K}_{bi}^{\Omega_N} & \mathbf{K}_{bb}^{\Omega_N} \end{bmatrix} \begin{bmatrix} u_{\mathrm{i}}^{\mathrm{R}} \\ u_{\mathrm{b}}^{\mathrm{R}} \end{bmatrix} = \begin{bmatrix} 0 \\ P_{\mathrm{b}}^{\mathrm{R}} \end{bmatrix}, \tag{3.1}$$

and in Ω_{F} the Navier's equation is also discretized as:

$$\begin{bmatrix} \mathbf{M}_{bb}^{\Omega_F} & \mathbf{M}_{be}^{\Omega_F} \\ \mathbf{M}_{eb}^{\Omega_F} & \mathbf{M}_{ee}^{\Omega_F} \end{bmatrix} \begin{bmatrix} \ddot{u}_{\mathrm{b}}^{\mathrm{R}} \\ \ddot{u}_{\mathrm{e}}^{\mathrm{R}} \end{bmatrix} + \begin{bmatrix} \mathbf{C}_{ii}^{\Omega_F} & \mathbf{C}_{ib}^{\Omega_F} \\ \mathbf{C}_{bi}^{\Omega_F} & \mathbf{M}_{bb}^{\Omega_F} \end{bmatrix} \begin{bmatrix} \dot{u}_{\mathrm{b}}^{\mathrm{R}} \\ \dot{u}_{\mathrm{e}}^{\mathrm{R}} \end{bmatrix} + \begin{bmatrix} \mathbf{K}_{bb}^{\Omega_F} & \mathbf{K}_{be}^{\Omega_F} \\ \mathbf{K}_{eb}^{\Omega_F} & \mathbf{K}_{ee}^{\Omega_F} \end{bmatrix} \begin{bmatrix} u_{\mathrm{b}}^{\mathrm{R}} \\ u_{\mathrm{e}}^{\mathrm{R}} \end{bmatrix} = \begin{bmatrix} -P_{\mathrm{b}}^{\mathrm{R}} \\ P_{\mathrm{e}}^{\mathrm{R}} \end{bmatrix}. \tag{3.2}$$

The matrices $\mathbf{M}$, $\mathbf{C}$, and $\mathbf{K}$ denote mass, damping, and stiffness matrices, and the subscripts "i," "e," and "b" refer to nodes in either the interior, exterior, or on their common boundary. Note that the traditional form of the equation of motion in Ω_{S} is obtained by adding Equation (3.1) and (3.2):

$$\begin{bmatrix} \mathbf{M}_{ii}^{\Omega_N} & \mathbf{M}_{ib}^{\Omega_N} & \mathbb{O} \\ \mathbf{M}_{bi}^{\Omega_N} & \mathbf{M}_{bb}^{\Omega_N} + \mathbf{M}_{bb}^{\Omega_F} & \mathbf{M}_{be}^{\Omega_F} \\ \mathbb{O} & \mathbf{M}_{eb}^{\Omega_F} & \mathbf{M}_{ee}^{\Omega_F} \end{bmatrix} \begin{bmatrix} \ddot{u}_{\mathrm{i}}^{\mathrm{R}} \\ \ddot{u}_{\mathrm{b}}^{\mathrm{R}} \\ \ddot{u}_{e}^{\mathrm{R}} \end{bmatrix} + \begin{bmatrix} \mathbf{C}_{ii}^{\Omega_N} & \mathbf{C}_{ib}^{\Omega_N} & \mathbb{O} \\ \mathbf{C}_{bi}^{\Omega_N} & \mathbf{C}_{bb}^{\Omega_N} + \mathbf{C}_{bb}^{\Omega_F} & \mathbf{C}_{be}^{\Omega_F} \\ \mathbb{O} & \mathbf{C}_{eb}^{\Omega_F} & \mathbf{C}_{ee}^{\Omega_F} \end{bmatrix} \begin{bmatrix} \dot{u}_{\mathrm{i}}^{\mathrm{R}} \\ \dot{u}_{\mathrm{b}}^{\mathrm{R}} \\ \dot{u}_{\mathrm{e}}^{\mathrm{R}} \end{bmatrix} +$$
$$\begin{bmatrix} \mathbf{K}_{ii}^{\Omega_N} & \mathbf{K}_{ib}^{\Omega_N} & \mathbb{O} \\ \mathbf{K}_{bi}^{\Omega_N} & \mathbf{K}_{bb}^{\Omega_N} + \mathbf{K}_{bb}^{\Omega_F} & \mathbf{K}_{be}^{\Omega_F} \\ \mathbb{O} & \mathbf{K}_{eb}^{\Omega_F} & \mathbf{K}_{ee}^{\Omega_F} \end{bmatrix} \begin{bmatrix} u_{\mathrm{i}}^{\mathrm{R}} \\ u_{\mathrm{b}}^{\mathrm{R}} \\ u_{\mathrm{e}}^{\mathrm{R}} \end{bmatrix} = \begin{bmatrix} 0 \\ 0 \\ P_{\mathrm{e}}^{\mathrm{R}} \end{bmatrix}, \tag{3.3}$$

where $\mathbb{O} \in \mathbb{R}^{\mathrm{n_i} \times \mathrm{n_e}}$ represents a matrix of zeroes, and $\mathrm{n_i}$ and $\mathrm{n_e}$ the total number of interior and exterior degree-of-freedom, respectively.

Now, to transfer the seismic excitation from the fault to the boundary Γ_{NF}, we consider an auxiliary problem in which the exterior region and the material, as well as the causative fault, are identical with those of the original problem. The interior domain, now denoted as Ω_B, is, however, a simpler background model, that does not include the localized geological features as illustrated in Figure 3.2a. Notice that Ω_{B} is chosen such that the new problem defined over the total domain $\Omega_{\mathrm{B}} \cup \Omega_{\mathrm{F}}$ is easier to solve than the original problem. We thus use the superscript B to denote the background model, and $u_{\mathrm{i}}^{\mathrm{B}}$ (interior), $u_{\mathrm{e}}^{\mathrm{B}}$ (exterior), and $u_{\mathrm{b}}^{\mathrm{B}}$ (boundary), and $P_{\mathrm{b}}^{\mathrm{B}}$ the corresponding nodal displacements and the interface forces as shown in Figure 3.2b.

Then, for the background problem in the far-field Ω_{F}, we have,

$$\begin{bmatrix} \mathbf{M}_{bb}^{\Omega_F} & \mathbf{M}_{be}^{\Omega_F} \\ \mathbf{M}_{eb}^{\Omega_F} & \mathbf{M}_{ee}^{\Omega_F} \end{bmatrix} \begin{bmatrix} \ddot{u}_{\mathrm{b}}^{\mathrm{B}} \\ \ddot{u}_{\mathrm{e}}^{\mathrm{B}} \end{bmatrix} + \begin{bmatrix} \mathbf{C}_{bb}^{\Omega_F} & \mathbf{C}_{be}^{\Omega_F} \\ \mathbf{C}_{eb}^{\Omega_F} & \mathbf{C}_{ee}^{\Omega_F} \end{bmatrix} \begin{bmatrix} \dot{u}_{\mathrm{b}}^{\mathrm{B}} \\ \dot{u}_{\mathrm{e}}^{\mathrm{B}} \end{bmatrix} + \begin{bmatrix} \mathbf{K}_{bb}^{\Omega_F} & \mathbf{K}_{be}^{\Omega_F} \\ \mathbf{K}_{eb}^{\Omega_F} & \mathbf{K}_{ee}^{\Omega_F} \end{bmatrix} \begin{bmatrix} u_{\mathrm{b}}^{\mathrm{B}} \\ u_{\mathrm{e}}^{\mathrm{B}} \end{bmatrix} = \begin{bmatrix} -P_{\mathrm{b}}^{\mathrm{B}} \\ P_{\mathrm{e}}^{\mathrm{B}} \end{bmatrix}. \tag{3.4}$$

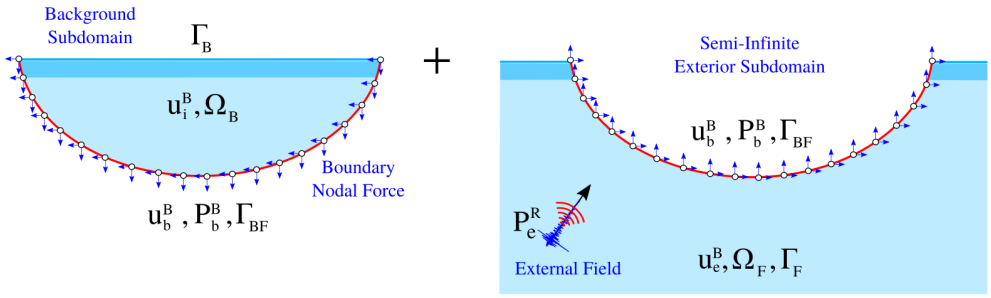

(a) (b)

Figure 3.2: Auxiliary truncated seismic region partitioned explicitly into two sub-structures across interface Γ_{BF} where P_b^B are nodal forces transmitted from Ω_F onto Ω_B. (a) Localized features of the actual problem in Ω_N have been replaced by a simpler background model over domain Ω_B, and (b) the domain Ω_F is the semi-infinite exterior sub-domain which includes the fault defined identical to Ω_F.

Note that the partitioned mass, damping, and stiffness matrices, as well as P_e^B, are the same as in Equation (3.2) because the material properties in Ω_F and the earthquake source are identical in both cases. Therefore, from the second Equation (3.4), we can now express the nodal forces P_e^B in terms of the free field, as follows:

$$P_e^B = \mathbf{M}_{eb}^{\Omega_F} \ddot{u}_b^B + \mathbf{M}_{ee}^{\Omega_F} \ddot{u}_e^B + \mathbf{C}_{eb}^{\Omega_F} \dot{u}_b^B + \mathbf{C}_{ee}^{\Omega_F} \dot{u}_e^B + \mathbf{K}_{be}^{\Omega_F} u_b^B + \mathbf{K}_{ee}^{\Omega_F} u_e^B \,. \tag{3.5}$$

We introduce a change of variables w_e^R, by which we express the total displacement u_e^R as the sum of the free field due to the background structure and the residual field due to the localized feature:

$$u_e^R = u_e^B + w_e^R, \tag{3.6}$$

where w_e^N is the relative displacement (residual) field with respect to the reference free field u_e^B. Then, substituting Equation (3.6) into Equation (3.3), and writing the terms that contain the free field on the right side, results in:

$$\begin{bmatrix} \mathbf{M}_{ii}^{\Omega_N} & \mathbf{M}_{ib}^{\Omega_N} & \mathbb{O} \\ \mathbf{M}_{bi}^{\Omega_N} & \mathbf{M}_{bb}^{\Omega_N} + \mathbf{M}_{bb}^{\Omega_F} & \mathbf{M}_{be}^{\Omega_F} \\ \mathbb{O} & \mathbf{M}_{eb}^{\Omega_F} & \mathbf{M}_{ee}^{\Omega_F} \end{bmatrix} \begin{bmatrix} \ddot{u}_i^R \\ \ddot{u}_b^R \\ \ddot{w}_e^R \end{bmatrix} + \begin{bmatrix} \mathbf{C}_{ii}^{\Omega_N} & \mathbf{C}_{ib}^{\Omega_N} & \mathbb{O} \\ \mathbf{C}_{bi}^{\Omega_N} & \mathbf{C}_{bb}^{\Omega_N} + \mathbf{C}_{bb}^{\Omega_F} & \mathbf{C}_{be}^{\Omega_F} \\ \mathbb{O} & \mathbf{C}_{eb}^{\Omega_F} & \mathbf{C}_{ee}^{\Omega_F} \end{bmatrix} \begin{bmatrix} \dot{u}_i^R \\ \dot{u}_b^R \\ \dot{w}_e^R \end{bmatrix} +$$
$$\begin{bmatrix} \mathbf{K}_{ii}^{\Omega_N} & \mathbf{K}_{ib}^{\Omega_N} & \mathbb{O} \\ \mathbf{K}_{bi}^{\Omega_N} & \mathbf{K}_{bb}^{\Omega_N} + \mathbf{K}_{bb}^{\Omega_F} & \mathbf{K}_{be}^{\Omega_F} \\ \mathbb{O} & \mathbf{K}_{eb}^{\Omega_F} & \mathbf{K}_{ee}^{\Omega_F} \end{bmatrix} \begin{bmatrix} u_i^R \\ u_b^R \\ w_e^R \end{bmatrix} = \begin{bmatrix} 0 \\ -\mathbf{M}_{be}^{\Omega_F} \ddot{u}_e^B - \mathbf{C}_{be}^{\Omega_F} \dot{u}_e^B - \mathbf{K}_{be}^{\Omega_F} u_e^B \\ P_e^B - \mathbf{M}_{ee}^{\Omega_F} \ddot{u}_e^B - \mathbf{C}_{ee}^{\Omega_F} \dot{u}_e^B - \mathbf{K}_{ee}^{\Omega_F} u_e^B \end{bmatrix}. \tag{3.7}$$

Finally, after substituting the force vector $P_{\mathrm{e}}^{\mathrm{R}}$ from Equation (3.5) into Equation (3.7), we obtain the desired equation:

$$\begin{bmatrix} \mathbf{M}_{ii}^{\Omega_{\mathrm{N}}} & \mathbf{M}_{ib}^{\Omega_{\mathrm{N}}} & \mathbb{O} \\ \mathbf{M}_{bi}^{\Omega_{\mathrm{N}}} & \mathbf{M}_{bb}^{\Omega_{\mathrm{N}}} + \mathbf{M}_{bb}^{\Omega_{\mathrm{F}}} & \mathbf{M}_{be}^{\Omega_{\mathrm{F}}} \\ \mathbb{O} & \mathbf{M}_{eb}^{\Omega_{\mathrm{F}}} & \mathbf{M}_{ee}^{\Omega_{\mathrm{F}}} \end{bmatrix} \begin{bmatrix} \ddot{u}_{\mathrm{i}}^{\mathrm{R}} \\ \ddot{u}_{\mathrm{b}}^{\mathrm{R}} \\ \ddot{\mathrm{w}}_{\mathrm{e}}^{\mathrm{R}} \end{bmatrix} + \begin{bmatrix} \mathbf{C}_{ii}^{\Omega_{\mathrm{N}}} & \mathbf{C}_{ib}^{\Omega_{\mathrm{N}}} & \mathbb{O} \\ \mathbf{C}_{bi}^{\Omega_{\mathrm{N}}} & \mathbf{C}_{bb}^{\Omega_{\mathrm{N}}} + \mathbf{C}_{bb}^{\Omega_{\mathrm{F}}} & \mathbf{C}_{be}^{\Omega_{\mathrm{F}}} \\ \mathbb{O} & \mathbf{C}_{eb}^{\Omega_{\mathrm{F}}} & \mathbf{C}_{ee}^{\Omega_{\mathrm{F}}} \end{bmatrix} \begin{bmatrix} \dot{u}_{\mathrm{i}}^{\mathrm{R}} \\ \dot{u}_{\mathrm{b}}^{\mathrm{R}} \\ \dot{\mathrm{w}}_{\mathrm{e}}^{\mathrm{R}} \end{bmatrix} +$$
$$\begin{bmatrix} \mathbf{K}_{ii}^{\Omega_{\mathrm{N}}} & \mathbf{K}_{ib}^{\Omega_{\mathrm{N}}} & \mathbb{O} \\ \mathbf{K}_{bi}^{\Omega_{\mathrm{N}}} & \mathbf{K}_{bb}^{\Omega_{\mathrm{N}}} + \mathbf{K}_{bb}^{\Omega_{\mathrm{F}}} & \mathbf{K}_{be}^{\Omega_{\mathrm{F}}} \\ \mathbb{O} & \mathbf{K}_{eb}^{\Omega_{\mathrm{F}}} & \mathbf{K}_{ee}^{\Omega_{\mathrm{F}}} \end{bmatrix} \begin{bmatrix} u_{\mathrm{i}}^{\mathrm{R}} \\ u_{\mathrm{b}}^{\mathrm{R}} \\ \mathrm{w}_{\mathrm{e}}^{\mathrm{R}} \end{bmatrix} = \begin{bmatrix} 0 \\ -\mathbf{M}_{be}^{\Omega_{\mathrm{F}}} \ddot{u}_{\mathrm{e}}^{\mathrm{B}} - \mathbf{C}_{be}^{\Omega_{\mathrm{F}}} \dot{u}_{\mathrm{e}}^{\mathrm{B}} - \mathbf{K}_{be}^{\Omega_{\mathrm{F}}} u_{\mathrm{e}}^{\mathrm{B}} \\ \mathbf{M}_{eb}^{\Omega_{\mathrm{F}}} \ddot{u}_{\mathrm{b}}^{\mathrm{B}} + \mathbf{C}_{eb}^{\Omega_{\mathrm{F}}} \dot{u}_{\mathrm{b}}^{\mathrm{B}} + \mathbf{K}_{eb}^{\Omega_{\mathrm{F}}} u_{\mathrm{b}}^{\mathrm{B}} \end{bmatrix}. \tag{3.8}$$

The mass matrix, damping, and stiffness matrices in the left hand side of Equation (3.8) are identical with those of Equation (3.3). However, the seismic forces $P_{\mathrm{e}}^{\mathrm{R}}$ on the fault have been replaced by the effective nodal forces P_{eff}, given by:

$$P_{\mathrm{eff}} = \begin{bmatrix} P_{\mathrm{i}}^{\mathrm{R}} \\ P_{\mathrm{b}}^{\mathrm{R}} \\ P_{\mathrm{e}}^{\mathrm{R}} \end{bmatrix} = \begin{bmatrix} 0 \\ -\mathbf{M}_{be}^{\Omega_{\mathrm{F}}} \ddot{u}_{\mathrm{e}}^{\mathrm{B}} - \mathbf{C}_{be}^{\Omega_{\mathrm{F}}} \dot{u}_{\mathrm{e}}^{\mathrm{B}} - \mathbf{K}_{be}^{\Omega_{\mathrm{F}}} u_{\mathrm{e}}^{\mathrm{B}} \\ \mathbf{M}_{eb}^{\Omega_{\mathrm{F}}} \ddot{u}_{\mathrm{b}}^{\mathrm{B}} + \mathbf{C}_{eb}^{\Omega_{\mathrm{F}}} \dot{u}_{\mathrm{b}}^{\mathrm{B}} + \mathbf{K}_{eb}^{\Omega_{\mathrm{F}}} u_{\mathrm{b}}^{\mathrm{B}} \end{bmatrix}. \tag{3.9}$$

The effective force vector in Equation (3.9) only involves the sub-matrices $\mathbf{M}_{be}^{\Omega_{\mathrm{F}}}$, $\mathbf{C}_{be}^{\Omega_{\mathrm{F}}}$, $\mathbf{K}_{be}^{\Omega_{\mathrm{F}}}$, $\mathbf{M}_{eb}^{\Omega_{\mathrm{F}}}$, $\mathbf{C}_{eb}^{\Omega_{\mathrm{F}}}$, and $\mathbf{K}_{eb}^{\Omega_{\mathrm{F}}}$, and its components vanish everywhere except in a single layer of finite elements in Ω_{F} adjacent to Γ_{NF}. Therefore, the effective force vector P_{eff} acts exclusively within that layer of elements. In addition, the only wave field needed to determine P_{eff} is that obtained from the auxiliary (background) problem at the nodes that lie on Γ_{NF}, Γ_{e}, and between these surfaces as shown in Figure 3.3. This localization of the equivalent seismic forces around the geologic feature is the key advantage of the change of variables in Equation (3.6).

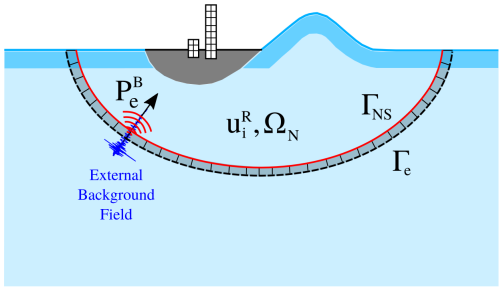

Figure 3.3: Seismic region with two neighboring surfaces Γ_{NL} and Γ_{e} on which effective nodal forces P_{eff} defined by Equation (3.9) are to be applied. These forces are equivalent to and replace the original seismic forces P_{e}^{R} , which act in the vicinity of the causative fault.

Finally, another important consequence of Equation (3.9) is that all the waves in the exterior region Ω_F will be outgoing. This suggests that for solving Equation (3.8), the size of the region Ω_N can be drastically reduced if one is interested only in the motion near the features, provided with suitable absorbing boundaries conditions used to limit the occurrence of spurious waves.

3.2 Hybrid formulation of perfectly matched layer for truncated domain

Kucukcoban and Kallivokas [51, 95] proposed a fully-mixed symmetric PML formulation for both plane-strain and three-dimensional problems. In this formulation, displacement and stress fields are considered as primary fields in both the regular domain and PMLs. In this section, we are concerned only with two-dimensional plane-strain problems.

The governing equations

Without loss of generality, consider a linear elastic an homogeneous soil medium in Ω_S, surrounded by a perfectly matched layer in Ω_A as shown in Figure 3.4.

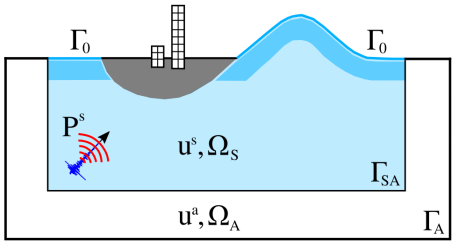

Figure 3.4: The problem geometry and boundary conditions of a perfectly matched layer for truncated domain in a plane-strain setting.

The elastic wave equation in the regular domain Ω_s in absence of body force is:

$$\operatorname{div} \boldsymbol{\sigma}^s(\mathbf{u}^s(\mathbf{x},t)) = \rho_s\, \ddot{\mathbf{u}}^s(\mathbf{x},t) \;\text{ in } \Omega_S\,, \tag{3.10}$$

where $\mathbf{x} = (x_1, x_2)$ is a point coordinate inside Ω_s and $t \in (0, T]$ is the defined time interval; $\boldsymbol{\sigma}^s(\mathbf{u}^s) = \mu\left(\nabla\mathbf{u}^s + (\nabla\mathbf{u}^s)^\top\right) + \lambda \operatorname{div}(\mathbf{u}^s)\mathbf{I}$ is the stress tensor, $\mathbf{I}$ is the second-rank identity tensor, ρ_s is the soil density, and λ and μ are the Lamé constants for an elastic solid. Their relationships with the Young's modulus (E) and the Poisson's ratio (ν) are given as

$$\lambda = \frac{E\,\nu}{(1+\nu)(1-2\nu)}\,, \tag{3.11}$$

and,

$$\mu = \frac{E}{2(1+\nu)}\,. \tag{3.12}$$

In the PML domain Ω_{A}, where the wave is attenuated, the wave motion is governed by the following partial differential equations:

$$\operatorname{div}\left(\dot{\mathbf{S}}^{\top}\Lambda_{\mathrm{E}} + \mathbf{S}^{\top}\Lambda_{\mathrm{P}}\right) - \rho_a\left(a\,\ddot{\mathbf{u}}^a + b\,\dot{\mathbf{u}}^a + c\,\ddot{\mathbf{u}}^a\right) = 0\,, \tag{3.13}$$

$$\begin{aligned}\Lambda_{\mathrm{E}}^{\top}\left(\mathbb{D}:\ddot{\mathbf{S}}\right)\Lambda_{\mathrm{E}} + \Lambda_{\mathrm{E}}^{\top}\left(\mathbb{D}:\dot{\mathbf{S}}\right)\Lambda_{\mathrm{P}} + \Lambda_{\mathrm{P}}^{\top}\left(\mathbb{D}:\dot{\mathbf{S}}\right)\Lambda_{\mathrm{E}} + \Lambda_{\mathrm{E}}^{\top}\left(\mathbb{D}:\mathbf{S}\right)\Lambda_{\mathrm{P}} - \\ \frac{1}{2}\left(\Lambda_{\mathrm{P}}^{\top}\nabla\mathbf{u}^a + (\nabla\mathbf{u}^a)^{\top}\Lambda_{\mathrm{P}}^{\top}\right) - \frac{1}{2}\left(\Lambda_{\mathrm{E}}^{\top}\nabla\dot{\mathbf{u}}^a + (\nabla\dot{\mathbf{u}}^s)^{\top}\Lambda_{\mathrm{E}}^{\top}\right) = 0\,,\end{aligned} \tag{3.14}$$

where the superscript "a" denotes the attenuated domain, the constants $a = \alpha_1\alpha_2$, $b = \alpha_1\beta_2 + \alpha_2\beta_1$, $c = \beta_1\beta_2$, and $\mathbf{S}$ denotes the stress-history tensor defined as

$$\mathbf{S} = \int_0^t \boldsymbol{\sigma}^a(\mathbf{u}^a(\mathbf{x},\tau))d\tau\,, \tag{3.15}$$

$\mathbb{D}$ denotes the fourth-order compliance tensor such that

$$\boldsymbol{\epsilon}(\mathbf{x},t) = \mathbb{D}:\dot{\mathbf{S}}(\mathbf{x},t)\,, \tag{3.16}$$

and the coordinate stretching tensors Λ_{E}, and Λ_{P} in Equation (3.13) are:

$$\Lambda_{\mathrm{E}} = \begin{bmatrix}\alpha_2 & 0\\ 0 & \alpha_1\end{bmatrix},\ \Lambda_{\mathrm{P}} = \begin{bmatrix}\beta_2 & 0\\ 0 & \beta_1\end{bmatrix}. \tag{3.17}$$

Equation (3.10) valid in Ω_{S} and Equation (3.13) valid in Ω_{A} are coupled through the following kinematic conditions,

$$\mathbf{u}^s(\mathbf{x},t) = \mathbf{u}^a(\mathbf{x},t)\ \text{ on } \Gamma_{\mathrm{SA}}\,, \tag{3.18}$$

$$\boldsymbol{\sigma}^s(\mathbf{u}^s(\mathbf{x},t))\,\hat{\mathbf{n}}_s = -\left(\dot{\mathbf{S}}\Lambda_{\mathrm{E}} + \mathbf{S}\Lambda_{\mathrm{P}}\right)\hat{\mathbf{n}}_a\ \text{ on } \Gamma_{\mathrm{SA}}\,, \tag{3.19}$$

where $\hat{\mathbf{n}}_s$ and $\hat{\mathbf{n}}_a$ denote the normal vectors on boundary Γ_{SA} and pointing outwards.

The governing wave equations are also subject to fixed boundary conditions:

$$\mathbf{u}^s(\mathbf{x},t) = 0\ \text{ on } \Gamma_{\mathrm{A}}\,, \tag{3.20}$$

$$\mathbf{u}^a(\mathbf{x},t) = 0\ \text{ on } \Gamma_{\mathrm{A}}\,, \tag{3.21}$$

and traction free boundary conditions:

$$\boldsymbol{\sigma}^s(\mathbf{u}^s(\mathbf{x},t))\,\hat{\mathbf{n}}_s = 0\ \text{ on } \Gamma_0\,, \tag{3.22}$$

$$\left(\dot{\mathbf{S}}^{\top}\Lambda_{\mathrm{E}} + \mathbf{S}^{\top}\Lambda_{\mathrm{P}}\right)\hat{\mathbf{n}}_a = 0\ \text{ on } \Gamma_0\,. \tag{3.23}$$

The semi-discrete form

The semi-discrete form consists of discretizing the partial differential equation (PDE) presented in Equations (3.10), (3.13), and (3.14) using finite element analysis (FEA). A proper treatment for achieving this can be found in Kucukcoban and Kallivokas (2013). For now, assume that the field variables of the two governing equations–i.e., Equations (3.10) and (3.13)–are written as follows:

$$\mathbf{u}(\mathbf{x},t) = \begin{bmatrix} \mathbf{u}^s(\mathbf{x},t) \\ \mathbf{u}^a(\mathbf{x},t) \end{bmatrix}, \text{ with } \mathbf{x} \in \Omega_{\mathrm{F}}, \tag{3.24}$$

$$\mathbf{S}(\mathbf{x},t) = \begin{bmatrix} S_{11}(\mathbf{x},t) & S_{12}(\mathbf{x},t) \\ S_{21}(\mathbf{x},t) & S_{22}(\mathbf{x},t) \end{bmatrix}, \text{ with } \mathbf{x} \in \Omega_{\mathrm{A}}, \tag{3.25}$$

where $\Omega_F = \Omega_S \cup \Omega_A$, and $\mathbf{u}^s(\mathbf{x},t)$, $\mathbf{u}^a(\mathbf{x},t)$, $S_{11}(\mathbf{x},t)$, $S_{22}(\mathbf{x},t)$, and $S_{12}(\mathbf{x},t)$ are the displacement field and stress-history tensor components, respectively.

Let $\mathbf{u}^s = \left[u_i^s, u_b^s\right]^\top$ and $\mathbf{u}^a = \left[u_b^a, u_e^a, S_e^a\right]^\top$ to represent the vectors of degree of freedom at the interior, boundary, and exterior of Γ_{SA}. Then it can be shown that the semi-discrete form of Equations (3.10), (3.13), and (3.14) is:

$$\begin{bmatrix} \mathbf{M}_{ii}^{\Omega_S} & \mathbf{M}_{ib}^{\Omega_S} & 0 & 0 \\ \mathbf{M}_{bi}^{\Omega_S} & \mathbf{M}_{bb}^{\Omega_S} + \mathbf{M}_{bb}^{\Omega_A} & \mathbf{M}_{ba}^{\Omega_A} & 0 \\ 0 & \mathbf{M}_{eb}^{\Omega_A} & \mathbf{M}_{ee}^{\Omega_A} & \mathbf{M}_{es}^{\Omega_A} \\ 0 & 0 & \mathbf{M}_{se}^{\Omega_A} & \mathbf{M}_{ss}^{\Omega_A} \end{bmatrix} \begin{bmatrix} \ddot{u}_{\mathrm{i}}^s \\ \ddot{u}_{\mathrm{b}}^s \\ \ddot{u}_{\mathrm{e}}^a \\ \ddot{S}_{\mathrm{e}}^a \end{bmatrix} + \begin{bmatrix} \mathbf{C}_{ii}^{\Omega_S} & \mathbf{C}_{ib}^{\Omega_S} & 0 & 0 \\ \mathbf{C}_{bi}^{\Omega_S} & \mathbf{C}_{bb}^{\Omega_S} + \mathbf{C}_{bb}^{\Omega_A} & \mathbf{C}_{ba}^{\Omega_A} & 0 \\ 0 & \mathbf{C}_{eb}^{\Omega_A} & \mathbf{C}_{ee}^{\Omega_A} & \mathbf{C}_{es}^{\Omega_A} \\ 0 & 0 & \mathbf{C}_{se}^{\Omega_A} & \mathbf{C}_{ss}^{\Omega_A} \end{bmatrix} \begin{bmatrix} \dot{u}_{\mathrm{i}}^s \\ \dot{u}_{\mathrm{b}}^s \\ \dot{u}_{\mathrm{e}}^a \\ \dot{S}_{\mathrm{e}}^a \end{bmatrix} +$$
$$\begin{bmatrix} \mathbf{K}_{ii}^{\Omega_S} & \mathbf{K}_{ib}^{\Omega_S} & 0 & 0 \\ \mathbf{K}_{bi}^{\Omega_S} & \mathbf{K}_{bb}^{\Omega_S} + \mathbf{K}_{bb}^{\Omega_A} & \mathbf{K}_{ba}^{\Omega_A} & 0 \\ 0 & \mathbf{K}_{eb}^{\Omega_A} & \mathbf{K}_{ee}^{\Omega_A} & \mathbf{K}_{es}^{\Omega_A} \\ 0 & 0 & \mathbf{K}_{se}^{\Omega_A} & \mathbf{K}_{ss}^{\Omega_A} \end{bmatrix} \begin{bmatrix} u_{\mathrm{i}}^s \\ u_{\mathrm{b}}^s \\ u_{\mathrm{e}}^a \\ S_{\mathrm{e}}^a \end{bmatrix} = \begin{bmatrix} P_{\mathrm{i}}^s \\ 0 \\ 0 \\ 0 \end{bmatrix}. \tag{3.26}$$

Note that continuity of displacements along the interface Γ_{SA} requires $u_{\mathrm{b}}^s = u_{\mathrm{b}}^a$ for all $t \in (0, T]$. Additionally, the wave response of the soil model in Figure 3.4 can be obtained by solving the following semi-discrete system of equations:

$$\mathbf{M}\,\ddot{\mathbf{d}}(t) + \mathbf{C}\,\dot{\mathbf{d}}(t) + \mathbf{K}\,\mathbf{d}(t) = \mathbf{f}(t), \tag{3.27}$$

where $\mathbf{M}$, $\mathbf{C}$, and $\mathbf{K}$ denote the mass, damping, and stiffness matrices, $\mathbf{d}$ denotes the mixed solution vector, i.e., $\mathbf{d}(t) = [\mathbf{u}^s(t), \mathbf{u}^a(t), \boldsymbol{\mathcal{S}}_{11}(t), \boldsymbol{\mathcal{S}}_{22}(t), \boldsymbol{\mathcal{S}}_{12}(t)]^\top$, and $\mathbf{f}$ denotes the force vector that corresponds to the known forces in the soil. We note that soil heterogeneity is incorporated into the $\mathbf{M}$, $\mathbf{C}$, and $\mathbf{K}$ matrices when the element matrices are built through numerical integration.

3.3 Domain reduction method formulated in a perfectly matched layer for truncated domain

Let us consider, as shown in Figure 3.5a, a semi-infinite domain with localized near-field features under remote seismic excitation. The total-field wave equations in absence of body forces is:

$$\operatorname{div} \boldsymbol{\sigma}^{\mathrm{t}}(\mathbf{u}^{\mathrm{t}}(\mathbf{x}, t)) = \rho_s \, \ddot{\mathbf{u}}^{\mathrm{t}}(\mathbf{x}, t), \text{ in } \Omega_{\mathrm{N}}, \text{ and } t \in (0, T]. \tag{3.28}$$

Similarly as shown in Figure 3.5b, the free-field wave equations in the absence of body forces for a semi-infinite background domain is:

$$\operatorname{div} \boldsymbol{\sigma}^{\mathrm{f}}(\mathbf{u}^{\mathrm{f}}(\mathbf{x}, t)) = \rho_s \, \ddot{\mathbf{u}}^{\mathrm{f}}(\mathbf{x}, t), \text{ in } \Omega_{\mathrm{F}}, \text{ and } t \in (0, T]. \tag{3.29}$$

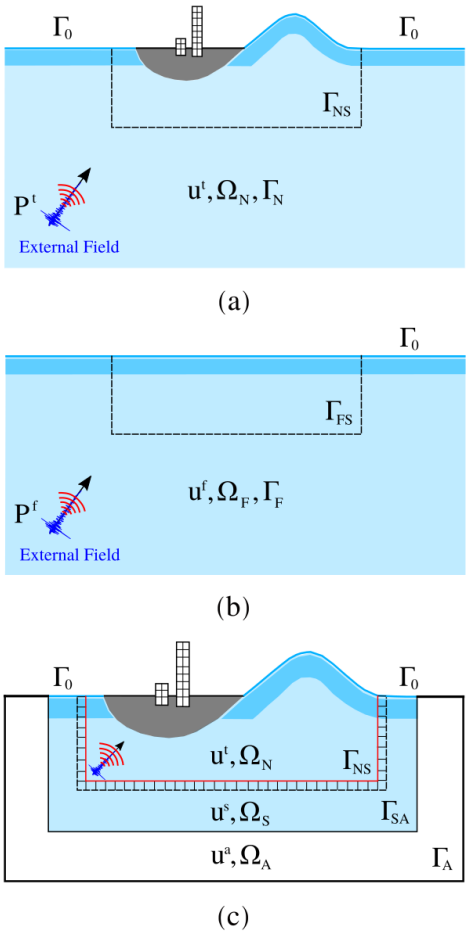

Figure 3.5: Domain reduction method formulated in a perfectly matched layer. (a) The total-field displacement $\mathbf{u}^{\mathrm{t}} = \mathbf{u}^{\mathrm{f}} + \mathbf{u}^{\mathrm{s}}$ around structures due to the soil-structure interaction induced by the remote seismic excitation in a semi-infinite domain; (b) the free-field displacement $\mathbf{u}_{\mathrm{free}}$ due to remote seismic excitation in a semi-infinite domain; (c) the DRM modeling approach for a domain truncated by ABCs (adopted from Bielak et al. [24]).

The remote excitation input that is embarked from the outside of the truncated domain with a localized feature in Ω_N is taken inside the attenuated domain Ω_A using the DRM proposed by Bielak et al. (2003) as shown in Figure 3.5c. In this regard, the governing wave equation is:

$$\operatorname{div} \boldsymbol{\sigma}(\mathbf{u}(\mathbf{x},t)) = \rho_s\, \ddot{\mathbf{u}}(\mathbf{x},t)\,, \text{ in } \Omega_N \cup \Omega_S\,, \text{ and } t \in (0,T]\,, \tag{3.30}$$

with the response field $\mathbf{u}$ defined as follows:

$$\mathbf{u}(\mathbf{x},t) := \mathbf{u}^t(\mathbf{x},t)\,, \text{ for } \mathbf{x} \in \Omega_N\,, \text{ and } t \in (0,T]\,, \tag{3.31}$$

$$\mathbf{u}(\mathbf{x},t) := \mathbf{u}^t(\mathbf{x},t) - \mathbf{u}^f(\mathbf{x},t)\,, \text{ for } \mathbf{x} \in \Omega_S\,, \text{ and } t \in (0,T]\,, \tag{3.32}$$

where $\mathbf{u}(\mathbf{x},t)$ is defined in Equation (3.31) and (3.32) is discontinuous on Γ_{NS} , the interface between Ω_N and Ω_S, which denote, respectively, the domain near the localized feature and the domain surrounding the Ω_N. Moreover, the scattered motion $\mathbf{u}^s(\mathbf{x},t) = \mathbf{u}^t(\mathbf{x},t) - \mathbf{u}^f(\mathbf{x},t)$ satisfies the radiation condition. Therefore, the equation in terms of $\mathbf{u}(\mathbf{x},t)$ defined in (3.30) can be solved in a domain of the semi-infinite extent, truncated by PMLs. This aforementioned discontinuity (a.k.a. the jump condition (Bielak and Christiano [22]) serves as a driving or effective force vector defined in Equation (3.9).

The governing equations

The scattered wave field that includes the jump condition and uses PML is shown in Figure 3.5c. The near-field displacement is obtained solving simultaneously the total-field wave equations in the absence of body forces

$$\operatorname{div} \boldsymbol{\sigma}^t(\mathbf{u}^t(\mathbf{x},t)) = \rho_s\, \ddot{\mathbf{u}}^t(\mathbf{x},t)\,, \text{ with } \mathbf{x} \in \Omega_N\,, \tag{3.33}$$

the scatter-field wave equations in the absence of body forces

$$\operatorname{div} \boldsymbol{\sigma}^s(\mathbf{u}^s(\mathbf{x},t)) = \rho_s\, \ddot{\mathbf{u}}^s(\mathbf{x},t)\,, \text{ with } \mathbf{x} \in \Omega_S\,, \tag{3.34}$$

the time domain PML equations in the absence of body forces

$$\operatorname{div}\left(\dot{\mathbf{S}}^\top \Lambda_E + \mathbf{S}^\top \Lambda_P\right) - \rho_s\,(a\,\ddot{\mathbf{u}}^a + b\,\dot{\mathbf{u}}^a + c\,\ddot{\mathbf{u}}^a) = 0\,, \text{ with } \mathbf{x} \in \Omega_A\,, \tag{3.35}$$

and,

$$\begin{aligned}\Lambda_E^\top\left(\mathbb{D} : \ddot{\mathbf{S}}\right)\Lambda_E + \Lambda_E^\top\left(\mathbb{D} : \dot{\mathbf{S}}\right)\Lambda_P + \Lambda_P^\top\left(\mathbb{D} : \dot{\mathbf{S}}\right)\Lambda_E + \Lambda_E^\top\left(\mathbb{D} : \mathbf{S}\right)\Lambda_P - \\ \frac{1}{2}\left(\Lambda_P^\top \nabla\mathbf{u}^a + (\nabla\mathbf{u}^a)^\top\Lambda_P^\top\right) - \frac{1}{2}\left(\Lambda_E^\top\nabla\dot{\mathbf{u}}^a + (\nabla\dot{\mathbf{u}}^a)^\top\Lambda_E^\top\right) = 0\,, \text{ with } \mathbf{x} \in \Omega_A\,,\end{aligned} \tag{3.36}$$

where the superscripts "t," "s," and "a" in Equation (3.33) to (3.36) denote the total, scattered, and attenuated variables, and $\mathbf{S}$ is the stress-history tensor corresponding to the scattered fields $\mathbf{u}^a$ and $\boldsymbol{\sigma}^a$.

The general semi-discrete form

The semi-discrete form consists of discretizing the partial differential equation (PDE) presented in Equation (3.33) using finite element analysis (FEA). The semi-discrete form of Equation (3.33) is:

$$\begin{bmatrix} \mathbf{M}_{ii}^{\Omega_N} & \mathbf{M}_{ib}^{\Omega_N} \\ \mathbf{M}_{bi}^{\Omega_N} & \mathbf{M}_{bb}^{\Omega_N} \end{bmatrix} \begin{bmatrix} \ddot{u}_{\mathrm{i}}^{\mathrm{t}} \\ \ddot{u}_{\mathrm{b}}^{\mathrm{t}} \end{bmatrix} + \begin{bmatrix} \mathbf{C}_{ii}^{\Omega_N} & \mathbf{C}_{ib}^{\Omega_N} \\ \mathbf{C}_{bi}^{\Omega_N} & \mathbf{C}_{bb}^{\Omega_N} \end{bmatrix} \begin{bmatrix} \dot{u}_{\mathrm{i}}^{\mathrm{t}} \\ \dot{u}_{\mathrm{b}}^{\mathrm{t}} \end{bmatrix} + \begin{bmatrix} \mathbf{K}_{ii}^{\Omega_N} & \mathbf{K}_{ib}^{\Omega_N} \\ \mathbf{K}_{bi}^{\Omega_N} & \mathbf{K}_{bb}^{\Omega_N} \end{bmatrix} \begin{bmatrix} u_{\mathrm{i}}^{\mathrm{t}} \\ u_{\mathrm{b}}^{\mathrm{t}} \end{bmatrix} = \begin{bmatrix} 0 \\ P_{\mathrm{b}}^{\mathrm{t}} \end{bmatrix} . \quad (3.37)$$

The semi-discrete form of Equations (3.34) to (3.36) is:

$$\begin{bmatrix} \mathbf{M}_{bb}^{\Omega_F} & \mathbf{M}_{be}^{\Omega_F} & 0 \\ \mathbf{M}_{eb}^{\Omega_F} & \mathbf{M}_{ee}^{\Omega_F} & \mathbf{M}_{es}^{\Omega_F} \\ 0 & \mathbf{M}_{se}^{\Omega_F} & \mathbf{M}_{ss}^{\Omega_F} \end{bmatrix} \begin{bmatrix} \ddot{u}_{\mathrm{b}}^{\mathrm{f}} \\ \ddot{u}_{\mathrm{e}}^{\mathrm{f}} \\ \ddot{S}_{\mathrm{e}}^{\mathrm{f}} \end{bmatrix} + \begin{bmatrix} \mathbf{C}_{bb}^{\Omega_F} & \mathbf{C}_{be}^{\Omega_F} & 0 \\ \mathbf{C}_{eb}^{\Omega_F} & \mathbf{C}_{ee}^{\Omega_F} & \mathbf{C}_{es}^{\Omega_F} \\ 0 & \mathbf{C}_{se}^{\Omega_F} & \mathbf{C}_{ss}^{\Omega_F} \end{bmatrix} \begin{bmatrix} \dot{u}_{\mathrm{b}}^{\mathrm{f}} \\ \dot{u}_{\mathrm{e}}^{\mathrm{f}} \\ \dot{S}_{\mathrm{e}}^{\mathrm{f}} \end{bmatrix} +$$
$$\begin{bmatrix} \mathbf{K}_{bb}^{\Omega_F} & \mathbf{K}_{be}^{\Omega_F} & 0 \\ \mathbf{K}_{eb}^{\Omega_F} & \mathbf{K}_{ee}^{\Omega_F} & \mathbf{K}_{es}^{\Omega_F} \\ 0 & \mathbf{K}_{se}^{\Omega_F} & \mathbf{K}_{ss}^{\Omega_F} \end{bmatrix} \begin{bmatrix} u_{\mathrm{b}}^{\mathrm{f}} \\ u_{\mathrm{e}}^{\mathrm{f}} \\ S_{\mathrm{e}}^{\mathrm{f}} \end{bmatrix} = \begin{bmatrix} P_{\mathrm{b}}^{\mathrm{f}} \\ 0 \\ 0 \end{bmatrix} . \quad (3.38)$$

Considering $\mathbf{u}_{\mathrm{b}}^{\mathrm{t}} = \mathbf{u}_{\mathrm{b}}^{\mathrm{f}} + \mathbf{u}_{\mathrm{b}}^{\mathrm{free}}$, the terms associated with known free-field motions–i.e. $\mathbf{u}_{\mathrm{b}}^{\mathrm{free}}$–can be moved from the left hand side of Equation (3.38) to the right hand side, which results in:

$$\begin{bmatrix} \mathbf{M}_{bb}^{\Omega_F} & \mathbf{M}_{be}^{\Omega_F} & 0 \\ \mathbf{M}_{eb}^{\Omega_F} & \mathbf{M}_{ee}^{\Omega_F} & \mathbf{M}_{es}^{\Omega_F} \\ 0 & \mathbf{M}_{se}^{\Omega_F} & \mathbf{M}_{ss}^{\Omega_F} \end{bmatrix} \begin{bmatrix} \ddot{u}_{\mathrm{b}}^{\mathrm{f}} \\ \ddot{u}_{\mathrm{e}}^{\mathrm{f}} \\ \ddot{S}_{\mathrm{e}}^{\mathrm{f}} \end{bmatrix} + \begin{bmatrix} \mathbf{C}_{bb}^{\Omega_F} & \mathbf{C}_{be}^{\Omega_F} & 0 \\ \mathbf{C}_{eb}^{\Omega_F} & \mathbf{C}_{ee}^{\Omega_F} & \mathbf{C}_{es}^{\Omega_F} \\ 0 & \mathbf{C}_{se}^{\Omega_F} & \mathbf{C}_{ss}^{\Omega_F} \end{bmatrix} \begin{bmatrix} \dot{u}_{\mathrm{b}}^{\mathrm{f}} \\ \dot{u}_{\mathrm{e}}^{\mathrm{f}} \\ \dot{S}_{\mathrm{e}}^{\mathrm{f}} \end{bmatrix} +$$
$$\begin{bmatrix} \mathbf{K}_{bb}^{\Omega_F} & \mathbf{K}_{be}^{\Omega_F} & 0 \\ \mathbf{K}_{eb}^{\Omega_F} & \mathbf{K}_{ee}^{\Omega_F} & \mathbf{K}_{es}^{\Omega_F} \\ 0 & \mathbf{K}_{se}^{\Omega_F} & \mathbf{K}_{ss}^{\Omega_F} \end{bmatrix} \begin{bmatrix} u_{\mathrm{b}}^{\mathrm{f}} \\ u_{\mathrm{e}}^{\mathrm{f}} \\ S_{\mathrm{e}}^{\mathrm{f}} \end{bmatrix} = \begin{bmatrix} P_{\mathrm{b}}^{\mathrm{f}} + \mathbf{M}_{bb}^{\Omega_F} \ddot{\mathbf{u}}_{\mathrm{b}}^{\mathrm{free}} + \mathbf{C}_{bb}^{\Omega_F} \dot{\mathbf{u}}_{\mathrm{b}}^{\mathrm{free}} + \mathbf{K}_{bb}^{\Omega_F} \mathbf{u}_{\mathrm{b}}^{\mathrm{free}} \\ \mathbf{M}_{be}^{\Omega_F} \ddot{\mathbf{u}}_{\mathrm{b}}^{\mathrm{free}} + \mathbf{C}_{be}^{\Omega_F} \dot{\mathbf{u}}_{\mathrm{b}}^{\mathrm{free}} + \mathbf{K}_{be}^{\Omega_F} \mathbf{u}_{\mathrm{b}}^{\mathrm{free}} \\ 0 \end{bmatrix} . \quad (3.39)$$

Since the solution vectors in Equations (3.38) and (3.39) share $\mathbf{u}_{\mathrm{b}}^{\mathrm{i}}$, both can be coupled to the following form:

$$\begin{bmatrix} \mathbf{M}_{ii}^{\Omega_N} & \mathbf{M}_{ib}^{\Omega_N} & 0 & 0 \\ \mathbf{M}_{bi}^{\Omega_N} & \mathbf{M}_{bb}^{\Omega_N} + \mathbf{M}_{bb}^{\Omega_F} & \mathbf{M}_{be}^{\Omega_F} & 0 \\ 0 & \mathbf{M}_{eb}^{\Omega_F} & \mathbf{M}_{ee}^{\Omega_F} & \mathbf{M}_{es}^{\Omega_F} \\ 0 & 0 & \mathbf{M}_{se}^{\Omega_F} & \mathbf{M}_{ss}^{\Omega_F} \end{bmatrix} \begin{bmatrix} \ddot{u}_{\mathrm{i}}^{\mathrm{t}} \\ \ddot{u}_{\mathrm{b}}^{\mathrm{t}} \\ \ddot{u}_{\mathrm{e}}^{\mathrm{f}} \\ \ddot{S}_{\mathrm{e}}^{\mathrm{f}} \end{bmatrix} + \begin{bmatrix} \mathbf{C}_{ii}^{\Omega_N} & \mathbf{C}_{ib}^{\Omega_N} & 0 & 0 \\ \mathbf{C}_{bi}^{\Omega_N} & \mathbf{C}_{bb}^{\Omega_N} + \mathbf{C}_{bb}^{\Omega_F} & \mathbf{C}_{be}^{\Omega_F} & 0 \\ 0 & \mathbf{C}_{eb}^{\Omega_F} & \mathbf{C}_{ee}^{\Omega_F} & \mathbf{C}_{es}^{\Omega_F} \\ 0 & 0 & \mathbf{C}_{se}^{\Omega_F} & \mathbf{C}_{ss}^{\Omega_F} \end{bmatrix} \begin{bmatrix} \dot{u}_{\mathrm{i}}^{\mathrm{t}} \\ \dot{u}_{\mathrm{b}}^{\mathrm{t}} \\ \dot{u}_{\mathrm{e}}^{\mathrm{f}} \\ \dot{S}_{\mathrm{e}}^{\mathrm{f}} \end{bmatrix} +$$
$$\begin{bmatrix} \mathbf{K}_{ii}^{\Omega_N} & \mathbf{K}_{ib}^{\Omega_N} & 0 & 0 \\ \mathbf{K}_{bi}^{\Omega_N} & \mathbf{K}_{bb}^{\Omega_N} + \mathbf{K}_{bb}^{\Omega_F} & \mathbf{K}_{be}^{\Omega_F} & 0 \\ 0 & \mathbf{K}_{eb}^{\Omega_F} & \mathbf{K}_{ee}^{\Omega_F} & \mathbf{K}_{es}^{\Omega_F} \\ 0 & 0 & \mathbf{K}_{se}^{\Omega_F} & \mathbf{K}_{ss}^{\Omega_F} \end{bmatrix} \begin{bmatrix} u_{\mathrm{i}}^{\mathrm{t}} \\ u_{\mathrm{b}}^{\mathrm{t}} \\ u_{\mathrm{e}}^{\mathrm{f}} \\ S_{\mathrm{e}}^{\mathrm{f}} \end{bmatrix} = \begin{bmatrix} P_{\mathrm{i}}^{\mathrm{t}} \\ P_{\mathrm{b}}^{\mathrm{t}} \\ P_{\mathrm{e}}^{\mathrm{f}} \\ S_{\mathrm{e}}^{\mathrm{f}} \end{bmatrix} , \quad (3.40)$$

where the external force vector is,

$$P_{\text{eff}} = \begin{bmatrix} P_{\text{i}}^{\text{t}} \\ P_{\text{b}}^{\text{t}} \\ P_{\text{e}}^{\text{f}} \\ S_{\text{e}}^{\text{f}} \end{bmatrix} = \begin{bmatrix} 0 \\ P_{\text{b}}^{\text{t}} + P_{\text{b}}^{\text{f}} + \mathbf{M}_{bb}^{\Omega_F} \ddot{\mathbf{u}}_{\text{b}}^{\text{free}} + \mathbf{C}_{bb}^{\Omega_F} \dot{\mathbf{u}}_{\text{b}}^{\text{free}} + \mathbf{K}_{bb}^{\Omega_F} \mathbf{u}_{\text{b}}^{\text{free}} \\ \mathbf{M}_{be}^{\Omega_F} \ddot{\mathbf{u}}_{\text{b}}^{\text{free}} + \mathbf{C}_{be}^{\Omega_F} \dot{\mathbf{u}}_{\text{b}}^{\text{free}} + \mathbf{K}_{be}^{\Omega_F} \mathbf{u}_{\text{b}}^{\text{free}} \\ 0 \end{bmatrix}, \tag{3.41}$$

and

$$P_b^{\text{t}} = \int_{\Gamma_{\text{NS}}} \boldsymbol{\sigma}^{\text{free}}(\mathbf{x}, t)\, \hat{\mathbf{n}}_n d\Gamma\,, \quad P_b^{\text{f}} = \int_{\Gamma_{\text{NS}}} \boldsymbol{\sigma}^{\text{free}}(\mathbf{x}, t)\, \hat{\mathbf{n}}_s d\Gamma\,. \tag{3.42}$$

As shown in Equation (3.40), only the free-field displacement and stress–i.e. $\mathbf{u}^{\text{free}}$ and $\boldsymbol{\sigma}^{\text{free}}$–are needed to compute the effective force vector that translates the effects of remote excitation along the introduced fictitious interface Γ_{NL}. Moreover, it is useful to note here that, as shown in Bielak et al. [24], the effective force vector can also be formulated such that only a free-field displacement information over a one-layer element thickness surrounding the interface Γ_{NL} is needed. This is because (i) the mass, damping, and stiffness matrices in the region Ω_{S} are the same for both scattered- and free-field problems and (ii) nonzero terms in matrices $\mathbf{M}_{ba}^{\Omega_F}$, $\mathbf{C}_{ba}^{\Omega_F}$, and $\mathbf{K}_{ba}^{\Omega_F}$ are only confined to elements sharing the nodes along the interface Γ_{NL}. In general, one needs to solve an auxiliary problem to obtain the free-field wave response. Bielak et al. [24] used the method provided by Hisada [67] to compute the Green's functions of the layered half-space. Jeong [79] also explored the accuracy of different methods [e.g. 64, 155, 161] to compute the input needed for the DRM. In this work, we assume that the incoming waves are vertically propagating shear waves. Considering this assumption, the effective force vector can be efficiently computed using a solution of a soil column as an auxiliary problem.

3.4 Examples of wave propagation using DRM and PML

In this section, two examples of wave propagation problem are solved using the software Seismo-VLAB. The first example reproduces the free-field motion of a half-space soil using DRM elements. The second example adds a feature on the soil surface, so that PML elements absorb the scattered field generated. The description of the problem as well as results obtained in these analyses are presented in the examples below.

Example 1. Let us consider a truncated soil domain with a horizontal length $L_x = 70\,[m]$ and vertical length $L_z = 75\,[m]$. Four-node quadrilateral elements are employed to discretize the domain, and linear elastic soil-elements are employed

such that $\rho_s = 2000\,[kg/m^3]$, $\nu_s = 0.35$, $t_h = 1.0\,[m]$, and plane-strain conditions are enforced. The mesh is divided such that space discretization is $\Delta x = 0.5\,[m]$, and $\Delta z = 0.5\,[m]$, respectively. In addition, a zone with PML of $10\,[m]$ thickness is provided along the truncated domain. The domain reduction method (DRM) is employed in order to transmit the ground motion of an in-plane sv-wave propagating upwards inside the near-field domain. The incident ground motion $\dot{u}_g(t)$ used in the finite element models is prescribed as an effective force Ricker function, proportional to Equation (3.43):

$$\dot{u}_g(t) = \left(1 - 2\gamma\,(t - t_0)^2\right) \exp\left[-\gamma\,(t - t_0)^2\right] \,. \tag{3.43}$$

In this numerical example, we have employed a central frequency $f_0 = 2.0\,[Hz]$, and the sv-wave velocity is set to be $V_s = 100\,[m/s]$, leading to a wave-length of $\lambda_n = V_s/f_0 = 50.0\,[m]$, a shear modulus $G_s = \rho\,V_s^2$, and an elasticity modulus $E_s = 2\,(1 + \nu)\,G_s$. The finite element model has 31392 nodes, 521 restrains, 882 constraints, and 30600 elements, and the simulation time is set to be $t_{\text{sim}} = 3.0\,[s]$, with a temporal discretization of $\Delta t = 0.0015\,[s]$, leading to a number of $n_t = 2000$ time steps required for the entire simulation. The finite element model is not large enough, so a single-core execution is performed in Seismo-VLAB. The total time to complete this task is $34\,[min]$ in total.

In Figure 3.6, the velocity field amplitude at (a) $t = 1.11\,[s]$, (b) $t = 1.65\,[s]$, (c) $t = 2.05\,[s]$, and (d) $t = 2.25\,[s]$ for the truncated soil-structure domain are shown. Note that, only inside the near-field domain, the DRM elements successfully generate the sv-wave propagating upwards.

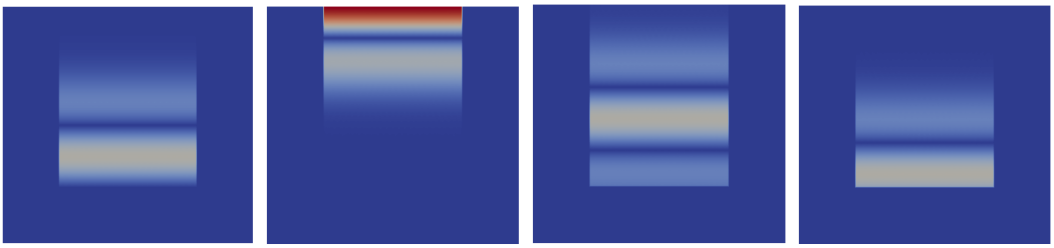

Figure 3.6: Velocity field amplitude at time (a) $t = 1.10\,[s]$, (b) $t = 1.65\,[s]$, (c) $t = 1.95\,[s]$, and (d) $t = 2.25\,[s]$ for testing the DRM elements. The blue color represents a velocity amplitude of $0.0\,[m/s]$, while the red color represents a velocity amplitude of $0.2\,[m/s]$.

In addition, Figure 3.7 shows the synthetic seismogram[1] of the velocity for the horizontal and vertical components. The velocity field is measured at the surface, i.e., $z = 0.0\,[m]$. The horizontal red solid lines represent the interface between the DRM domain and the scattered field domain. The vertical dashed blue lines represent the particular time when the snapshots in Figure 3.6 are illustrated.

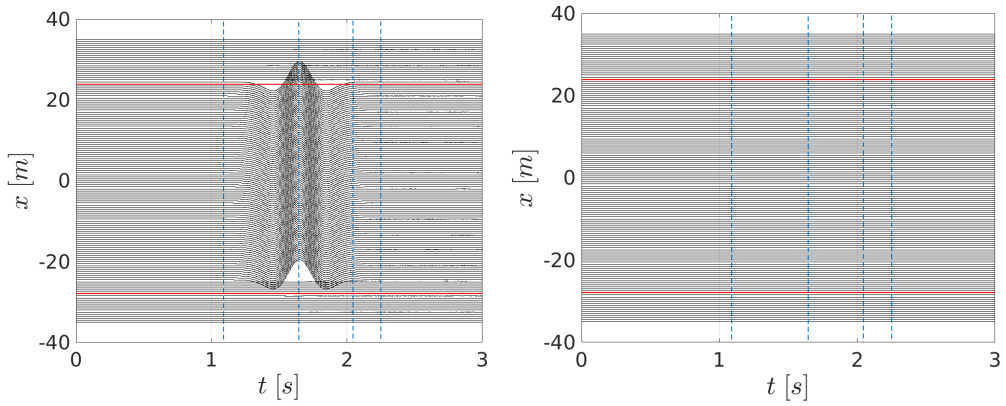

Figure 3.7: Synthetic seismogram (a) horizontal component $v_x(t)$, and (b) vertical component $v_z(t)$ of the velocity, recorded on the soil surface for the soil-structure interaction problem.

Since the truncated soil domain has no features that can generate scattering waves, the near-field response in this case has to match the free-field conditions imposed at the DRM elements. The results displayed in Figure 3.7 for both the horizontal and vertical components of the velocity field make it evident that the implemented DRM conditions work perfectly for this case. Here, one can observe that there is no-reflection outside the DRM domain (near-field) delimited by the red-solid lines, and as expected, no velocities in the vertical direction are developed throughout the simulation.

Example 2. Let us consider a similar truncated soil domain with a horizontal length $L_x = 70\,[m]$ and vertical length $L_z = 75\,[m]$, but this time a dam is placed on top of the soil surface. Four-node quadrilateral elements are employed to discretize the domain, and linear elastic soil-elements are employed such that $\rho_s = 2000\,[kg/m^3]$, $\nu_s = 0.35$, $t_h = 1.0\,[m]$, and plane-strain conditions are enforced. The mesh is divided such that space discretization is $\Delta x = 0.5\,[m]$ and $\Delta z = 0.5\,[m]$, respectively. In addition, a zone with PML of $10\,[m]$ thickness is provided along the truncated

[1] A synthetic seismogram is a plot that allows to easily track wave-reflection or wave-generation at the boundary of a truncated domain using the presented framework.

domain. The domain reduction method (DRM) is employed in order to transmit the ground motion of an in-plane sv-wave propagating upwards inside the near-field domain. The incident ground motion $\dot{u}_g(t)$ used in the finite element models is prescribed as an effective force Ricker function, proportional to Equation (3.43).

In this numerical example, we have employed a central frequency $f_0 = 2.0\,[Hz]$, and the sv-wave velocity is set to be $V_s = 100\,[m/s]$, leading to a wave-length of $\lambda_n = V_s/f_0 = 50.0\,[m]$, a shear modulus $G_s = \rho V_s^2$, and an elasticity modulus $E_s = 2(1+\nu)G_s$. The finite element model has 31798 nodes, 521 restrains, 882 constraints, and 31001 elements, and the simulation time is set to be $t_{\text{sim}} = 3.0\,[s]$, with a temporal discretization of $\Delta t = 0.0015\,[s]$, leading to a number of $n_t = 2000$ time steps required for the entire simulation. The finite element model is not large enough, so a single-core execution is performed in Seismo-VLAB. The total time to complete this task is $36\,[min]$ in total.

In Figure 3.8 the velocity field amplitude at (a) $t = 1.10\,[s]$, (b) $t = 1.65\,[s]$, (c) $t = 1.95\,[s]$, and (d) $t = 2.25\,[s]$ for the truncated soil-structure domain are shown. Note that, only inside the near-field domain, the DRM elements successfully generate the sv-wave propagating upwards, however, this time because of the presence of the dam, a scattered field is generated outside the DRM (near-field) domain.

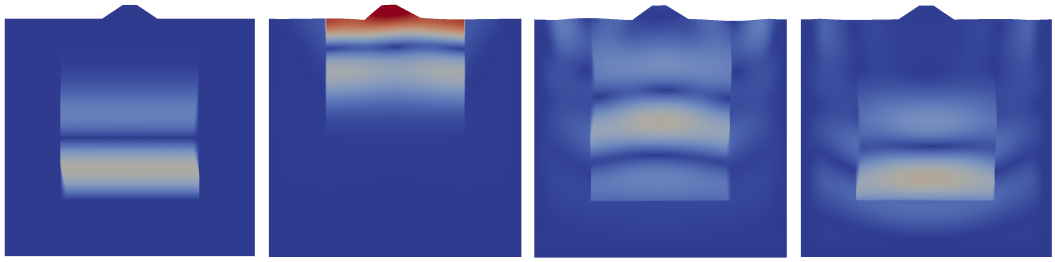

Figure 3.8: Velocity field amplitude and deformed configuration at time (a) $t = 1.05\,[s]$, (b) $t = 1.65\,[s]$, (c) $t = 1.95\,[s]$, and (d) $t = 2.25\,[s]$ for the dam problem. The blue color represents a velocity amplitude of $0.0\,[m/s]$, while the red color represents a velocity amplitude of $0.2\,[m/s]$.

In addition, Figure 3.9 shows the synthetic seismogram of the velocity for the horizontal and vertical components. The velocity field is measured at the surface, i.e., $z = 0.0\,[m]$. The horizontal red solid lines represent the interface between the DRM domain and the scattered field domain. The vertical dashed blue lines represent the particular time when the snapshots in Figure 3.8 are illustrated.

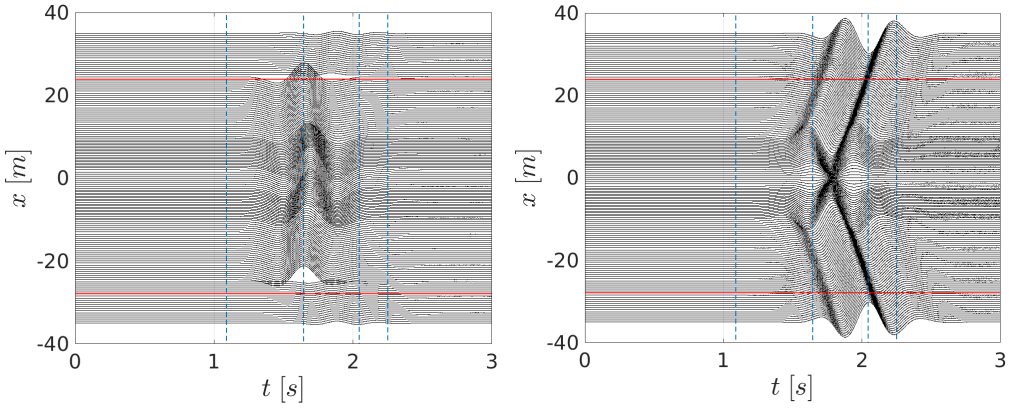

Figure 3.9: Synthetic seismogram (a) horizontal component $v_x(t)$, and (b) vertical component $v_z(t)$ of the velocity, recorded on the soil surface for the dam problem.

Since the truncated soil domain has a feature that can generate scattering waves, the near-field response in this case does not match the free-field conditions imposed at the DRM elements. The results displayed in Figure 3.9 for both the horizontal and vertical components of the velocity field make it evident that the implemented PML absorbing boundary interface works perfectly for this case. Here, one can observe that there is no-reflection coming in from the boundaries, and as expected, velocities in the vertical direction are developed due to the presence of the dam, but the generated field is again absorbed entirely.

These simple examples show that a DRM formulation along with PML for absorbing scattered waves provides the necessary features for high-fidelity simulation of wave propagation.

3.5 Conclusions

This chapter presented a brief review on the domain reduction method (DRM) and a perfectly matched layer (PML) formulation for absorbing boundaries. The hybrid PML formulation in plane-strain setting is then extended such that the effective forces associated with the seismic excitation can be incorporated through DRM.

The DRM formulated in a PML for truncated domain only requires displacement, velocity, and acceleration fields to be prescribed in the one-layer of soil elements. The required DRM fields can be computed analytically using the method proposed in Graff [58], Poursartip [122], Zhang et al. [160] for semi-infinite half-space. However, more complicated soil patterns–i.e., layered soil, nonlinear soil, requires to solve an auxiliary problem to obtain the free-field wave response.

The performance of the proposed framework in terms of robustness and accuracy was illustrated through two verification examples. For each example, the response of the velocity field amplitude on the soil surface as well as synthetic seismogram are generated to measure the accuracy of the implemented DRM-PML framework for wave propagation problems. In the first example, the DRM implementation is verified. The velocity field in Figure 3.6 made it evident that the implemented DRM conditions work perfectly, since no-reflection outside the DRM domain (near-field) is generated. In the second example, the PML implementation is verified by adding a source of scattering. The synthetic seismogram in Figure 3.9 made it evident that the implemented PML absorbing boundary interface works perfectly since no-reflection coming in from the boundaries are generated.

Finally, both examples involved generating and assembling about 32000 quadrilateral elements and evolving the solution 2000 time steps. The execution time was less than 35 mins, which is 1.0 seconds per time step. This is in fact an small fraction considering that first, an implicit Newmark method for numerical integration to solve differential equations is employed, and then an LDL-decomposition for solving the linear system is performed at each time step.

Chapter 4

THE DIRECT MODELING METHOD FOR SOIL-STRUCTURE INTERACTION PROBLEMS

The process in which the response of the soil influences the motion of the structure and the motion of the structure influences the response of the soil is termed as soil-structure interaction (SSI) [150]. In civil engineering, almost all structures (buildings, dams, bridges, tunnels, and retaining walls to name a few) are somehow in contact with soil–i.e., have foundations or support elements that either rest on or are embedded in soil [157–159]. Thus, the SSI phenomenon involves naturally an unbounded (semi-infinite or infinite) domain. Usually, the semi-infinite domain or far-field is represented by Earth, and the finite domain or near-field is represented by the structure and the surrounding soil. One approach to solve the SSI problem is the so-called direct modeling method [138, 157–159]. In this method, standard numerical techniques such as the finite element method (see Bathe [16], Hughes [70]), boundary elements method (see Brebbia and Dominguez [28], Katsikadelis [90]) or finite difference method (see Strikwerda [142], Thomas [148]) are commonly used to approximate the solution in space and time. Over the years, the finite element method has become one of the preferred techniques, since it can handle complex geometry, and allows to obtain a certain level of accuracy through $p-$ and $h-$refinements. However, the method does not allow semi-infinite domain directly. Thus, special elements on the boundary must be added to emulate its infinite nature.

In this chapter, the continuum formulation for the soil-structure interaction problems is presented, then the discretized version or weak-form of the continuum problem is outlined using the finite element method. Lastly, one example using the finite element method to solve the soil-structure interaction problem is discussed.

4.1 The continuum formulation of the soil-structure interaction problems

In Figure 4.1, the complete soil-structure domain is denoted by Ω and is decomposed into two sub-domains: the unbounded soil denoted by Ω_s and the bounded structure denoted by Ω_b. In addition, the interface between the structure and the soil is denoted by Γ_{bs}, and the free structure boundary surface is denoted by Γ_b and the free soil boundary surface is denoted by Γ_s. Finally, the boundary of $\Omega = \Omega_s \cup \Omega_b$ is denoted by $\Gamma = \Gamma_s \cup \Gamma_b$.

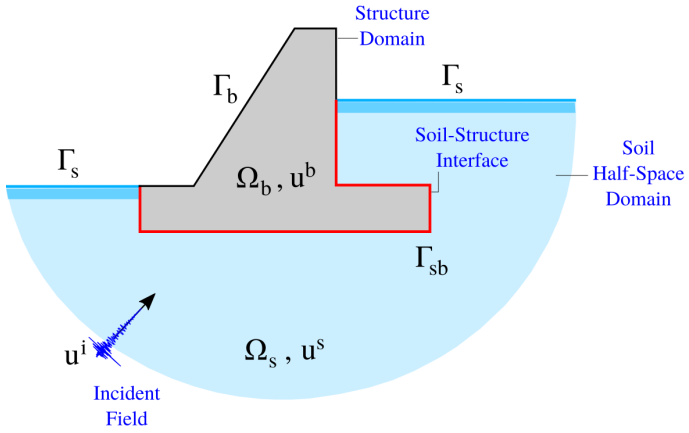

Figure 4.1: The continuum soil-structure interaction layout.

The displacement fields on Ω_s and Ω_b due to dynamic loading are denoted by $\mathbf{u}^s(\mathbf{x}, t)$ and $\mathbf{u}^b(\mathbf{x}, t)$, respectively, where $\mathbf{x} \in \Omega$ represents a point coordinate, and $t \in \mathbb{R}^+$ the continuous time variable. Both displacement fields are assumed to be small enough to allow a linear approximation of the constitutive and equilibrium equations[1]. Thus, for linear elastic and isotropic problems, the stress tensor in the soil is written as $\boldsymbol{\sigma}^s(\mathbf{u}^s)$ and is related to the strain tensor inside the soil $\boldsymbol{\epsilon}^s(\mathbf{u}^s)$ through the generalized Hooke's law,

$$\boldsymbol{\sigma}^s(\mathbf{u}^s) = \mathbb{C}^s\, \boldsymbol{\epsilon}^s(\mathbf{u}^s) = \lambda_s\, \mathrm{div}(\mathbf{u}^s)\, \mathbf{I} + 2\, \mu_s\, \boldsymbol{\epsilon}^s(\mathbf{u}^s), \tag{4.1}$$

where $\mathbb{C}^s$ represents the fourth-rank elastic moduli tensor, $\mathbf{I}$ is the identity tensor, λ_s and μ_s the Lamé constants for the soil. Similarly, the stress tensor for the structure $\boldsymbol{\sigma}^b(\mathbf{u}^b)$ is related to the strain tensor inside the structure $\boldsymbol{\epsilon}^b(\mathbf{u}^b)$ through the generalized Hooke's law,

$$\boldsymbol{\sigma}^b(\mathbf{u}^b) = \mathbb{C}^b\, \boldsymbol{\epsilon}^b(\mathbf{u}^b) = \lambda_b\, \mathrm{div}(\mathbf{u}^b)\, \mathbf{I} + 2\, \mu_b\, \boldsymbol{\epsilon}^b(\mathbf{u}^b), \tag{4.2}$$

where $\mathbb{C}^b$ represents the fourth-rank elastic moduli tensor, and λ_b and μ_b are the Lamé constants for the structure.

The Cauchy stress theorem[2] is used to compute the traction vectors applied on the interface oriented by the unit outer normal vector $\hat{\mathbf{n}}$ in the soil,

$$\mathbf{t}^s(\mathbf{u}^s) = \boldsymbol{\sigma}^s\, \hat{\mathbf{n}}, \tag{4.3}$$

[1] This assumption can be removed to allow finite kinematics; however, the equilibrium equations are expressed in the deformed configuration as functions of the deformation gradient $\mathbf{F}$ and the second Piola-Kirchhoff stress tensor $\mathbf{S}$.

[2] Cauchy's stress theorem is also known as the Cauchy's tetrahedron theorem.

where $\mathbf{t}^s(\mathbf{u}^s)$ represents the traction exerted on the soil surface. Likewise, the traction vectors applied on the interface oriented by the unit outer normal vector $\hat{\mathbf{n}}$ in the structure is,

$$\mathbf{t}^b(\mathbf{u}^b) = \boldsymbol{\sigma}^b\,\hat{\mathbf{n}}\,, \tag{4.4}$$

where $\mathbf{t}^b(\mathbf{u}^b)$ represents the traction exerted on the structure surface.

In most cases, external loads in soil-structure interaction problems are either incident fields or applied forces and traction inside or on the boundaries of the domain. Here, we consider the seismic loading defined inside the soil domain Ω_s, and denoted by $\mathbf{u}^i(\mathbf{x}, t)$. We assume that if the incident field $\mathbf{u}^i$ is such that satisfies the Navier equation and free surface boundary conditions in Ω_s, then the seismic force $\mathbf{f}^i$ in the soil and the seismic traction $\mathbf{t}^i$ are properly defined. The diffracted or scattered field $\mathbf{u}^d(\mathbf{x}, t)$ is defined in the soil as a function of the total field $\mathbf{u}^s$ as,

$$\mathbf{u}^d(\mathbf{x}, t) = \mathbf{u}^s(\mathbf{x}, t) - \mathbf{u}^i(\mathbf{x}, t) \quad \text{in } \Omega_s\,. \tag{4.5}$$

The diffracted field has to satisfy the Navier equations in Ω_s for any $t > 0$, with $\mathbf{f}^s = \mathbf{f}^i$ as source term and $\mathbf{t}^s = \mathbf{t}^i$ as boundary conditions on Γ_s,

$$\operatorname{div}\boldsymbol{\sigma}^s(\mathbf{u}^d) + \rho_s\,\ddot{\mathbf{u}}^s(\mathbf{x}, t) = \mathbf{f}^s \quad \text{in } \Omega_s\,, \tag{4.6}$$

$$\mathbf{t}^s(\mathbf{u}^d) = \mathbf{t}^i \quad \text{on } \Gamma_s\,. \tag{4.7}$$

Similarly, the displacement in the structure $\mathbf{u}^b(\mathbf{x}, t)$ must satisfy,

$$\operatorname{div}\boldsymbol{\sigma}^b(\mathbf{u}^b) + \rho_b\,\ddot{\mathbf{u}}^b(\mathbf{x}, t) = \mathbf{f}^b \quad \text{in } \Omega_b\,, \tag{4.8}$$

$$\mathbf{t}^b(\mathbf{u}^b) = \mathbf{0} \quad \text{on } \Gamma_b\,, \tag{4.9}$$

meaning that the structure is traction free. In addition, both fields have to satisfy homogeneous initial conditions:

$$\mathbf{u}^d(\mathbf{x}, 0) = \mathbf{u}^d(\mathbf{x}, 0) = 0 \quad \text{for all } \mathbf{x} \in \Omega_s\,, \tag{4.10}$$

$$\mathbf{u}^b(\mathbf{x}, 0) = \mathbf{u}^b(\mathbf{x}, 0) = 0 \quad \text{for all } \mathbf{x} \in \Omega_b\,, \tag{4.11}$$

and the field $\mathbf{u}^b$ and $\mathbf{u}^d$ must satisfy local equilibrium along the interface Γ_{bs},

$$\mathbf{t}^b(\mathbf{u}^b) + \mathbf{t}^s(\mathbf{u}^d) = \mathbf{t}^i \quad \text{on } \Gamma_{bs}\,, \tag{4.12}$$

as well as the kinematic condition on Γ_{sb}

$$\mathbf{u}^b(\mathbf{x}, t) - \mathbf{u}^d(\mathbf{x}, t) = \mathbf{u}^i(\mathbf{x}, t) \quad \text{on } \Gamma_{bs}\,. \tag{4.13}$$

Equations (4.6) – (4.13) form a well posed boundary value problem with homogeneous initial conditions. These sets of equations establish the continuum formulation of the soil-structure interaction phenomenon.

4.2 The finite element method applied to soil-structure interaction

We consider the soil-structure interaction boundary value problem:

$$\operatorname{div} \boldsymbol{\sigma}^s(\mathbf{u}^d) + \rho_s \, \mathbf{u}^d(\mathbf{x}, t) = \mathbf{f}^s \quad \text{in } \Omega_s \,, \tag{4.14}$$

$$\mathbf{t}^s(\mathbf{u}^d) = \mathbf{t}^i \quad \text{on } \Gamma_s \,, \tag{4.15}$$

$$\operatorname{div} \boldsymbol{\sigma}^b(\mathbf{u}^b) + \rho_b \, \mathbf{u}^b(\mathbf{x}, t) = \mathbf{f}^b \quad \text{in } \Omega_b \,, \tag{4.16}$$

$$\mathbf{t}^b(\mathbf{u}^b) = \mathbf{0} \quad \text{on } \Gamma_b \,, \tag{4.17}$$

$$\mathbf{t}^b(\mathbf{u}^b) + \mathbf{t}^s(\mathbf{u}^d) = \mathbf{t}^i \quad \text{on } \Gamma_{bs} \,, \tag{4.18}$$

$$\mathbf{u}^b(\mathbf{x}, t) - \mathbf{u}^d(\mathbf{x}, t) = \mathbf{u}^i(\mathbf{x}, t) \quad \text{on } \Gamma_{bs} \,, \tag{4.19}$$

and assume that the source terms $\mathbf{f}^s, \mathbf{f}^b \in L^2(\Omega)$. We then let $C_c^\infty(\Omega)$ be the space of test function defined as:

$$C_c^\infty(\Omega) = \left\{ \mathbf{v}(\mathbf{x}) \in C^\infty(\Omega) \;\text{ such that }\; \mathbf{v}(\mathbf{x}) = 0 \;\text{ for all } \mathbf{x} \in \Gamma \right\}, \tag{4.20}$$

and define the space $H_0^1(\Omega)$ as the closure of $C_c^\infty(\Omega)$ under the norm

$$\|\mathbf{v}(\mathbf{x})\|^2_{H_0^1(\Omega)} := \int_\Omega |\nabla \mathbf{v}(\mathbf{x})|^2 d\Omega \,. \tag{4.21}$$

Let $V := H_0^1(\Omega)$, and then multiply Equations (4.16) and (4.17) for a test function $\mathbf{v}(\mathbf{x}) \in V$ to obtain,

$$\int_{\Omega_b} \Big(\operatorname{div} \boldsymbol{\sigma}^b(\mathbf{u}^b) + \rho_b \, \mathbf{u}^b(\mathbf{x}, t) \Big) \, \mathbf{v}(\mathbf{x}) \, d\Omega_b - \int_{\Gamma_b} \mathbf{t}^b(\mathbf{u}^b) \mathbf{v}(\mathbf{x}) \, d\Gamma_b = \int_{\Omega_b} \mathbf{f}^b \mathbf{v}(\mathbf{x}) \, d\Omega_b \,.$$

The latter can be written in a more compact form using index notation as,

$$\int_{\Omega_b} \Big(\sigma^b_{ij,j}(\mathbf{u}^b) + \rho_b \, \ddot{u}^b_i(\mathbf{x}, t) \Big) \, v_i(\mathbf{x}) d\Omega_b - \int_{\Gamma_b} \sigma^b_{ij}(\mathbf{u}^b) \, \hat{n}_j v_i(\mathbf{x}) \, d\Gamma_b = \int_{\Omega_b} f^b_i v_i(\mathbf{x}) \, d\Omega_b \,.$$

If we drop the space and time $\mathbf{x}, t$ variables, and apply the divergence theorem using the generalized Hooke's law $\sigma^b_{ij} = \mathbb{C}^b_{ijkl} \, u^b_{k,l}$ and $\mathbb{C}^b_{ijkl} \, u^b_{k,l} \, v^h_i = \left(\mathbb{C}^b_{ijkl} u^b_{k,l} v^h_i \right)_{,j} - \mathbb{C}^b_{ijkl} u^b_{k,l} v^h_{i,j}$ in the first integral, we obtain

$$- \int_{\Omega_b} \mathbb{C}^b_{ijkl} u^b_{k,l} v^h_{i,j} d\Omega_b - \int_{\Omega_b} \rho_b \, \ddot{u}^b_i \, v^h_i \, d\Omega_b + \int_{\Gamma_{bs}} t^b_i v^h_i \, d\Gamma_{bs} = \int_{\Omega_b} f^b_i v^h_i \, d\Omega_b \,.$$

Similarly, we multiply Equation (4.18) by the same test function and using the kinematic relation provided in Equation (4.19), we integrate over Γ_{bs} to obtain

$$- \int_{\Gamma_{bs}} \left(\mathbb{C}^s_{ijkl} \left(u^i_{k,l} + u^d_{k,l} \right) \hat{n}_j v^h_i - t^i_b v^h_i - \mathbb{C}^s_{ijkl} u^d_{k,l} \hat{n}_j v^h_i \right) d\Gamma_{bs} = 0 \,.$$

This result can be added to our previous expression to finally obtain the weak-form of the soil-structure interaction problem,

$$-\int_{\Omega_b} \mathbb{C}^b_{ijkl} u^b_{k,l} v^h_{i,j} d\Omega_b - \int_{\Omega_b} \rho_b \ddot{u}^b_i v^h_i \, d\Omega_b - \int_{\Gamma_{bs}} \mathbb{C}^s_{ijkl} u^d_{k,l} \hat{n}_j v^h_i \, d\Gamma_{bs} = \int_{\Gamma_{bs}} \mathbb{C}^s_{ijkl} \left(u^i_{k,l} + u^d_{k,l} \right) \hat{n}_j v^h_i \, d\Gamma_{bs} + \int_{\Omega_b} f^b_i v^h_i \, d\Omega_b \,, \tag{4.22}$$

or,

$$\mathbf{B}(\mathbf{u}, \mathbf{v}) = g(\mathbf{v}) \,. \tag{4.23}$$

Then any function $\mathbf{v}(\mathbf{x}) \in V$ that satisfies Equation (4.23) is called a weak solution of the soil-structure interaction problem.

Let $V^h \subseteq V$ be a finite dimensional subspace of V, with nodal basis $\{N^h_\alpha\}^N_{\alpha=1}$. In this case, V^h is a Hilbert space equipped with the inner product $\langle \cdot, \cdot \rangle_V$. Moreover, let $\mathbf{B} : V^h \times V^h \to \mathbb{R}$ be a bi-linear form, and $g : V^h \to \mathbb{R}$ to denote a linear operator. It can be shown that there exists a unique solution[3] $\mathbf{u}^h \in V^h$ to the problem:

$$\mathbf{B}(\mathbf{u}^h, \mathbf{v}^h) = g(\mathbf{v}^h) \,. \tag{4.24}$$

Now, let $\mathbf{u}^h(\mathbf{x}, t) \in V^h$ to denote such solution. Since $N^h_1(\mathbf{x}), \ldots, N^h_{N_h}(\mathbf{x})$ form a basis for V^h, there exist scalars $U^h_1, \ldots, U^h_{N_h} \in \mathbb{R}$ such that

$$\mathbf{u}^h(\mathbf{x}, t) = \sum_{\alpha=1}^{N_h} U^h_\alpha(t) \, N^h_\alpha(\mathbf{x}) \,. \tag{4.25}$$

Similarly if $\mathbf{v}^h(\mathbf{x}, t)$ can be approximated using the same base, then there exist scalars $V^h_1, \ldots, V^h_{N_h} \in \mathbb{R}$ such that

$$\mathbf{v}^h(\mathbf{x}, t) = \sum_{\beta=1}^{N_h} V^h_\beta(t) \, N^h_\beta(\mathbf{x}) \,. \tag{4.26}$$

Therefore choosing $\mathbf{v}^h(\mathbf{x}, t)$ to be elements of the basis $\{N^h_\beta\}^N_{\beta=1}$ is equivalent to choosing $\{V^h_\beta\}^{N_h}_{\beta=1}$ from $\{(1, 0, 0 \ldots, 0), (0, 1, 0 \ldots, 0), \ldots, (0, 0, 0 \ldots, 1)\}$. Then, substitution of Equation (4.25) and Equation (4.26) into Equation (4.22) generates the following system of differential equations:

$$\mathbf{M}^h_b \ddot{U}^h + \left(\mathbf{K}^h_b + \mathbf{K}^h_s \right) U^h = F^h_b + F^h_s \,. \tag{4.27}$$

[3]The Lax-Milgram theorem essentially guarantees that for linear elasticity, there is a unique solution if the operator $\mathbf{B}(\mathbf{u}^h, \mathbf{v}^h)$ is bounded, coercive, symmetric, and positive definite.

In Equation (4.27), the matrices $\mathbf{M}_b^h$, $\mathbf{K}_b^h$, and $\mathbf{K}_s^h$ are defined as:

$$\mathbf{M}_b^h = M_{\alpha\beta}^b := \int_{\Omega_b} \rho_b \, N_\beta^h(\mathbf{x}) N_\alpha^h(\mathbf{x}) \, d\Omega_b \,, \tag{4.28}$$

$$\mathbf{K}_b^h = K_{\alpha\beta}^b := \int_{\Omega_b} \frac{dN_\beta^h(\mathbf{x})}{dx_j} \, \mathbb{C}_{ijkl}^b \, \frac{dN_\alpha^h(\mathbf{x})}{dx_l} \, d\Omega_b \,, \tag{4.29}$$

$$\mathbf{K}_s^h = K_{\alpha\beta}^s := \int_{\Gamma_{bs}} \hat{n}_j N_\beta^h(\mathbf{x}) \, \mathbb{C}_{ijkl}^s \, \frac{dN_\alpha^h(\mathbf{x})}{dx_l} \, d\Gamma_{bs} \,, \tag{4.30}$$

likewise the force vectors F_b^h, and F_s^h are defined as follows,

$$F_b^h = F_\beta^b := \int_{\Omega_b} f_i^b N_\beta^h(\mathbf{x}) \, d\Omega_b \,, \tag{4.31}$$

$$F_s^h = F_\beta^s := \int_{\Gamma_{bs}} \mathbb{C}_{ijkl}^s \left(u_{k,l}^i + u_{k,l}^d \right) \hat{n}_j \, N_\beta^h(\mathbf{x}) \, d\Gamma_{bs} \,. \tag{4.32}$$

The equations derived here are consistent to the one presented in "Nonlinear Dynamic Soil-Structure Interaction in Earthquake Engineering," by Alex Nieto Ferro, if the Laplace transform is used in Equations 4.14 to 4.19 and then the variational formulation is applied. The basic ideas of this derivation is (a) to define new unknown fields on the interfaces, either displacements or tractions, so that one of the two coupling equations on each interface holds apriori, (b) to solve a boundary value problems in each subdomain using these new unknown fields as boundary conditions, and (c) to enforce the other coupling equation in a weak sense, e.g. for any trial admissible fields on the interfaces.

Remark. *The matrix $\boldsymbol{K}_s^h$ is the stiffness of the soil along the interface Γ_{bs}, while the vector F_s^h is the induced foundation input forces developed at the interface Γ_{bs} due to the scattered field.*

4.3 Some numerical modeling considerations

The finite element method [16, 70] is employed to approximate the soil-structure interaction phenomenon. In this regard, the soil and foundation domain can be for instance modeled with four-node two-dimensional plain-strain quadrilateral elements. These elements have at each node two translational degrees of freedom as it is shown in Figure 4.2a. On the other hand, the structure domain is for instance modeled considering two-node linear elastic frame elements. The nodes connecting this type of element have three degrees of freedom of which two are for translation and one is for rotation as is shown in Figure 4.2b. The materials employed to model structural and soil elements are isotropic linear and elastic.

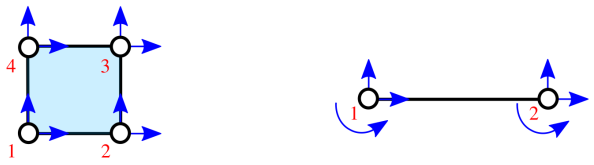

(a) (b)

Figure 4.2: Degrees of freedom for the soil element and structural elements.

Because solid elements (i.e., soil and foundation) and structural elements (i.e., beams and columns) have different number of degrees of freedom per node, it is necessary to couple them in an indirect manner. Figure 4.3 shows schematically how this coupling is performed between the foundation (solid) and the columns (frame) nodes. A clean and numerically stable method is applied through kinematic constraints to the translational degree of freedom at the contact interface [42, 80]. In this method, the connections are basically performed by extending each frame (column) element inside the surrounding solids (foundation) elements. Then, the connection of frame element nodes to solids elements nodes is done only for translational degrees of freedom (two of them for each node), while rotational degrees of freedom (one of them) from beam-column element are left unconnected. This sort of connection relays on the fact that the foundation is much more stiffer than the column so that the foundation will impose the same displacement and rotation to the column nodes. It is important to highlight that some localized deformation is developed in the surrounding soil due to this sort of connection, but equilibrium and compatibility are always met using this approach. Now, if the foundation behaves as a rigid diaphragm, the latter issue can be avoided by adding an auxiliary node with three-degree of freedom (i.e., diaphragm node) and then impose kinematic constraints to all nodes at the foundation and columns.

A dynamical analysis needs to be performed in order to study the interaction developed between the soil, foundation, and structure over time. In this regard, the accuracy of the numerical simulation for a seismic wave propagating in the soil depends on two main parameters,

(a) The space discretization, Δh.

(b) The time discretization, Δt.

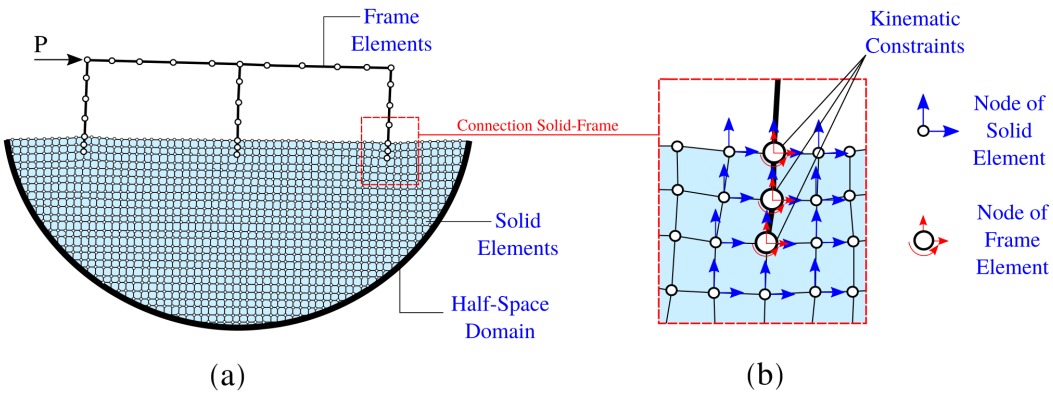

Figure 4.3: Frame and soil element connection through kinematic constraints.

Assuming that the numerical method is consistent[4], the desired accuracy of the solution can be obtained as long as sufficient computational resources are available [142]. However, in order to represent accurately a traveling wave of a given frequency, between 12 to 20 nodes per wavelength are usually required [81, 108]. Fewer nodes can lead to numerical dissipation[5] as the discretization misses certain peaks of seismic wave. Therefore, the appropriate maximum grid spacing is computed using the highest relevant frequency f_{max} which is present in the model. Typically, this frequency can be obtained using Fourier analysis of the signal, but in earthquake engineering one can assume $f_{max} = 10\,[Hz]$. This frequency allows to compute the minimum wavelength $\lambda_{min} = V_s/f_{max}$ provided with the shear wave velocity V_s of the soil. Thus, if the minimum wavelength is to be represented by 20 nodes, the maximum grid spacing should not be larger than:

$$\Delta h \leq \frac{\lambda_{min}}{20} = \frac{V_s^{min}}{20\, f_{max}}\,. \tag{4.33}$$

In Equation (4.33), the variable V_s^{min} is smallest shear wave velocity that is of interest in the simulation, usually taken as the wave velocity of the softest soil layer. For instance, if the smallest velocity is $V_s^{min} = 100\,[m/s]$, then a spatial discretization of $\Delta h = 0.5\,[m]$ needs to be used to discretize the soil to guarantee 20 points per wavelength.

On the same line, the time step size used for solving numerically linear and nonlinear wave propagation problems has to be limited as well. The stability requirement

[4]We say that a discretization $\mathbf{P}_{\Delta t,\Delta h}$ is consistent with the partial differential equation $\mathbf{P}u = f$ for any smooth function $\phi(x,t)$ if we have that $\lim_{\Delta t,\Delta h\to 0}\left(\mathbf{P}_{\Delta t,\Delta h}\phi - \mathbf{P}\phi\right) = 0$, as $\Delta t, \Delta h \to 0$.

[5]We say that a numerical scheme is free of dissipation, when the energy of the initial wave is not reduced in a way analogous to a diffusional process.

depends on the employed time integration scheme, and similarly to the spatial discretization, the smallest period T_n of the system needs to be represented with about 10 time steps. However, as a wave front progresses in space, it reaches one node after the other, and if the time step in a finite element analysis is too large, then the wave front can reach two consecutive several nodes at the same time. This would violate a fundamental property of wave propagation and can lead to instability. Therefore, time step is usually limited using the so-called Courant-Friedrichs-Lewy[6] (CFL) condition:

$$\Delta t \leq \text{CFL} \frac{\Delta h}{V_s^{max}} \,. \tag{4.34}$$

In Equation (4.34), the variable V_s^{max} is the highest shear wave velocity for the simulation, and CFL is a constant value less than or equal to one. For example, if the maximum shear-wave velocity is $V_s^{max} = 500\,[m/s]$, and an element size of $\Delta h = 0.5\,[m]$ is used for the spatial discretization for a CFL = 1.00, then a time step of $\Delta t \leq 0.001\,[s]$ is required. It is important to note that increasing or decreasing time step Δt decreases or increases the range of frequencies that the temporal mesh is able to capture for a given element size Δh. On the other hand, decreasing or increasing the size element Δh increases or decreases the range of frequencies that the spatial mesh can capture. In other words, some frequencies will be aliased[7] depending on which one, the time step size or the element size is increased based on the fact that the same frequency in both meshes are to be captured.

Lastly, there is no unique unified approach in the literature for 2D analyses of SSI. For example, in Arboleda-Monsalve et al. [7], the 2D simulations are done with quad elements in plane strain with 1 $[m]$ thickness, and considering one axis of elongated building where most sections (except close to the borders) deform the same. In Conti et al. [41], the 2D simulation is done for the soil with quad elements in plane-strain with 1 $[m]$ thickness and the modeling part (simplifications) comes when dealing with the building. Also, in Kraus and Džakić [93], the 2D simplification is done by using shell elements but with thickness 1 $[m]$ as well. Finally, in Tomeo et al. [149], they have considered a plane-strain soil with thickness $3B$, but they state that they want to match a 3D analysis. In this thesis, we follow [7] and [41].

[6] The Courant-Friedrichs-Lewy condition (CFL) condition is a stability criterion for explicit time integration schemes, which are conditionally stable. However, it can be used as a criterion to specify the time step for unconditionally stable methods as well.

[7] Numerical aliasing occurs when the mesh is too coarse to capture high frequency; therefore, such frequencies are lost and the energy of the signal decreases.

4.4 Demonstration of the finite element applied to soil-structure-interaction

In this section, a numerical example is provided to verify the implemented finite element model for soil-structure interaction problems. The finite element model and response simulation are performed using Seismo-VLAB [96–98] assuming a set of realistic parameter values for both soil and building structures. Features such as PML and DRM are included to emulate the semi-infinite half-space soil domain. A Ricker pulse [124] ground motion is used as input to obtain the response history simulations. The simulated displacement response time histories are computed at different floors. The robustness and performance of the proposed FEM is then evaluated and discussed.

Example 3. The reinforced concrete building has columns of rectangular cross section $1.00 \times 0.80\,[m]$, each of $3.5\,[m]$ height. Beams have rectangular cross sections $0.80 \times 0.60\,[m]$ and $6.0\,[m]$ length. The reinforced concrete density is $2500\,[kg/m^3]$, the reinforced concrete elasticity modulus is taken as $25\,[GPa]$, and beams are subjected to a overload of $3600\,[kg/m]$. This configuration gives a total height of $42\,[m]$ and a total width of $18\,[m]$ for the building. The solid core foundation has a half-width of $10\,[m]$, an equivalent length (thickness) of $1.0\,[m]$, and embedment depth of $2.5\,[m]$. The reinforced concrete material properties for the foundation are taken such that the density is $600\,[kg/m^3]$, elasticity modulus is $30\,[GPa]$, and Poisson's ratio is 0.20.

On the other hand, the soil domain is represented as an elastic, homogeneous, and semi-infinite medium with density $\rho_s = 2000\,[kg/m^3]$, Poisson's ratio $\nu = 0.35$, and shear wave velocity $V_s = 100\,[m/s]$. The soil and foundation domains are modeled as four-node two dimensional plain strain quadrilateral elements, and the building structure domain is modeled as two-node linear elastic frame elements. All material models assigned to structural and soil elements are isotropic linear and elastic, and no viscous damping is added. The connection between solid and structural elements as well as the rigid diaphragm behavior of the foundation are enforced using kinematic constraints.

The dimension of the truncated domain is taken such that the horizontal direction is $L_x = 70\,[m]$ and the vertical direction is $L_z = 75\,[m]$. We employ the perfectly-matched layer for plane-strain in two dimensions, and a PML of $10\,[m]$ thickness is provided around the near-field to truncate the semi-infinite half space. The domain reduction method (DRM) is employed in order to transmit the ground motion of an in-plane sv-wave propagating upwards inside the near-field domain. The incident

ground motion $\dot{u}_g(t)$ used in the finite element models is prescribed as an effective force Ricker function, proportional to Equation (4.35):

$$\dot{u}_g(t) = \left(1 - 2\gamma\,(t - t_0)^2\right) \exp\left[-\gamma\,(t - t_0)^2\right], \tag{4.35}$$

where $\gamma = (\pi f_0)^2$, $f_0 = 2.0\,[Hz]$ is the characteristic frequency, and $t_0 = 1.0\,[s]$ is the time of peak velocity. These values yield a Ricker wavelet of peak ground velocity $0.1\,[m/s]$ and frequency content between $0 - 7.5\,[Hz]$.

The time step Δt is limited using the Courant-Friedrichs-Lewy condition. In this regard, for an element size of $\Delta h = 0.5\,[m]$ and a fixed value CFL $= 0.30$, the time step $\Delta t = 0.0015\,[s]$ is used for the simulation. The resulting finite element mesh has approximately 32000 elements, and a simulation time of $t_{\text{sim}} = 12.0\,[s]$ is considered. The total number of time steps for the entire simulation is $n_t = 8000$, and Seismo-VLAB [96–98] is employed to carry out the analysis. The model domain is not large enough, therefore we use a single core execution. The time to complete this task is 135 $[min]$ in total.

The nodal time history response at three different locations in the building are represented in Figure 4.4 in solid-blue line. In particular, the total horizontal u_X^h and vertical u_Y^h displacement of the first-modal height, the total-horizontal u_X^r and vertical u_Y^r displacement of the roof, and the total horizontal displacement and rotation of the foundation are displayed. A normalized representation of the building structure indicating the control points is displayed as well.

Note how in Figure 4.4 after $t = 2.5\,[s]$ the building not only starts a free vibration motion, but also because of the radiation damping, the displacement response starts to decay. In addition, the foundation presents an important amount of rocking due to the flexibility of the soil and the inertial forces generated in the building.

The velocity field amplitude at (a) $t = 1.05\,[s]$, (b) $t = 1.65\,[s]$, (c) $t = 1.95\,[s]$, and (d) $t = 2.25\,[s]$ for the soil-structure interaction problem is shown in Figure 4.5. Note that Figure 4.5c at time $t = 1.95\,[s]$ is particularly interesting because it shows the waves front generated by the building due to the so-called inertia interaction[8].

[8]Inertial interaction refers to displacements and rotations at the foundation level of a structure that result from inertia-driven forces such as base shear and moment. Inertial displacements and rotations can be a significant source of flexibility and energy dissipation in the soil-structure system. In fact, inertial interaction generates period lengthening in the structure due to the increased overturning moment and foundation rotation, and also a modification in the damping of the structure due to two effects: contributions from soil hysteresis or hysteretic damping, and radiation of energy away in the form of stress waves, from the foundation to the soil known as radiation damping.

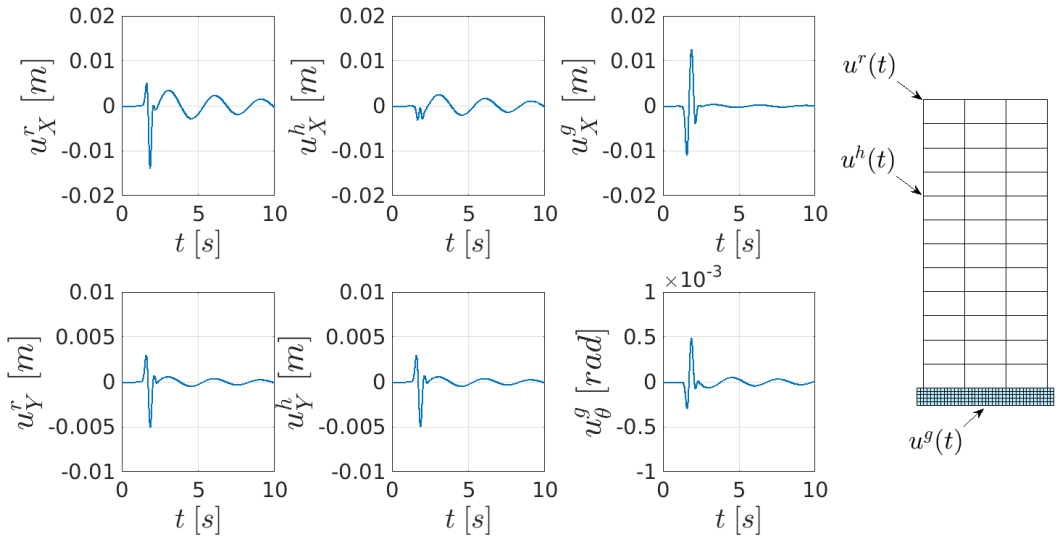

Figure 4.4: Displacement time history signals at (a) first-modal height at coordinates $(x, z) = (-9, 28)\,[m]$, (b) the roof at coordinates $(x, z) = (-9, 42)\,[m]$, and (c) the foundation at coordinates $(x, z) = (0, -2.5)\,[m]$ of the building.

Similarly Figure 4.5b at time $t = 1.65\,[s]$ shows the averaging process enforced by the foundation due to the so-called kinematic interaction[9].

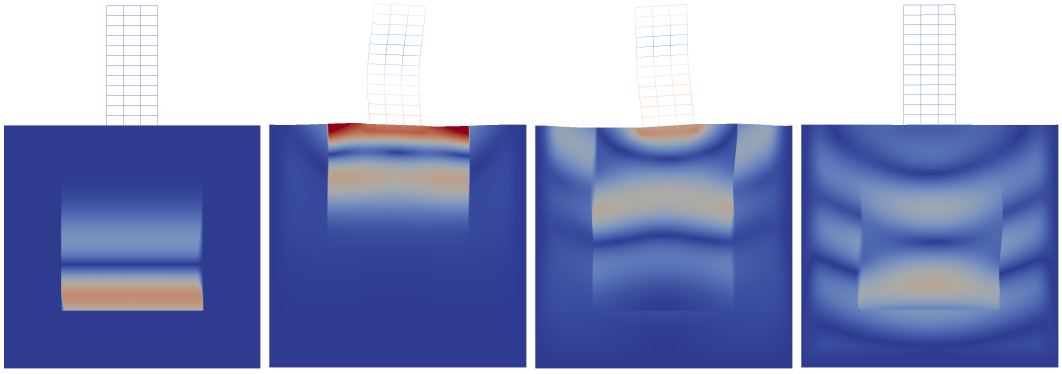

Figure 4.5: Velocity field amplitude and deformed configuration at time (a) $t = 1.05\,[s]$, (b) $t = 1.65\,[s]$, (c) $t = 1.95\,[s]$, and (d) $t = 2.25\,[s]$ for the soil-structure interaction problem. The blue color represents a velocity amplitude of $0.0\,[m/s]$, while the red color represents a velocity amplitude of $0.2\,[m/s]$.

[9] Kinematic interaction results from the presence of stiff foundation elements on/in the soil, which causes motions at the foundation to deviate from free-field motions. One cause of these deviations is base-slab averaging, in which the spatial variable of the ground motions is averaged within the foundation footprint due to the stiffness and strength of the foundation system. Another cause of this deviation is embedment effects, in which foundation-level motions are reduced as a result of ground motion reduction with depth below the free surface.

In Figure 4.6, the synthetic seismogram of the velocity for the horizontal and vertical components are shown. The horizontal red-solid lines represent the interface between the DRM domain and the scattered field domain. On the other hand, the vertical dashed blue lines represent the particular time when the snapshots in Figure 4.5 are taken.

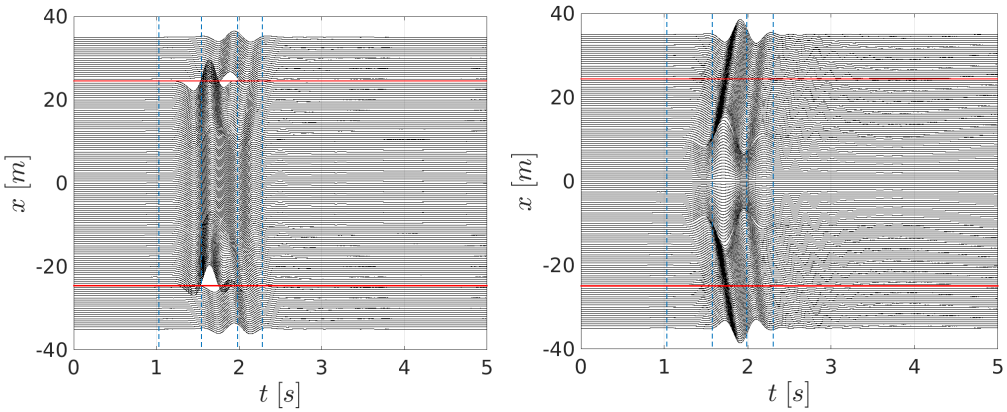

Figure 4.6: Synthetic seismogram (a) horizontal component $v_x(t)$, and (b) vertical component $v_z(t)$ of the velocity, recorded on the soil surface for the soil-structure interaction problem.

In Figure 4.6, three important results are shown. The first one has to do with the averaging effect that the foundation enforces on the soil. This can be seen on the synthetic seismogram after a time $t = 2.0\,[s]$ along a position $x = \pm 10\,[m]$. The second outcome is that the PML elements absorb all the outgoing waves, since there is no reflection coming from the boundaries, i.e., $x = \pm 35\,[m]$. The last outcome shows that two different waves are developed around the interface soil-foundation. First, there is a compressive wave which is generated by the system building-foundation because of the sway motion that the building imposes on the soil. The second wave is generated by the rocking-inertial motion and this corresponds to a surface wave which is generated after.

4.5 Conclusions

This chapter presented the finite element formulation (linear case) for soil-structure interaction (SSI) problems. Additionally, some numerical modeling considerations for SSI problems are provided regarding spatial and temporal discretization and connection between solid and structural elements.

The direct modeling method for SSI is demonstrated in a very simple example. The standard components such as: wave propagation, kinematic interaction, and inertial interaction found in SSI problems, are illustrated clearly in Figure 4.5. In particular, Figure 4.6 shows that the vertical motion generated at the soil's surface is a consequence of the rocking motion of the building generated by inertial interaction. The example makes also evident that a DRM formulation along with PML for absorbing scattered waves provides the necessary features for high-fidelity simulation of soil-structure interaction problems. Finally, we can conclude that both the DRM and PML implementation along with the structural elements and kinematic constraints in Seismo-VLAB are properly implemented.

On the performance side, the Seismo-VLAB execution for a single core process turned out to be fast. The finite element generation, assembly, and solution of the linear system took less than 1 second per time step. In addition, the RAM memory required for the entire simulation was less than 680 Mega-Bytes, showing that Seismo-VLAB utilizes little computer resources.

Chapter 5

THE REDUCED ORDER MODEL FOR SOIL-STRUCTURE INTERACTION PROBLEMS

The lack of numerical algorithms and computer capabilities along with the increase of model complexity makes the solution of engineering problems difficult. Thus, reduced order models (ROMs) arise as a technique to simplify the model's complexity while keeping the physics of the problem. In particular, two major contributions have made ROMs an appealing technique to analyze complex systems: (a) static condensation introduced by Guyan [61] and Irons [73], and (b) component mode synthesis introduced by Craig and Bampton [14, 43]. Both methods have been extensively used in the past 50 years, and have become essential in probabilistic engineering and resilient design of interconnected civil infrastructure systems [26, 34, 76–78] because of their reduced computational cost.

Developing ROMs for SSI problems usually relies on replacing the surrounding soil by impedance functions while keeping the structure intact. Although a large number of ROMs have been previously proposed to quantify SSI effects, most have been formulated in the frequency-domain. Therefore, these models are restricted either by oversimplifying assumptions, e.g. [21, 154] or by relying on superposition, e.g. [57, 138, 139] to a limited class of linear elastic problems. ROMs for quantifying SSI effects in building structures are usually developed based solely on (semi-) analytical impedance functions (or dynamic springs) available for rigid foundations with simplified configurations, e.g. [56, 119]. Even if the impedance functions are known, their distribution along the building foundation is cumbersome, and by extension, so is their use for buildings with large, complex footprints that do not conform to the original simplified configurations. Moreover, integrating the impedance values in time-domain analyses for SSI by selecting a representative, frequency-independent value is not clear.

The latter problems can be addressed using for instance a series of uniformly distributed frequency-independent spring and dashpot elements distributed over the soil-foundation interface. The role of these elements is to reflect the aggregate stiffness and energy dissipation characteristics of the soil system as seen from the building foundation. However, the spring and dashpot coefficients become param-

eters of the ROM and require to be calibrated such that the interaction mechanisms are properly incorporated. Regardless of calibrating such spring and dashpot coefficients, a ROM formulated in this manner provides the following advantages: (1) describing the soil behavior as a set of spring and dashpot elements allows the ROM to be easily incorporated in any FEM software; (2) modeling the soil as horizontal and vertical spring and dashpot elements offers the possibility to be condensed into a translational and rotational degrees-of-freedom in a straightforward manner; and (3) more sophisticated non-linear material behavior as well as contact behavior between soil and foundation can be incorporated at the spring and dashpot elements level.

In this chapter, the reduced order model for soil-structure interaction problems is formulated using condensation techniques. In particular, the reduction is performed in three steps: first, the effects of foundation embedment is studied by performing equilibrium of the foundation alone; then, the building system complexity is simplified using the static condensation method; lastly, the later results are integrated to generate the reduced order model for the soil-structure interaction. The ROM developed in this manner is compared against high-fidelity finite element models, and some examples are provided to demonstrate the accuracy of the proposed ROM in time domain analysis.

5.1 Effects of shallow foundation embedment

The behavior of the foundation is formulated considering analytical expressions for the stiffness and damping matrices of the soil as a function of the springs (k_x, k_z) and dashpots (c_x, c_z) distributed along the soil-foundation interface. In this analysis, we assume that the distributed spring and dashpot coefficients are known. The expressions derived hereafter can be considered as an extension of the ones proposed in [57, 139] for which the coupling restoring moment term is generated by the horizontal and vertical spring elements as it is shown in Figure 5.1.

In Figure 5.1a, the foundation has a half-width B and a depth D. The external forces applied to the system are an axial force N, a shear force V, and a moment M. These external forces are such that $N, V, M : \mathbf{u}(x, z) \rightarrow \mathbb{R}$, where $\mathbf{u}(x, z) = [\hat{u}(x, z), \hat{w}(x, z)]$ represents the displacement field. The restoring forces exerted by the soil are represented as springs acting over the foundation perimeter as shown in Figure 5.1b. Moreover, the foundation is assumed to be rigid so that the displacement field can be described by three degrees-of-freedom as shown in Figure 5.1c. Thus, the

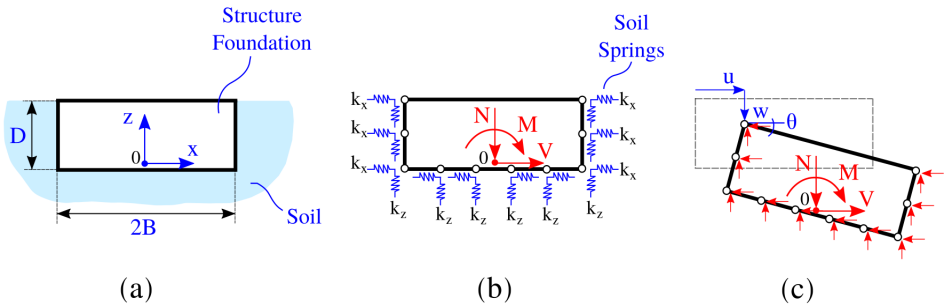

(a) (b) (c)

Figure 5.1: The soil-foundation system. (a) Geometry of the foundation system, (b) modeling of the soil continuum as distributed springs, and (c) free-body diagram of the foundation.

displacement field components $\hat{u}(x, z)$ and $\hat{w}(x, z)$ are:

$$\hat{u}(x, z) = u - \theta\, z\,, \tag{5.1}$$

$$\hat{w}(x, z) = w + \theta\, x\,, \tag{5.2}$$

where the variable u, w, and θ represents the horizontal, vertical and rotational rigid deformation (i.e., degree of freedom) of the foundation, respectively. Next, and without loss of generality, we assume that the distributed horizontal springs k_x and vertical springs k_z are constant over the soil-foundation interface; this is $k_x(x, z) = k_x$ and $k_z(x, z) = k_z$. This assumption is acceptable since we assume shallow embedment. Under this assumption, the soil-stiffness matrix is derived enforcing equilibrium of forces as represented in Figure 5.1c. Therefore, performing equilibrium of forces in the z-direction of the foundation yields

$$\begin{aligned} N = &\int_0^D \hat{w}(x = -B, z)\, k_z(z)\, dz + \int_0^D \hat{w}(x = B, z)\, k_z(z)\, dz + \\ &\int_{-B}^{B} \hat{w}(x, z = 0)\, k_z(z = 0)\, dx\,, \\ = &\, 2k_z\,(D + B)\, w\,. \end{aligned} \tag{5.3}$$

Taking equilibrium of forces in the x-direction of the foundation yields

$$\begin{aligned} V = &\int_0^D \hat{u}(x = -B, z)\, k_x(z)\, dz + \int_0^D \hat{u}(x = B, z)\, k_x(z)\, dz + \\ &\int_{-B}^{B} \hat{u}(x, z = 0)\, k_x(z = 0)\, dx\,, \\ = &\, 2\,k_x\,(D + B)\, u + k_x\, D^2\, \theta\,. \end{aligned} \tag{5.4}$$

Performing equilibrium of moments in the z-direction about point 0 yields

$$\begin{aligned} M = &\int_0^D \hat{u}(x=-B,z)\, k_x(z)\, z\, dz + \int_0^D \hat{u}(x=B,z)\, k_x(z)\, z\, dz + \\ &\int_0^D \hat{w}(x=-B,z)\, k_z(z)\, B\, dz - \int_0^D \hat{w}(x=B,z)\, k_z(z)\, B\, dz - \\ &\int_{-B}^{B} \hat{w}(x,z=0)\, k_z(z=0)\, x\, dx\,, \\ = &\, k_x\, D^2\, u + \left(\frac{2}{3} k_x\, D^3 + \frac{2}{3} k_z\, B^3 + 2B^2 D k_z\right)\theta\,. \end{aligned} \tag{5.5}$$

Equations (5.3), (5.4), and (5.5) can be written in matrix form. A similar analysis can be carried out to obtain the damping matrix. Thus, the lumped stiffness and damping matrices are written in the following compact form:

$$\mathbf{\Lambda} = \begin{bmatrix} 2\,\lambda_z\,(D+B) & 0 & 0 \\ 0 & 2\,\lambda_x\,(D+B) & \lambda_x\, D^2 \\ 0 & \lambda_x\, D^2 & \frac{2}{3}\lambda_x\, D^3 + \frac{2}{3}\lambda_z\, B^3 + 2\,\lambda_z\, B^2 D \end{bmatrix}, \tag{5.6}$$

where the matrix $\mathbf{\Lambda} \in \mathbb{R}^{3\times 3}$ represents either the stiffness or damping matrix of the foundation system, and λ the distributed spring or dashpot coefficients. The lumped stiffness coefficients are defined as:

$$k_{xx} = 2\,k_x\,(D+B)\,, \tag{5.7}$$

$$k_{x\theta} = k_x\, D^2\,, \tag{5.8}$$

$$k_{\theta\theta} = \frac{2}{3} k_x\, D^3 + \frac{2}{3} k_z\, B^3 + 2\,k_z\, B^2 D\,. \tag{5.9}$$

The lumped damping coefficients are defined as:

$$c_{xx} = 2\,c_x\,(D+B)\,, \tag{5.10}$$

$$c_{x\theta} = c_x\, D^2\,, \tag{5.11}$$

$$c_{\theta\theta} = \frac{2}{3} c_x\, D^3 + \frac{2}{3} c_z\, B^3 + 2\,c_z\, B^2 D\,. \tag{5.12}$$

Remark. *The matrix in (5.6) allows us to compute the reduced reactive soil forces that must be added to the foundation so that the dynamic equilibrium using D'alambert's principle can be carried out without the soil.*

5.2 Static condensation of building structures

We consider the planar fixed-base building structure of n-story as shown in Figure 5.2. The finite element method described in [16, 70] is here employed to approximate the dynamic building behavior. The structure domain is discretized considering two-node linear elastic frame elements. The nodes connecting this type of element have three degrees of freedom of which two are for translation and one is for rotation. The materials employed to model structural and soil elements are isotropic linear and elastic. We assume that each floor acts as a rigid diaphragm, thus the horizontal degree of freedom at each floor level are the same.

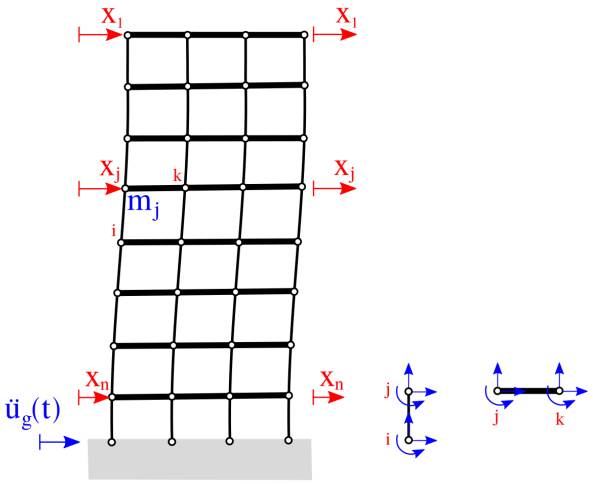

Figure 5.2: The fixed-base building structure in which $x_1, \ldots, x_n$ represents the relative displacement of each floor on the horizontal axis and $\ddot{u}_g(t)$ the free-field acceleration. The i, j, k are nodes in the finite element model and the blue arrows the degree of freedom in each node.

The equation of motion of the system under such conditions is written as:

$$\mathbf{M}\,\ddot{x} + \mathbf{C}\,\dot{x} + \mathbf{K}\,x = -\mathbf{M}\mathbf{L}\,\ddot{u}_g(t), \tag{5.13}$$

where $\mathbf{M}, \mathbf{C}, \mathbf{K} \in \mathbb{R}^{N\times N}$ are the mass, damping, and stiffness matrices of the building. The vectors $\ddot{x}, \dot{x}, x \in \mathbb{R}^N$ are the acceleration, velocity, and displacements of each degree-of-freedom. The signal $\ddot{u}_g(t)$ represents the free-field acceleration applied at the fixed-base, the operator $\mathrm{L} \in \mathbb{R}^N$ represents the seismic influence vector, and N is the total number of degrees of freedom of the model.

Unfortunately, the actual number N of degrees of freedom in Equation (5.13) can be very large. We want to describe its dynamics employing only n degrees of freedom.

A practical method of accomplishing the reduction of the number of degrees of freedom of a finite element model is static condensation (see, [16, 61]). Basically, in this method we reduce secondary (inactive) degrees of freedom by expressing them in terms of the primary (active) degrees of freedom.

In order to describe the Static Condensation Method, assume that those primary degrees of freedom are located in the first n vector components, and secondary degrees of freedom to be reduced are located in the last m vector components. In this regard, Equation (5.13) can be recasted in the following manner:

$$\begin{bmatrix} \mathbf{M}_{n\times n} & \mathbf{M}_{n\times m} \\ \mathbf{M}_{m\times n} & \mathbf{M}_{m\times m} \end{bmatrix} \begin{bmatrix} \ddot{x}_n \\ \ddot{x}_m \end{bmatrix} + \begin{bmatrix} \mathbf{C}_{n\times n} & \mathbf{C}_{n\times m} \\ \mathbf{C}_{m\times n} & \mathbf{C}_{m\times m} \end{bmatrix} \begin{bmatrix} \dot{x}_n \\ \dot{x}_m \end{bmatrix} + \begin{bmatrix} \mathbf{K}_{n\times n} & \mathbf{K}_{n\times m} \\ \mathbf{K}_{m\times n} & \mathbf{K}_{m\times m} \end{bmatrix} \begin{bmatrix} x_n \\ x_m \end{bmatrix} = - \begin{bmatrix} \mathbf{ML} \\ \mathbb{O}_m \end{bmatrix} \ddot{u}_g(t)\,.$$

Now, if the lumped-mass matrix assumption is employed, then the sub-matrices $\mathbf{M}_{m\times n}^{\top} = \mathbf{M}_{n\times m} = \mathbb{O}_{n\times m}$. Moreover, if we also assume that the rotational mass terms are negligible, then $\mathbf{M}_{m\times m} \approx \mathbb{O}_{m\times m}$. In addition, if we also assume that the building has no damping, i.e. $\mathbf{C} = \mathbb{O}_{N\times N}$; this means that $\mathbf{C}_{m\times n}^{\top} = \mathbf{C}_{n\times m} = \mathbb{O}_{n\times m}$, and $\mathbf{C}_{m\times m} = \mathbb{O}_{m\times m}$. Then, the latter expression can be written as,

$$\mathbf{M}_{n\times n}\,\ddot{x}_n + \mathbf{C}_{n\times n}\,\dot{x}_n + \mathbf{K}_{n\times n}\,x_n + \mathbf{K}_{n\times m}\,x_m = -\mathbf{ML}\,\ddot{u}_g(t)\,, \tag{5.14}$$

$$\mathbf{K}_{m\times n}\,x_n + \mathbf{K}_{m\times m}\,x_m = 0\,. \tag{5.15}$$

From Equation (5.15), we obtain: $x_m = -\mathbf{K}_{m\times m}^{-1}\mathbf{K}_{m\times n}\,x_n$, which, once it is replaced into Equation (5.14), yields:

$$\mathbf{M}_{n\times n}\,\ddot{x}_n + \mathbf{C}_{n\times n}\,\dot{x}_n + \left(\mathbf{K}_{n\times n} - \mathbf{K}_{n\times m}\mathbf{K}_{m\times m}^{-1}\mathbf{K}_{m\times n}\right) x_n = -\mathbf{ML}\,\ddot{u}_g(t)\,. \tag{5.16}$$

We then write the condensed equation of motion for the fixed-base case in the following manner,

$$\mathbf{M}_s\,\ddot{x}_n + \mathbf{C}_s\,\dot{x}_n + \mathbf{K}_s\,x_n = -\mathbf{M}_s\mathrm{L}\,\ddot{u}_g(t)\,. \tag{5.17}$$

where $\ddot{x}_n, \dot{x}_n, x_n \in \mathbb{R}^n$ are the acceleration, velocity, and displacement vectors for the condensed horizontal degree of freedom. Similarly, $\mathbf{M}_s = \mathbf{M}_{n\times n}$, $\mathbf{C}_s = \mathbf{C}_{n\times n}$, and $\mathbf{K}_s = \mathbf{K}_{n\times n} - \mathbf{K}_{n\times m}\mathbf{K}_{m\times m}^{-1}\mathbf{K}_{m\times n} \in \mathbb{R}^{n\times n}$ are the condensed mass, damping, and stiffness matrices of the building.

Remark. *The equation of motion described in (5.17) not only preserves the axial effects of the columns as well as the rotational effects of the beams, but it also allows to include structural damping through the* $\mathbf{C}_s$ *matrix in a straightforward manner, without computing the full* $\mathbf{C}$ *damping matrix.*

5.3 Equation of motion for soil-structure interaction

Consider the reduced order model of a planar n-story building and foundation as shown in Figure 5.3. We assume that each floor acts as a rigid diaphragm, thus the building's mass can be lumped at the floor levels. In this regard, the building structure is represented by $\mathbf{M}_s, \mathbf{C}_s, \mathbf{K}_s \in \mathbb{R}^{n\times n}$ matrices computed using static condensation provided in Equation (5.17). Thus, the vector $x \in \mathbb{R}^n$ represents the horizontal degree of freedom of the building, since there is only one translational degree of freedom on each floor. In addition, we assume a rigid rectangular foundation of half-width B and depth D sitting on an elastic half-space, for which 2 additional degrees of freedom $u, \theta \in \mathbb{R}$ appear because of the flexibility of the soil. The foundation has a total mass m_f, and a moment of inertia I_0. The equivalent elastic and viscous forces that the soil exerts on the foundation are computed using Equation (5.6). We finally consider that the building is subjected to a ground motion $u_g(t)$.

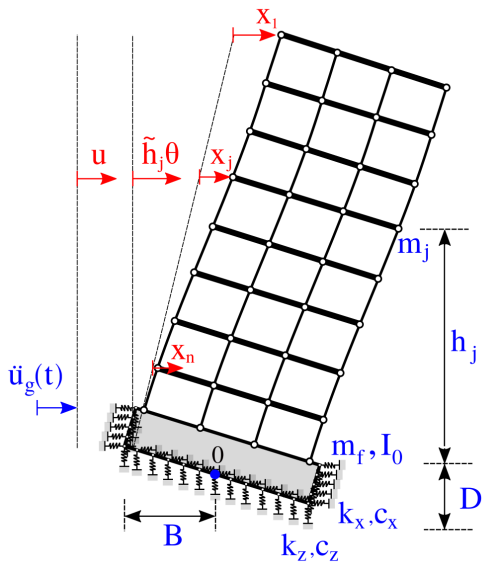

Figure 5.3: The flexible-base soil-structure interaction system in which $x = (x_1, \ldots, x_n)$ represents the relative displacement of each floor, u represents the relative deformation of the soil, and θ the rigid rotation of the foundation, and $\ddot{u}_g(t)$ the free-field acceleration.

In order to simplify computation, we define $\mathbb{1} \in \mathbb{R}^n$ the vector of ones, which is $\mathbb{1} = (1, 1, \ldots, 1)^\top$, and $\mathbb{h} \in \mathbb{R}^n$ the vector of height, which is $\mathbb{h} = (h_1 + D, \ldots, h_n + D)^\top$. We also define $\mathbb{O}_{n\times m} \in \mathbb{R}^{n\times m}$ as the matrix of zeros.

The equilibrium of forces at the base in x-direction considering the complete struc-

ture becomes:

$$\left[\sum_{j=1}^{n} m_j \ddot{x}_j\right] + \left[m_f + \sum_{j=1}^{n} m_j\right] \ddot{u} + \left[m_f \frac{D}{2} + \sum_{j=1}^{n} m_j (D + h_j)\right] \ddot{\theta} + 2c_x(D + B)\dot{u} + c_x D^2 \dot{\theta} +$$
$$2k_x(D + B)u + k_x D^2 \theta = -\left[m_f + \sum_{j=1}^{n} m_j\right] \ddot{u}_g(t),$$

or written in compact form using Equations (5.7) to (5.12):

$$\mathbb{1}^\top \mathbf{M}_s \ddot{x} + \left(m_f + \mathbb{1}^\top \mathbf{M}_s \mathbb{1}\right) \ddot{u} + \left(m_f \frac{D}{2} + \mathbb{h}^\top \mathbf{M}_s \mathbb{1}\right) \ddot{\theta} + c_{xx}\, \dot{u} + c_{x\theta}\, \dot{\theta} + k_{xx}\, u + k_{x\theta}\, \theta =$$
$$-\left(m_f + \mathbb{1}^\top \mathbf{M}_s \mathbb{1}\right) \ddot{u}_g(t). \tag{5.18}$$

The equilibrium of rotation at the base about point 0 of the complete structure is:

$$\left[\sum_{j=1}^{n} m_j (D + h_j) \ddot{x}_j\right] + \left[m_f \frac{D}{2} + \sum_{j=1}^{n} m_j (D + h_j)\right] \ddot{u} + \left[I_0 + m_f \frac{D^2}{4} + \sum_{j=1}^{n} m_j (D + h_j)^2\right] \ddot{\theta} +$$
$$c_x D^2 \dot{u} + \left(\frac{2}{3} c_x D^3 + \frac{2}{3} c_z B^3 + 2c_z B^2 D\right) \dot{\theta} + k_x D^2 u + \left(\frac{2}{3} k_x D^3 + \frac{2}{3} k_z B^3 + 2k_z B^2 D\right) \theta =$$
$$-\left[m_f \frac{D}{2} + \sum_{j=1}^{n} m_j (D + h_j)\right] \ddot{u}_g(t),$$

or written in compact form using Equations (5.7) to (5.12):

$$\mathbb{h}^\top \mathbf{M}_s \ddot{x} + \left(m_f \frac{D}{2} + \mathbb{h}^\top \mathbf{M}_s \mathbb{1}\right) \ddot{u} + \left(I_0 + m_f \frac{D^2}{4} + \mathbb{h}^\top \mathbf{M}_s \mathbb{h}\right) \ddot{\theta} + c_{x\theta}\, \dot{u} + c_{\theta\theta}\, \dot{\theta} + k_{x\theta}\, u +$$
$$k_{\theta\theta}\, \theta = -\left(m_f \frac{D}{2} + \mathbb{h}^\top \mathbf{M}_s \mathbb{1}\right) \ddot{u}_g(t). \tag{5.19}$$

The equilibrium of forces in x-direction of only the j-th building floor is:

$$m_j\, \ddot{x}_j + m_j\, \ddot{u} + m_j (D + h_j)\, \ddot{\theta} + \sum_{k=1}^{n} C_{jk}\, \dot{x}_k + \sum_{k=1}^{n} K_{jk}\, x_k = -m_j \ddot{u}_g(t)$$

or written in more suitable manner,

$$\mathbf{M}_s\, \ddot{x} + \mathbf{M}_s\, \mathbb{1}\, \ddot{u} + \mathbf{M}_s\, \mathbb{h}\, \ddot{\theta} + \mathbf{C}_s\, \dot{x} + \mathbf{K}_s\, x = -\mathbf{M}_s\, \mathbb{1}\, \ddot{u}_g(t). \tag{5.20}$$

Finally, Equations (5.18) to (5.20) can be employed to define the reduced order model for the soil-structure interaction problem. These expressions can further be

written in matrix form as,

$$\begin{bmatrix} \mathbf{M}_s & \mathbf{M}_s\,\mathbb{1} & \mathbf{M}_s\,\mathbb{h} \\ \mathbb{1}^\top\mathbf{M}_s & m_f + \mathbb{1}^\top\mathbf{M}_s\,\mathbb{1} & m_f\frac{D}{2} + \mathbb{h}^\top\mathbf{M}_s\,\mathbb{1} \\ \mathbb{h}^\top\mathbf{M}_s & m_f\frac{D}{2} + \mathbb{h}^\top\mathbf{M}_s\,\mathbb{1} & I_0 + m_f\frac{D^2}{4} + \mathbb{h}^\top\mathbf{M}_s\,\mathbb{h} \end{bmatrix} \begin{bmatrix} \ddot{x} \\ \ddot{u} \\ \ddot{\theta} \end{bmatrix} + \begin{bmatrix} \mathbf{C}_s & \mathbb{O}_{n\times 1} & \mathbb{O}_{n\times 1} \\ \mathbb{O}_{1\times n} & c_{\mathrm{x}\mathrm{x}} & c_{\mathrm{x}\theta} \\ \mathbb{O}_{1\times n} & c_{\mathrm{x}\theta} & c_{\theta\theta} \end{bmatrix} \begin{bmatrix} \dot{x} \\ \dot{u} \\ \dot{\theta} \end{bmatrix} +$$

$$\begin{bmatrix} \mathbf{K}_s & \mathbb{O}_{n\times 1} & \mathbb{O}_{n\times 1} \\ \mathbb{O}_{1\times n} & k_{\mathrm{x}\mathrm{x}} & k_{\mathrm{x}\theta} \\ \mathbb{O}_{1\times n} & k_{\mathrm{x}\theta} & k_{\theta\theta} \end{bmatrix} \begin{bmatrix} x \\ u \\ \theta \end{bmatrix} = - \begin{bmatrix} \mathbf{M}_s\,\mathbb{1} \\ m_f + \mathbb{1}^\top\mathbf{M}_s\,\mathbb{1} \\ m_f\frac{D}{2} + \mathbb{h}^\top\mathbf{M}_s\,\mathbb{1} \end{bmatrix} \ddot{u}_{\mathrm{g}}(t)\,. \tag{5.21}$$

Remark. *For Equation (5.21) to provide accurate results – i.e., similar responses to a full-finite element model, the spring coefficients k_x, k_z and dashpots coefficients c_x, c_z needs to be computed accurately.*

5.4 The effects of soil-structure interaction

It has been well documented that soil-structure interaction modifies the response of buildings. In particular, when a building is sitting on flexible soil, the system considering the superstructure and the soil-foundation interface will have a larger fundamental period than its rigid counterpart [19, 23, 120, 154]. This increase of the period is commonly referred as period elongation. Additionally, even when the inherent (hysteretic) damping of the structure is neglected, having a flexible base will add an additional source of energy dissipation in the form of stress waves traveling away from the system. This type of energy dissipation is commonly referred as radiation damping. In this section, we want to evaluate both the period elongation and radiation damping generated for the reduced order model derived in (5.21).

Let us start by considering two different systems. The first, depicted in Figure 5.4a, represents the reduced order model presented in Equation (5.21) for one floor, with effective height $\bar{h} = h + D$, stiffness $k \in \mathbb{R}^+$, structural damping $\beta_i \in \mathbb{R}^+$, supported by a distributed horizontal spring $k_x \in \mathbb{R}^+$ and distributed vertical springs $k_z \in \mathbb{R}^+$. The second system, depicted in Figure 5.4b, represents a fixed-base single degree of freedom system with mass $m \in \mathbb{R}^+$, modified stiffness $\tilde{k} \in \mathbb{R}^+$, modified-fundamental period $\tilde{T} \in \mathbb{R}^+$, and modified damping $\beta_0 \in \mathbb{R}^+$ as it is presented in [57, 139]. In the case of the equivalent fixed-base system, the total static displacement $\tilde{\Delta}$ generated by an applied external load F is computed as:

$$\tilde{\Delta} = \frac{F}{\tilde{k}}, \text{ with } \tilde{\Delta} \in \mathbb{R}\,. \tag{5.22}$$

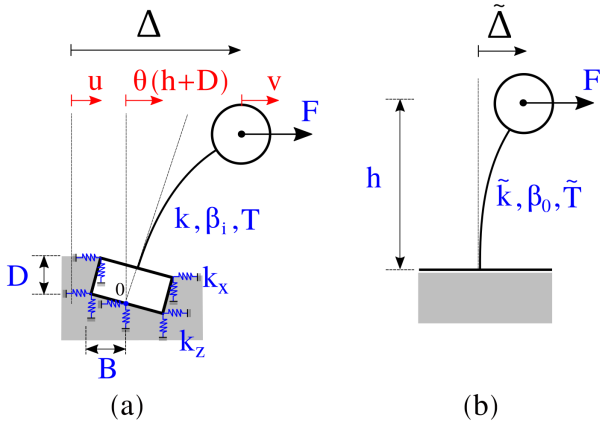

Figure 5.4: Model reduction from (a) the simplified flexible-base system into (b) the equivalent fixed-base system.

In this regard, the fixed-base period of the system becomes

$$\tilde{T} = 2\pi\sqrt{\frac{m}{\tilde{k}}}, \text{ with } \tilde{T} \in \mathbb{R}^{+}. \tag{5.23}$$

In addition, the total displacement of the reduced order model, when an external load F is applied, becomes

$$\begin{aligned}\Delta &= u + v + \theta\bar{h} \\ &= \frac{F}{k} + \frac{F\left(k_{\theta\theta} - \bar{h}k_{x\theta}\right)}{k_{\theta\theta}k_{xx} - k_{x\theta}^2} + \frac{F\left(k_{x\theta} - \bar{h}k_{xx}\right)}{k_{x\theta}^2 - k_{xx}k_{\theta\theta}}\bar{h}^2 \\ &= F\left(\frac{1}{k} + \frac{\bar{h}^2 k_{xx} - 2\bar{h}\,k_{x\theta} + k_{\theta\theta}}{k_{xx}k_{\theta\theta} - k_{x\theta}^2}\right).\end{aligned} \tag{5.24}$$

Note that, in order to equate the stiffness $\tilde{k}$ of the fixed-base system to that of the flexible-base system, the displacements must be equal, i.e., $\tilde{\Delta} = \Delta$. By comparison of Equations (5.22) and (5.24), we conclude that the following relation between the stiffness of the two systems must hold

$$\frac{1}{\tilde{k}} = \frac{1}{k} + \frac{\bar{h}^2\,k_{xx} - 2\,\bar{h}\,k_{x\theta} + k_{\theta\theta}}{k_{xx}k_{\theta\theta} - k_{x\theta}^2}. \tag{5.25}$$

Therefore, the corresponding fixed-base period will be given as

$$\tilde{T} = 2\pi\sqrt{\frac{m}{k}\left(1 + \frac{k}{k_{xx}k_{\theta\theta} - k_{x\theta}^2}\left(\bar{h}^2 k_{xx} - 2\bar{h}\,k_{x\theta} + k_{\theta\theta}\right)\right)}. \tag{5.26}$$

In turn, the period elongation of the reduced order model T relative to the period of the fixed-based system, $\tilde{T}$, is defined as follows:

$$\frac{\tilde{T}}{T} = \sqrt{1 + \frac{k}{k_{xx}k_{\theta\theta} - k_{x\theta}^2}\left(\bar{h}^2\, k_{xx} - 2\,\bar{h}\, k_{x\theta} + k_{\theta\theta}\right)}\,. \tag{5.27}$$

Remark. *Note that in Equation (5.27), when the stiffness $k_{x\theta} = 0$, the expression reduces to the same as the one presented in [23, 57, 139, 154] .*

Next, we want to derive the foundation damping ratio β_0 for the fixed-base-system. In order to do so, we represent the impedance $\mathbb{K} \in \mathbb{C}$ of the system in complex format,

$$\mathbb{K}_j = k_j + c_j\,\omega\,\mathbb{i} = k_j\left(1 + 2\beta_j\,\mathbb{i}\right), \tag{5.28}$$

where $\beta_j = \frac{\omega\, c_j}{2\,k_j}$ is the damping ratio, and the index j represents the horizontal, vertical, or coupled degree of freedom to be considered. Employing Equation (5.25) and the impedance represented in complex format, one can write

$$\frac{1}{\tilde{k}\,(1 + 2\beta_0\mathbb{i})} = \frac{1}{k\,(1 + 2\beta_i\mathbb{i})} + \frac{\bar{h}^2 k_{xx}\,(1 + 2\beta_x\mathbb{i}) - 2\bar{h}\,k_{x\theta}\,(1 + 2\beta_{x\theta}\mathbb{i}) + k_{\theta\theta}\,(1 + 2\beta_\theta\mathbb{i})}{k_{xx}k_{\theta\theta}\,(1 + 2\beta_x\,\mathbb{i})\,(1 + 2\beta_\theta\mathbb{i}) - k_{x\theta}^2\,(1 + 2\beta_{x\theta}\mathbb{i})^2}\,.$$

If each term in the previous expression is multiplied by its complex conjugate and assuming that the damping ratio for all degrees of freedom are small so that $(\beta_j)^2 \approx 0$, then the latter expression becomes

$$\frac{k}{\tilde{k}}\,(1 - 2\beta_0\,\mathbb{i}) = (1 - 2\beta_i\,\mathbb{i}) + k\left(\hat{k} - 2\hat{\beta}\,\mathbb{i}\right), \tag{5.29}$$

where the variables $\hat{k} \in \mathbb{R}^+$ and $\hat{\beta} \in \mathbb{R}^+$ in Equation (5.29) are defined as follows

$$\hat{k} = \frac{\bar{h}^2 k_{xx} - 2\bar{h}\,k_{x\theta} + k_{\theta\theta}}{k_{xx}k_{\theta\theta} - k_{x\theta}^2},$$

$$\hat{\beta} = \frac{k_{xx}\left(k_{\theta\theta} - \bar{h}k_{x\theta}\right)^2\beta_x - 2k_{x\theta}\left(\bar{h}k_{xx} - k_{x\theta}\right)\left(\bar{h}k_{x\theta} - k_{\theta\theta}\right)\beta_{x\theta} + k_{\theta\theta}\left(k_{x\theta} - \bar{h}k_{xx}\right)^2\beta_\theta}{\left(k_{xx}k_{\theta\theta} - k_{x\theta}^2\right)^2}\,.$$

Solving for the imaginary component of Equation (5.29) yields

$$\beta_0 = \frac{\tilde{k}}{k}\beta_i + \frac{\tilde{k}}{k}\left[\frac{k}{k_x}\beta_x\left(\frac{1 - \bar{h}\frac{k_{x\theta}}{k_{\theta\theta}}}{1 - \frac{k_{x\theta}^2}{k_{xx}k_{\theta\theta}}}\right)^2 - \frac{2\bar{h}k\,k_{x\theta}}{k_{xx}k_{\theta\theta}}\beta_{x\theta}\frac{\left(1 - \frac{k_{x\theta}}{\bar{h}k_{xx}}\right)\left(\bar{h}\frac{k_{x\theta}}{k_{\theta\theta}} - 1\right)}{\left(1 - \frac{k_{x\theta}^2}{k_{xx}k_{\theta\theta}}\right)^2} + \frac{k\bar{h}^2}{k_{\theta\theta}}\beta_\theta\left(\frac{1 - \frac{k_{x\theta}}{\bar{h}k_{xx}}}{1 - \frac{k_{x\theta}^2}{k_{xx}k_{\theta\theta}}}\right)^2\right].$$

Using the translational period and the rocking period definitions, the following identities can be written:

$$\frac{\tilde{k}}{k} = \frac{\tilde{k}}{m}\frac{m}{k} = \frac{\tilde{\omega}_n^2}{\omega_n^2} = \frac{1}{\left(\frac{\tilde{T}}{T}\right)^2},$$

$$\frac{k}{k_{xx}} = \frac{k}{m}\frac{m}{k_{xx}} = \frac{\omega_n^2}{\omega_x^2} = \frac{1}{\left(\frac{T}{T_x}\right)^2},$$

$$\frac{k\bar{h}^2}{k_{\theta\theta}} = \frac{k}{m}\frac{m\bar{h}^2}{k_{\theta\theta}} = \frac{\omega_n^2}{\omega_\theta^2} = \frac{1}{\left(\frac{T}{T_\theta}\right)^2},$$

$$\frac{k\bar{h}}{\sqrt{k_{xx}k_{\theta\theta}}} = \sqrt{\frac{k}{k_{xx}}}\sqrt{\frac{k\bar{h}^2}{k_\theta}} = \frac{1}{\left(\frac{T}{T_x}\right)}\frac{1}{\left(\frac{T}{T_\theta}\right)}.$$

Replacing the later expressions yields

$$\beta_0 = \frac{\beta_i}{\left(\frac{\tilde{T}}{T}\right)^2} + \frac{\beta_x}{\left(\frac{\tilde{T}}{T_x}\right)^2}\left(\frac{1-\bar{h}\frac{k_{x\theta}}{k_{\theta\theta}}}{1-\frac{k_{x\theta}^2}{k_{xx}k_{\theta\theta}}}\right)^2 - \frac{2}{\left(\frac{\tilde{T}}{T_x}\right)}\frac{\beta_{x\theta}}{\left(\frac{\tilde{T}}{T_\theta}\right)}\frac{k_{x\theta}}{\sqrt{k_{xx}k_{\theta\theta}}}\frac{\left(1-\frac{k_{x\theta}}{\bar{h}k_{xx}}\right)\left(\bar{h}\frac{k_{x\theta}}{k_{\theta\theta}}-1\right)}{\left(1-\frac{k_{x\theta}^2}{k_{xx}k_{\theta\theta}}\right)^2} + \frac{\beta_\theta}{\left(\frac{\tilde{T}}{T_\theta}\right)^2}\left(\frac{1-\frac{k_{x\theta}}{\bar{h}k_{xx}}}{1-\frac{k_{x\theta}^2}{k_{xx}k_{\theta\theta}}}\right)^2. \tag{5.30}$$

Remark. *Note once again that, when the stiffness $k_{x\theta} = 0$ in Equation (5.30), the expression reduces to the one presented in [23, 57, 139, 154] for the foundation damping ratio.*

5.5 Comparison of reduced order model and finite element analysis

In this section, a numerical example is provided to verify the proposed reduced order model for time domain analysis. A high-fidelity finite element model and response simulation are computed using Seismo-VLAB [96–98] assuming a set of realistic soil parameter values. The ROM is implemented in MATLAB [110], and is employed to compute response simulation. The soil spring and dashpot coefficients of the ROM are first computed using NIST [138] recommendation, and then calibrated to match the FEM. Both models are subjected to a Ricker pulse [124] ground motion to generate the displacement history responses. The error between

both cases is measured using the ℓ_2-error as:

$$\|y_{\text{FEM}} - \hat{y}_{\text{ROM}}\|_{\ell_2}^2 = \frac{1}{N_t\, N_m} \sum_{k=1}^{N_m} \sum_{j=1}^{N_t} \left(y_j^{(k)} - \hat{y}_j^{(k)} \right)^2 , \tag{5.31}$$

where $y_j^{(k)}$ represents the k-th observation (from the FEM) at j-th time step, $\hat{y}_j^{(k)}$ represents the k-th response (from the ROM) at j-th time step, N_t corresponds to the number of time steps, and N_m represents the number of observations considered. The performance and accuracy of the proposed ROM is then evaluated and discussed.

Example 4. In this example, the ROM is created considering a reinforced concrete building with columns of rectangular cross section $1.00 \times 0.80\,[m]$, each of $3.5\,[m]$ height. Beams have rectangular cross sections $0.80 \times 0.60\,[m]$ and $6.0\,[m]$ length. This configuration gives a building with a total height of $42\,[m]$ and an $18\,[m]$ width. The reinforced concrete density is $2500\,[kg/m^3]$, the reinforced concrete elasticity modulus is taken as $25\,[GPa]$, and beams are subjected to an overload of $3600\,[kg/m]$. The solid core foundation has a half-width of $10\,[m]$ and an embedment depth of $2.5\,[m]$. The reinforced concrete material properties for the foundation are taken such that the density is $600\,[kg/m^3]$ and the elasticity modulus of $30\,[GPa]$. The building model is assembled using standard two-node frame finite elements, and static condensation, as described in § 5.2, is performed to the horizontal degree of freedom. The resulting mass, damping, and stiffness FE matrices are thus coupled to the soil-foundation system, as described in § 5.3, to produce the ROM that accounts for SSI. The ROM is exited using the true foundation-input motion obtained using the transfer function in Figure 7.6 and 7.7 so that the input signal are the same in both the ROM and FEM.

On the other hand, for the high-fidelity finite element method, the soil domain is represented as an elastic, homogeneous, and semi-infinite medium with density $\rho_s = 2000\,[kg/m^3]$, Poisson's ratio $\nu = 0.35$, and shear wave velocity $V_s = 100\,[m/s]$. The soil and foundation domains are modeled as four-node two dimensional plane strain quadrilateral elements, and the building structure domain is modeled as two-node linear elastic frame elements, with the same characteristics as described above. All material models assigned to structural and soil elements are isotropic linear and elastic, and no viscous damping is added. The connection between solid and structural elements as well as the rigid diaphragm behavior of the foundation are enforced using kinematic constraints. The dimension of the truncated domain is taken such that the horizontal direction is $L_x = 70\,[m]$ and the vertical direction

is $L_z = 75\,[m]$. Perfectly-matched layers for plane-strain in two dimensions are employed, and a PML of $10\,[m]$ thickness is provided around the near-field to truncate the semi-infinite half space. The domain reduction method (DRM) is chosen in order to transmit the ground motion of an in-plane sv-wave propagating upwards inside the near-field domain. The FEM is subjected to an incident ground motion $\dot{u}_g(t)$ prescribed as an effective Ricker function with $f_0 = 2.0\,[Hz]$ the characteristic frequency, $t_0 = 1.0\,[s]$ is the time of peak velocity, and a peak ground velocity of $0.1\,[m/s]$.

First, NIST recommendations, described in [138], are employed to estimate soil spring and dashpot coefficients in the ROM. NIST impedances and foundation input motion transfer functions for analyzing SSI in shallow foundations is meant to be used in 3D settings. However NIST methodology is general enough to be applied in 2D settings. Therefore, the true 2D impedance functions for plane-strain settings are used instead of the 3D impedance functions available in NIST; and the true 2D foundation input motion (FIM) transfer function (TF) in plane-strain conditions are used instead of those available in NIST[1]. In this regard, spring coefficients $k_x = 1.2505 \cdot 10^6\,[N/m]$, $k_z = 5.3198 \cdot 10^6\,[N/m]$, and dashpot coefficients $c_x = 4.065 \cdot 10^5\,[N\,s/m]$, $c_z = 0.866 \cdot 10^5\,[N\,s/m]$ are obtained using 2D impedance functions provided in Figure 7.2 to 7.4. The nodal time history response at three different locations in the building are represented in Figure 5.5. The finite element model responses are shown in solid-blue line, while the ROM are displayed in dashed-red lines. The total horizontal u_X^h and vertical u_Y^h displacement of the first-modal height, the total-horizontal u_X^r and vertical u_Y^r displacement of the roof, and the total horizontal displacement u_X^g and rotation u_θ^g of the foundation are displayed from left to right.

The responses illustrated in Figure 5.5 show that the elongated period as well as the radiation damping are not well captured when the NIST recommendations are used. Although the time history signals seems to agree, the model error obtained using NIST is 0.0651 for the entire simulation.

Second, the nodal time history response at three different locations are computed once again, but the spring and dashpot coefficients are judiciously taken as $k_x = 1.674 \cdot 10^6\,[N/m]$, $k_z = 4.875 \cdot 10^6\,[N/m]$, $c_x = 2.072 \cdot 10^5\,[N\,s/m]$, and $c_z = 2.965 \cdot 10^5\,[N\,s/m]$. The responses are illustrated in Figure 5.6, and in this case they match the elongated period as well as the radiation damping. In addition, note how

[1] The latter approach allows to have a fair comparisson between NIST and the ROM in 2D.

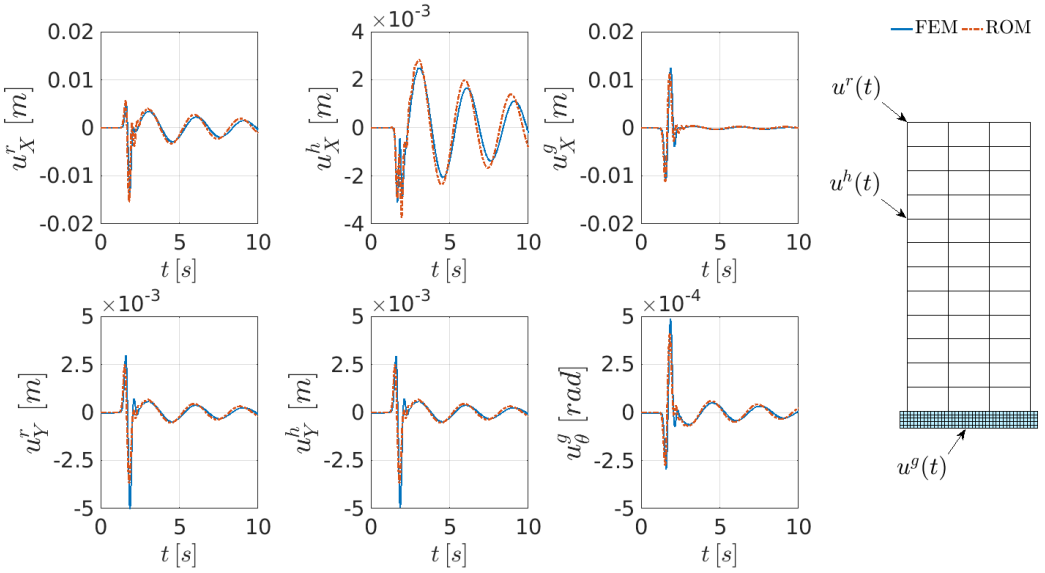

Figure 5.5: Displacement time history responses evaluated at the roof at coordinates $(x, z) = (-9, 42)\,[m]$, first-modal height at coordinates $(x, z) = (-9, 28)\,[m]$, and the foundation base at coordinates $(x, z) = (0, -2.5)\,[m]$ of the building. The finite element model responses are shown in solid-blue line, and the ROM using NIST recommendations are displayed in dashed-red lines.

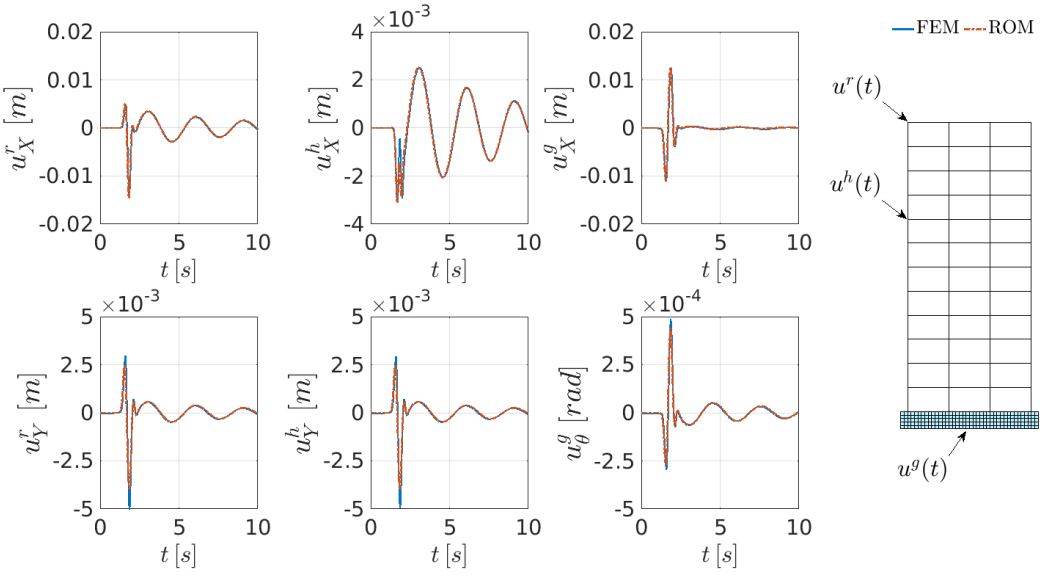

Figure 5.6: Displacement time history responses evaluated at the roof at coordinates $(x, z) = (-9, 42)\,[m]$, first-modal height at coordinates $(x, z) = (-9, 28)\,[m]$, and the foundation base at coordinates $(x, z) = (0, -2.5)\,[m]$ of the building. The finite element model responses are shown in solid-blue line, and the ROM using a judiciously chosen set of spring/dashpot values is displayed in dashed-red lines.

different in this case the value c_z is compared to NIST, and how well the elongated period as well as the radiation damping are well captured. The model error obtained using this set of spring and dashpot coefficients is 0.0130, which is five times smaller compared to NIST.

The previous example makes it evident that if the soil spring and dashpot coefficients are properly estimated, then the results of the ROM are identical to the FEM for the SSI problem. The framework that allows to estimate these coefficients accurately is presented in Chapter 6. This framework is termed as ensemble-Kalman inversion finite element (EnKI-FEM) model updating.

5.6 Conclusions

This chapter presented a suitable reduced order model (ROM) for time domain analysis of SSI problems. The ROM, illustrated in Figure 5.3 is essentially performed in three steps: (1) the dynamics effects of a rigid foundation is studied alone; (2) the building system complexity is simplified using a static condensation method; and (3) the latter simplifications are integrated to generate the reduced order model for the soil-structure interaction.

The ROM, developed in this manner, provides the following advantages: (1) describing the soil behavior/influence as a set of spring and dashpot coefficients/elements allows this formulation to be simple enough to be incorporated in any FEM software; (2) modeling the soil as horizontal and vertical spring and dashpot elements in the ROM offers the advantage that it can be condensed into a translational and rotational degrees of freedom in a simple manner; and (3) a more sophisticated nonlinear material behavior as well as contact behavior between soil and foundation can be incorporated at the spring and dashpot coefficients/elements.

It is important to mention that the proposed ROM provides accurate results–i.e., similar responses to a full-finite element model, as long as the spring coefficients k_x, k_z and dashpots coefficients c_x, c_z are computed accurately. NIST [138] provides simple recommendations, however, the results presented in Example 4 shows that period elongation and radiation damping are not well capture. Therefore, a better framework/recommendation to compute the frequency-independent soil spring and dashpot coefficients is required.

Chapter 6

FINITE ELEMENT UPDATING FOR PARAMETER ESTIMATION VIA ENSEMBLE KALMAN INVERSION

The concept of parameter estimation refers to a methodology of developing a mathematical framework in which states as well as parameters can be identified from data. This framework is in general known as system identification, and basically requires to accomplish the following steps: (1) measurements of the input and output signals from the system, (2) selection of a mathematical model that represents the desired phenomenon, (3) application of an estimation method to assess the parameter values in the candidate model, and (4) evaluation of the estimated model to check if the parameters are adequate or need to be updated. In real civil engineering applications, usually the mathematical models and data come from the finite elements model and the monitored structure. However, the estimation framework to assess the parameter values and correction feedback to evaluate the updated model can be addressed in different ways. Bayesian updating approach [18, 19, 87, 88], Kalman filter [83, 84] for linear systems, and its extension to non-linear systems[1] [68, 69, 75, 82, 92] have been commonly used as frameworks to identify states and parameters in the last 50 years. In particular, as from its development by Evensen [49] in 1994, the Ensemble Kalman filter[2] (EnKF) has had enormous impact on applications of data assimilation to state and parameter estimation [25, 50, 118]. The method essentially uses an ensemble of states and parameters that are sequentially updated by means of the Kalman formula which blends the model and data available at a given time. This simple idea has motivated researchers to develop several variants of EnKF for state and parameter estimation in dynamic systems [1, 25, 50].

As a result, and motivated by ensemble Kalman-based approaches, Iglesias et al. [72] proposed a novel application of an iterative ensemble Kalman method for the solution of inverse problems. The inverse problem is solved by introducing artificial dynamics based on state augmentation, which is typically used for joint state and

[1] The extended Kalman filter (ExKF) and the unscented Kalman filter (UnKF) are the most used in civil engineering for non-linear problems.

[2] In EnKF, the solution is solved in the affine space spanned by the ensemble. The ensemble, which evolves in time according to the nonlinear dynamical model, provides a representation of the subspace where the update is computed at each analysis time. The ensembles also lead to an efficient algorithm where the state error covariance matrix is not computed and is only implicitly used.

parameter estimation in the context of EnKF [6]. This approach for parameter estimation turns out to be very robust, accurate, and simple to implement, and is used as building block for the development of the ensemble-Kalman inversion finite element model (EnKI-FEM) updating framework for parameter estimation.

In this chapter, the inverse problem based on Ensemble Kalman inversion (EnKI) for the parameter estimation of the soil-structure interaction problem is formulated. In this regard, the forward model for SSI is first introduced, and then the inverse problem for parameter estimation is formulated. Some properties of EnKI-FEM updating formulation are also discussed, and some examples to demonstrate the robustness and accuracy of the proposed framework for parameter estimation are presented under the context of soil-structure interaction problems.

6.1 The forward model

The forward model in this case represents the solution of the soil-structure interaction problem, using for instance, methods presented in § 4.2 or 5.3. Mathematically speaking, the forward model can be understood as,

$$\text{Given} \quad u \in \mathcal{H}_1, \quad \text{evaluate} \quad y = \mathbf{G}(u) \in \mathcal{H}_2\,, \tag{6.1}$$

where $\mathcal{H}_1 := \mathbb{R}^m$ and $\mathcal{H}_2 := \mathbb{R}^n$ are separable Hilbert spaces[3], the vector y is known as the observation vector–i.e., the data, the vector $u \in \mathbb{R}^m$ contains the dynamical system parameters–i.e., to be identified, and $\mathbf{G}(u) : \mathbb{R}^m \to \mathbb{R}^n$ is the linear or nonlinear observation operator–i.e., the mathematical model.

The nonlinear observation operator is obtained using the reduced order model for the soil-structure interaction problem, as presented extensively in § 5.3. For this purpose, we consider a planar $N-2$ story building and foundation as shown in Figure 6.1. We assume that each floor acts as a rigid diaphragm, thus the building's mass can be lumped at the floor levels. We also assume that rotational inertia of each story with respect to a horizontal axis is negligible, as well as the axial deformations of the columns. Therefore, there is only one translational degree of freedom on each floor. In addition, we assume a rigid rectangular foundation of half-length B and depth D sitting on an elastic half-space, for which 2 additional degrees of freedom are added because of the flexibility of the soil.

[3] A topological space is said to be separable if it has a countable dense subset. In other words, this means that a Hilbert space is separable if and only if it admits a countable orthonormal basis.

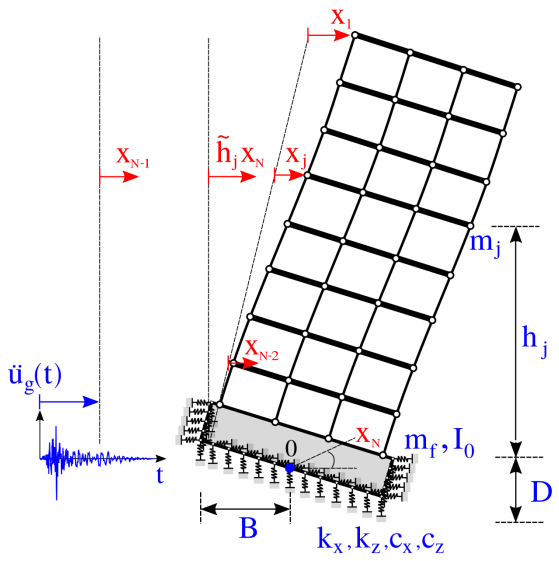

Figure 6.1: The flexible-base soil-structure interaction system in which $x_1, \ldots, x_{N-2}$ represents the relative displacement of each floor, x_{N-1} represents the relative deformation of the soil, and x_N the rigid rotation of the foundation.

Under the previous assumptions, the equation of motion (see Equation (5.21) for derivation details) of the system under such conditions is written as:

$$\mathbf{M}\,\ddot{x}(t) + \mathbf{C}(u)\,\dot{x}(t) + \mathbf{K}(u)\,x(t) = -\mathbf{M}\mathrm{L}\,\ddot{u}_g(t)\ , \text{with } t \in [0, T_{\text{sim}}], \tag{6.2}$$

where $\ddot{x}(t), \dot{x}(t), x(t) \in \mathbb{R}^N$ are the acceleration, velocity, and displacement vector responses. The matrices $\mathbf{M}, \mathbf{C}(u), \mathbf{K}(u) \in \mathbb{R}^{N\times N}$ are mass, damping, and stiffness matrices of the flexible-base soil-structure interaction system. The vector $\mathrm{L} \in \mathbb{R}^N$ is the seismic influence vector. The function $\ddot{u}_g(t)$ is the free-field (or foundation input motion) acceleration. The vector $u = (k_x, k_z, c_x, c_z)^\top$ collects the soil spring and dashpot coefficients needed to emulate the flexibility and irradiated energy of the soil, and $T_{\text{sim}} \in \mathbb{R}^+$ represents the simulation time.

We further introduce the state space representation of Equation (6.2) to obtain a first order differential equation,

$$\begin{bmatrix} \ddot{x} \\ \dot{x} \end{bmatrix} = \begin{bmatrix} -\mathbf{M}^{-1}\mathbf{C}(u) & -\mathbf{M}^{-1}\mathbf{K}(u) \\ \mathbb{I}_{n\times n} & \mathbb{O}_{n\times n} \end{bmatrix} \begin{bmatrix} \dot{x} \\ x \end{bmatrix} - \begin{bmatrix} \mathrm{L} \\ \mathbb{O}_{n\times 1} \end{bmatrix} \ddot{u}_g(t)\,. \tag{6.3}$$

The latter allows to compute the system's response by using Runge-Kutta methods for the integration of Equation (6.3). Note that one can use the Newmark method for integrating Equation (6.2) directly to obtain the system response as well.

In our framework, the observation vector $y(t)$ describes the absolute position $x(t)$ of each degree of freedom; hence, the absolute displacements of the flexible-base soil-structure interaction system can be written as:

$$y(t) = h(x,t) = \mathbb{H}\, x(t) = \begin{bmatrix} 1 & 0 & 0 & \cdots & 0 & 1 & \tilde{\mathrm{h}}_1 \\ 0 & 1 & 0 & \cdots & 0 & 1 & \tilde{\mathrm{h}}_2 \\ \vdots & & & \ddots & & & \vdots \\ 0 & 0 & 0 & \cdots & 1 & 1 & \tilde{\mathrm{h}}_{n-2} \\ 0 & 0 & 0 & \cdots & 0 & 1 & 0 \\ 0 & 0 & 0 & \cdots & 0 & 0 & 1 \end{bmatrix} x(t)\,. \tag{6.4}$$

Note that the observation vector $y(t)$ is a linear operator in this case, and $\tilde{\mathrm{h}}_j = \mathrm{h}_j + D$ is the j-th total floor height.

6.2 The inverse problem

We are interested in the inverse problem of finding $u \in \mathcal{H}_1$ from $y \in \mathcal{H}_2$ such that,

$$y = \mathbf{G}(u) + \eta\,, \text{ with } \eta \sim N(0, \boldsymbol{\Gamma})\,. \tag{6.5}$$

Once again, $\mathcal{H}_1 := \mathbb{R}^m$ and $\mathcal{H}_2 := \mathbb{R}^n$ are separable Hilbert spaces, the vector u comprises all the unknown parameters that we want to estimate, the variable y is known as the observation vector and consists of the ground truth quantities of interest, and η is a zero-mean Gaussian noise with covariance $\boldsymbol{\Gamma}$. The nonlinear observation operator (a.k.a. forward model) $\mathbf{G}(u) : \mathbb{R}^m \to \mathbb{R}^n$ maps the parameter space to the data space. In this thesis, we work with one type of data-set: the displacement time series recorded at the floors and foundation levels and computed using the model described in § 4.2.

We would like to apply the EnKF to Equation (6.5); however, the observation operator $\mathbf{G}(\cdot)$ is in general nonlinear, and this does not render our system in a form where we can readily apply it. Thus, we introduce a new variable $w = \mathbf{G}(u)$ and rewrite the equation (6.5) as:

$$\begin{aligned} w &= \mathbf{G}(u)\,, \\ y &= w + \eta\,. \end{aligned} \tag{6.6}$$

The key point of this change of variable is that the data y is now linearly related to the variable $z = (u, w)^\top$. We then introduce the following dynamical system, taking

$y_{j+1} = y$ as the given data:

$$\begin{aligned} u_{j+1} &= u_j\,, \\ w_{j+1} &= \mathbf{G}\left(u_j\right)\,, \\ y_{j+1} &= w_{j+1} + \eta_{j+1}\,. \end{aligned} \tag{6.7}$$

Therefore, if we introduce not only the new variables $z = (u, w)^\top$, but also the nonlinear map $\boldsymbol{\Psi}(z) = (u, \boldsymbol{G}(u))^\top$ and linear operators $\boldsymbol{H} = [\mathbb{O}, \mathbb{I}]$, and its adjoint $\boldsymbol{H}^\perp = [\mathbb{I}, \mathbb{O}]$, then we can write the dynamical system in the form:

$$\begin{aligned} z_{j+1} &= \boldsymbol{\Psi}\left(z_j\right)\,, \\ y_{j+1} &= \boldsymbol{H}\, z_{j+1} + \eta_{j+1}\,, \end{aligned} \tag{6.8}$$

where $\mathbb{I}$ is the identity matrix, $\mathbb{O}$ represents a zero matrix, and $\boldsymbol{H}\, z = w$ and $\boldsymbol{H}^\perp z = u$.

Remark. *Given a single instance of data y, typically one of the following criterion is used to construct artificial data y_j for the filtering algorithm:*

$$y_{j+1} = y + s\,\omega_{j+1}\,,$$

where $\omega \sim (0, \boldsymbol{\Gamma})$, and $s = 0$ if is an unperturbed observation, or $s = 1$ if is a perturbed observation.

6.3 The ensemble Kalman inversion for parameter estimation

We now apply the EnKF to the dynamics/data model (6.8). We obtain for each ensemble $n = 1, \ldots, N$,

$$\begin{aligned} \hat{z}_{j+1}^{(n)} &= \boldsymbol{\Psi}\big(z_j^{(n)}\big)\,, \\ \overline{z}_{j+1} &= \frac{1}{N}\sum_{n=1}^{N} \hat{z}_{j+1}^{(n)}\,, \\ \hat{\mathbf{C}}_{j+1} &= \frac{1}{N}\sum_{n=1}^{N} \left(\hat{z}_{j+1}^{(n)} - \overline{z}_{j+1}\right) \otimes \left(\hat{z}_{j+1}^{(n)} - \overline{z}_{j+1}\right)\,, \\ z_{j+1}^{(n)} &= \left(I - \mathbf{K}_{j+1}\mathbf{H}\right) \hat{z}_{j+1}^{(n)} + \mathbf{K}_{j+1} y_{j+1}^{(n)}\,, \end{aligned} \tag{6.9}$$

with the Kalman gain

$$\begin{aligned} \mathbf{K}_{j+1} &= \hat{\mathbf{C}}_{j+1}\mathbf{H}^\top \mathbf{S}_{j+1}\,, \\ \mathbf{S}_{j+1} &= \left(\mathbf{H}\,\hat{\mathbf{C}}_{j+1}\,\mathbf{H}^\top + \boldsymbol{\Gamma}\right)^{-1}\,. \end{aligned} \tag{6.10}$$

We now use the specific structure on $\mathbf{\Psi}$, z, and $\mathbf{H}$ arising in the inverse problem and given in equation (6.8); this results in block form vectors and matrices. First, we note that

$$\hat{\mathbf{C}}_{j+1} = \begin{bmatrix} \mathbf{C}^{uu}_{j+1} & \mathbf{C}^{uw}_{j+1} \\ \left(\mathbf{C}^{uw}_{j+1}\right)^{\top} & \mathbf{C}^{ww}_{j+1} \end{bmatrix},$$
$$\bar{z}_{j+1} = \begin{bmatrix} \bar{u}_{j+1} \\ \bar{w}_{j+1} \end{bmatrix}, \tag{6.11}$$

where,

$$\bar{u}_{j+1} = \frac{1}{N}\sum_{n=1}^{N} u_j^{(n)}, \quad \bar{w}_{j+1} = \frac{1}{N}\sum_{n=1}^{N} \mathbf{G}\left(u_j^{(n)}\right) := \overline{\mathbf{G}}_j, \tag{6.12}$$

and,

$$\mathbf{C}^{uw}_{j+1} = \frac{1}{N}\sum_{n=1}^{N}\left(u_j^{(n)} - \bar{u}_j\right) \otimes \left(\mathbf{G}\left(u_j^{(n)}\right) - \overline{\mathbf{G}}_j\right),$$
$$\mathbf{C}^{ww}_{j+1} = \frac{1}{N}\sum_{n=1}^{N}\left(\mathbf{G}\left(u_j^{(n)}\right) - \overline{\mathbf{G}}_j\right) \otimes \left(\mathbf{G}\left(u_j^{(n)}\right) - \overline{\mathbf{G}}_j\right). \tag{6.13}$$

In Equation (6.11), the covariance matrix $\mathbf{C}^{ww}_{j+1}$ denotes the empirical covariance of the ensemble in data space, $\mathbf{C}^{uu}_{j+1}$ denotes the empirical covariance of the ensemble in space of the unknown u, and $\mathbf{C}^{uw}_{j+1}$ denotes the empirical cross-covariance from data space to the space of the unknown.

Noting that $S_{j+1} = \left(\mathbf{C}^{ww}_{j+1} + \mathbf{\Gamma}\right)^{-1}$, we obtain

$$\mathbf{K}_{j+1} = \begin{bmatrix} \mathbf{C}^{uw}_{j+1}\left(\mathbf{C}^{ww}_{j+1} + \mathbf{\Gamma}\right)^{-1} \\ \mathbf{C}^{ww}_{j+1}\left(\mathbf{C}^{ww}_{j+1} + \mathbf{\Gamma}\right)^{-1} \end{bmatrix}. \tag{6.14}$$

Combining equation (6.14) with the updating equation in (6.9), it follows that

$$u^{(n)}_{j+1} = \mathbf{H}^{\perp} z^{(n)}_{j+1} = u^{(n)}_j + \mathbf{C}^{uw}_{j+1}\left(\mathbf{C}^{ww}_{j+1} + \mathbf{\Gamma}\right)^{-1}\left(y^{(n)}_{j+1} - \mathbf{G}\left(u^{(n)}_j\right)\right). \tag{6.15}$$

The previous artificial dynamics, based on state augmentation in 6.8, allows the use of sequential EnKF for the solution of the inverse problem presented in 6.5. In this regard, the proposed EnKI algorithm (described in [72]) can be employed for estimating soil parameters in the following manner,

Algorithm 1 Iterative ensemble method for inverse problems applied to soil-structure interaction.

1: The **initialization step**: Let $\{z_0^{(n)}\}_{n=1}^N$ be the initial ensemble.

2: **for** $j = 0, \ldots, J$ **do**

3: The **Prediction step**: Propagate, under the artificial dynamics $z_{j+1} = \mathbf{\Psi}(z_j)$, the ensemble of particles

$$\hat{z}_{j+1}^{(n)} = \mathbf{\Psi}\left(z_j^{(n)}\right).$$

From this ensemble, we define a sample mean and covariance as follows:

$$\overline{z}_{j+1} = \frac{1}{N}\sum_{n=1}^{N} \hat{z}_{j+1}^{(n)},$$

$$\mathbf{C}_{j+1} = \frac{1}{N}\sum_{n=1}^{N} \left(\hat{z}_{j+1}^{(n)} - \overline{z}_{j+1}\right) \otimes \left(\hat{z}_{j+1}^{(n)} - \overline{z}_{j+1}\right).$$

4: **Analysis step.** Define the Kalman gain $\mathbf{K}_n$ by

$$\mathbf{K}_{j+1} = \mathbf{C}_{j+1}\mathbf{H}^\top \left(\mathbf{H}\,\mathbf{C}_{j+1}\,\mathbf{H}^\top + \mathbf{\Gamma}\right)^{-1},$$

where $H^\top$ is the adjoint operator of $\boldsymbol{H} = [\mathbb{O}, \mathbb{I}]$. Update each ensemble member as follows

$$z_{j+1}^{(n)} = \left(I - \mathbf{K}_{j+1}\mathbf{H}\right)\hat{z}_{j+1}^{(n)} + \mathbf{K}_{j+1}y_{j+1}^{(n)},$$

where

$$\hat{y}_{j+1}^{(n)} = y + \eta_{j+1}^{(n)},$$

and the $\eta_{j+1}^{(n)}$ are an independent identically distributed collections of vectors indexed by (n, j) with $\eta_1^{(1)} \sim N(0, \mathbf{\Gamma})$.

5: Compute the mean of the parameter update

$$u_{j+1} = \frac{1}{N}\sum_{n=1}^{N} u_{j+1}^{(n)}$$

and check for convergence (see discussion below).

6: **end for**

The implementation of Algorithm 1 can be represented schematically as shown in Figure 6.2. Note how each iteration of the ensemble Kalman inversion algorithm breaks into two parts: a prediction step and an update step. The prediction step

maps the current ensemble of particles into the data space, and thus introduces information about the forward model. The update (analysis) step makes comparisons of the mapped ensemble in the data space, with the data; it is at this stage that the ensemble is modified in an attempt to better match the data.

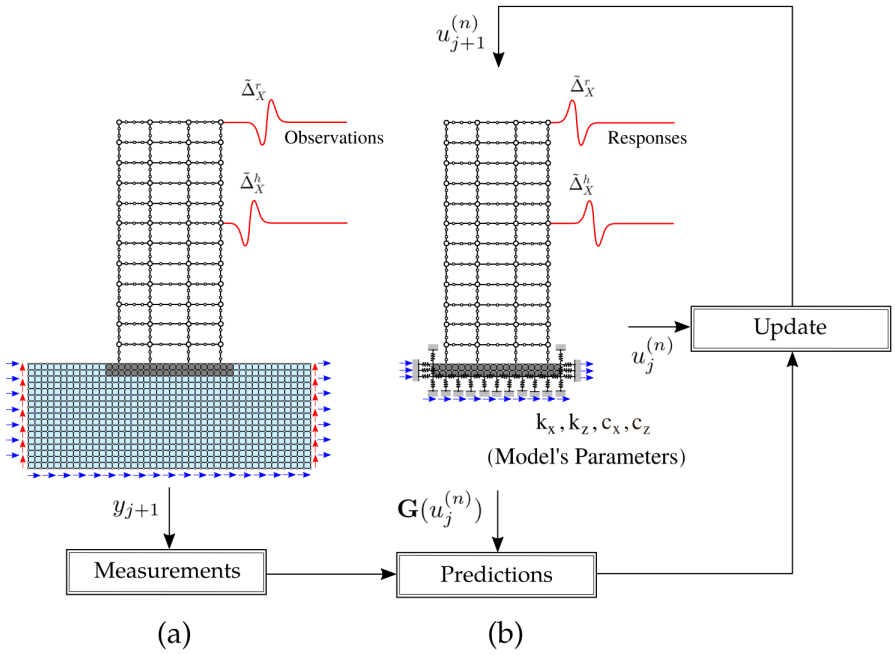

Figure 6.2: Ensemble-Kalman inversion finite element model updating framework applied to SSI. (a) Full finite element model from which the "true" responses are computed (observations), and (b) reduced order method from which the spring and dashpot coefficients are estimated. Note how each iteration of the ensemble Kalman inversion algorithm breaks into two parts: a prediction step and an update step.

It is also worth mentioning a few computational and numerical aspects regarding the EnKI-FEM implementation for SSI problems:

(1) The criterion to stop the EnKI is taken such that a relative change of 0.001 in all the parameters is reached in two consecutive EnKI iterations, or a maximum number of 500 iterations is reached.

(2) The initial parameter values $\{u_0^{(n)}\}_{n=1}^N$ are taken to coincide with the lumped stiffness and dashpot coefficients obtained using NIST [138].

(3) The positiveness of the stiffness and dashpot coefficients in the parameter vector $u = (k_x, k_z, c_x, c_z)^\top$ are enforced through the change of variables $u_i \in \mathbb{R}$, $\exp(u_i) : \mathbb{R} \to [0, \infty)$ to which the EnKI is applied.

6.4 Properties of the iterative ensemble Kalman inversion method

The EnKI algorithm has the following invariant subspace property:

Theorem 6.4.1. *Define* $\mathcal{A} = \text{span}\{u_0^{(n)}\}_{n\in\mathbb{N}}$, *then for all* $j \in \{0,\dots,J\}$ *and for all* $n \in \{1,\dots,N\}$, $u_{j+1}^{(n)} \in \mathcal{A}$.

Proof. We proceed by induction. Let $\mathbf{u}_j$ denote the collection of $\{u_j^{(n)}\}_{n\in\mathbb{N}}$. First, let $j \in \{0,\dots,J\}$ and $n \in \{1,\dots,N\}$ and define

$$d_j^{(n)} := \left(\mathbf{C}_{j+1}^{ww} + \mathbf{\Gamma}\right)^{-1}\left(y_{j+1}^{(n)} - \mathbf{G}\big(u_j^{(n)}\big)\right),$$
$$D_{mn}(\mathbf{u}_j) := \langle d_j^{(n)},\, \mathbf{G}\big(u_j^{(m)}\big) - \overline{\mathbf{G}}_j\rangle\,.$$

Furthermore we can write,

$$u_{j+1}^{(n)} = u_j^{(n)} - \frac{1}{N}\sum_{m=1}^{N} D_{mn}(\mathbf{u}_j)\left(u_j^{(m)} - \overline{u}_j\right),$$

and from definition of $\overline{\mathbf{G}}_j$ and bilinearity of the inner product, it follows that

$$\sum_{m=1}^{N} D_{mn}(\mathbf{u}_j) = 0\,.$$

Therefore the update expression may be rewritten, for all $j \in \{0,\dots,J\}$ and for all $n \in \{1,\dots,N\}$, as

$$u_{j+1}^{(n)} = u_j^{(n)} - \frac{1}{N}\sum_{m=1}^{N} D_{mn}(\mathbf{u}_j)\, u_j^{(m)}\,.$$

Hence if the property holds for all the particles of the time step j, it will clearly be the case for all the particles at time step $j+1$. □

Moreover, two remarks can be stated from Theorem 6.4.1 and Algorithm 1:

Remark. *The choice of the initial ensemble, i.e.,* $\{u_0^{(n)}\}_{n\in\mathbb{N}}$ *is key to the success of the algorithm, since the algorithm remains in the initial ensemble space. In this regard, the number of particles (or ensemble) must be at least the number of parameters to be identified.*

Remark. *Enough data needs to be provided so that the parameters can be identified. In other words, the identifiability conditions must be guaranteed.*

Remark. *Algorithm 1 may be viewed as a derivative-free optimization method.*

6.5 Ensemble-Kalman inversion finite element model updating framework

In this section, two numerical examples are provided to verify the proposed finite element model updating framework. For each example, the finite element model and response simulation are performed using Seismo-VLAB [96–98] assuming a set of realistic soil parameter values. The material parameters are later treated as unknown and then identified. In particular, four physical parameters characterizing the soil behavior are defined in the finite element model to be identified. The EnKI is implemented in MATLAB [110] and interfaced with Seismo-VLAB for finite element response computations. A Ricker pulse [124] ground motion is used for the response history simulations. The simulated displacement response time histories are artificially perturbed and used as the measured response data in the estimation phase. The performance of the proposed framework is then evaluated and discussed.

Example 5. In this example, the ROM is created considering a reinforced concrete building with columns of rectangular cross section $1.00 \times 0.80\,[m]$, each of $3.5\,[m]$ height. Beams have rectangular cross sections $0.80 \times 0.60\,[m]$ and $6.0\,[m]$ length. This configuration gives a building with a total height of $42\,[m]$ and an $18\,[m]$ width. The reinforced concrete density is $2500\,[kg/m^3]$, the reinforced concrete elasticity modulus is taken as $25\,[GPa]$, and beams are subjected to a overload of $3600\,[kg/m]$. The solid core foundation has a half-width of $10\,[m]$ and embedment depth of $2.5\,[m]$. The reinforced concrete material properties for the foundation are taken such that the density is $600\,[kg/m^3]$ and the elasticity modulus is $30\,[GPa]$.

The building model is assembled using standard two-node frame finite elements, and static condensation, as described in § 5.2, is performed to the horizontal degree of freedom. The resulting mass, damping, and stiffness FE matrices are thus coupled to the soil-foundation system, as described in § 5.3. The observations required for the EnKI framework are computed using the ROM developed in this manner. Thus, no model error is generated in this analysis, since the same ROM is employed to obtain the observations as well as response simulation of the updated model. The ROM is subjected to a Ricker pulse ground motion, and the response history simulations are artificially perturbed to construct artificial data.

The performance of the ensemble-Kalman inversion finite element model updating framework is evaluated considering: a number of ensembles of $n = 5, 10, 25, 50, 100$, an initial ensemble estimation of 10%, 25%, 50%, 100% larger than the true parameter values, and an artificially perturbed noise increase of 10%, 1%, 0.1% of the maximum observation responses. The analysis is performed on a base of a maxi-

mum number of $J = 25$ iterations.

Figure 6.3 illustrates the normalized ℓ_2-error at each EnKI-FEM updating iterations. On the vertical plots the artificially perturbed noise is changed, while on the horizontal plots the initial ensemble estimation is changed. Each plots presents the normalized error for different numbers of ensembles.

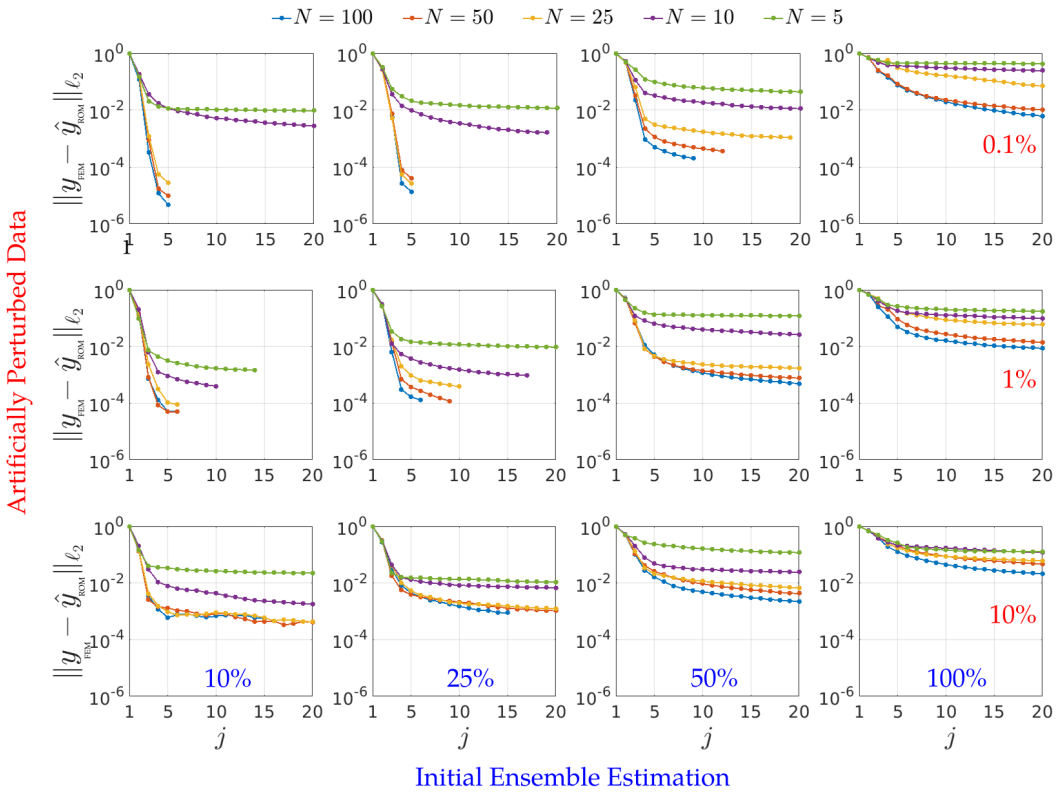

Figure 6.3: ℓ_2-norm misfit error between the finite element model (FEM) and the reduced order model (ROM) for different percentage of artificially perturbed data, initial ensemble estimation, and number of ensemble.

Figure 6.3 illustrates that at each iteration the ℓ_2-norm misfit error always decreases. As expected, the smallest error is obtained when the amplitude of the perturbed artificial data is small, the initial ensemble estimation is closer to the true values, and the number of ensembles is large. The increase on the perturbed artificial data, for a given initial ensemble estimation, requires the EnKI-FEM update to employ more iterations to reach convergence tolerance. However, a small amplitude on the artificially perturbed data generates the algorithm to perform better. Starting too far from the true values obliges the EnKI-FEM update to iterate more; also the model error tends to be larger even when a small number of ensembles are used. In general,

using 100, 50, or even 25 ensembles achieves the same model accuracy for an initial ensemble estimation and perturbed artificial data value.

In addition, the convergence of the soil parameters using the EnKI-FEM updating algorithm is next studied. Figure 6.4 illustrates how the estimation of the soil spring and dashpot coefficients evolves in each iteration. In this figure, the coefficients have been normalized by their true values, and an amplitude of the perturbed artificial data of 1% is kept constant.

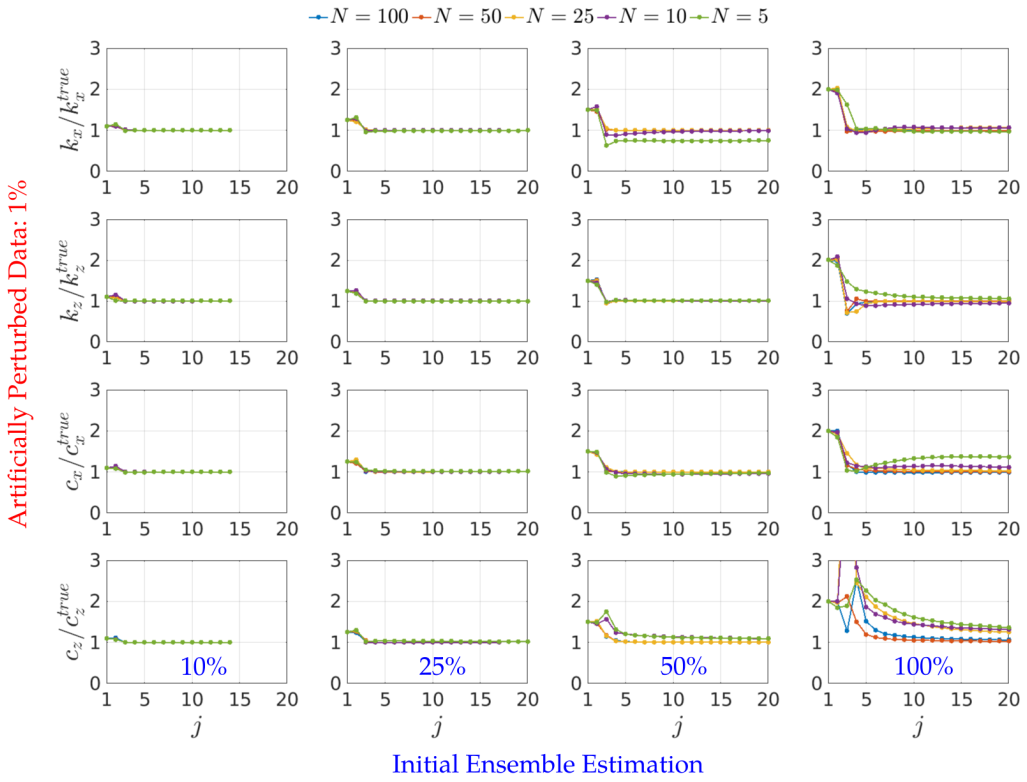

Figure 6.4: Normalized soil spring and dashpot coefficients using a 1% of artificially perturbed data, different initial ensemble estimation, and different number of ensemble.

Figure 6.3 shows that the EnKI-FEM updating algorithm converges always to the true parameters. Additionally, for a few particles–i.e., $N = 5$, the EnKI-FEM updating becomes sensitive to the random ensemble generation. It can be seen in Figure 6.3 that only in 2 cases for $N = 5$ did not reach the true values; however, if the same analysis is repeated with another seed, then the method will converge. A large number of ensembles (desirable) allows the EnKI-FEM updating framework to converge faster, however the computational time at the analysis phase increases,

since more finite element analyses are required. Therefore, a good compromise between ensemble number and computational time should be further investigated.

In general, the method always converges to the true parameters after a large number of iterations. However, a minimum number of ensembles are required, or at least, greater than the number of identified parameters to guarantee convergence. This is in fact consistent with Theorem 6.4.1, since a number of ensembles $n < 4$ is not able to span properly the parameter space.

Example 6. In this example, the observations required for the EnKI-FEM updating framework are computed using a high-fidelity finite element method. This means that the soil domain is represented as an elastic, homogeneous, and semi-infinite medium with density $\rho_s = 2000\,[kg/m^3]$, Poisson's ratio $\nu = 0.35$, and shear wave velocity $V_s = 100\,[m/s]$. The soil and foundation domains are modeled as four-node two dimensional plane strain quadrilateral elements and the building structure domain is modeled as two-node linear elastic frame elements, with the same characteristics as in the previous examples. All material models assigned to structural and soil elements are isotropic linear and elastic, and no viscous damping is added. The connection between solid and structural elements as well as the rigid diaphragm behavior of the foundation are enforced using kinematic constraints. The dimension of the truncated domain is taken such that the horizontal direction is $L_x = 70\,[m]$ and the vertical direction is $L_z = 75\,[m]$. Perfectly-matched layers for plane-strain in two dimensions are employed, and a PML of $10\,[m]$ thickness is provided around the near-field to truncate the semi-infinite half space. The domain reduction method (DRM) is chosen in order to transmit the ground motion of an in-plane sv-wave propagating upwards inside the near-field domain. The incident ground motion $\dot{u}_g(t)$ used in the finite element models is prescribed as an effective Ricker function with $f_0 = 2.0\,[Hz]$ the characteristic frequency, $t_0 = 1.0\,[s]$ the time of peak velocity, and a peak ground velocity of $0.1\,[m/s]$.

On the other hand, the reduced order model–presented in Equation (5.21)–is employed as the forward model. The parameter vector $u = (k_x, k_z, c_x, c_z)^\top$ is identified using the EnKI-FEM framework illustrated in Figure 6.2. In the EnKI-FEM updating framework, an artificially perturbed data of 1% is assumed, a number of $N = 50$ ensembles are used, a mean model of 20% standard deviation is generated, and the initial ensemble is estimated using NIST [138] recommendations. It is important to mention that model error is introduced in this case, since the ROM employed to compute the response simulation of the updated model is different from the high-

fidelity finite element from which the observations are obtained. Finally, the soil parameters vector components, obtained using the EnKI-FEM updating framework, are $k_x = 1.674 \cdot 10^6\,[N/m]$, $k_z = 4.875 \cdot 10^6\,[N/m]$, $c_x = 2.072 \cdot 10^5\,[N\,s/m]$, and $c_z = 2.965 \cdot 10^5\,[N\,s/m]$, respectively.

The nodal time history response at three different locations are illustrated in Figure 6.5. In this figure, the blue-solid line represents the time history displacement of the high-fidelity finite element model, while the red-solid line represents the displacement responses obtained using the ROM and the identified soil parameters. Note how the responses match the elongated period as well as the radiation damping very well.

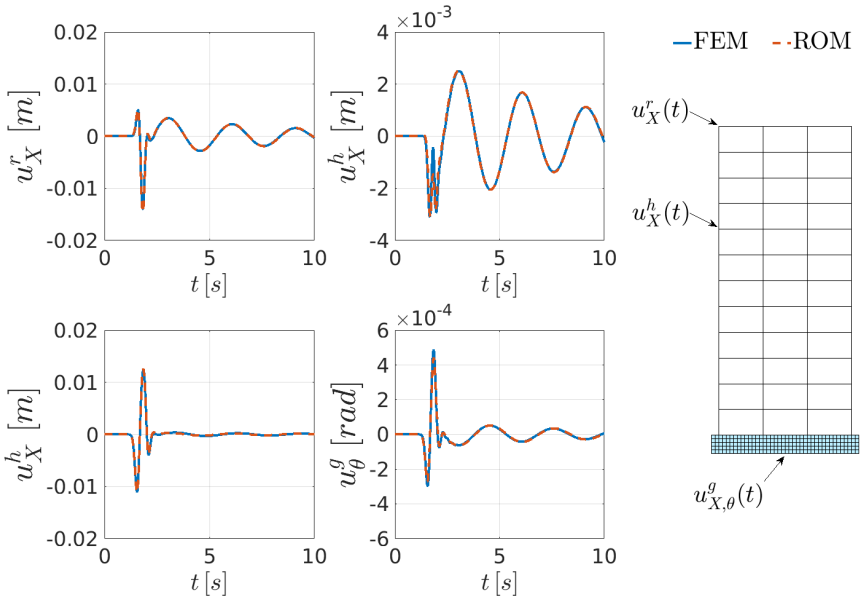

Figure 6.5: Displacement time history signals at first-modal height $u^h_X(t)$ at coordinates $(x, z) = (-9, 28)\,[m]$, the roof $u^h_r(t)$ at coordinates $(x, z) = (-9, 42)\,[m]$, and the foundation $u^g_{X,\theta}(t)$ at coordinates $(x, z) = (0, -2.5)\,[m]$ of the building. The high-fidelity finite element model responses are shown in solid-blue lines, and the ROM responses are displayed in dashed-red lines.

In addition, Figure 6.6 shows the convergence of the soil parameters using the EnKI-FEM updating framework. It can be seen in Figure 6.6(a) and (b) that the particles in the ensemble converge tightly and quickly. In particular, Figure 6.6(a) shows the evolution of the soil parameter values at each iteration. The variances of the ensembles are indicated by the gray area. It can be seen that each soil parameter converges to the mean after 5 iterations. Additional, Figure 6.6(b) shows

the normalized ℓ_2-error obtained at each iteration. The final obtained error is 0.0130 after 6 EnKI iterations.

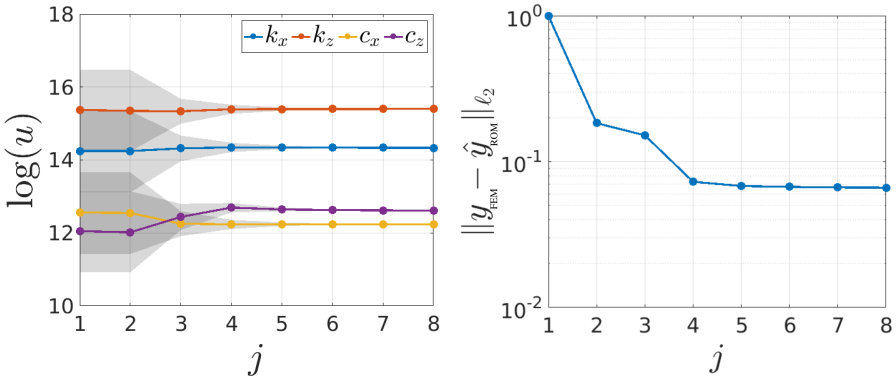

Figure 6.6: Ensemble Kalman inversion finite element updating algorithm evolution. On the left, the evolution of the soil parameters, and on the right the normalized misfit ℓ_2-error obtained for each j-iteration between the FEM and ROM.

6.6 Conclusions

This chapter presented a robust framework for finite element model (FEM) updating. The EnKI-FEM updating framework, illustrated in Figure 6.2, essentially integrates two components: (1) a robust and efficient ensemble-Kalman inversion (EnKI) method for parameter estimation, and (2) a sophisticated and reliable software, Seismo-VLAB, for nonlinear seismic wave propagation and soil-structure interaction simulation, to estimate time-invariant material soil parameters.

The performance of the proposed framework in terms of robustness, accuracy, and convergence was illustrated through two verification examples. For each example, the response of the ROM was simulated from the "true" finite element model, and artificially perturbed data is constructed for the filtering algorithm. The so-generated artificially perturbed data was then introduced into the proposed EnKI-FEM updating framework and the unknown time-invariant soil parameters were estimated. In particular, the estimation performance of the proposed framework was found to be very good even when an initial ensemble estimation of 100% difference was employed for the identification. The EnKI-FEM updating framework showed always convergence, and the number of iterations required for convergence depended on the number of ensembles, initial ensemble estimation, and weakly on the magnitude of the artificially perturbed data.

Example 6 showed that the EnKI-FEM model updating framework is efficient and robust, even when there is modeling error. This fact can be attributed to the ROM which captures very well the behavior of the high-fidelity finite element model. However, further studies are needed to investigate modeling uncertainty (error) on the performance of the proposed EnKI-FEM parameter estimation framework.

Lastly, it is important to mention that the proposed framework can be easily extended to nonlinear finite elements (e.g., large-deformation, material non-linearity, and contact) to model structural and/or geotechnical systems. Moreover, the EnKI-FEM updating framework cannot only be limited to material parameters. It can also be used to estimate input motion and initial configurations or states.

Chapter 7

APPLICATION: IMPROVING THE STATE-OF-PRACTICE DIMENSIONLESS FREQUENCY ESTIMATION

7.1 Motivation

Accurate quantification of dynamic soil-structure interaction (SSI) effects is critical in the design of earthquake resistant structures. Poorly estimated or neglected SSI effects have been shown to yield unsafe or overly conservative designs, depending on the resulting over- or under-estimation of the critical response of the structure. Therefore, the effects of soil-structure interaction (SSI) have been extensively studied the last few decades, and proper analysis for the linear elastic case in frequency domain has been established successfully. However, SSI is rarely considered in the design of building structures, and instead, buildings are frequently analyzed using a rigid base assumption and quasi-static loading conditions that ignore SSI and its dynamic nature. Acknowledging these shortcomings, the National Institute of Standards and Technology (NIST) published in 2012 a set of recommendations on time domain analyses of SSI for building structures compatible with standard finite element packages for consideration in engineering design. The NIST GCR 12-917-21 report introduced two fundamental simplifications to enable frequency domain tools to be implemented in time domain analyses: (a) the use of frequency-dependent foundation impedance values at the flexible-base frequency; and (b) the use of the same phase for the foundation input motion (FIM) and the free field motion (FFM). Pertaining to the above recommendations, there are no rigorous studies that seek to quantify their accuracy relative to fully coupled finite element models (FEM), and to examine the conditions under which changes in the input motion phase incurred by the foundation embedment can be safely neglected.

In particular, the so-called flexible-base frequency suggested in NIST depends solely on the structure-to-soil-wavelength ratio, which is assumed to be dominant during the interaction. However, if such frequency exists for the combined system, it must depend on the frequency of the input signal, foundation's embedment ratio, building's aspect ratio, and soil's Poisson ratio among others. In this chapter, we propose a methodology to obtain the optimal dimensionless frequency at which the frequency independent soil's impedance should be obtained. The analysis

is carried out using five dimensionless parameters, and the importance of each dimensionless parameter to the estimation of the optimal dimensionless frequency is investigated. We extract the "true" frequency of the interaction from fully coupled 2D SSI simulations using the EnKI-FEM framework. The data obtained in this manner is used in a machine learning framework to map these five dimensionless parameters to such a frequency. The generated mapping is finally validated, and a significant improvement with respect to the state-of-practice is shown.

7.2 The problem statement and method of analysis

We want to evaluate the dimensionless frequency (a_0^*) at which a SSI configuration responds when it is subjected to a given input motion. This goal is achieved using a 2D reduced order model (ROM) that preserves the characteristics of the surrounding soil as well as the ability of emulating the inertial and kinematic interaction effects. The ROM, as proposed in [138–140], employs frequency independent soil spring and dashpot placed on the foundation interface that emulates the surrounding soil. The dimensionless frequency, at which soil spring and dashpot coefficients of the combined system respond, are estimated using ensemble Kalman Inversion (EnKI) [50, 72, 102]. The EnKI requires data that is generated from a set of 2D finite element model with appropriate absorbing boundary conditions [51, 94, 95] (also known as the direct modeling approach [157–159]). The data is generated varying the shear wave velocity, Poisson's ratios, building's height, and foundation's geometry, so that we span the range of real case scenarios. These cases are constructed using Dimensional analysis [31] to avoid similar solutions [40, 55, 100].

In the following subsections, we proceed to describe in details how dimensional analysis is employed to span the parameter space. We then present how the impedance functions and foundation input transfer functions are estimated using the direct modeling method. We then use the previous results and describe how EnKI is employed to estimate the dimensionless frequency that minimizes the discrepancies between the finite element model and the ROM. Finally, we use Random Forest to obtain a dimensionless frequencies mapping given a set of dimensionless parameters. The mapping is validated using a different set of SSI configurations and real-earthquake input motions.

Dimensional analysis for spanning the parameter space

In mathematical terms, a physically-meaningful relation between the response of a system (termed u for the purpose of this discussion) and its parameters and variables

can be expressed as a dimensional homogeneous equation,

$$u = \mathrm{f}(\hat{\mathbf{x}}\,;\,\hat{\mathbf{q}}), \tag{7.1}$$

with $\hat{\mathbf{q}} = (q_1, q_2, \ldots\ q_n)^\top$ and $\hat{\mathbf{x}} = (x_1, x_2, \ldots\ x_d)^\top$. The vector $\hat{\mathbf{x}} \in \mathbb{R}^d$ represents the independent variables of the system (traditionally, in physical systems, these would be three spatial coordinates and time), $\hat{\mathbf{q}} \in \mathbb{R}^n$ represents the n-physical parameters, and $\mathrm{f} : \mathbb{R}^d \times \mathbb{R}^n \to \mathbb{R}$ represents a function whose structure will depend on the nature of the physical phenomenon and the number k of physical dimensions. Since the aim of Dimensional Analysis [31, 100] is discerning the role of the physical parameters, we will not show $\hat{\mathbf{x}}$ explicitly henceforth.

Without loss of generality, it is assumed that the k elements of the basis correspond to the first entries of the vector, for which q_i is the i-th parameter that does not belong to the basis, and $q_1, \cdots, q_\mathrm{k}$ are the basis parameters. Returning to Equation (7.1), we assume that the left-hand side is divided by a characteristic value, $u_{ch} = u_{ch}(q_1, \ldots, q_\mathrm{k})$, yielding a non-dimensional value, U. As this member is dimensionless, so must be the right-hand side. In mathematical terms this implies:

$$U = \frac{u}{u_{ch}} = F(\hat{\boldsymbol{\pi}}), \tag{7.2}$$

with $\hat{\boldsymbol{\pi}} = (\Pi_1, \Pi_2, \ldots, \Pi_m)^\top$, and $\hat{\boldsymbol{\pi}} \in \mathbb{R}^m$ the vector of the m-dimensionless parameters constructed from the $\hat{\mathbf{q}} \in \mathbb{R}^n$ vector of n-physical variables by solving $m = n - \mathrm{k}$ dimensionless equations from a set of k base units. In this regard, the so-called Π groups can be expressed as

$$\Pi_i = \frac{(q_i)^{a_i}}{(q_1)^{a_2} \cdots (q_k)^{a_\mathrm{k}}}, \tag{7.3}$$

where the exponents a_i: $a_1, \ldots, a_k$ are set to ensure that the final result is dimensionless, thus, the exponents are either integer or rational numbers.

We consider for the soil-structure interaction problem a building (characterized by its first modal mass, height, and fundamental period), a rectangular shallow foundation (characterized by its homogeneous density and by two linear-elastic isotropic constants), the underlying soil half-space (characterized by its density and by two linear-elastic isotropic constants), and the seismic loading characteristics (represented in our case by a Ricker pulse [124] of a given dominant frequency and dominant acceleration amplitude). A brief description of the physical parameters q_i that govern this phenomenon, as well as their physical dimensions, are provided in Table 7.1.

Parameters		
Variable	Dimension	Description of the physical variable
T_b	T	Building's fundamental period
h_b	L	Building's first-modal height
B	L	Building foundation's half-width
D	L	Building foundation's embedment
m_b	M	Building's first-modal mass
ρ_f	ML^{-3}	Foundation's density
ν_f	$-$	Foundation's Poisson's ratio
ρ_s	ML^{-3}	Soil's density
ν_s	$-$	Soil's Poisson's ratio
V_s	LT^{-1}	Soil's shear-wave velocity
V_f	LT^{-1}	Foundation's shear-wave velocity
a_p	LT^{-2}	Ground's acceleration amplitude
$\mathrm{f_p}$	T^{-1}	Ground's dominant energy's frequency

Table 7.1: The n-physical parameters of the SSI problem to be considered in the dimensional analysis.

The response of the SSI system (represented by u, not necessarily a displacement) in the idealized SSI context can be written in terms of the physical parameters $\hat{\mathbf{q}}$ listed in Table 7.1 as,

$$u = \mathrm{f}\left(T_b\,, h_b\,, B, D, m_b\,, \rho_f, \nu_f, \rho_s\,, \nu_s, V_s, V_f, a_p\,, \mathrm{f_p}\right). \tag{7.4}$$

Note that in Equation (7.4), the number of variables for the SSI problem are thirteen ($n = 13$), whereas the number of independent units for this case are three (k = 3), i.e., time T, length L, and mass M. Thus, the number of dimensionless groups that can be found is ten ($m = 10$). We next consider a dimensional basis from the parameters in Table 7.1. The selected parameters are B (which provides relative length to characterize the geometry), V_s (which defines a characteristic time in conjunction with B), and ρ_s (to represent inertia). This choice is arbitrary inasmuch as there are other possible bases that could provide an equally valid dimensional basis. In this work, we assume that u represents a frequency of the SSI system. A characteristic frequency is given by the Ricker highest energy's frequency ($\sim f_\mathrm{p}$), thus $U = u/f_\mathrm{p}$ in our case. Equation (7.4) can thus be rewritten in dimensionless fashion:

$$\begin{aligned} U &= F\left(\frac{T_b V_s}{B}, \frac{h_b}{B}, 1, \frac{D}{B}, \frac{m_b}{\rho_s B^3}, \frac{\rho_f}{\rho_s}, \nu_f, 1, \nu_s, 1, \frac{V_f}{V_s}, \frac{a_p B}{V_s^2}, \frac{V_s}{\mathrm{f_p}\, B}\right) \\ &= F\left(\frac{B}{T_b V_s}, \frac{h_b}{B}, \frac{D}{B}, \frac{m_b}{\rho_s B^3}, \frac{\rho_f}{\rho_s}, \nu_f, \nu_s, \frac{V_f}{V_s}, \frac{a_p B}{V_s^2}, \frac{\mathrm{f_p}\, B}{V_s}\right) \end{aligned}$$

$$= F(\Pi_1, \Pi_2, \Pi_3, \Pi_4, \Pi_5, \Pi_6, \Pi_7, \Pi_8, \Pi_9, \Pi_{10}) \,. \tag{7.5}$$

Let us briefly analyze these dimensionless groups, and argue their relative importance. Π_1 represents the ratio between the wave-length traveling in the soil over the wave-length traveling in the building, Π_2 provides a measure of the objective slenderness of the building (inertial interaction), and Π_3 quantifies the influence of the coupling between soil and foundation (kinematic interaction). These parameter play an important role in the SSI system, and they must be kept. However, assuming a rigid foundation behavior allows to neglect Π_6, and Π_8, and since the density of soil and reinforced concrete are similar–i.e., $\Pi_5 \sim 1$, this parameter can be removed from the list. For linear elasticity to be valid, $\Pi_9 \ll 1$; thus we can ignore this parameter as well. In this regard, we could further reduce the parameter space as,

$$U = F(\Pi_1, \Pi_2, \Pi_3, \Pi_7, \Pi_{10}) \,. \tag{7.6}$$

Based on these five dimensional parameters, we consider a set of three different buildings with fixed-base-fundamental period $T_b \sim 0.5, 1.0, 1.5\,[s]$, fixed first modal height $h_b \sim 15.0, 30.0, 40.0\,[m]$, foundation depth $D = 1.0, 2.5, 5.0, 10.0, 20.0\,[m]$, and supported on ten different soils with Poisson's ratios $\nu_s = 0.25, 0.35, 0.45$, and shear wave velocities $V_s = 100, 125, 150, 175, 200, 225, 250, 300, 400, 500\,[m/s]$, subjected to Ricker pulse with central frequency $\mathrm{f_p} = 1, 2, 4\,[Hz]$. In the dimensionless parameter space, the *structure-to-soil wavelength ratio* $\Pi_1 \in [0.01, 0.2]$, the *building-aspect ratio* $\Pi_2 \in [1.5, 4.0]$, and the *foundation aspect ratio* $\Pi_3 \in [0.1, 2.0]$, the soil's Poisson ration $\Pi_7 \in [0.25, 0.45]$, and *signal-to-soil wavelength ratio* $\Pi_{10} \in [0.02, 0.4]$. We highlight that the range of parameters Π_1, Π_2, and Π_3 are chosen to be consistent with the range of applicability presented in Stewart et al. [140].

Soil impedances in frequency domain

Seylabi et al. [131, 132] developed a method to extract the impedance functions of a semi-infinite half-space from a finite element model. The approach is general enough that can be applied equally well to flexible interfaces and to three-dimensional problems. However, we use this method considering a rigid interface and a two-dimensional plane-strain problem.

The motion of a rigid foundation interface in a plane-strain setting is shown in Figure 7.1. The motion is described by three degrees of freedom: the horizontal, the vertical, and the rotational motions denoted here by $\Delta_{\mathrm{x}}(t)$, $\Delta_{\mathrm{z}}(t)$, and $\theta(t)$,

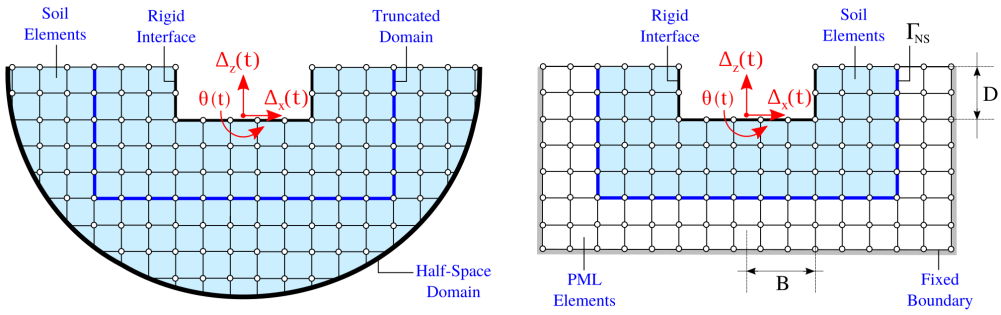

(a) (b)

Figure 7.1: Rigid foundation kinematics for the numerical estimation of soil impedance-functions. (a) Infinite half-space finite element model, and (b) truncated half-space finite element model using PML elements.

respectively. The force-displacement relations for $\hat{R}(\omega) \in \mathbb{C}^3$, $\hat{\mathbb{K}}(\omega) \in \mathbb{C}^{3\times3}$, and $\hat{\Delta}(\omega) \in \mathbb{C}^3$, over the rigid interface, in the frequency domain can be written as

$$\hat{R}(\omega) = \hat{\mathbb{K}}(\omega)\,\hat{\Delta}(\omega), \tag{7.7}$$

where $\omega \in \mathbb{R}$ is the angular frequency, $\hat{R}(\omega)$ is the reaction vector, $\hat{\mathbb{K}}(\omega)$ is the soil impedance matrix, and $\hat{\Delta}(\omega)$ the displacement vector at the interface. Equation (7.7) can be written in matrix form

$$\begin{bmatrix} \hat{R}_z \\ \hat{R}_x \\ \hat{M}/B \end{bmatrix} = \begin{bmatrix} \hat{K}_z & 0 & 0 \\ 0 & \hat{K}_{xx} & \hat{K}_{x\theta} \\ 0 & \hat{K}_{\theta x} & \hat{K}_{\theta\theta} \end{bmatrix} \begin{bmatrix} \hat{\Delta}_z \\ \hat{\Delta}_x \\ B\,\hat{\theta} \end{bmatrix}. \tag{7.8}$$

Equation (7.8) is termed as the dimensionless impedance matrix, where $\hat{R}_x$, and $\hat{R}_z$ are resultant reaction forces in x and z directions, respectively. The characteristic length B–i.e., half-width, is used for normalizing $\hat{M}$ and $\hat{\theta}$ which denote the moment and the rotation angle with respect to the centroid of the foundation boundary. Each component of the impedance matrix can be computed using a time domain finite element analysis. In order to do so, we first prescribe the displacement time-histories, which are $\Delta_x(t)$, $\Delta_z(t)$, and $\theta(t)$, and then, we compute reaction forces $R_x(t)$, $R_z(t)$ and the moment $M(t)$. Once these quantities are computed, the following procedure should be performed:

(a) Use Fourier transform to compute the vertical reaction $\hat{R}_z$ for a given vertical motion, which enforces $\Delta_x(t) = 0$, $\Delta_z(t) \neq 0$, and $\theta(t) = 0$, and then compute $\hat{K}_z = \hat{R}_z/\pi\, G_s\, \hat{\Delta}_z$.

(b) Use Fourier transform to compute the horizontal and moment reaction $\hat{R}_{\mathrm{x}}$ and $\hat{M}$ for a given horizontal motion, which enforces $\Delta_{\mathrm{x}}(t) \neq 0$, $\Delta_{\mathrm{z}}(t) = 0$, and $\theta(t) = 0$, and then compute $\hat{K}_{\mathrm{xx}} = \hat{R}_{\mathrm{x}}/\pi\, G_s\, \hat{\Delta}_{\mathrm{x}}$ and $\hat{K}_{\theta\mathrm{x}} = \hat{M}/\pi\, G_s\, B\, \hat{\Delta}_{\mathrm{x}}$.

(c) Use Fourier transform to compute the horizontal and moment reaction $\hat{R}_1$ and $\hat{M}$ for a given rotational motion, which enforces $\Delta_{\mathrm{x}}(t) = 0$, $\Delta_{\mathrm{z}}(t) = 0$, and $\theta(t) \neq 0$, and then compute $\hat{K}_{\mathrm{x}\theta} = \hat{R}_{\mathrm{x}}/\pi\, G_s B\, \hat{\theta}$ and $\hat{K}_{\theta\theta} = \hat{M}/\pi\, G_s\, B^2\, \hat{\Delta}_{\mathrm{x}}$.

These steps will thus yield the impedance matrix components in frequency domain excited through the prescribed loading time-history. Now, the stiffness and damping components, as seen from the foundation, can be easily extracted employing Equations (7.9), (7.10), and (7.11) by taking the real and imaginary part of each of the impedance matrix component.

$$\hat{K}_{\mathrm{xx}} = k_{xx} + c_{\mathrm{xx}}\, \omega\, \mathbb{i}, \tag{7.9}$$

$$\hat{K}_{\mathrm{x}\theta} = k_{\mathrm{x}\theta} + c_{\mathrm{x}\theta}\, \omega\, \mathbb{i}, \tag{7.10}$$

$$\hat{K}_{\theta\theta} = k_{\theta\theta} + c_{\theta\theta}\, \omega\, \mathbb{i}\,. \tag{7.11}$$

In order to span the range for the soil impedance functions, as described in § 7.2, we consider the foundation aspect ratio to be $\Pi_3 = 0.1, 0.25, 0.5, 1.0, 2.0$ and the soil's Poisson ration to be $\Pi_7 = 0.25, 0.35, 0.45$. Therefore, in the numerical experiment, we consider a Ricker pulse to generate the time-history excitation for $\Delta_{\mathrm{x}}(t)$ and $\theta(t)$. The Ricker's characteristic frequency is $\mathrm{f_p} = 5.5\,[Hz]$, and a simulation time of $t_{\mathrm{sim}} = 3.5\,[s]$ with a time step of $\Delta\mathrm{t} = 0.001\,[s]$ is considered for all analyses. The Ricker-wavelet amplitude is scaled so that it has a maximum displacement of $0.001\,[m]$ and a maximum rotation of $0.001\,[rad]$, respectively. The generated frequency contents is thus concentrated between $0 - 15\,[Hz]$.

Regarding the FE analyses, a surface foundation of total length $20\,[m]$, which is $B = 10\,[m]$, and different embedments of $D = 1.0, 2.5, 5.0, 10.0, 20.0\ [m]$ are considered. The rigid foundation interface is enforced using kinematic constraints as explained in [16, 42, 80]. The soil is modeled using quad elements with shear velocity $V_s = 25, 50, 75, 100, 100\ [m/s]$ (depending on the embedment) and a soil density of $2000\,[kg/m^3]$, with different Poisson's ratios $\nu_s = 0.25, 0.35, 0.45$. A number of 16 points per wave-length are enforced to resolve a maximum frequency of $15\,[Hz]$; thus, a mesh size of $\Delta\mathrm{h} = 0.1, 0.2, 0.3, 0.4, 0.4\ [m]$ are used. The mesh size along with the time step provides a CFL = 0.25 in all the analyses. In addition, PML elements are added along the domain boundary so that outgoing waves are

absorbed. The PML thickness layer is taken so that $L_{\text{PML}} = 25,\ 30,\ 30,\ 50,\ 50\ [m]$. The computed impedance functions are shown in Figures 7.2, 7.3, and 7.4.

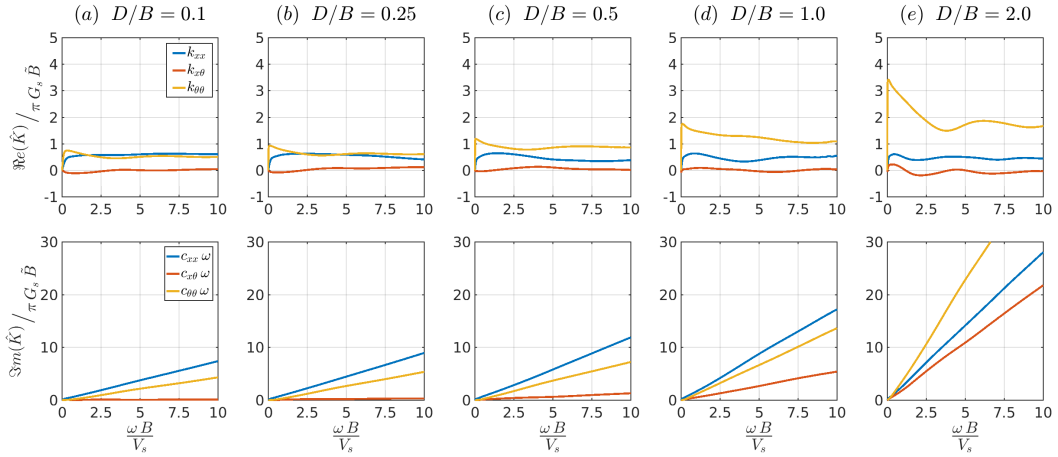

Figure 7.2: Real and imaginary components for the normalized soil impedance function. The soil impedances are computed considering a Poisson's ratio of 0.25 and embedments ratios $D/B = 0.1, 0.25, 0.5, 1.0, 2.0$ from left to right. The blue solid line represents the translational impedance with $\tilde{B} = 1$, the yellow solid line represents the rotational impedance with $\tilde{B} = B^2$, and the red solid line represents the coupled impedance with $\tilde{B} = B$.

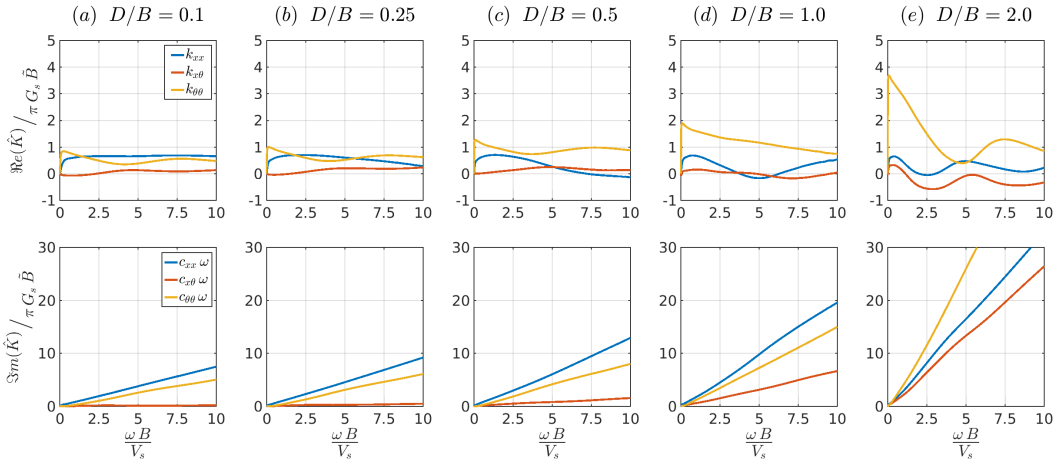

Figure 7.3: Real and imaginary components for the normalized soil impedance function. The soil impedances are computed considering a Poisson's ratio of 0.35 and embedments ratios $D/B = 0.1, 0.25, 0.5, 1.0, 2.0$ from left to right. The blue solid line represents the translational impedance with $\tilde{B} = 1$, the yellow solid line represents the rotational impedance with $\tilde{B} = B^2$, and the red solid line represents the coupled impedance with $\tilde{B} = B$.

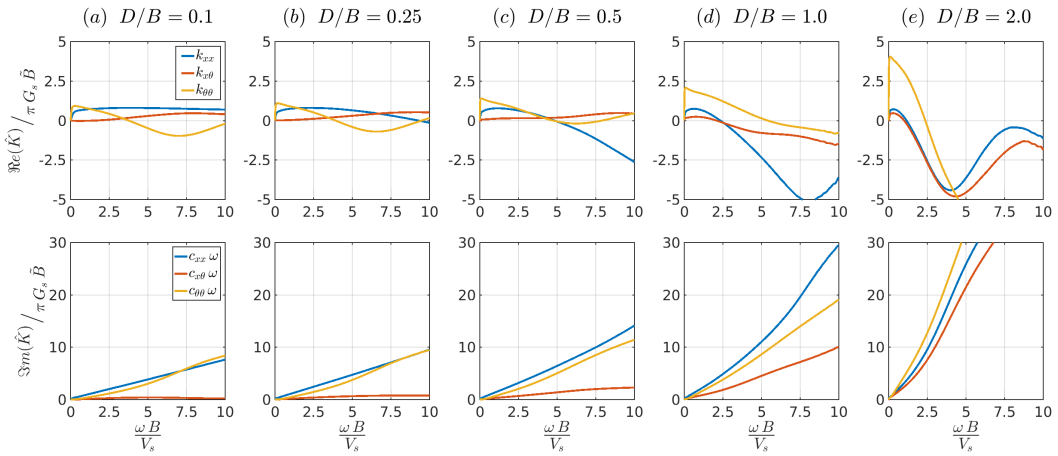

Figure 7.4: Real and imaginary components for the normalized soil impedance function. The soil impedances are computed considering a Poisson's ratio of 0.45 and embedments ratios $D/B = 0.1, 0.25, 0.5, 1.0, 2.0$ from left to right. The blue solid line represents the translational impedance with $\tilde{B} = 1$, the yellow solid line represents the rotational impedance with $\tilde{B} = B^2$, and the red solid line represents the coupled impedance with $\tilde{B} = B$.

Foundation input motion transfer functions

The method developed by Seylabi et al. [131, 132] can also be applied to extract the foundation input motion (FIM) transfer functions. In simple words, the method essentially uses a finite element model to compute the scattered responses, and provided with the free-field motion (FFM), computes the associated transfer function at the soil-structure interface. The motion of a rigid foundation interface is described by three degrees of freedom: the horizontal, the vertical, and the rotational motions denoted here by $\Delta_x(t)$, $\Delta_z(t)$, and $\theta(t)$, respectively.

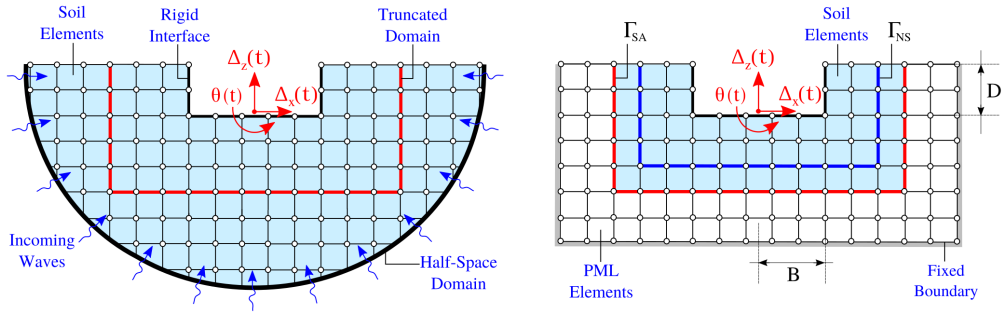

Figure 7.5: Rigid foundation kinematics for the numerical estimation of soil impedance-functions.

The free-field displacements at the fictitious interface (Γ_{NS}), as shown in Figure 7.5, are employed to compute the free-field traction. The free-field motion $u_g(t)$ is computed using standard 1D wave propagation in a soil column on an elastic bedrock. Then, the DRM [24] allows to propagate the incident wave inside the domain, and thus, evaluate the time history response of the rigid interface, which is $\Delta_x(t)$, $\Delta_z(t)$, and $\theta(t)$, respectively. Once these quantities are computed, the following procedure should be performed:

(a) Use the Fourier transform to compute the horizontal motion $\hat{\Delta}_x(\omega)$ from $\Delta_x(t)$, then the Fourier transform of the free-field motion $\hat{u}_g(\omega)$, and compute $\mathcal{H}_u(\omega) = \hat{\Delta}_x(\omega)/\hat{u}_g(\omega)$.

(b) Use the Fourier transform to compute the rotational motion $\hat{\theta}(\omega)$ from $B \cdot \theta(t)$, then the Fourier transform of the free-field motion $\hat{u}_g(\omega)$, and compute $\mathcal{H}_\theta(\omega) = \hat{\theta}(\omega)/\hat{u}_g(\omega)$.

In order to span the range for the foundation transfer functions, as described in § 7.2, we consider the foundation aspect ratio to be $\Pi_3 = 0.1, 0.25, 0.5, 1.0, 2.0$, and the soil's Poisson ration to be $\Pi_7 = 0.25, 0.35, 0.45$. Therefore, in the numerical experiment, we consider a Ricker pulse to generate the time-history excitation for $\Delta_x(t)$ and $\theta(t)$. The Ricker's characteristic frequency is $f_p = 5.0\,[Hz]$, and a simulation time of $t_{sim} = 3.0\,[s]$ with a time step of $\Delta t = 0.001\,[s]$ is consider for all analyses. The Ricker-wavelet amplitude is scaled so that it has a maximum displacement of $0.001\,[m]$. The generated frequency contents are thus concentrated between $0 - 15\,[Hz]$.

Regarding the FE analyses, a surface foundation of total length $20\,[m]$, which is $B = 10\,[m]$, and different embedments of $D = 1.0, 2.5, 5.0, 10.0, 20.0\ [m]$ are considered. The rigid foundation interface is enforced using kinematic constraints [16, 42, 80]. The soil is modeled using quad elements with shear velocity $V_s = 25, 50, 75, 100, 100\ [m/s]$ (depending on the embedment) and a soil density of $2000\,[kg/m^3]$. A number of 32 points per wave-length are enforced to resolve a maximum frequency of $15\,[Hz]$; thus, a mesh size of $\Delta h = 0.05, 0.1, 0.15, 0.2, 0.2\ [m]$ is used. The mesh size along with the time step provides a CFL = 0.50 in all the analyses. In addition, PML elements are added along the domain boundary so that scattered waves are absorbed. The PML thickness layer is taken so that $L_{PML} = 10, 20, 30, 40, 40\ [m]$. The computed foundation motion transfer functions are shown in Figures 7.6 and 7.7.

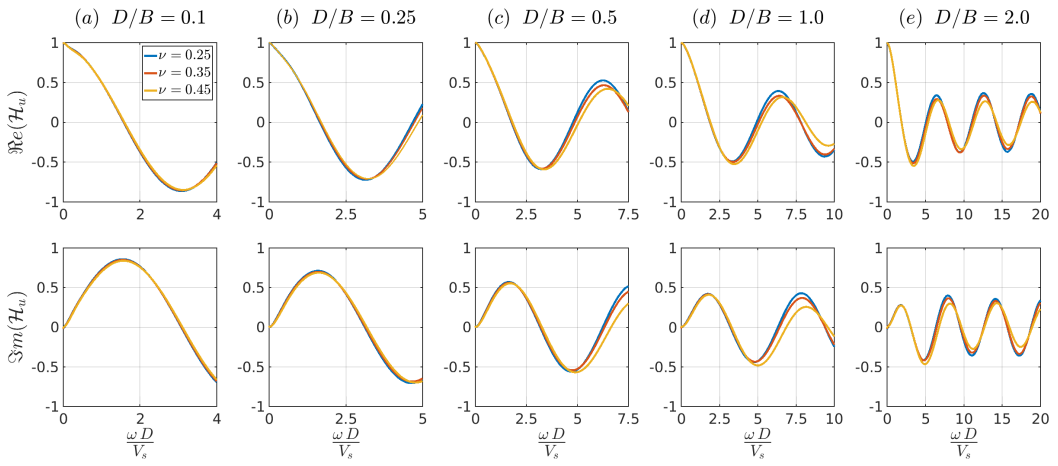

Figure 7.6: Normalized magnitude for the foundation input motion transfer function. The transfer function is computed considering different embedments ratios $D/B = 0.1, 0.25, 0.5, 1.0, 2.0$. The blue solid line represents the translational transfer function for a Poisson's ratio of $\nu = 0.25$, the yellow solid line represents the translational transfer function for a Poisson's ratio of $\nu = 0.35$, and the red solid line represents the translational transfer function for a Poisson's ratio of $\nu = 0.45$.

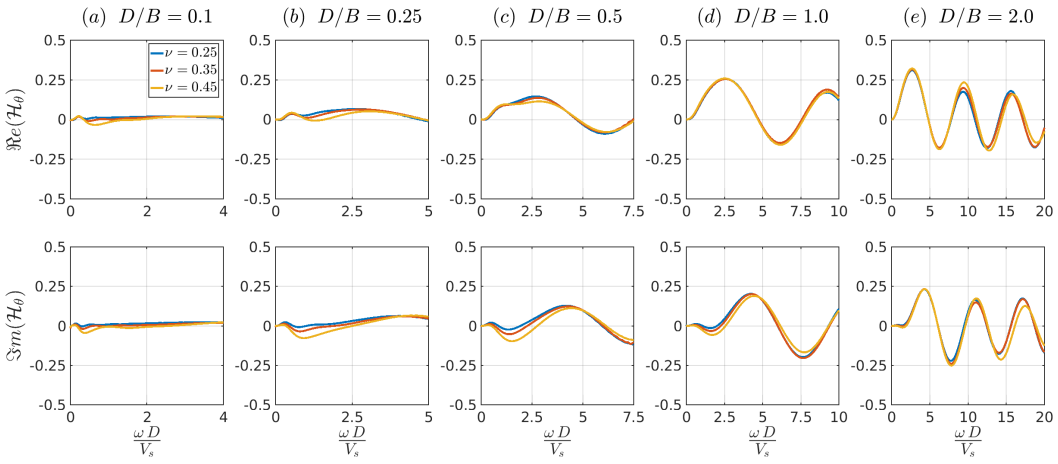

Figure 7.7: Normalized magnitude for the foundation input motion transfer function. The transfer function is computed considering different embedments ratios $D/B = 0.1, 0.25, 0.5, 1.0, 2.0$. The blue solid line represents the rotational transfer function for a Poisson's ratio of $\nu = 0.25$, the yellow solid line represents the rotational transfer function for a Poisson's ratio of $\nu = 0.35$, and the red solid line represents the rotational transfer function for a Poisson's ratio of $\nu = 0.45$.

Direct modeling of the problem

For direct modeling of the building structure response on elastic half-space, we use the procedure shown in Figure 7.8.

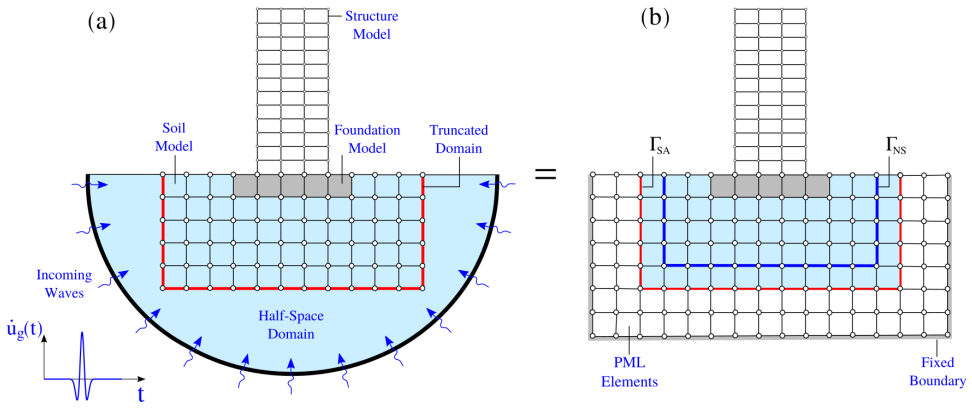

Figure 7.8: Reduced infinite half-space model using DRM and absorbing PML elements.

We truncate the semi-infinite half-space along the red line–i.e., Γ_{SA} as shown in Figure 7.8a, and introduce an absorbent interface using perfectly matched layers (PML) [51, 94, 95]. The PML are placed for absorbing outgoing or scattered waves produced by the presence of the building. In order to propagate the input signal inside the PML domain, we employ the DRM presented in [24]. In this regard, the free-field displacements at the fictitious interface–i.e., Γ_{NS} is employed to compute the free-field tractions. These tractions are thus transformed into an effective force vector over a one-layer element thickness surrounding the interface Γ_{NS}. The free-field motion $u_g(t)$ is computed using for instance standard 1D wave propagation in a soil column on an elastic bedrock, see [8, 99].

The incident ground motion $\dot{u}_g(t)$ used in the finite element models is prescribed as a Ricker function, proportional to Equation (7.12):

$$\dot{u}_g(t) = \left(1 - 2\beta\,(t - t_0)^2\right) \exp\left[-\beta\,(t - t_0)^2\right], \tag{7.12}$$

where $\beta = \left(\pi \mathrm{f_p}\right)^2$, $\mathrm{f_p}$ is the characteristic frequency, and t_0 is the time position where the velocity will become maximum. We select a Ricker pulse as input since it provides a clear dominant frequency and covers a range up to $\mathrm{f_{max}} \approx 3\mathrm{f_p}$.

In order to span the range for which the dimensionless frequency may vary, as described in § 7.2, we consider the building-to-soil wave-length ratio $\Pi_1 \in [0.01, 0.2]$, the building-aspect ratio $\Pi_2 = 1.5, 3.0, 4.0$, the foundation aspect ratio to be $\Pi_3 = 0.1, 0.25, 0.5, 1.0, 2.0$, the soil's Poisson ration to be $\Pi_7 = 0.25, 0.35, 0.45$, and the signal-to-soil wavelength ratio $\Pi_{10} \in [0.02, 0.4]$. Therefore, three different topologies of buildings are considered, which are illustrated from the shortest (in

Figure 7.9a) to the tallest (in Figure 7.9c). The first reinforced concrete building has

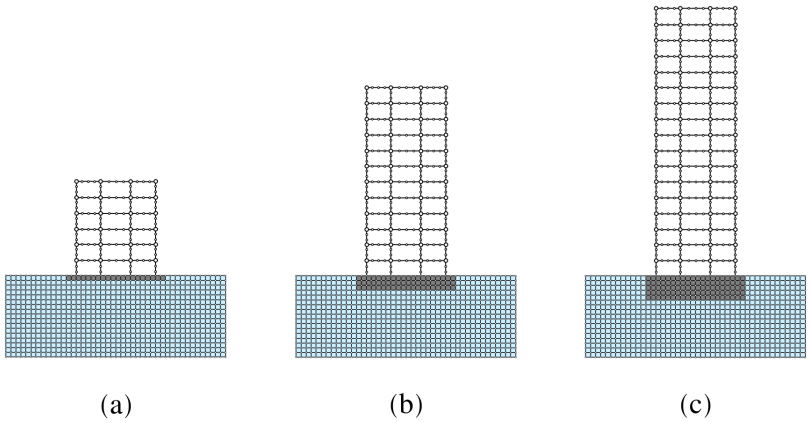

Figure 7.9: Building configurations employed in the dimensional analysis for the SSI problem.

columns of rectangular cross section $0.90 \times 0.60\,[m]$, each of $3.5\,[m]$ height. Beams have rectangular cross sections $0.80 \times 0.60\,[m]$ and $6.0\,[m]$ length. The reinforced concrete density is $2500\,[kg/m^3]$, the reinforced concrete elasticity modulus is taken as $25\,[GPa]$, and beams are subjected to a dead load of $3600\,[kg/m]$. This configuration gives a total height of $21\,[m]$, a total mass of $6.45 \cdot 10^5\,[kg]$, a fixed-base fundamental period of $0.507\,[s]$, a first-modal height of $14.91\,[m]$, and a first modal mass $0.545 \cdot 10^6\,[kg]$. The solid core foundation has a half-width of $10\,[m]$, and an equivalent length (thickness) of $1.0\,[m]$. The reinforced concrete material properties for the foundation are an elasticity modulus of $30\,[GPa]$ and a Poisson's ratio of 0.25. The second and third reinforced concrete buildings only differ in terms of the column cross-sections, which for the taller buildings are $1.00 \times 0.80\,[m]$. Beams and material properties of building and foundation are the same as above. The foundation is assumed to be a rigid diaphragm and to have perfect bonding with the surrounding soil. Table 7.2 summarizes some of the buildings' characteristics.

Building Parameters			Eigen-Analysis	
Period $[s]$	Mass $[kg]$	Height $[m]$	Modal Mass $[kg]$	Modal Height $[m]$
0.50	$6.45 \cdot 10^5$	21.00	$5.45 \cdot 10^5$	~ 15.0
1.00	$1.40 \cdot 10^6$	42.00	$1.15 \cdot 10^6$	~ 30.0
1.50	$1.98 \cdot 10^6$	59.50	$1.48 \cdot 10^6$	~ 40.0

Table 7.2: Building's first fixed-modal parameters using eigen-analysis.

The soil is modeled as an elastic, homogeneous, and semi-infinite medium with density $\rho_s = 2000\,[kg/m^3]$ and shear wave velocity $V_s = 80, 100, 125, 150, 175, 200, 225, 250, 300, 400, 500\,[m/s]$. The soil and foundation domains are modeled as four-node two-dimensional plane-strain quadrilateral elements, and the building structure domain is modeled as two-node linear elastic frame elements. All material models assigned to structural and soil elements are isotropic linear and elastic, and no viscous damping is added. The connection between solid and structural elements as well as the rigid diaphragm behavior of the foundation are enforced using kinematic constraints. The dimension of the truncated domain is taken such that the horizontal direction is $L_x = 70\,[m]$ and the vertical direction is $L_z = 75\,[m]$. The perfectly-matched layer of $10\,[m]$ thickness is provided around the near-field to truncate the semi-infinite half space. The incident ground motion is considered such that $\mathrm{f_p} = 1.0, 2.0, 4.0\,[Hz]$, covering a range between $0 - 15\,[Hz]$.

The time step Δt is limited using the Courant-Friedrichs-Lewy condition. In this regard, for an element size of $\Delta\mathrm{h} = 0.5\,[m]$ and a fixed value CFL = 0.30, the time step can be evaluated for each simulation. The resulting finite element mesh has approximately 32000 elements, and a simulation time of $t_{\mathrm{sim}} = 12.0\,[s]$ is considered. The total number of time steps for the entire simulation is n_t and it is variable, and Seismo-VLAB [96–98] is employed to carry out the analysis. The model domain is not large enough, therefore we use a single core execution. The time to complete this task is in average $132\,[min]$. In total, 1031 simulations are required to span the dimensionless parameters space, therefore we employ parallel computing for the simulations using the OpenMPI[1] [30, 54, 71] to run several cases at once. All simulations are run on a standard desktop (server) with an Intel(R) Xeon(R) CPU E5-2687W v3 3.10GHz with 20 CPU(s), using a batch file of 15 model per execution, in less than seven days.

Reduced order modeling of the problem

For developing a simplified version of the finite element model presented in § 7.2, we consider the reduced order model (ROM) shown in Figure 7.10c.

The ROM is constructed in such a way that it preserves the modal information of the fixed base building. To this end, we employ frame elements with three degrees of freedom per node to represent the structure's geometry as shown in Figure 7.10a. We assume that each floor acts as a rigid diaphragm, so that the buildings mass

[1] The message passing interface (MPI) allows to exchange messages between multiple computers running a parallel program (single execution) across distributed memory.

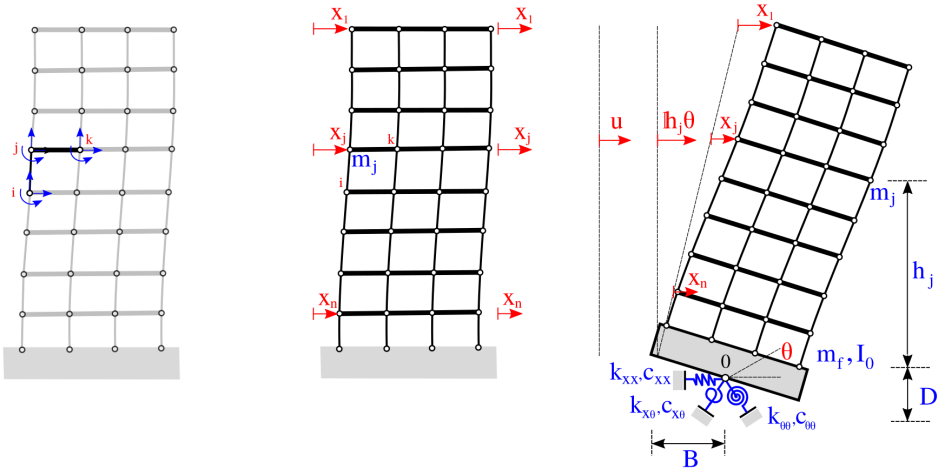

(a) (b) (c)

Figure 7.10: The reduced order model. (a) The column and beam element used to construct the fixed base FEM. (b) The fixed base FEM building model where $\mathbf{M}_s, \mathbf{C}_s, \mathbf{K}_s$ are obtained using static condensation. (c) The flexible-base soil-structure interaction system in which $x = (x_1, \ldots, x_n)$ represents the relative displacement of each floor, u represents the relative deformation of the soil, and θ the rigid rotation of the foundation.

can be lumped at the floor levels as shown in Figure 7.10b. We then use static condensation [61, 73] on the fixed-base building to compute the $\mathbf{M}_s, \mathbf{C}_s, \mathbf{K}_s \in \mathbb{R}^{n\times n}$ matrices, where n is the number of floors; additionally, the vector $x \in \mathbb{R}^n$ represents the horizontal degree of freedom of the building, since there is only one translational degree of freedom on each floor. We assume a rigid rectangular foundation of half-width B and depth D sitting on an elastic half-space, for which two additional degrees of freedom $u, \theta \in \mathbb{R}$ appear because of the flexibility of the soil. The foundation has a total mass m_f, and a moment of inertia I_0. The motion that one can use to excite the model is considered to be the foundation-input-motion (FIM). It can be shown that under the above assumptions, the semi-discrete equations of motion are:

$$\begin{bmatrix} \mathbf{M}_s & \mathbf{M}_s\,\mathbb{1} & \mathbf{M}_s\,\mathbb{h} \\ \mathbb{1}^\top\mathbf{M}_s & m_f + \mathbb{1}^\top\mathbf{M}_s\,\mathbb{1} & m_f\frac{D}{2} + \mathbb{h}^\top\mathbf{M}_s\,\mathbb{1} \\ \mathbb{h}^\top\mathbf{M}_s & m_f\frac{D}{2} + \mathbb{h}^\top\mathbf{M}_s\,\mathbb{1} & \mathrm{I}_0 + m_f\frac{D^2}{4} + \mathbb{h}^\top\mathbf{M}_s\,\mathbb{h} \end{bmatrix} \begin{bmatrix} \ddot{x} \\ \ddot{v} \\ \ddot{\theta} \end{bmatrix} + \begin{bmatrix} \mathbf{C}_s & \mathbb{O}_{n\times 1} & \mathbb{O}_{n\times 1} \\ \mathbb{O}_{1\times n} & c_{xx} & c_{x\theta} \\ \mathbb{O}_{1\times n} & c_{x\theta} & c_{\theta\theta} \end{bmatrix} \begin{bmatrix} \dot{x} \\ \dot{v} \\ \dot{\theta} \end{bmatrix} +$$

$$\begin{bmatrix} \mathbf{K}_s & \mathbb{O}_{n\times 1} & \mathbb{O}_{n\times 1} \\ \mathbb{O}_{1\times n} & k_{xx} & k_{x\theta} \\ \mathbb{O}_{1\times n} & k_{x\theta} & k_{\theta\theta} \end{bmatrix} \begin{bmatrix} x \\ v \\ \theta \end{bmatrix} = \mathbf{F}_{\mathrm{FIM}}(t), \tag{7.13}$$

where the foundation-input-motion force are computes as,

$$\mathbf{F}_{\text{FIM}}(t) = -\begin{bmatrix} \mathbf{M}_s\,\mathbb{1} \\ m_f + \mathbb{1}^\top \mathbf{M}_s\,\mathbb{1} \\ m_f\frac{D}{2} + \mathbb{h}^\top \mathbf{M}_s\,\mathbb{1} \end{bmatrix} \ddot{u}_{\text{FIM}}(t) - \begin{bmatrix} \mathbf{M}_s\,\mathbb{h} \\ m_f + \mathbb{1}^\top \mathbf{M}_s\,\mathbb{h} \\ m_f\frac{D^2}{4} + \mathbb{h}^\top \mathbf{M}_s\,\mathbb{h} + \mathbf{I}_0 \end{bmatrix} \ddot{\theta}_{\text{FIM}}(t),$$

and $\ddot{x}, \dot{x}, x \in \mathbb{R}^n$ are the acceleration, velocity, and displacement vectors for the condensed horizontal degrees of freedom of the building; also $\ddot{v}, \dot{v}, v \in \mathbb{R}$ and $\ddot{\theta}, \dot{\theta}, \theta \in \mathbb{R}$ are the foundation horizontal and rotational acceleration, velocity, and displacement, respectively. Note that we define $\mathbb{1} \in \mathbb{R}^n$, the vector of ones, which is $\mathbb{1} = (1, 1, \ldots, 1)^\top$. And, $\mathbb{h} \in \mathbb{R}^n$ the vector of height, which is $\mathbb{h} = (h_1 + D, \ldots, h_n + D)^\top$. We finally define $\mathbb{O}_{n\times m} \in \mathbb{R}^{n\times m}$, the matrix of zeros.

In addition, it is important to highlight that in the ROM, the spring and dashpot components in Equation (7.13) are obtained for a given dimensionless frequency a_0^*, foundation aspect ratio $\frac{D}{B}$, and soil Poisson's ratio ν_s from the impedance function in § 7.2.3. Similarly, the FIM requires to compute $\ddot{u}_{\text{FIM}}(t)$ and $\ddot{\theta}_{\text{FIM}}(t)$, which are obtained using the transfer functions described in § 7.2.4 for a given FFM.

Dimensionless frequency estimation using ensemble Kalman inversion

In order to find the optimal dimensionless frequency for computing the spring and dashpot coefficients for the ROM described in § 7.2, we use the Bayesian approach based on the ensemble Kalman inversion (EnKI) [50, 72, 102]. In the inversion setting, we consider the problem of finding $u \in \mathbb{R}^n$ from $y \in \mathbb{R}^m$ where

$$y = \mathbf{G}(u) + \eta\,. \tag{7.14}$$

The variable $u \in \mathbb{R}^n$ consists of all the unknown parameters that we want to estimate. In our case $u = a_0$, the variable $y \in \mathbb{R}^m$ consists of the ground truth quantities of interest, here obtained using the direct modeling method, and η is a zero-mean Gaussian noise with covariance $\mathbf{\Gamma}$. The nonlinear function (a.k.a. forward model or ROM) $\mathbf{G} : \mathbb{R}^n \to \mathbb{R}^m$ maps the parameter space to the data space. In this application, we work with one type of data-sets: the displacement time series recorded at the floors and foundation levels computed using the model described in §7.2.5. Given N particles $u_j^{(n)}$, $n = 1, \ldots, N$ within the ensemble and at each iteration j, we use the predictions $\mathbf{G}(u_j^{(n)})$ by the forward model and the observation data y to update the particles for iteration $j + 1$. The formal derivation of the update is presented in [3, 102] and is,

$$u_{j+1}^{(n)} = u_j^{(n)} + \mathbf{C}_{j+1}^{uw}(\mathbf{C}_{j+1}^{ww} + \mathbf{\Gamma})^{-1}(y_{j+1}^{(n)} - \mathbf{G}(u_j^{(n)})) \quad \text{for} \quad n = 1, \ldots, N\,. \tag{7.15}$$

In Equation (7.15), $y_{j+1}^{(n)}$ can be either identical to y (the observation data) or randomly perturbed using zero-mean Gaussian noise η; $\mathbf{C}_{j+1}^{uw}$ and $\mathbf{C}_{j+1}^{ww}$ are empirical covariance matrices that can be computed at each iteration based on predictions and the ensemble mean $\bar{u}_{j+1}$ using the following equations:

$$\mathbf{C}_{j+1}^{uw} = \frac{1}{N}\sum_{n=1}^{N}(u_j^{(n)} - \bar{u}_{j+1}) \otimes (\mathbf{G}(u_j^{(n)}) - \overline{\mathbf{G}}_j) \tag{7.16}$$

$$\mathbf{C}_{j+1}^{ww} = \frac{1}{N}\sum_{n=1}^{N}(\mathbf{G}(u_j^{(n)}) - \overline{\mathbf{G}}_j) \otimes (\mathbf{G}(u_j^{(n)}) - \overline{\mathbf{G}}_j) \tag{7.17}$$

and

$$\bar{u}_{j+1} = \frac{1}{N}\sum_{n=1}^{N} u_j^{(n)}, \quad \overline{\mathbf{G}}_j = \frac{1}{N}\sum_{n=1}^{N} \mathbf{G}(u_j^n)\,. \tag{7.18}$$

It is worth mentioning that the stopping criterion is defined as either reaching a relative change of 0.001 in the parameter in two consecutive EnKI iterations or a maximum number of 500 iterations. Furthermore, the initial ensemble mean is defined to be equal to the lumped stiffness and dashpot coefficients obtained using the NIST [138] procedure. In addition, if the prior distribution of the dimensionless frequency is unknown, then we use a uniform distribution as a prior to represent this uncertainty. We have used $N = 100$ ensembles[2] in each model to estimate the parameters. Finally, the positiveness of the dimensionless frequency is enforced through a change of variables $u \in \mathbb{R}$, $\exp(u) : \mathbb{R} \rightarrow [0, \infty]$ on which the EKI is applied.

Provided with Equation (7.15), we proceed to identify the best dimensionless frequency for the configurations described in § 7.2 using the ROM described in § 7.2.5 and the data generated using the direct modeling approach in § 7.2.4. The results of this analysis require 1031 identifications, and they are next used in order to learn the dimensionless frequency mapping.

7.3 Computing dimensionless frequencies using Random Forest

In this section, we use Random Forest (RF) regression [29] to find a mapping $\mathrm{f} : \mathbb{R}^5 \rightarrow \mathbb{R}$ to estimate the dimensionless flexible-base frequency (a_0) using five parameters as input:

$$a_0 = \mathrm{f}\left(\Pi_1 = \frac{B}{V_s\, T_b}, \Pi_2 = \frac{h_b}{B}, \Pi_3 = \frac{D}{B}, \Pi_7 = \nu_s, \Pi_{10} = \frac{B\,\mathrm{f_p}}{V_s}\right). \tag{7.19}$$

[2] Since the number of parameters to be identified is one, we theoretically only need one ensemble to span the parameter space [72].

Random Forest is an ensemble method that uses Bootstrap Aggregating (Bagging) to draw random samples from a training set. A tree with a subset of features is trained on each random sample, and a voting scheme determines the value of output for each instance of input. More formally, if we assume a training set $\mathbf{X} \in \mathbb{R}^{n \times m}$ (n is the number of instances, and m is the number of features) and $y \in \{y_1, y_2, ..., y_n\}$, we want to find f such that $y = f(\mathbf{X})$. RF draws random samples of size n with replacement from the training data, and train a tree with m' ($m' \leq m$) features for each sample [121]. RF is popular because (1) it reduces overfitting by training multiple trees with different set of features, (2) it is interpretable and feature importance analysis can be easily accomplished, and (3) it is generally faster than other bagging methods [52].

Learning the dimensionless frequency

The training set is collected from EnKI results for a wide range of input parameters (1031 cases). We trained a RF model using a grid-search approach to determine optimum tree depth, number of estimators, and number of samples by applying 4-fold cross-validation, and mean-square-error as the cost function. For the training purpose, we split the data into two groups of 80% for training and the rest for test.

The histogram of Figure 7.11 shows the distribution of a_0^* in training and test data sets. Both sets have a similar distribution which results in a "fair" evaluation of the trained model. As shown, the majority of data is focused in the $a_0^* \leq 0.5$ range with the minority being above this threshold. Moreover, a few cases of $a_0^* > 1$ are also available in both data sets.

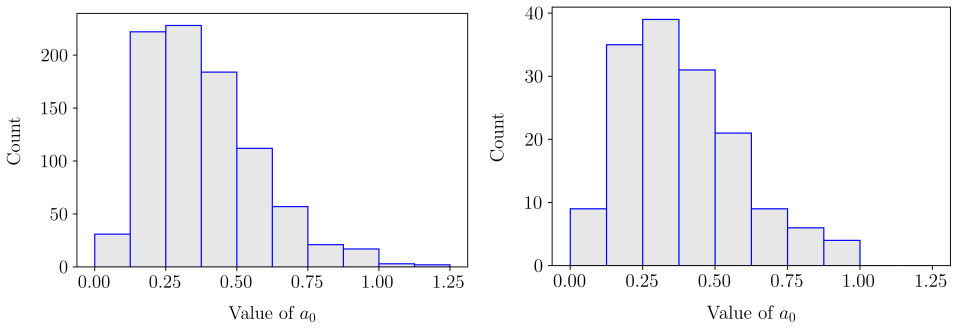

Figure 7.11: Distribution of a_0^* values in training (left) and test (right) data sets.

The training is performed on 878 data points, and the test set includes 158 data points. Figure 7.12 shows the comparison between the values obtained using EnKI

(Y_{true}), and the prediction from the trained model ($Y_{prediction}$). As can be seen, a high accuracy ($R^2 = 0.98$) of the trained model shows its capabilities in estimating an accurate a_0^*. Moreover, having a similar accuracy for the test set ($R^2 = 0.97$) manifests the absence of overfitting and the generalization capability of this model. In next section, we will discuss how one can use this model to retrieve impedance components for an arbitrary set of input parameters.

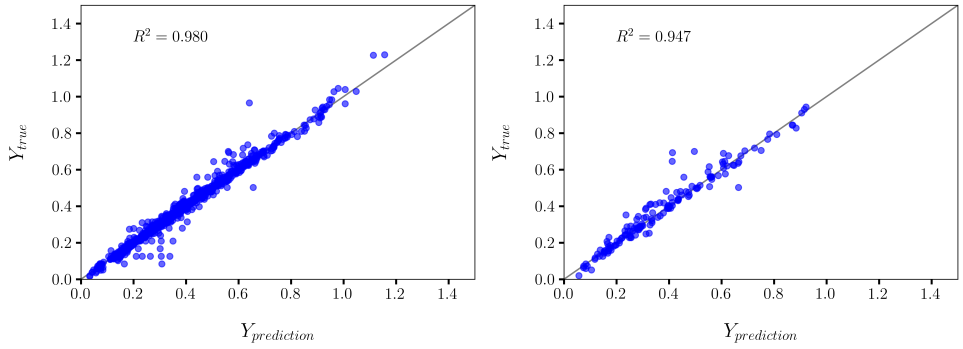

Figure 7.12: A comparison between true values (FE analysis) and RF predictions for training set (left) and test set (right).

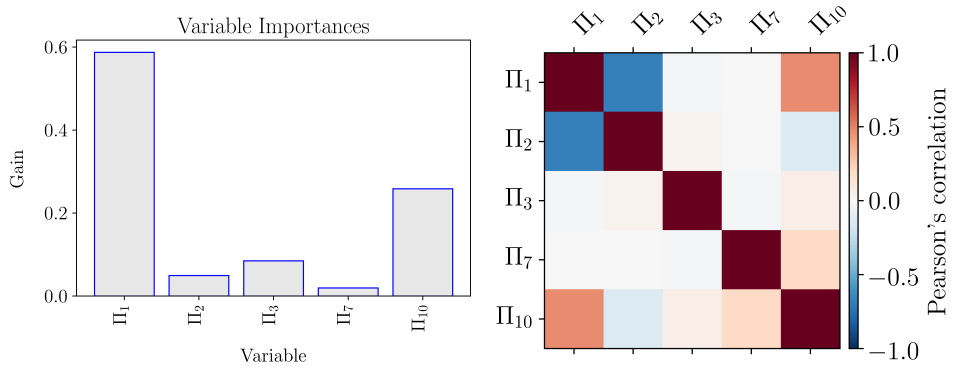

Figure 7.13: Feature importance (left) and correlation of features (right).

An important capability of RF is the ease of feature importance analysis, which illustrates how impactful each parameter is on the final result of the trained RF model. Figure 7.13 shows feature importance analysis, where $\Pi_1 = \frac{B}{V_s T_b}$ has the highest impact, as expected, since it takes into account both structure and soil properties. The second rank goes to $\Pi_{10} = \frac{B\,\mathrm{f_p}}{V_s}$, which demonstrates the interaction of input motion, soil, and structure. Other parameters have a lower impact on a_0^* estimation, and, therefore, have lower values of gain. In this regard, the dimensionless parameters (in

order of importance) are as follows: the structure-to-soil wavelength ratio (Π_1), the signal-to-soil wavelength ratio (Π_{10}), the foundation aspect ratio (Π_3), the building-aspect ratio (Π_2), and the soil's Poisson ratio (Π_7).

The correlation between each of the parameters are also presented. Here, we apply Pearson's correlation criterion, which is an interpretable measure of correlation between two parameters based on the covariance matrix of the two. This parameter ranges between $-1 \leq r \leq 1$, where having $r = 1$ means a perfect positive correlation, $r = -1$ means a perfect negative correlation, and $r = 0$ means no correlation. In real data, this correlation takes some values within the defined range. Figure 7.13 shows the correlation matrix using a color scheme where warmer colors show positive and cooler colors illustrate negative correlations. In our problem, Π_1 and Π_2 have a negative correlation. This is physically interpretable since by increasing the height of dominant mode (h_b), the fixed-based period (T_b) of a building increases as the building becomes more flexible. In addition, there are minimally-correlated (almost uncorrelated) parameters in our designated input vector, for example Π_1 and Π_7. This means Π_1 and Poisson's ratio (Π_7) would not significantly interact on estimating final output of the model.

Returning the lumped soil impedances components

In § 7.3, a mapping to obtain the dimensionless flexible-base frequency a_0 as a function of the dimensionless group $\Pi_1, \Pi_2, \Pi_3, \Pi_7, \Pi_{10}$ was provided. In other words, a relation of the form:

$$a_0 = \mathrm{f}\left(\frac{B}{V_s\, T_b}, \frac{h_b}{B}, \frac{D}{B}, \nu_s, \frac{B\, \mathrm{f_p}}{V_s}\right), \tag{7.20}$$

can now be used to estimate the frequency-independent lumped impedance values– i.e., k_{xx}, $k_{x\theta}$, $k_{\theta\theta}$, c_{xx}, $c_{x\theta}$, and $c_{\theta\theta}$, which can further be employed in Equation (7.13) to perform a dynamic analysis. However, in order to increase the accuracy of the impedance value estimation, we perform a quadratic interpolation on the impedance functions provided in Figures 7.2 to 7.4 using a_0 for the three Poisson's ratio $\nu_s^{(k)}$, $k = 1, \ldots, 3$. We thus obtain a quadratic function as follows:

$$k_{ij} = \mathrm{g}\left(a_0, \nu_s\right). \tag{7.21}$$

The value of k_{ij} can finally be read for a given Poisson's ratio. The complete process for estimating the lumped frequency-independent impedance value is summarized in Algorithm 2.

Algorithm 2 Lumped soil impedance estimation.

1: The **initialization step**: Compute the dimensionless parameters:

$$\Pi_1 = \frac{B}{T_b\, V_s}\,, \Pi_2 = \frac{h_b}{B}\,, \Pi_3 = \frac{D}{B}\,, \Pi_7 = \nu_s\,, \text{ and } \Pi_{10} = \frac{\mathrm{f_p}\, B}{V_s}\,,$$

where B is the foundation half-width, D is the foundation embedment, V_s is the soil shear wave velocity, ν_s is the soil's Poisson ratio, T_b is the fundamental fixed-base period, h_b is the first fixed-base modal height, and $\mathrm{f_p}$ is the dominant frequency of the input signal.

2: The **prediction step**: Compute the dimensionless frequency $a_0^{(k)}$ using Equation (7.20) for the three Poisson's ratio–i.e., $\nu_s^{(k)} = 0.25, 0.35, 0.45$.

3: The **analysis step:** Read from the normalized impedance functions in Figures 7.2 to 7.4, the real or imaginary component of $\hat{K}_{ij}^{(k)}$ for $i, j = \{x, \theta\}$ for the three dimensionless frequencies $a_0^{(k)}$ obtained in the prediction step.

4: The **interpolation step:** Perform a quadratic interpolation using the three previous impedance values to obtain Equation (7.21). Then multiply k_{ij} by the normalizing factor, $\pi\, \bar{B}\, G_s$, where $\bar{B} = 1.0, B, B^2$ for $\hat{K}_{xx}, \hat{K}_{x\theta}$, and $\hat{K}_{\theta\theta}$, respectively.

5: Return the interpolated soil impedance value $k_{ij} = \mathrm{g}\,(a_0, \nu_s)$.

The process to obtain the dimensionless flexible-base frequency a_0^* as well as the frequency-independent lumped impedance values are provided in a python jupyter-notebook [152] script that can be downloaded from https://github.com/dankusanovic/SSI-Optimal-Impedance.

7.4 Validation of proposed dimensionless frequency mapping

Validation using different SSI configurations

The methodology presented in Algorithm 2, for computing the dimensionless frequency and soil impedances, is tested for different buildings and soil combinations. The global soil, foundation, building, and signal parameters for each case are summarized in Table 7.3. For each case, a finite element analysis, as described in § 7.2.4, is performed to obtain the true responses. The responses obtained in this manner are thus employed to evaluate the error. In particular, we measure the ℓ_2-error for each case as:

$$\text{error} = \|y - \hat{y}\|_{\ell_2}^2 = \sum_{k=1}^{N_m} \sum_{j=1}^{N_t} \left(y_j^{(k)} - \hat{y}_j^{(k)} \right)^2\,, \tag{7.22}$$

where $y_j^{(k)}$ represents the k-th observation (from the FEM) at j-th time step, $\hat{y}_j^{(k)}$ represents the k-th response (from the ROM or NIST) at j-th time step, N_t corresponds to the number of time steps, and N_m represents the number of observations[3] considered.

In Table 7.3, we also compute the improvement factor $\mathcal{I} : \mathbb{R} \rightarrow [0, 1]$ obtained against NIST [138]. The improvement is quantified as follows:

$$\mathcal{I} = \left| 1 - \frac{\text{error(ML)}}{\text{error(NIST)}} \right| . \tag{7.23}$$

The improvement factor quantifies how much better is the overall RF solution in terms of NIST solution. Ideally if there is no error $\mathcal{I} = 1$, then a 100% of improvement is obtained. On the other hand if $\mathcal{I} = 0$, then there is no improvement at all.

Model Building's Parameters							RF		NIST		$\mathcal{I}$
B $[m]$	D $[m]$	h_b $[m]$	T_b $[s]$	V_s $[m/s]$	f_{p} $[Hz]$	ν_s	a_0^*	error	a_0^*	error	%
10	1	40	1.50	400	2.00	0.35	0.289	0.135	0.081	0.205	34.1
10	1	15	0.50	100	4.00	0.35	1.164	0.012	0.466	0.018	33.7
10	1	15	0.50	125	1.00	0.33	0.692	0.049	0.449	0.355	86.3
10	20	30	1.00	100	2.00	0.33	0.336	0.007	0.314	0.046	83.9
10	20	40	1.50	150	2.00	0.40	0.243	0.015	0.192	0.068	77.6
10	20	40	1.50	125	3.00	0.25	0.300	0.010	0.202	0.016	39.1
10	10	30	1.00	200	2.75	0.35	0.330	0.016	0.212	0.036	56.2
15	10	19.2	0.55	150	3.00	0.33	1.021	0.006	0.591	0.017	63.5
15	10	28.4	0.85	200	3.00	0.33	0.583	0.007	0.357	0.029	77.0
15	10	64.0	2.25	250	3.50	0.33	0.634	0.016	0.122	0.051	69.4

Table 7.3: Improvement of the proposed dimensionless frequency compared to the state-of-the-art for different soil, foundation, and building configurations.

Table 7.3 highlights two important results: (a) The dimensionless flexible-base frequency obtained using this methodology is always larger than the one proposed in NIST, and (b) the improvement factor is always larger than 30% and thus the error of the proposed methodology is always smaller than NIST. Note that larger values of dimensionless flexible-base frequency guarantee a proper estimation of the lumped impedance values, in particular for c_{xx}, $c_{x\theta}$, and $c_{\theta\theta}$ as discussed in [99].

[3] In computing the error, we use all the observations.

Additionally, in Figure 7.14 and 7.15, the time-history displacements at the first-modal height for the total-horizontal displacement u_X^h, the total-horizontal displacement of the roof u_X^r, and the total-horizontal displacement of the ground level u_X^g are displayed in a similar manner. The blue-solid line represents the response using the full-fidelity FEM, while the red-dashed line represents the solution using the ROM, and the yellow-dashed line represents the solution using NIST.

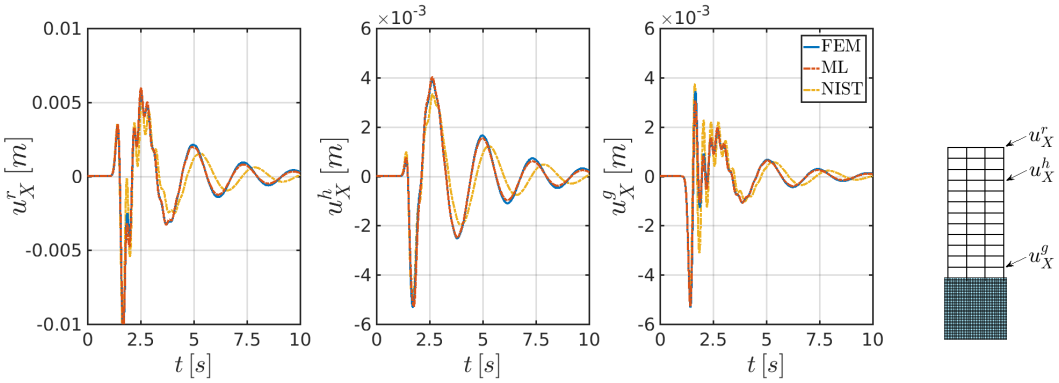

Figure 7.14: The parameters considered in the validation are for the building a fixed-fundamental period $T_b = 1.0\,[s]$ and a fixed-first modal height $h_b = 30.0\,[m]$. The foundation dimensions are a half-width $B = 10\,[m]$ and a foundation depth $D = 20.0\,[m]$. The soil shear velocity is $V_s = 100\,[m/s]$.

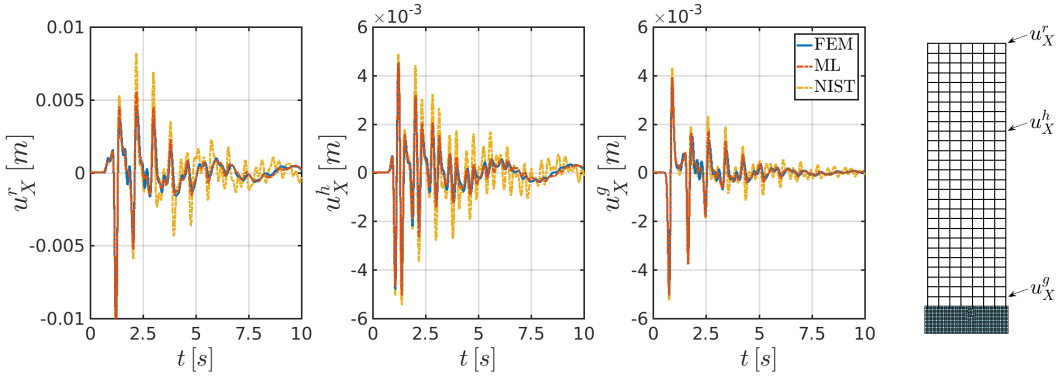

Figure 7.15: The parameters considered in the analysis are for the building a fixed-fundamental period $T_b = 2.25\,[s]$ and a fixed-first modal height $h_b = 64.0\,[m]$. The foundation dimensions are a half-width $B = 15\,[m]$ and a foundation depth $D = 10.0\,[m]$. The soil shear velocity is $V_s = 250\,[m/s]$.

Both figures show how the proposed methodology captures the period elongation and the radiation damping of the combined system very well. Also, a good agreement is obtained for the free-vibration response. In particular, note how in Figure 7.15

NIST fails to capture the radiation damping and thus high oscillations are generated inside the building. Remember that a fair comparison against NIST required the 2D foundation transfer functions and 2D impedance functions to be computed for the plane-strain case. Thus we have not used the 3D version described in NIST.

Verification using real-earthquake input motions

We test the dimensionless flexible-base frequency mapping with real-earthquake signals. We employ the *CESMD - Information for Strong-Motion Station* [62] to select real-earthquake signals with different intensities. In particular, we use:

(a) Berkeley, January 4^{th}, 2018, station 58496. Site class D (low).

(b) Chino Hills West Covina-Cortez, July 29^{th}, 2008, station 23056. Site class D (moderate).

(c) Northridge Newhall-County Fire, January 17^{th}, 1994, station 24279. Site class D (high).

The earthquake signal listed above is employed as FFM motion for both the full-fidelity FEM and the ROM using the dimensionless flexible-base frequency mapping. The FFM are then transformed into FIM using the foundation transfer function in Figures 7.6 and 7.7. The FFM velocity time history as well as their frequency content are displayed in Figure 8.4.

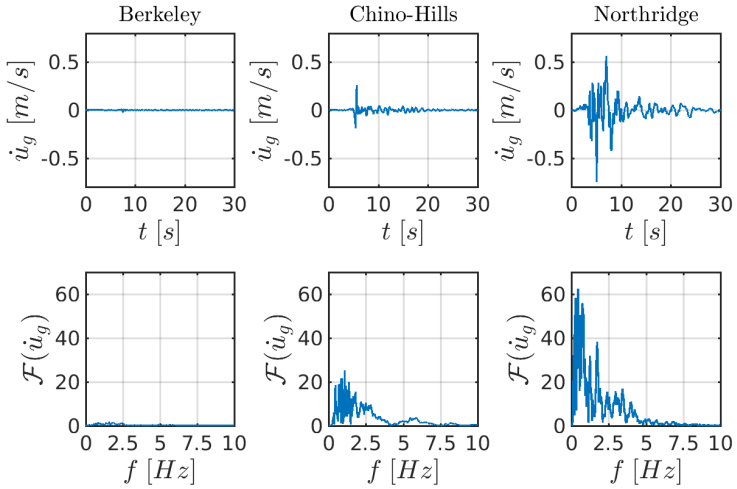

Figure 7.16: Earthquake signals and frequency content used for the dimensionless flexible-base frequency mapping validation.

For simplicity, in this section we use the building described in Table 7.2 with embedments $D = 1, 2.5, 5\,[m]$, a shear wave velocity $V_s = 200\,[m/s]$, and a Poisson's ratio $\nu_s = 0.25$. The ground's highest energy's frequency $\mathrm{f_p}$ is estimated as:

$$\mathrm{f_p} = \frac{\int_0^{\mathrm{f_m}} \mathrm{f} \cdot \hat{u}\, d\mathrm{f}}{\int_0^{\mathrm{f_m}} \hat{u}\, d\mathrm{f}}, \tag{7.24}$$

where f is the frequency, $\hat{u} = \mathcal{F}(u)$ is the Fourier transform of $u(t)$, and $\mathrm{f_m} = 10\,[Hz]$. The ground's highest energy frequencies computed in this manner are: Northridge $1.84\,[Hz]$, Berkeley $2.90\,[Hz]$, and Chino-Hills $2.57\,[Hz]$.

In Figures 7.17–7.19, the time history response at the first-modal height for the total-horizontal displacement u_X^h and the total-vertical displacement u_Y^h are represented in solid-blue lines and dashed-red lines for both the full-fidelity FEM and the ROM, respectively. In addition, the total-horizontal displacement of the roof u_X^r and the total-horizontal displacement of the ground level u_X^g are displayed in a similar manner. Moreover, the frequency contents of such signals for the total displacement are represented below. A normalized representation of the evaluated frame is also displayed, so that the three different topologies considered in these cases are much clearer. At a first glance, it can be seen in these figures that a good agreement is reached in both the total displacements at different building levels and the frequency content of such signals.

Additionally, in Table 7.4 the discrepancies between the full-fidelity FEM and the ROM are quantified. In particular, we quantify the error associated to maximum displacement in the complete model and the error associated to period elongation. We also compute the slope as well as the correlation of the time-series between the FEM and the ROM at each node, and the maximum discrepancy between them is reported. The slope of such correlation measures how well the simulated signal scales from the true response, while the Pearson's coefficient measures how similar the signals are.

In overall, Table 7.4 shows a good agreement in both time history responses and their frequency content. The discrepancies, which in these cases are minor, are attributed to the dimensionless flexible-base frequency mapping, since the number of building frames considered in the analysis to span the whole dimensional-parameter space may not be enough. Nevertheless, we can conclude that prescribing the FIM at the foundation interface using the ROM described in § 7.2.5 provides reasonable results

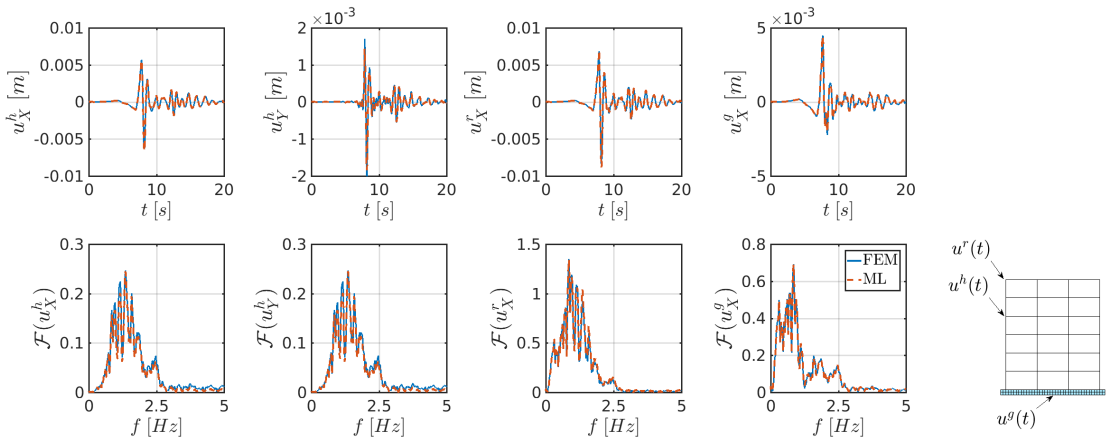

Figure 7.17: The parameters considered in the analysis are for the building a fixed-fundamental period $T_b = 0.5\,[s]$ and a fixed-first modal height $h_b = 15\,[m]$. The foundation dimensions are a half-length $B = 10\,[m]$ and a foundation depth $D = 1.0\,[m]$. The soil shear velocity is $V_s = 200\,[m/s]$ and subjected to Berkeley earthquake.

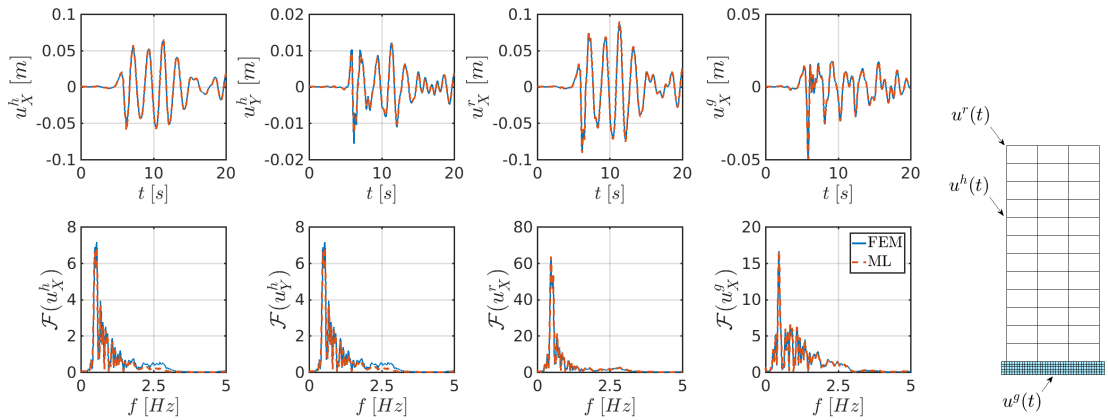

Figure 7.18: The parameters considered in the analysis are for the building a fixed-fundamental period $T_b = 1.0\,[s]$ and a fixed-first modal height $h_b = 30\,[m]$. The foundation dimensions are a half-length $B = 10\,[m]$ and a foundation depth $D = 2.5\,[m]$. The soil shear velocity is $V_s = 200\,[m/s]$ and subjected to Chino Hills earthquake.

in terms of errors when time history responses, maximum displacements, period lengthening, and radiation damping are compared to the full-fidelity FEM. Note that the maximum error obtained for the displacement for the entire model is always less than 5%, and also the error in estimating the period elongation using the proposed dimensionless flexible-base frequency mapping is small.

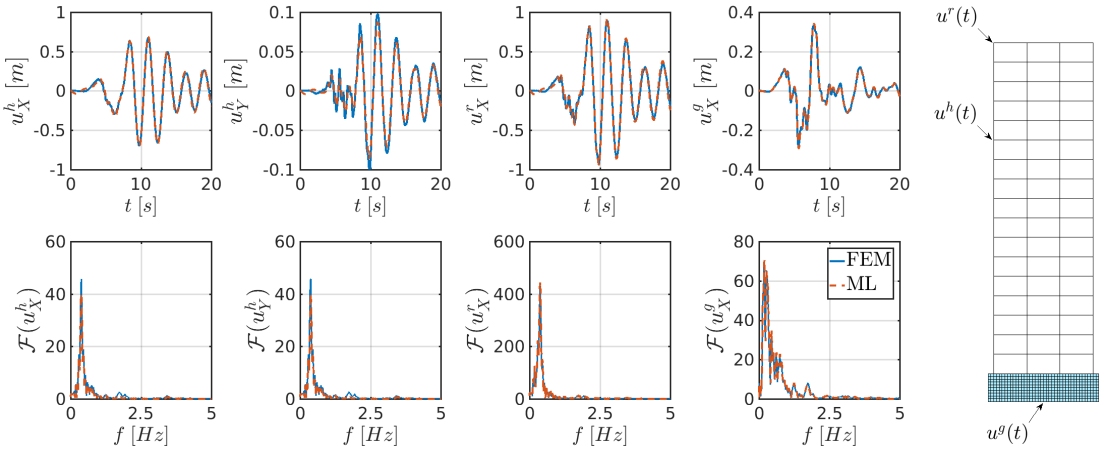

Figure 7.19: The parameters considered in the analysis are for the building a fixed-fundamental period $T_b = 1.5\,[s]$ and a fixed-first modal height $h_b = 40.0\,[m]$. The foundation dimensions are a half-length $B = 10\,[m]$ and a foundation depth $D = 5.0\,[m]$. The soil shear velocity is $V_s = 200\,[m/s]$ and subjected to Northridge earthquake.

Frame Name	Earthquake Name	Maximum Displacement Error	Period Elongation Error	Correlation Slope m	Correlation Pearson's R^2
	Berkeley	0.046	0.001	1.009	0.997
(a)	Chino Hills	0.035	0.000	1.004	0.996
	Northridge	0.015	0.002	1.005	0.999
	Berkeley	0.025	0.000	1.028	0.999
(b)	Chino Hills	0.005	0.000	1.027	0.999
	Northridge	0.026	0.013	0.986	0.987
	Berkeley	0.003	0.012	0.989	0.986
(c)	Chino Hills	0.033	0.150	1.007	0.990
	Northridge	0.004	0.002	1.022	0.994

Table 7.4: Errors associated to building's responses for the validation of real-earthquake motion.

7.5 Summary and conclusions

In this work, we presented a dimensionless flexible-base frequency mapping that improves the one used by the state-of-practice for time domain simulations of building structures on embedded foundations. The so-generated flexible-base frequency mapping is validated using full-fidelity finite element analyses, and an improvement greater than 30% is obtained for all tested cases when they are compared against NIST. We have not only shown that the dimensionless flexible-base frequency indeed

depends on five dimensionless quantities, but also we found that the structure-to-soil wavelength ratio, the foundation aspect ratio, and signal-to-soil wavelength ratio are the most important dimensionless parameters that control the frequency of the interaction.

The dimensionless flexible-base frequency a_0^* estimated using EnKI are the ones that best represent the frequency of vibration of the combined soil-foundation-building system. The 1031 cases used in this study to span the parameter space revealed that there always exists an optimal dimensionless flexible-base frequency a_0^* that matches the full-fidelity finite element model, and this frequency may not necessarily coincide with the one suggested in NIST. We used these cases to train a Random Forest model, which showed to work very well for several validation cases, including real-earthquake signals with different intensities. The proposed mapping is very robust as long as the dimensionless parameters are inside the domain defined in § 7.2. Extrapolation outside this domain may cause deviation, and they should be used with caution. However, the present methodology allows to include more analysis to improve the estimate of a_0^*. We have provided the data (training set) identified in this work as well as python routines and they can be downloaded from https://github.com/dankusanovic/SSI-Optimal-Impedance.

Finally, more complicated soil features such as non-linear material behavior of the soil or loose contact between soil and foundation can be easily considered using this methodology. However, more dimensionless parameters may be required, generating an increase in the number of simulation cases required to span the parameter space. Future extensions of this work may include assessment of the dimensionless fixed-base frequency to non-uniform half space and non-linear soil behavior.

Chapter 8

APPLICATION: SIMPLIFIED REGIONAL SOIL-STRUCTURE INTERACTION ASSESSMENT APPLIED TO SOUTHERN CALIFORNIA

8.1 Motivation

The increase of population in major cities have produced a large densification of buildings. As a result, the lack of space in already dense urban areas has generated unsafe sites to be considered as potential areas of construction. However, the seismic design of such structures are carried out using conventional methods [32, 128] that usually disregard soil-structure interaction (SSI) and structure-soil-structure interaction (SSSI) effects that can significantly change the estimated demand on urban sites and their surroundings. In general, earthquake damage scenarios for urban areas are commonly addressed by simplifying the analysis assuming fixed-base structures, i.e. without taking into account the compliance of the soil, and therefore neglecting inertial and kinematic interaction effects [116, 157].

During the last 20 years, the challenge in understanding and predicting city global scale responses has grown increasing interest to describe in depth SSI and SSSI [59, 91, 126, 129, 145]. Several works have addressed this topic in many different ways. For instance, sophisticated 3D finite element analysis to explore soil-underground structure-soil interaction (SUSSI) and site-city interaction (SCI) of Kowloon station in Hong Kong was developed by Kato and Wang [89]. 3D computations to characterize SSSI in Nice, France, and Mexico City has been done by Clouteau and Aubry [36]. 2D numerical models to describe the diffraction pattern of surface waves due to the influence of buildings and their impact on buildings has been assessed by Wirgin and Bard [156]. 2D reduced order model of SSI of buried structures with layered soil under vertical excitation have been presented by Esmaeilzadeh et al. [131, 132]. Simplified analysis to describe the global city effect using single oscillators that account for single and multiple interactions have been proposed by Guéguen et al. [59], Boutin and Roussillon [27]. However, most of these analyses are either (i) very sophisticated where sometimes is difficult to isolate the SSI effects, and thus to generalize the findings to some other cases, (ii) they employ several physical parameters to describe topographic effects, irregular-

ity of buildings, and soil properties that prevent to discriminate the main variables that control the interaction phenomenon, or (iii) they are too simplified that 2D/3D effects are ignored.

In this chapter, we attempt to capture the most relevant phenomenon of SSI at a regional scale by using only one dimensionless parameter, i.e, structure-to-soil stiffness ratio for a given building [125, 154]. This work aims at understand the SSI effects generated in simplified two-dimensional symmetric buildings at a regional-scale, which can be easily extended to three-dimensional analysis. In particular, we focus our analysis on the evaluation of SSI effects in Southern California combining different building topologies, a simulated real earthquake [145], and local site effects, in which the building's performance is evaluated based on period-lengthening, radiation damping, maximum displacement, maximum acceleration, and maximum inter-story drift. The building's responses are normalized based on an equivalent fixed-base building, so that the SSI effects are isolated, and they can be divided into (i) beneficial, (ii) indifferent, and (iii) detrimental depending on the magnitude. This approach will enable us to identify the areas in Southern California that are more susceptible to experience damages for a given building configuration.

8.2 The problem statement and method of analysis

We are interested in evaluating the SSI effects that a certain building in Southern California experiences when it is subjected to a given earthquake. Since a fully coupled 3D numerical simulation of such area requires a large amount of computer resources [129, 144, 145], we develop a simplified 2D reduced order model that preserves the characteristics of the surrounding soil as well as the ability of emulating the inertial and kinematic interaction effects. The latter is achieved using frequency independent soil spring and dashpot placed on the foundation interface that emulates the surrounding soil [138–140]. These soil spring and dashpot coefficients are estimated using ensemble Kalman Inversion (EnKI) [50, 72, 102]. The identification based on EnKI requires data that will be generated from a set of 2D finite element model with appropriate absorbing boundary conditions [51, 94, 95]. The data will be generated using different soil–i.e., varying the shear wave velocity, so that we can span all possible ranges of soil stiffness and radiation conditions. The data generated in this manner will be used in order to estimate the soil spring and dashpot that mimic the effect of the surrounding soil. The identified soil spring and dashpot coefficients will be then used in order to approximate the soil impedances as a function of the shear wave velocity. This will enable us to represent the spring and dashpot

coefficients to emulate the soil characteristics at any point in Southern California provided with only the shear wave velocity and dynamic properties of the building.

In the following subsections, we proceed to describe in details how the direct model problem is carried out for data generation, how the building and the surrounding soil are formulated as a reduced order model, and how using EnKI is employed to estimate the soil parameters so that the discrepancies between the direct modeling method and the proposed ROM are minimized.

Direct modeling of the problem

In Figure 8.1, the three 2D buildings considered in this work are illustrated. The first reinforced concrete building in Figure 8.1 (a) has columns of a rectangular cross section $0.90 \times 0.60\,[m]$, each of $3.5\,[m]$ height. Beams have rectangular cross sections $0.80 \times 0.60\,[m]$ and $6.0\,[m]$ length. The reinforced concrete density is $2500\,[kg/m^3]$, the reinforced concrete elasticity modulus is taken as $25\,[GPa]$, and beams are subjected to a dead load of $3600\,[kg/m]$. This configuration gives a total height of $21\,[m]$, a total mass of $6.45 \cdot 10^5\,[kg]$, a fixed-base fundamental period of $0.50\,[s]$, a first-modal height of $15.0\,[m]$, and a first modal mass $0.545 \cdot 10^6\,[kg]$. The solid core foundation has a half-width of $10\,[m]$, an equivalent length (thickness) of $1.0\,[m]$, and a foundation embedment depths of $1.0\,[m]$. The reinforced concrete material properties for the foundation are taken such that the foundation mass is $50.0 \cdot 10^3\,[kg]$, the elasticity modulus is $30\,[GPa]$, and the Poisson's ratio is 0.25.

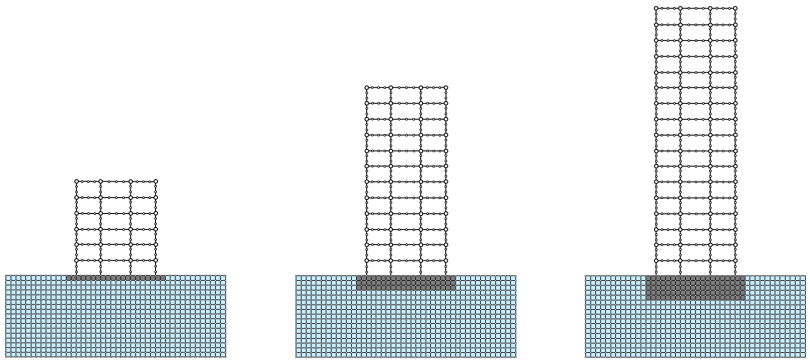

Figure 8.1: A truncated view of the building configurations employed for the 2D Southern California SSI problem.

The second and third reinforced concrete buildings in Figure 8.1 (b) and (c) only differ in terms of the column cross-sections, which for both cases are $1.00 \times 0.80\,[m]$.

The foundation embedment depths for both buildings are 2.5 and 5.0 $[m]$, respectively. Beams and material properties of the building and foundation are the same as above. The foundation is assumed to have perfect bonding with the surrounding soil, and the foundation is assumed to be rigid. Table 8.1 summarizes some of the building's global dynamic features.

Building			Foundation		Eigen-Analysis	
Period	Mass	Height	Half-width	Depth	Modal Mass	Modal Height
$[s]$	$[kg]$	$[m]$	$[m]$	$[m]$	$[kg]$	$[m]$
0.50	$6.45 \cdot 10^5$	21.00	10.0	1.00	$5.45 \cdot 10^5$	15.0
1.00	$1.40 \cdot 10^6$	42.00	10.0	2.50	$1.15 \cdot 10^6$	30.0
1.50	$1.98 \cdot 10^6$	59.50	10.0	5.00	$1.48 \cdot 10^6$	40.0

Table 8.1: Summary of geometry and first fixed-modal parameters for three buildings considered in Southern California.

In the finite element models, the soil is represented as an elastic, homogeneous, and semi-infinite medium with density $\rho_s = 2000\,[kg/m^3]$, Poisson's ratio $\nu = 0.25$, and shear wave velocity $V_s = 100, 125, 150, 175, 200, 225, 250, 300, 400, 500\,[m/s]$. The soil and foundation domains are modeled as four-node two-dimensional plane strain quadrilateral elements, and the building structure domain is modeled as two-node linear elastic frame elements. The quadrilateral elements have two translational degrees of freedom per node, whereas the elastic frame elements have three degrees of freedom per node (two translational and one rotational). All material models assigned to structural and soil elements are isotropic linear and elastic, and no viscous damping is added so at this stage of the study, the energy loss as seen from the building is solely because of radiation damping. The connection between solid and structural elements as well as the rigid diaphragm behavior of the foundation are enforced using kinematic constraints [16, 42].

The plane strain soil domain is truncated using absorbing boundaries conditions provided to limit the occurrence of spurious waves that are reflected from the far-field boundaries. In these analyses, we employ the absorbing boundaries proposed by Kucukcoban and Kallivokas [51, 95] for plane strain in two dimensions. The dimension of the truncated domain is taken such that the horizontal direction is $L_x = 75\,[m]$ and the vertical direction is $L_z = 75\,[m]$. A perfectly-matched layer (PML) of 10 $[m]$ thickness is provided around the near-field. The absorbent boundary conditions were verified for plane wave propagation in the soil in absence of

foundation and building, and were found to yield perfectly coherent motions (1D conditions) on the ground surface.

In addition, the domain reduction method (DRM) proposed by Bielak et al. [24] is employed in order to transmit the ground motion of an in-plane sv-wave propagating upwards inside the near-field domain. The incident ground motion $\dot{u}_g(t)$ used in the finite element models is prescribed as an effective force Ricker function, proportional to Equation (8.1):

$$\dot{u}_g(t) = \left(1 - 2\gamma\,(t - t_0)^2\right) \exp\left[-\gamma\,(t - t_0)^2\right], \tag{8.1}$$

where $\gamma = (\pi \mathrm{f}_0)^2$, $\mathrm{f}_0 = 2.0\,[Hz]$ is the characteristic frequency and $t_0 = 1.0\,[s]$ is the time of peak velocity. These values yield a Ricker wavelet of peak ground velocity $0.1\,[m/s]$ and frequency content between $0 - 7.5\,[Hz]$. The displacement, velocity, and acceleration fields needed to be prescribed in the one-layer of soil elements for the DRM can be computed analytically using the method proposed in [58, 122, 160].

Lastly, the time step Δt is usually limited using the so-called Courant-Friedrichs-Lewy[1] (CFL) condition:

$$\Delta t \leq \mathrm{CFL}\,\frac{\Delta \mathrm{h}}{V_s}\,. \tag{8.2}$$

In Equation (8.2), the variable V_s is the shear wave velocity for the simulation. Therefore, for an element size of $\Delta h = 0.5\,[m]$ and a fixed value $\mathrm{CFL} = 0.30$, the maximum time step can be computed for each simulation. The resulting finite element mesh has approximately 32000 elements; and we employed Seismo-VLAB [96–98] for the simulations, and since the mesh is not large enough, we use a single core execution. It is important to note that increasing or decreasing time step Δt decreases or increases the range of frequencies that the temporal mesh is able to capture for a given element size Δh. On the other hand, decreasing or increasing the size element Δh increases or decreases the range of frequencies that the spatial mesh can capture. In other words, some frequencies will be aliased[2] depending on which one, the time step size or the element size is increased based on the fact that the same frequency in both meshes are to be captured.

[1] The Courant-Friedrichs-Lewy (CFL) condition is a necessary condition for convergence of hyperbolic PDEs, which arises studying the numerical domain of dependence.

[2] Numerical aliasing occurs when the mesh is too coarse to capture high frequency; therefore, such frequencies are lost and the energy of the signal decreases.

Reduced order modeling of the problem

For developing a simplified version of the finite element model presented in § 8.2.1, we consider the reduced order model (ROM) shown in Figure 8.2c.

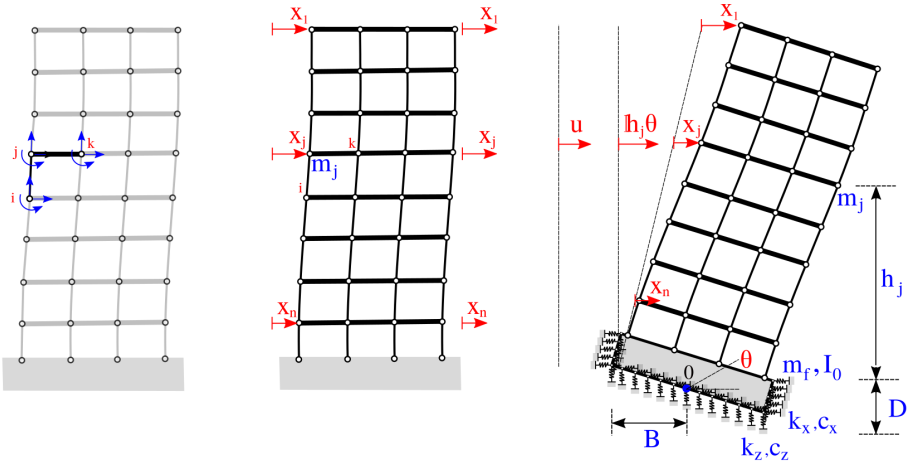

Figure 8.2: The reduced order model. (a) The column and beam element used to construct the fixed base FEM. (b) The fixed base FEM building model where $\mathbf{M}_s, \mathbf{C}_s, \mathbf{K}_s$ are obtained using static condensation. (c) The flexible-base soil-structure interaction system in which $x = (x_1, \ldots, x_n)$ represents the relative displacement of each floor, u represents the relative deformation of the soil, and θ the rigid rotation of the foundation.

The ROM is constructed in such a way that it preserves the modal information of the fixed base building. To this end, we employ frame elements with three degrees of freedom per node to represent the structure's geometry as shown in Figure 8.2a. We assume that each floor acts as a rigid diaphragm, so that the building's mass can be lumped at the floor levels as shown in Figure 8.2b. We then use static condensation [61, 73] on the fixed-base building to compute the $\mathbf{M}_s, \mathbf{C}_s, \mathbf{K}_s \in \mathbb{R}^{n\times n}$ matrices, where n is the number of floors; additionally, the vector $x \in \mathbb{R}^n$ represents the horizontal degree of freedom of the building, since there is only one translational degree of freedom on each floor. We assume a rigid rectangular foundation of half-width B and depth D sitting on an elastic half-space, for which two additional degrees of freedom $u, \theta \in \mathbb{R}$ appear because of the flexibility of the soil. The foundation has a total mass m_f, and a moment of inertia I_0. The motion that one can use to excite the model is consider to be the free-field-motion (FFM).

It can be shown that under the assumptions above, the semi-discrete equation of

motion is:

$$\begin{bmatrix} \mathbf{M}_s & \mathbf{M}_s\,\mathbb{1} & \mathbf{M}_s\,\mathbb{h} \\ \mathbb{1}^\top\mathbf{M}_s & m_f + \mathbb{1}^\top\mathbf{M}_s\,\mathbb{1} & m_f\frac{D}{2} + \mathbb{h}^\top\mathbf{M}_s\,\mathbb{1} \\ \mathbb{h}^\top\mathbf{M}_s & m_f\frac{D}{2} + \mathbb{h}^\top\mathbf{M}_s\,\mathbb{1} & I_0 + m_f\frac{D^2}{4} + \mathbb{h}^\top\mathbf{M}_s\,\mathbb{h} \end{bmatrix} \begin{bmatrix} \ddot{x} \\ \ddot{v} \\ \ddot{\theta} \end{bmatrix} + \begin{bmatrix} \mathbf{C}_s & \mathbb{O}_{n\times 1} & \mathbb{O}_{n\times 1} \\ \mathbb{O}_{1\times n} & c_{xx} & c_{x\theta} \\ \mathbb{O}_{1\times n} & c_{x\theta} & c_{\theta\theta} \end{bmatrix} \begin{bmatrix} \dot{x} \\ \dot{v} \\ \dot{\theta} \end{bmatrix} +$$

$$\begin{bmatrix} \mathbf{K}_s & \mathbb{O}_{n\times 1} & \mathbb{O}_{n\times 1} \\ \mathbb{O}_{1\times n} & k_{xx} & k_{x\theta} \\ \mathbb{O}_{1\times n} & k_{x\theta} & k_{\theta\theta} \end{bmatrix} \begin{bmatrix} x \\ v \\ \theta \end{bmatrix} = - \begin{bmatrix} \mathbf{M}_s\,\mathbb{1} \\ m_f + \mathbb{1}^\top\mathbf{M}_s\,\mathbb{1} \\ m_f\frac{D}{2} + \mathbb{h}^\top\mathbf{M}_s\,\mathbb{1} \end{bmatrix} \ddot{u}_{\mathrm{FFM}}(t)\,, \tag{8.3}$$

where $\ddot{x}, \dot{x}, x \in \mathbb{R}^n$ are the acceleration, velocity, and displacement vector for the condensed horizontal degrees of freedom of the building, also $\ddot{v}, \dot{v}, v \in \mathbb{R}$ and $\ddot{\theta}, \dot{\theta}, \theta \in \mathbb{R}$ are the foundation horizontal and the rotational acceleration, velocity, and displacement. Note that we define $\mathbb{1} \in \mathbb{R}^n$ the vector of ones, which is $\mathbb{1} = (1, 1, \ldots, 1)^\top$, and $\mathbb{h} \in \mathbb{R}^n$ the vector of height, which is $\mathbb{h} = (h_1 + D, \ldots, h_n + D)^\top$. We finally define $\mathbb{O}_{n\times m} \in \mathbb{R}^{n\times m}$ the matrix of zeros.

In addition, it is important to highlight that in the ROM, the horizontal and vertical spring and dashpot elements are distributed uniformly over the foundation perimeter. However, the contribution can be lumped as follows for both stiffness and damping components:

$$k_{xx} = 2\,k_x\,(D + B)\,, \quad k_{x\theta} = k_x\,D^2\,, \quad k_{\theta\theta} = \frac{2}{3}k_x\,D^3 + \frac{2}{3}k_z\,B^3 + 2\,k_z\,B^2 D\,, \tag{8.4}$$

$$c_{xx} = 2\,c_x\,(D + B)\,, \quad c_{x\theta} = c_x\,D^2\,, \quad c_{\theta\theta} = \frac{2}{3}c_x\,D^3 + \frac{2}{3}c_z\,B^3 + 2\,c_z\,B^2 D\,. \tag{8.5}$$

Distributing the spring and dashpot elements as represented in Figure 8.2(c) allows us to take the coupling effects in the stiffness and damping matrices into account explicitly. Finally, note that prescribing the FFM on the base of the ROM is not correct, since kinematic interaction due to the presence of the foundation is ignored. However, a novel feature of estimating the soil spring and soil dashpot coefficients using the EnKI is to implicitly compensate for kinematic interaction effects due to foundation embedment (if any), since it uses the data from the finite element models.

Ensemble Kalman inversion for parameter estimation

In order to find the optimal spring and dashpot coefficients for the ROM described in § 8.2.2, we use the Bayesian approach based on the ensemble Kalman inversion (EnKI) [50, 72, 102]. In the inversion setting, we consider the problem of finding $u \in \mathbb{R}^n$ from $y \in \mathbb{R}^m$ where

$$y = \mathbf{G}(u) + \eta\,. \tag{8.6}$$

The variable $u \in \mathbb{R}^n$ consists of all the unknown parameters that we want to estimate. In our case $u = (k_x, k_z, c_x, c_z)$, the variable $y \in \mathbb{R}^m$ consists of the ground truth quantities of interest, here obtained using the direct modeling method, and η is a zero-mean Gaussian noise with covariance $\mathbf{\Gamma}$. The nonlinear function (a.k.a. forward model or ROM) $\mathbf{G} : \mathbb{R}^n \to \mathbb{R}^m$ maps the parameter space to the data space. In this application, we work with one type of data-set; the displacement time series recorded at the floors and foundation levels computed using the model described in §8.2. Given N particles $u_j^{(n)}$, $n = 1, \ldots, N$ within the ensemble and at each iteration j, we use the predictions $\mathbf{G}(u_j^{(n)})$ by the forward model and the observation data y to update the particles for iteration $j + 1$. The formal derivation of the update is presented in [3, 102] and is,

$$u_{j+1}^{(n)} = u_j^{(n)} + \mathbf{C}_{j+1}^{uw}(\mathbf{C}_{j+1}^{ww} + \mathbf{\Gamma})^{-1}(y_{j+1}^{(n)} - \mathbf{G}(u_j^{(n)})) \quad \text{for} \quad n = 1, \ldots, N\,. \tag{8.7}$$

It is worth mentioning that the stopping criterion is defined as either reaching a relative change of 0.001 in all the parameters in two consecutive EnKI iterations or a maximum number of 500 iterations. Furthermore, the initial ensemble mean is defined to be equal to the lumped stiffness and dashpot coefficients obtained using the NIST [138] procedure. In addition, if the prior distribution of the soil parameter is unknown, then we use a uniform distribution as a prior to represent this uncertainty. We have used $N = 100$ ensembles[3] in each model to estimate the parameters. Finally, the positiveness of the stiffness and dashpot coefficients are enforced through a change of variables $u \in \mathbb{R}$, $\exp(u) : \mathbb{R} \to [0, \infty]$ on which the EKI is applied.

Provided with Equation (8.7), we proceed to identify the soil spring and dashpot coefficients for the three building structures resting on ten different soils using the ROM described in § 8.2.2 and the data generated using the direct modeling approach in § 8.2.1. The results of this analysis is summarized in Figure 8.3 for which the normalized factors are $k_0 = 3 \cdot 10^7[N/m]$ and $c_0 = 2 \cdot 10^6[Ns/m]$. The blue circle represents the identified values for the building with fixed base period $0.5[s]$, while the red and yellow circles represent the identified values for the building with fixed base period $1.0[s]$ and $1.5[s]$, respectively. The blue, red, and black dashed lines represent the non-linear curve fitting applied to these values. A good agreement is obtained for the three buildings considered.

[3] Since the number of parameters to be identified are four, we theoretically only need four ensembles to span the parameter space [72].

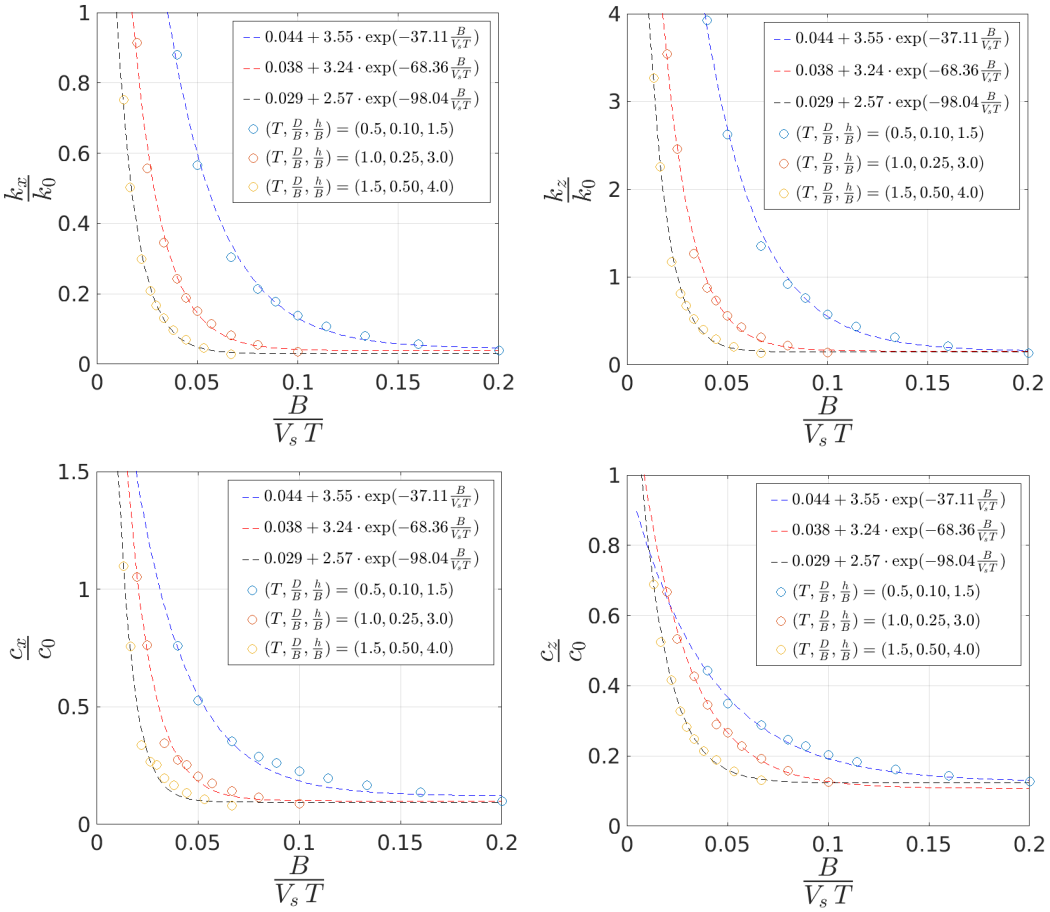

Figure 8.3: Non-linear curve fitting for the soil-structure interaction function to the generated data provided with the identified parameters of the 30 analyses.

8.3 Verification of the reduced order model for SSI assessment

We employ the *CESMD - Information for Strong-Motion Station* [62] to select real-earthquake signals with different intensities. In particular, we use:

(a) Berkeley, January 4^{th}, 2018, station 58496. Site class D (low).

(b) Chino Hills West Covina Cortez, July 29^{th}, 2008, station 23056. Site class D (moderate).

(c) Northridge Newhall County Fire, January 17^{th}, 1994, station 24279. Site class D (high).

The earthquake signal listed above is employed as free-field motion (FFM) motion for both the direct method and the ROM method. These velocity time histories as

well as their frequency content are displayed in Figure 8.4.

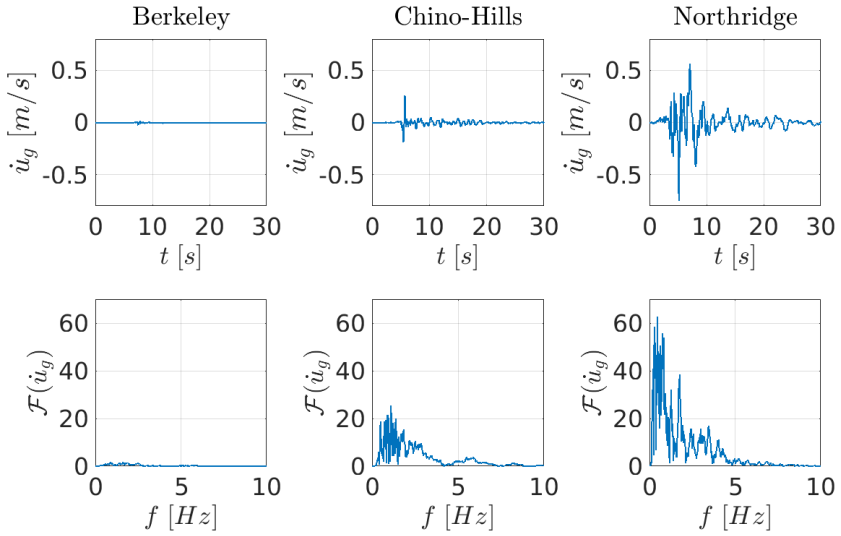

Figure 8.4: Earthquake signals and frequency content used for the ROM validation.

We perform the validation to the three buildings presented in Table 8.1 using the direct modeling method described in § 8.2.1. We assume that this analysis will generate the true response since it accounts for all sorts of interactions. We then perform the same analysis using the ROM described in § 8.2.2. In this analysis, we replace the surrounding soil by a set of spring and dashpot elements placed all over the foundation interface whose values are estimated using the non-linear curve fitting showed in Figure 8.3.

In Figures 8.5–8.7, the time history response at the first-modal height for the total-horizontal displacement Δ_X^h and the total-vertical displacement Δ_Y^h are represented in solid-blue line and dashed-red line for both the direct modeling method and the ROM respectively. In addition, the total-horizontal displacement of the roof Δ_X^r and the total-horizontal displacement of the ground level Δ_X^g are displayed in a similar fashion. Moreover, the frequency contents of such signals for the total displacement are represented below in the same figures. A normalized representation of the evaluated frame is also displayed, so that the three-different topologies considered in these cases are much clearer.

At a first glance, it can be seen in these figures that a good agreement is reached in both the total displacements at different building levels and the frequency content of such signals. More rigorously, in Table 8.2 the discrepancies between the *direct-modeling method* and the *reduced-order method* are quantified. In particular, we

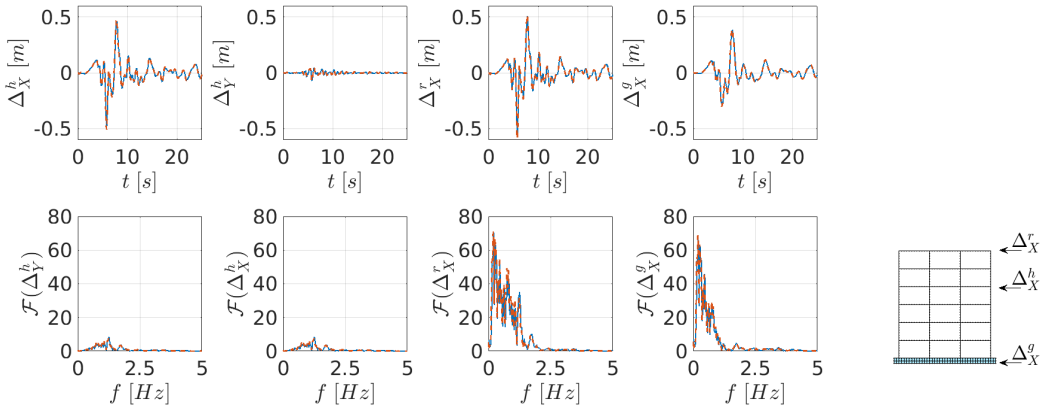

Figure 8.5: The parameters considered in the analysis for the building are a fixed-fundamental period $T = 0.5\,[s]$ and a fixed-first modal height $h = 15\,[m]$. The foundation dimensions are a half-length $B = 10\,[m]$ and a foundation depth $D = 1.0\,[m]$. The soil shear velocity is $V_s = 200\,[m/s]$ and subjected to Northridge earthquake.

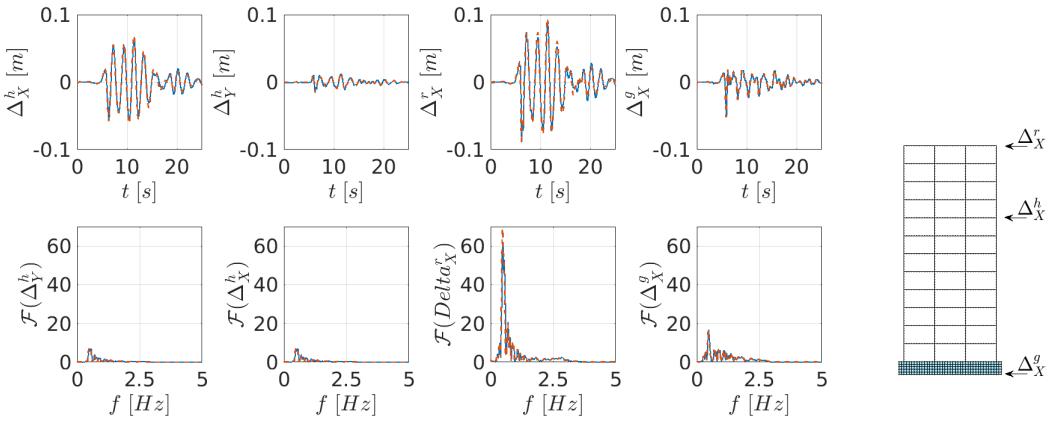

Figure 8.6: The parameters considered in the analysis for the building are a fixed-fundamental period $T = 1.0\,[s]$ and a fixed-first modal height $h = 30\,[m]$. The foundation dimensions are a half-length $B = 10\,[m]$ and a foundation depth $D = 2.5\,[m]$. The soil shear velocity is $V_s = 200\,[m/s]$ and subjected to Chino Hills earthquake.

quantify: (a) the error associated to maximum displacement in the complete model, and (b) the error associated to period elongation. Finally the slope as well as the correlation of the time-series between the direct modeling and the ROM are computed at each node, and the maximum discrepancy between them is reported. The slope measures how well the simulated signal scales from the true response, while the Pearson's coefficient measures how similar the signals are.

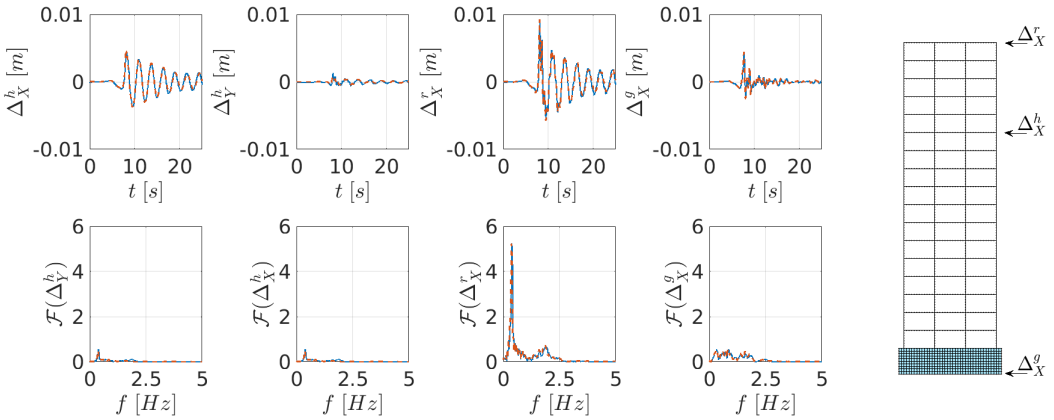

Figure 8.7: The parameters considered in the analysis for the building are a fixed-fundamental period $T = 1.5\,[s]$ and a fixed-first modal height $h = 40.0\,[m]$. The foundation dimensions are a half-length $B = 10\,[m]$ and a foundation depth $D = 5.0\,[m]$. The soil shear velocity is $V_s = 200\,[m/s]$ and subjected to Berkeley earthquake.

Frame Name	Earthquake Name	Maximum Displacement Error	Period Elongation Error	Correlation Slope m	Correlation Pearson's R^2
	Berkeley	0.045	0.000	1.050	0.993
(a)	Chino Hills	0.038	0.002	1.047	0.985
	Northridge	0.065	0.001	1.030	0.996
	Berkeley	0.028	0.013	0.985	0.980
(b)	Chino Hills	0.067	0.100	1.053	0.991
	Northridge	0.007	0.003	1.025	0.998
	Berkeley	0.016	0.052	0.991	0.981
(c)	Chino Hills	0.036	0.120	1.018	0.986
	Northridge	0.018	0.007	0.996	0.987

Table 8.2: Errors associated with displacement responses and period elongation for the buildings described in § 8.2 to a transient analysis.

Overall, Table 8.2 shows a good agreement in both time history responses and their frequency content. The discrepancies are attributed to the extrapolation of the soil spring and dashpot elements, since the number of building frames considered in the analysis to span the whole dimensional parameter space may not enough. Nevertheless, we can conclude that prescribing the free-field motion at the interface foundation nodes and adding soil spring and soil dashpot coefficients computed using the non-linear fitting provided in Figure 8.3 provide reasonable results when time history responses, maximum displacements, period lengthening and radiation

damping are computed. Such soil spring and soil dashpot elements are used next to quantify the simplified regional soil-structure interaction in Southern California.

8.4 Evaluation of SSI effects on regional scale

The simplified regional SSI applied to Southern California is performed to each one of the buildings described in Table 8.1. In this analysis, we first assume that buildings of a given fixed-base period are placed all over the Southern California area. Since in our analysis each building is separated by approximately 500 $[m]$, we assume that the free-field motion is not affected by the motion of the surrounding buildings. The three-dimensional earthquake signal simulated in [145] covers an approximate area of 180 $[km]\times 135\,[km]$, and corresponds to the M_w 5.4, 2008 Chino Hills earthquake for a maximum frequency of 4 $[Hz]$ and a minimum shear-wave velocity of 200 $[m/s]$. This simulation is validated by comparing data obtained from seismic networks with simulation synthetics on more than 300 recording stations, and further details on how this analysis was carried out are provided extensively in [145, 146]. The simulation uses a kinematic source model and the Southern California Earthquake Center (SCEC) Community Velocity Model (CVM-S v4.1) developed by the Southern California Earthquake Center. This information is used along with the building geometry to estimate the soil spring and soil dashpot coefficients as presented in § 8.2.3 and employed along with the ROM developed in § 8.2.2 and verified in § 8.3.

Because of the symmetry of the building frames, we have decoupled the buildings' 3D response into a 2D analyses in the N- and W-directions. The responses evaluated at each building corresponds to the maximum value between these two directions. Now, and in order to identify the effects of SSI, we have simulated the fixed-base condition as well. In the fixed-base analyses, small Rayleigh damping [20, 63] proportional to the stiffness matrix only is included, and the free-field motion is applied directly to the foundation. The results of the fixed-base case are used as normalizing factor so we can separate the effects of SSI into *beneficial*, *indifferent*, and *detrimental* depending on this ratio.

Spatial distribution of fundamental period and radiation damping

The period lenghtening ($\tilde{T}$) and radiation damping (β_0) of buildings is evaluated using the expression derived in Chapter 5.4 through an equivalent single-degree-of-freedom system, with dynamic properties concentrated at its first-modal height and geometry of the foundation provided in Table 8.2.

Figures 8.8 represents the spatial distribution of the period lenghtening and radiation damping in the Southern California area. In this figure, the yellower the color, the more prone the building is to experience SSI effects.

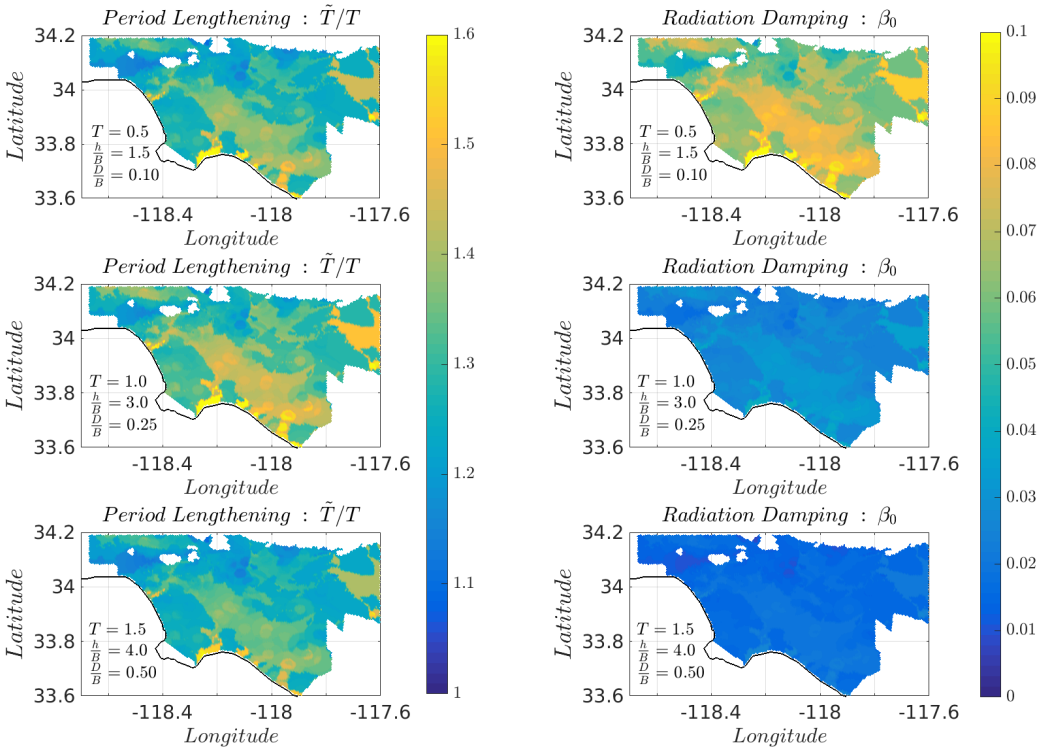

Figure 8.8: The period lenghtening and radiation damping distribution in the Southern California area.

Figure 8.8 shows that for the three buildings of fixed-base period $T = 0.5, 1.0, 1.5\,[s]$, the SSI in terms of period lenghtening is concentrated in the area of Los Angeles basin, as well as Long Beach area. This effect is accentuated even more when flexible structures are considered. Overall, it can be observed that more than 50% of the Southern California area experiences a period elongation period greater than 1.25. On the other hand, radiation damping becomes important only for the stiffer structure, i.e, fixed period $0.5\,[s]$, in which only an area approximately of 30%, mostly concentrated in Long Beach, is grater than 0.075. For the buildings of fixed period $1.0\,[s]$, and $1.5\,[s]$, the radiation damping is less than 0.05; therefore, it seems to be conservative to assume a radiation damping of 0.05 for flexible buildings as designing codes usually suggest.

Urban-scale effects of SSI on seismic demands

The period lengthening in structures generated by SSI is usually considered to be detrimental in terms of displacement responses, and considered to be beneficial in terms of the acceleration when seismic loads are imposed on a flexible-base structure. Because of this, the fixed-base assumption has been adopted in seismic codes as a conservative design approach. However, SSI may also be detrimental under certain seismic and soil conditions, depending primarily on the soil topography and stratigraphy as well as the dynamic characteristics of the structure. In this analysis, we evaluate the seismic-demand in terms of *maximum displacements*, *maximum acceleration*, and *maximum inter-story drift*. We have also normalized the SSI responses against the fixed-base case so that we can separate the SSI effects in categories–i.e., *beneficial*, *indifferent*, and *detrimental* depending on the response ratio. The categories are taken such that: it is considered *beneficial* if the ratio is less than 0.85, it is considered *detrimental* if this ratio is greater than 1.15, and it is considered *indifferent* if the ratio ranges between $0.85 - 1.15$.

The maximum response demands evaluated for the three-buildings are presented in Table 8.1. The results of this analysis are displayed in Figure 8.9, for which the SSI effects on the seismic demands is represented over the area of Southern California. In this figure, the color limits are set such that blue represents a ratio of 0.0 and the yellow a ratio of 2.00 with respect to the fixed-base case.

We first present in Figure 8.9 the normalized *maximum displacement demand* at the upper-most row. In this figure, we notice that the normalized maximum displacement is concentrated in areas such as Los Angeles basin, Glendale, Alhambra, La Habra, Yorba Linda, and Long Beach. These results are consistent since these areas present mostly soft soils which increases the flexibility of the coupled system and thus the total displacement. Now, a more detailed analysis reveals that for the building of period 0.5 $[s]$, only 20% of the Southern California area experiences a detrimental SSI effect (ratios greater than 1.15), while 15% is beneficial (ratios less than 0.85). For the building of period 1.0 $[s]$, only a total area of 25% experiences a detrimental SSI effect, while 25% of Southern California area is beneficial. Finally, for the building of period 1.5 $[s]$, only 20% of the area experiences a detrimental SSI effect, while 45% is beneficial. These results suggest that detrimental SSI effects for the maximum displacement ratio occur in average in 20% of the area of Southern California; in particular the building with fixed-base period of 1 $[s]$ experiences the larger increase in areas close to Buena Park, Santa Fe Springs, Glendale, Burbank,

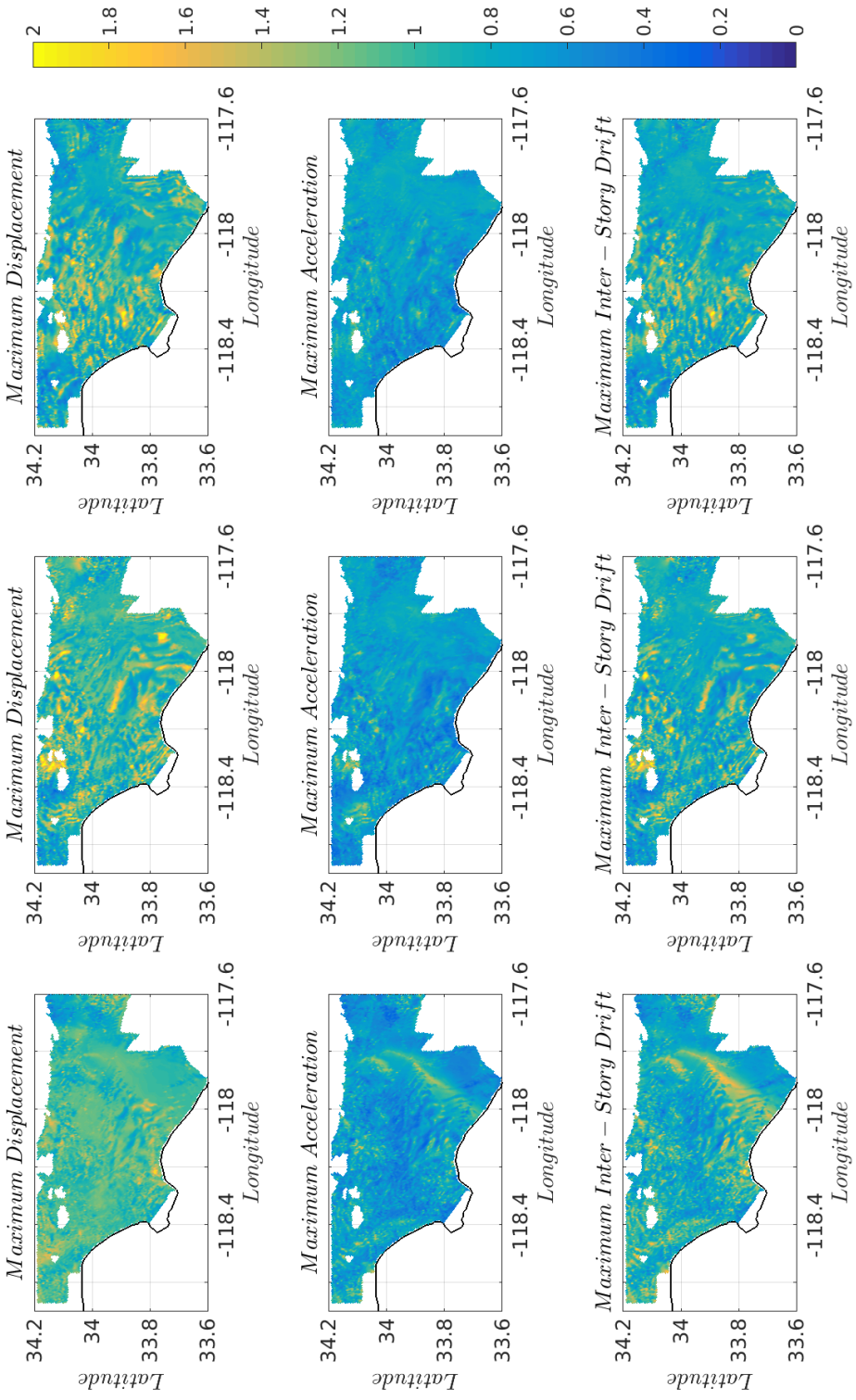

Figure 8.9: The urban-scale effects of SSI on seismic demands (rows) in the Southern California area for the three buildings (columns).

and Los Angeles Downtown.

We next present in Figure 8.9 the case of the normalized *maximum acceleration* on the second row. This set of maps shows that for flexible buildings, i.e., $T = 1.0\ [s]$, and $T = 1.5\ [s]$, indifferent and beneficial SSI effects are obtained almost everywhere, covering and area of 85% approximately. Amplification of acceleration is only obtained for the stiff structure, i.e., $T = 0.5\ [s]$ in areas around Pasadena, Santa Ana, Anaheim, Hawthorne, Inglewood, and Westwood. In particular, for the building of period $0.5\ [s]$, only 10% of the area experiences a detrimental SSI effect, while 70% is beneficial. For the building of period $1.0\ [s]$, only a 2.5% of the area experiences a detrimental SSI effect, while 85% is beneficial. Finally, for the building of period $1.5\ [s]$, only 0.7% of the area experiences a detrimental SSI effect, while 90% is beneficial. These percentages are consistent with the assumption that has been adopted in seismic codes in which a conservative design approach considers the fixed-base condition to estimate the seismic loads, but it could underestimate the seismic loads in stiffer structures, especially in areas previously mentioned.

The case of normalized *maximum inter-story drift* on the last row shows that detrimental effects are concentrated in areas such as Sunset Beach, Carson, and Los Alamitos for the three buildings presented. A more detailed quantification of this demand shows that for the building of period $0.5\ [s]$, only 15% of the area experiences a detrimental SSI effect, while 55% is beneficial. For the building of period $1.0\ [s]$, only 10% of the area experiences a detrimental SSI effect, while 67% is beneficial. Finally, for the building of period $1.5\ [s]$, only 3% of the area experiences a detrimental SSI effect, while 88% is beneficial. These results reveal that SSI effects seem to be overall beneficial or indifferent when the inter-story drift demand is evaluated.

Finally, there are some configurations for which, under certain shear wave velocities distribution and the dynamic characteristics of the structure, these effects can be detrimental, especially for stiffer structure in which the maximum displacement and inter-story drift can be drastically underestimated. However, the detrimental distribution pattern in the Southern California area depends upon the building dynamic properties as well as the foundation geometry. In this regard, the claim that SSI effects are beneficial is not always true.

8.5 Summary and conclusions

In this chapter, we presented a simplified regional SSI assessment of Southern California for three different building configurations. The analysis is carried out placing a particular building structure all over the Southern California area. This analysis helps to identify the places where SSI effects are more likely to be detrimental. In addition, this simplified analysis considers buildings with double symmetry in plan-view such that the response in two-orthogonal directions can be decoupled. This simplification allows us to use the ROM along with impedance expressions estimated in § 8.2 using EnKI. Moreover, since the considered area of Southern California is large, we discretized it every 500 $[m]$. This spatial spacing allow us to assume that the free-field motion is not affected by the surrounding buildings, and therefore the signals simulated in [145] are directly prescribed on the foundation. Finally, we assume that each building feels a semi-infinite half-space whose shear velocity value for the V_{s30} are obtained from the Community Velocity Model.

Regarding the ROM used in this study, impedance expressions provided in § 8.2 are validated for transient analyses using real earthquake signals. In particular, the Berkeley, Chino Hills, and Northridge earthquake signals are used in this work. The validation process is carried out by comparing the *reduced-order model* against the *direct-modeling method* not only for the time-history response (in terms of correlation and Pearson's coefficient), but also for the frequency content of such signals. This validation allow us to make sure that the error made in the approximation using the ROM is small, and then it can be employed to evaluate the regional SSI effect on Southern California.

The regional SSI assessment of Southern California reveals two interesting outcomes. First, the analysis once again confirms that SSI effects on period lengthening of buildings are negligible for stiff soils, becoming more important for soft soils. In particular, larger amplifications are obtained for flexible structures in soft soils, in which about 80% of the Southern California area experiences an increase greater than 20% in period lengthening. On the other hand, SSI effects on radiation damping of buildings becomes modestly important for stiff structures on soft soils. In particular, only a 20% of the covered area, i.e., in localized areas such as Long Beach and Los Angeles basin, experiences radiation damping larger than 5% for the stiff building. It is important to point out that the spatial distribution of shear-wave velocity and the first modal building information are only used in the computation of period-lengthening and radiation damping. Second, the analysis reveals that SSI

effects in terms of *maximum acceleration* and *maximum inter-story drift* are mostly beneficial; however, in certain areas specially where there is a high contrast between high and low shear-velocity, the *maximum inter-story drift* becomes large for the buildings with period $0.5, 1.0\,[s]$, more specifically in areas around Pasadena, Glendale, El Monte, Yorba Linda, Corvina, Pomona, and Corona. This outcome suggests that areas with large gradients in the shear-wave velocity should be analyzed using SSI modeling. Finally, the *maximum displacements* are detrimental almost everywhere for stiffer buildings; this suggests that a large underestimation in seismic demand can be produced employing for instance displacement-based design methods [32] as pointed out in [85] when the performance point in the design spectrum is estimated.

Although the simplified SSI assessment is demonstrated for a specific region and assumes that the building response is decoupled, the analysis is general enough that it can be applied in any area of interest or even in specific location if the earthquake signals (or free-field motion) are known. The framework based on EnKI also allows to account for several features such as soil nonlinearity, bounding interface between the foundation and soil, and general three-dimensional buildings if the impedances for such cases are known. The impedance function in this regard can be estimated using for instance any system identification techniques. In this study, the Ensemble-Kalman inversion (EnKI) turns out to be extremely robust and accurate when the impedance values are estimated. The EnKI showed to be convergent even when a small number of ensemble ($N \geq 4$) are employed. The impedances estimated in this manner can be used to develop analytical expressions to interpolate their value as a function of the building geometry and soil property. A good agreement is obtained when the full finite-element simulations are compared against the reduced-order model simulations for transient analysis. Future extensions along this line are to consider the building information database available in California, and to evaluate the possible seismic demand, and thus identify susceptible areas in Southern California. This analysis can potentially help to generate mitigation actions to buildings in vulnerable areas. Finally, a natural extension of this analysis is to consider the soil as nonlinear and study how the seismic demand changes for this new scenario and make comparison with the linear case presented here.

Chapter 9

SUMMARY AND CONCLUSIONS

The research work presented in this dissertation was focused on the development of an advanced ensemble Kalman inversion finite element model (EnKI-FEM) updating framework. Similar frameworks have been developed during the last 40 years using ExKF and UnKF for parameter estimation of simplified models [65, 68, 75, 82, 92, 135]. Additionally, natural extensions for more complex civil structures have been addressed using external packages as forward model [9, 48]. However, the novelty of our framework lies in the use of an inversion approach that allows (i) to identify parameters more efficiently (ii) to include constraints on the parameters if desired [3], and (iii) to be fully integrated in Seismo-VLAB. The EnKI-FEM framework is thus applied to improve reduced order models (ROMs) in the context of SSI using high-fidelity wave-propagation finite element (FE) models. The proposed framework, described in § 6, provides a methodology that could eventually be applied to real-world applications on large and complex civil infrastructures if enough instrumented data and a reliable FE model are available.

In this thesis, the development of the EnKI-FEM framework is presented in two parts. The first part is the object of Chapters 2, 3, and 4 for which Seismo-VLAB: a C++ multi-platform FE software designed to optimize large-scale simulations of dynamic soil-structure interaction (SSI) problems is presented. In particular, Chapters 3 and 4 provide the FE formulation for the simulation of wave propagation in homogeneous half-space in the context of linear SSI. These features required for high-fidelity SSI problems are described in depth and then implemented in Seismo-VLAB. The second part of this research is covered in Chapters 5 and 6. In particular, Chapter 5 introduces the ROM that is considered in both the EnKI-FEM framework and the forthcoming SSI applications. In Chapter 6, a novel framework for linear and nonlinear FE model updating is provided. In this framework, the ensemble Kalman inversion (EnKI) is utilized and later implemented in Seismo-VLAB to estimate the time-invariant parameters of the soil material properties for the ROM.

Finally, Chapters 7 and 8 presented two applications of the EnKI-FEM framework for estimating parameters of ROMs in SSI problems. In particular, a much better flexible-base dimensionless frequency to obtain the frequency-independent soil

impedance in a homogeneous media is proposed. The dimensionless flexible-base frequency mapping improves the one used by the state-of-practice for time domain simulations of building structures on embedded foundations. The so-generated flexible-base frequency mapping is validated using full-fidelity finite element analyses, and an improvement greater than 30% is obtained for all tested cases when they are compared against NIST. In this investigation, we have not only showed that the dimensionless flexible-base frequency indeed depends on five dimensionless quantities, but also we found that the structure-to-soil wavelength ratio, the foundation aspect ratio, and signal-to-soil wavelength ratio are the most important dimensionless parameters that control the frequency of the interaction. Lastly, in the second application, the EnKI-FEM framework is applied to investigate areas in Southern California where certain building configurations are more prone to experience detrimental SSI effects. In this study, the regional SSI assessment allowed to identify larger amplifications in period lengthening greater that 20% in the Southern California area, also localized areas, such as Long Beach and Los Angeles basin, experience radiation damping larger than 5% for the stiff-building–i.e, $T = 0.5\,[s]$. The latter applications are nothing but a proof of the unlimited range of applicability that the EnKI-FEM framework possess as long as data and a reliable ROM are available.

9.1 Limitations and major findings of the research work

During the modeling of the ROM, we assumed mostly linear elastic responses. It is important to acknowledge that responses of reinforce concrete (RC) components are governed by a complex phenomena. In particular, for a FE response simulation to be successful in predicting the actual response behavior of RC, the numerical model should be capable of capturing the following mechanism:

- Shear failure in beam-column frame members
- Bond-slip mechanism along the longitudinal and lateral reinforcements
- Buckling effects of the longitudinal reinforcement under excessive axial load
- Pinching behavior of RC frame components under cyclic loading
- Large deformation or RC beams, columns, and walls at high ductility demands

Additionally, if the aim of the FE model is to predict and simulate the response of high-fidelity SSI effects to dynamic excitations, other sources of uncertainty can take

place. Addressing properly these sources of uncertainty can decrease significantly the bias in the FE predictions versus actual building responses. For instance, the following aspects are relevant for a fully-coupled nonlinear SSI simulation:

- Energy dissipation mechanisms of the soil and structure
- Uncertainty related to the FE model parameters
- Nonlinear bonding between foundation and the surrounding soil

Note that throughout this thesis, we had generated and simulated the data from the same FE model, thus no bias in the FE model is generated. Also, because of the latter reason, uncertainty present in the FE is nonexistent. This is indeed a key point to keep in mind when parameters of real SSI problems are being identified.

The strong need of a forward model capable of simulating the response of high-fidelity SSI models to dynamic excitations led to the generation of the computer software Seismo-VLAB. The development of Seismo-VLAB allowed to create a FE model updating based on ensemble Kalman inversion. This framework resulted in the following major outcomes and findings:

(i) The EnKI-FEM framework showed to be robust and efficient when the following simplifying and idealizing assumptions are considered:

  (a) The dynamic input excitations (Ricker) are assumed to be known and noiseless (deterministic)

  (b) The effects of FE modeling uncertainties are neglected. This means that the actual SSI model is assumed to belong to the FE model class used to estimate the parameters.

(ii) The estimation of the model parameters for the ROM requires a proper number of ensembles as well as enough dynamic excitation intensity to trigger the inertial effects during the structural response.

(iii) ROMs offer the possibility of analyzing large scale simulations without loss of accuracy if they are developed using inverse problem techniques. In other words, highly accurate ROMs can be developed using data and the EnKI-FEM framework presented in this thesis.

(iv) Validation of the developed EnKI-FEM framework was performed using realistic and progressively complicated SSI configurations. The simulation time was small and single core execution was required even for models with more than 30,000 elements. Therefore, large SSI models can be identified if enough computer resources are available.

9.2 Recommendations for future research work

The recommendations for future research work are divided into two branches. The first is related to the EnKI-FEM framework itself, and they are summarized below:

(i) Successful performance of the proposed EnKI-FEM frameworks for real-world applications requires extensions of Seismo-VLAB to account for the nonlinear behavior of soil, soil liquefaction, large deformation, bonding between foundation, and the surrounding soil.

(ii) The EnKI-FEM framework should be further extended to incorporate the effects of modeling uncertainty. Such uncertainties arise essentially from:

  (a) Incorrect modeling assumptions that do not resemble the true physical conditions; this is incorrect modeling of material constitutive models, energy dissipation mechanisms, model geometry, boundary conditions, and so on.

  (b) Unmodeled physics, which are not included in the FE model; this includes non-structural components, soil liquefaction, structural nonlinear effects, and so on.

(iii) The EnKI-FEM framework should include other damaging events besides earthquakes. Depending on the importance of civil infrastructure, damaging events may include explosions, impacts, hurricanes, tsunamis, etc.

The second branch is related to extend the applications presented in this work. In particular, we highlight the following:

(i) The dimensionless flexible-base frequency mapping can be extended even further to include more complicated soil features such as non-linear material behavior of the soil or loose contact between soil and foundation. However, more dimensionless parameters may be required, generating an increase in the number of simulation cases required to span the parameter space. Future

extensions of this application may include the assessment of the dimensionless fixed-base frequency to non-uniform half space and non-linear soil behavior.

(ii) The simplified soil-structure-interaction assessment can be extended to account for several features such as soil-nonlinearity, bounding interface between the foundation and soil, and general three-dimensional buildings if the impedances for such cases are known.
Another extension along this line is to consider the building information database available in California, and to evaluate the possible seismic demand, and thus identify susceptible areas in Southern California. This analysis can potentially help to generate mitigation actions to buildings in vulnerable areas.

(iii) Finally, analytical expressions can be derived for the FIM transfer functions using different embedment ratios and angles of incidence. This analysis can be generalized even further using 3D models and including the foundation ratio as well.

9.3 Concluding remarks

Nowadays, the study of SSI is performed mostly using numerical simulations. The complex nature of simulating high-fidelity SSI problems requires a large amount of computer memory. Additionally, most of the computer software such as: OpenSEES, ABAQUS, ANSYS, and SAP do no have the minimum capabilities to handle SSI. For example, features such as PML and DRM are not present. To address this challenge, in this thesis we have developed Seismo-VLAB, a simple, fast, and extendable C++ finite element software designed to optimize meso-scale simulations of dynamic and nonlinear SSI problems. However, the computational cost of such simulations is still large. Thus, a suitable ROM was developed such that its accuracy is maximized by using data generated from the high-fidelity numerical models. The ROM created in this way will bridge the gap between simplified numerical models and data, becoming what we believe is the next generation of ROM for SSI.

BIBLIOGRAPHY

[1] Sigurd I. Aanonsen, Geir Nævdal, Dean S. Oliver, Albert C. Reynolds, and Brice Vallès. The ensemble Kalman filter in reservoir engineering–A review. *SPE Journal*, 14(03):393–412, 2009. ISSN 1086-055X. doi: 10.2118/117274-PA. URL https://doi.org/10.2118/117274-PA.

[2] José A. Abell, Nebojša Orbović, David B. McCallen, and Boris Jeremic. Earthquake soil-structure interaction of nuclear power plants, differences in response to 3-D, 3 × 1-D, and 1-D excitations. *Earthquake Engineering & Structural Dynamics*, 47(6):1478–1495, 2018. doi: 10.1002/eqe.3026. URL https://onlinelibrary.wiley.com/doi/abs/10.1002/eqe.3026.

[3] David J. Albers, Paul-Adrien Blancquart, Matthew E. Levine, Elnaz Esmaeilzadeh Seylabi, and Andrew Stuart. Ensemble Kalman methods with constraints. *Inverse Problems*, 35(9):095007, aug 2019. doi: 10.1088/1361-6420/ab1c09. URL https://doi.org/10.1088%2F1361-6420%2Fab1c09.

[4] Patrick R. Amestoy, Iain S. Duff, Jacko Koster, and Jean-Yves L'Excellent. A fully asynchronous multifrontal solver using distributed dynamic scheduling. *SIAM Journal on Matrix Analysis and Applications*, 23(1):15–41, 2001.

[5] Patrick R. Amestoy, Abdou Guermouche, Jean-Yves L'Excellent, and Stéphane Pralet. Hybrid scheduling for the parallel solution of linear systems. *Parallel Computing*, 32(2):136–156, 2006.

[6] Jeffrey L. Anderson. An ensemble adjustment Kalman filter for data assimilation. *Monthly Weather Review*, 129(12):2884–2903, 2001. doi: 10.1175/1520-0493(2001)129<2884:AEAKFF>2.0.CO;2. URL https://doi.org/10.1175/1520-0493(2001)129<2884:AEAKFF>2.0.CO;2.

[7] Luis G. Arboleda-Monsalve, Jaime A. Mercado, Vesna Terzic, and Kevin R. Mackie. Soil–structure interaction effects on seismic performance and earthquake-induced losses in tall buildings. *Journal of Geotechnical and Geoenvironmental Engineering*, 146(5):04020028, 2020. doi: 10.1061/(ASCE)GT.1943-5606.0002248. URL https://ascelibrary.org/doi/abs/10.1061/%28ASCE%29GT.1943-5606.0002248.

[8] Dominic Assimaki. *Topography effects in the 1999 Athens earthquake: Engineering issues in seismology*. PhD thesis, Massachusetts Institute of Technology, department of Civil and Environmental Engineering, 2004.

[9] Rodrigo Astroza. *Vibration-Based Health Monitoring and Mechanics-Based Nonlinear Finite Element Model Updating of Civil Structures*. PhD thesis, University of California San Diego, department of Civil and Environ-

mental Engineering, ProQuest ID: Astroza_ucsd_0033D_15048. Merritt ID: ark:/20775/bb1162204h, 2015. URL https://escholarship.org/uc/item/75r661d1.

[10] Utkarsh Ayachit. *The ParaView Guide: A Parallel Visualization Application*. Kitware, Inc., USA, 2015. ISBN 1930934300, 9781930934306.

[11] Satish Balay, William D. Gropp, Lois Curfman McInnes, and Barry F. Smith. Efficient management of parallelism in object oriented numerical software libraries. In E. Arge, A. M. Bruaset, and H. P. Langtangen, editors, *Modern Software Tools in Scientific Computing*, pages 163–202. Birkhäuser Press, 1997.

[12] Satish Balay, Shrirang Abhyankar, Mark F. Adams, Jed Brown, Peter Brune, Kris Buschelman, Lisandro Dalcin, Alp Dener, Victor Eijkhout, William D. Gropp, Dmitry Karpeyev, Dinesh Kaushik, Matthew G. Knepley, Dave A. May, Lois Curfman McInnes, Richard Tran Mills, Todd Munson, Karl Rupp, Patrick Sanan, Barry F. Smith, Stefano Zampini, Hong Zhang, and Hong Zhang. PETSc Web page. https://www.mcs.anl.gov/petsc, 2019. URL https://www.mcs.anl.gov/petsc.

[13] Satish Balay, Shrirang Abhyankar, Mark F. Adams, Jed Brown, Peter Brune, Kris Buschelman, Lisandro Dalcin, Alp Dener, Victor Eijkhout, William D. Gropp, Dmitry Karpeyev, Dinesh Kaushik, Matthew G. Knepley, Dave A. May, Lois Curfman McInnes, Richard Tran Mills, Todd Munson, Karl Rupp, Patrick Sanan, Barry F. Smith, Stefano Zampini, Hong Zhang, and Hong Zhang. PETSc users manual. Technical Report ANL-95/11 - Revision 3.12, Argonne National Laboratory, 2019. URL https://www.mcs.anl.gov/petsc.

[14] Mervyn C. C. Bampton and Roy R. Craig. Coupling of substructures for dynamic analyses. *AIAA Journal*, 6(7):1313–1319, 1968. doi: 10.2514/3.4741. URL https://doi.org/10.2514/3.4741.

[15] Ushnish Basu and Anil K. Chopra. Perfectly matched layers for time-harmonic elastodynamics of unbounded domains: theory and finite-element implementation. *Computer Methods in Applied Mechanics and Engineering*, 192(11):1337–1375, 2003. ISSN 0045-7825. doi: https://doi.org/10.1016/S0045-7825(02)00642-4. URL http://www.sciencedirect.com/science/article/pii/S0045782502006424.

[16] Klaus-Jürgen Bathe. *Finite Element Procedures*. Prentice Hall, 2006. ISBN 9780979004902. URL https://books.google.com/books?id=rWvefGICfO8C.

[17] Klaus-Jürgen Bathe. Conserving energy and momentum in nonlinear dynamics: A simple implicit time integration scheme. *Computers & Structures*, 85(7-8):437–445, April 2007. ISSN 0045-7949. doi: 10.1016/j.compstruc.

2006.09.004. URL http://dx.doi.org/10.1016/j.compstruc.2006.09.004.

[18] James L. Beck. Bayesian system identification based on probability logic. *Structural Control and Health Monitoring*, 17(7):825–847, 2010. doi: 10.1002/stc.424. URL https://onlinelibrary.wiley.com/doi/abs/10.1002/stc.424.

[19] James L. Beck and Paul C. Jennings. Structural identification using linear models and earthquake records. *Earthquake Engineering & Structural Dynamics*, 8(2):145–160, 1980. doi: 10.1002/eqe.4290080205. URL https://onlinelibrary.wiley.com/doi/abs/10.1002/eqe.4290080205.

[20] Dionisio Bernal. Viscous damping in inelastic structural response. *Journal of Structural Engineering*, 120(4):1240–1254, 1994. doi: 10.1061/(ASCE)0733-9445(1994)120:4(1240). URL https://ascelibrary.org/doi/abs/10.1061/.

[21] Jacobo Bielak. Dynamic behaviour of structures with embedded foundations. *Earthquake Engineering & Structural Dynamics*, 3(3):259–274, 1974. doi: 10.1002/eqe.4290030305. URL https://onlinelibrary.wiley.com/doi/abs/10.1002/eqe.4290030305.

[22] Jacobo Bielak and Paul Christiano. On the effective seismic input for non-linear soil-structure interaction systems. *Earthquake Engineering and Structural Dynamics*, 12:107–119, 1984.

[23] Jacobo Bielak and Paul C. Jennings. Dynamics of building-soil interaction. *Bulletin of the Seismological Society of America*, 63(1):9–48, 02 1973. ISSN 0037-1106. URL https://doi.org/.

[24] Jacobo Bielak, Kostas Loukakis, Yoshiaki Hisada, and Chiaki Yoshimura. Domain reduction method for three-dimensional earthquake modeling in localized regions, part I: theory. *Bulletin of the Seismological Society of America*, 93:817–824, 2003.

[25] Barbara Blaschke-Kaltenbacher and Heinz W. Engl. *Regularization Methods for Nonlinear Ill-Posed Problems with Applications to Phase Reconstruction*, pages 17–35. Springer Vienna, Vienna, 1997. ISBN 978-3-7091-6521-8. doi: 10.1007/978-3-7091-6521-8_3. URL https://doi.org/10.1007/978-3-7091-6521-8_3.

[26] Paolo Bocchini, Dan M. Frangopol, Thomas Ummenhofer, and Tim Zinke. Resilience and sustainability of civil infrastructure: Toward a unified approach. *Journal of Infrastructure Systems*, 20(2):04014004, 2014. doi: 10.1061/(ASCE)IS.1943-555X.0000177. URL https://ascelibrary.org/doi/abs/10.1061/%28ASCE%29IS.1943-555X.0000177.

[27] Claude Boutin and Pierre Roussillon. Assessment of the urbanization effect on seismic response. *Bulletin of the Seismological Society of America*, 94 (1):251, 2004. doi: 10.1785/0120030050. URL http://dx.doi.org/10.1785/0120030050.

[28] Carlos Brebbia and José Dominguez. *Boundary Elements An Introductory Course*. WIT Press, 1st edition, 1992.

[29] Leo Breiman. Random forests. *Machine learning*, 45(1):5–32, 2001.

[30] François Broquedis, Jérôme Clet Ortega, Stéphanie Moreaud, Nathalie Furmento, Brice Goglin, Guillaume Mercier, Samuel Thibault, and Raymond Namyst. hwloc: a Generic Framework for Managing Hardware Affinities in HPC Applications. In IEEE, editor, *PDP 2010 - The 18th Euromicro International Conference on Parallel, Distributed and Network-Based Computing*, Pisa Italie, 02 2010. URL http://www.pdp2010.org/.

[31] Edgar Buckingham. *On Physically Similar Systems; Illustrations of the Use of Dimensional Analysis*. Number 4. Physical Review, California Division of Mines and Geology, Office of Strong Motion Studies, 1914.

[32] Pacific Earthquake Engineering Research Center. *Guidelines for Performance-based Seismic Design of Tall Buildings*. FEMA, 2017. URL https://books.google.com/books?id=hNnhswEACAAJ.

[33] Minwoo Chang and Shamim N. Pakzad. Optimal sensor placement for modal identification of bridge systems considering number of sensing nodes. *Journal of Bridge Engineering*, 19(6):04014019, 2014. doi: 10.1061/(ASCE)BE.1943-5592.0000594. URL https://ascelibrary.org/doi/abs/10.1061/%28ASCE%29BE.1943-5592.0000594.

[34] Stephanie E. Chang and Masanobu Shinozuka. Measuring improvements in the disaster resilience of communities. *Earthquake Spectra*, 20(3):739–755, 2004. doi: 10.1193/1.1775796. URL https://doi.org/10.1193/1.1775796.

[35] Lyndon Clarke, Ian Glendinning, and Rolf Hempel. The MPI message passing interface standard. In Karsten M. Decker and René M. Rehmann, editors, *Programming Environments for Massively Parallel Distributed Systems*, pages 213–218, Basel, 1994. Birkhäuser Basel. ISBN 978-3-0348-8534-8.

[36] Didier Clouteau and Denis Aubry. Modifications of the ground motion in dense urban areas. *Journal of Computational Acoustics*, 09(04):1659–1675, 2001. doi: 10.1142/S0218396X01001509. URL https://doi.org/10.1142/S0218396X01001509.

[37] Computers and Structures Inc. ETABS: Extended three dimensional analysis of building system, . URL https://www.csiamerica.com/products/etabs.

[38] Computers and Structures Inc. PERFORM3D: Nonlinear analysis and performance assesment for 3D structures, . URL https://www.csiamerica.com/products/perform-3d.

[39] Computers and Structures Inc. SAP2000: Integrated software for structural analysis and design, . URL https://www.csiamerica.com/products/sap2000.

[40] Riccardo Conti, Marco Morigi, and Giulia MB Viggiani. Filtering effect induced by rigid massless embedded foundations. *Bulletin of Earthquake Engineering*, 15(3):1019–1035, 2017.

[41] Riccardo Conti, Marco Morigi, Emmanouil Rovithis, Nikos Theodoulidis, and Christos Karakostas. Filtering action of embedded massive foundations: New analytical expressions and evidence from 2 instrumented buildings. *Earthquake Engineering & Structural Dynamics*, 47(5):1229–1249, 2018. doi: 10.1002/eqe.3014. URL https://onlinelibrary.wiley.com/doi/abs/10.1002/eqe.3014.

[42] Robert D. Cook, David S. Malkus, Michael E. Plesha, and Robert J. Witt. *Concepts and Applications of Finite Element Analysis*. John Wiley; Sons, Inc., USA, 2007. ISBN 0470088214.

[43] Roy R. Craig. A Brief Tutorial on Substructure Analysis and Testing. In *Proceedings of IMAC-XVIII: A Conference on Structural Dynamics*, volume 4062, page 899, January 2000.

[44] Leonardo Dagum and Ramesh Menon. OpenMP: An industry-standard api for shared-memory programming. *IEEE Computing in Science & Engineering*, 5(1):46–55, January 1998. ISSN 1070-9924. doi: 10.1109/99.660313. URL https://doi.org/10.1109/99.660313.

[45] James W Daniel. The conjugate gradient method for linear and nonlinear operator equations. *SIAM Journal on Numerical Analysis*, 4(1):10–26, 1967.

[46] Gabriel DeSalvo and Robert W Gorman. *ANSYS engineering analysis system user's manual: For ANSYS Revision 4.4*. Swanson Analysis Systems, 1989.

[47] Yves Dubois-Pe'lerin and Thomas Zimmermann. Object-oriented finite element programming: III. An efficient implementation in C++. *Computer Methods in Applied Mechanics and Engineering*, 108(1):165 – 183, 1993. ISSN 0045-7825. doi: https://doi.org/10.1016/0045-7825(93)90159-U. URL http://www.sciencedirect.com/science/article/pii/004578259390159U.

[48] Hamed Ebrahimian. *Nonlinear Finite Element Model Updating for Non-Linear System and Damage Identification of Civil Structures*. PhD thesis, University of California San Diego, department of Civil and Environmental Engineering, ProQuest ID: Ebrahimian_ucsd_0033D_15191. Merritt

ID: ark:/13030/m5c56qf9, 2015. URL https://escholarship.org/uc/item/62r7p58r.

[49] Geir Evensen. Sequential data assimilation with a nonlinear quasi-geostrophic model using Monte Carlo methods to forecast error statistics. *Journal of Geophysical Research: Oceans*, 99(C5):10143–10162, 1994. doi: 10.1029/94JC00572. URL https://agupubs.onlinelibrary.wiley.com/doi/abs/10.1029/94JC00572.

[50] Geir Evensen. *Data Assimilation: The Ensemble Kalman Filter*. Springer-Verlag, Berlin, Heidelberg, 2006. ISBN 354038300X.

[51] Arash Fathi, Babak Poursartip, and Loukas F. Kallivokas. Time-domain hybrid formulations for wave simulations in three-dimensional PML-truncated heterogeneous media. *International Journal for Numerical Methods in Engineering*, 101(3):165–198, 2015. doi: 10.1002/nme.4780. URL https://onlinelibrary.wiley.com/doi/abs/10.1002/nme.4780.

[52] Khaled Fawagreh, Mohamed Medhat Gaber, and Eyad Elyan. Random forests: From early developments to recent advancements. *Systems Science & Control Engineering*, 2(1):602–609, 2014.

[53] Bruce W. R. Forde, Ricardo O. Foschi, and Siegfried F. Stiemer. Object-oriented finite element analysis. *Computers & Structures*, 34(3):355–374, 1990.

[54] Edgar Gabriel, Graham E. Fagg, George Bosilca, Thara Angskun, Jack J. Dongarra, Jeffrey M. Squyres, Vishal Sahay, Prabhanjan Kambadur, Brian Barrett, Andrew Lumsdaine, Ralph H. Castain, David J. Daniel, Richard L. Graham, and Timothy S. Woodall. Open MPI: Goals, concept, and design of a next generation MPI implementation. In *Proceedings, 11th European PVM/MPI Users' Group Meeting*, pages 97–104, Budapest, Hungary, September 2004.

[55] Joaquin Garcia-Suarez, Danilo S. Kusanovic, and Domniki Asimaki. Dimensional analysis: Overview and applications to problems of soil-structure interaction, Nov 2019. URL engrxiv.org/m3ycp.

[56] George Gazetas. *Foundation Vibrations*, pages 553–593. January 1991. ISBN 978-1-4613-6752-9. doi: 10.1007/978-1-4615-3928-5_15.

[57] Michael J. Givens, George Mylonakis, and Jonathan P. Stewart. Modular analytical solutions for foundation damping in soil-structure interaction applications. *Earthquake Spectra*, 32(3):1749–1768, 2016. doi: 10.1193/071115EQS112M. URL https://doi.org/10.1193/071115EQS112M.

[58] Karl F. Graff. *Wave Motion in Elastic Solids*. Dover books on Physics. Dover, New York, NY, 1991. URL http://cds.cern.ch/record/2019221.

[59] Philippe Guéguen, Pierre-Yves Bard, and Francisco J. Chávez-García. Site-city seismic interaction in Mexico City–like environments: An analytical study. *Bulletin of the Seismological Society of America*, 92(2):794, 2002. doi: 10.1785/0120000306. URL http://dx.doi.org/10.1785/0120000306.

[60] Gaël Guennebaud, Benoît Jacob, et al. Eigen's user manual (v3). http://eigen.tuxfamily.org, 2010.

[61] Robert J. Guyan. Reduction of stiffness and mass matrices. *AIAA Journal*, 3(2):380–380, 1965. doi: 10.2514/3.2874. URL https://doi.org/10.2514/3.2874.

[62] Hamid Haddadi, Christopher Stephen, Anthony Shakal, Moh Huang, D. Oppenheimer, William Savage, William Leith, and John Parrish. Center for engineering strong-motion data (CESMD). In *The 14^{t}h World Conference on Earthquake Engineering*, October 2008. URL https://www.strongmotioncenter.org/.

[63] John F. Hall. Problems encountered from the use (or misuse) of Rayleigh damping. *Earthquake Engineering & Structural Dynamics*, 35(5):525–545, 2006. doi: 10.1002/eqe.541. URL https://onlinelibrary.wiley.com/doi/abs/10.1002/eqe.541.

[64] Norman A. Haskell. Radiation pattern of surface waves from point sources in a multi-layered medium. *Bulletin of the Seismological Society of America*, 54(1):377–393, 1964.

[65] François M. Hemez and Scott W. Deobling. Review and assessment of model updating for non-linear, transient dynamics. *Mechanical Systems and Signal Processing*, 15(1):45 – 74, 2001. ISSN 0888-3270. doi: https://doi.org/10.1006/mssp.2000.1351. URL http://www.sciencedirect.com/science/article/pii/S0888327000913517.

[66] David Hibbett, Bengt Karlsson, and Paul Sorensen. *ABAQUS/standard: User's Manual*, volume 1. Hibbitt, Karlsson & Sorensen, 1998.

[67] Yoshiaki Hisada. An efficient method for computing green's functions for a layered half-space with sources and receivers at close depths. *Bulletin of Seismological Society of America*, 84:1456–1472, 1994.

[68] Masaru Hoshiya and Etsuro Saito. Structural identification by extended Kalman filter. *Journal of Engineering Mechanics*, 110 (12):1757–1770, 1984. doi: 10.1061/(ASCE)0733-9399(1984)110:12(1757). URL https://ascelibrary.org/doi/abs/10.1061/%28ASCE%290733-9399%281984%29110%3A12%281757%29.

[69] Guoquan P. Huang, Anastasios I. Mourikis, and Stergios I. Roumeliotis. Analysis and improvement of the consistency of extended kalman filter based

SLAM. In *2008 IEEE International Conference on Robotics and Automation*, pages 473–479, May 2008. doi: 10.1109/ROBOT.2008.4543252.

[70] Thomas J. R. Hughes. *The Finite Element Method: Linear Static and Dynamic Finite Element Analysis*. Dover Civil and Mechanical Engineering. Dover Publications, 2012. ISBN 9780486135021. URL https://books.google.com/books?id=cHH2n_qBK0IC.

[71] Joshua Hursey, Ethan Mallove, Jeffrey M. Squyres, and Andrew Lumsdaine. An extensible framework for distributed testing of mpi implementations. In *Proceedings, Euro PVM/MPI*, Paris, France, October 2007.

[72] Marco A. Iglesias, Kody J. H. Law, and Andrew M. Stuart. Ensemble Kalman methods for inverse problems. *Inverse Problems*, 29(4):045001, March 2013. doi: 10.1088/0266-5611/29/4/045001. URL https://doi.org/10.1088%2F0266-5611%2F29%2F4%2F045001.

[73] Bruce Irons. Structural eigenvalue problems - elimination of unwanted variables. *AIAA Journal*, 3(5):961–962, 1965. doi: 10.2514/3.3027. URL https://doi.org/10.2514/3.3027.

[74] Lydik S. Jacobsen. *Steady force vibration as influenced by damping*, volume 52. American Society of Mechanical Engineers, 1930.

[75] Lin Jeen-Shang and Zhang Yigong. Nonlinear structural identification using extended kalman filter. *Computers & Structures*, 52(4):757 – 764, 1994. ISSN 0045-7949. doi: https://doi.org/10.1016/0045-7949(94)90357-3. URL http://www.sciencedirect.com/science/article/pii/0045794994903573.

[76] Hector A. Jensen and Danilo S. Kusanovic. On the effect of near-field excitations on the reliability-based performance and design of base-isolated structures. *Probabilistic Engineering Mechanics*, 36:28 – 44, 2014. ISSN 0266-8920. doi: https://doi.org/10.1016/j.probengmech.2014.03.003. URL http://www.sciencedirect.com/science/article/pii/S0266892014000174.

[77] Hector A. Jensen, Marcos A. Valdebenito, Gerhart I. Schuëller, and Danilo S. Kusanovic. Reliability-based optimization of stochastic systems using line search. *Computer Methods in Applied Mechanics and Engineering*, 198 (49):3915 – 3924, 2009. ISSN 0045-7825. doi: https://doi.org/10.1016/j.cma.2009.08.016. URL http://www.sciencedirect.com/science/article/pii/S0045782509002710.

[78] Hector A. Jensen, Eduardo Millas, Danilo S. Kusanovic, and Costas Papadimitriou. Model-reduction techniques for bayesian finite element model updating using dynamic response data. *Computer Methods in Applied Mechanics and Engineering*, 279:301 – 324, 2014. ISSN 0045-7825. doi: https:

//doi.org/10.1016/j.cma.2014.06.032. URL http://www.sciencedirect.com/science/article/pii/S0045782514002187.

[79] Chang-Gyun Jeong. Verification of seismic motion input into the finite element models. Master's thesis, University of California, Davis, 2013.

[80] Boris Jeremić, Guanzhou Jie, Matthias Preisig, and Nima Tafazzoli. Time domain simulation of soil–foundation–structure interaction in non-uniform soils. *Earthquake Engineering & Structural Dynamics*, 38(5):699–718, 2009. doi: 10.1002/eqe.896. URL https://onlinelibrary.wiley.com/doi/abs/10.1002/eqe.896.

[81] Abdul J. Jerri. The Shannon sampling theorem–its various extensions and applications: A tutorial review. *Proceedings of the IEEE*, 65(11):1565–1596, Nov 1977. ISSN 0018-9219. doi: 10.1109/PROC.1977.10771.

[82] Simon J. Julier and Jeffrey K. Uhlmann. Unscented filtering and nonlinear estimation. In *Proceedings of the IEEE*, pages 401–422, 2004.

[83] Rudolf E. Kalman. On the general theory of control systems. *IRE Transactions on Automatic Control*, 4(3):491–502, December 1959. doi: 10.1109/tac.1959.1104873. URL https://doi.org/10.1109%2Ftac.1959.1104873.

[84] Rudolf E. Kalman. Contributions to the theory of optimal control. *Boletiń de la Sociedad Matemática Mexicana*, 5:102–119, 1960.

[85] Anna Karatzetzou, Evi Riga, and Kyriazis Pitilakis. Soil structure interaction effects at urban scale. In *The 16^{t}h European conference on Earthquake Engineering*, June 2018. URL https://www.strongmotioncenter.org/.

[86] George Karypis and Vipin Kumar. METIS – unstructured graph partitioning and sparse matrix ordering system, version 2.0. Technical report, University of Minnesota, Department of Computer Science & Engineering, 1995.

[87] Lambros S. Katafygiotis and James L. Beck. Updating models and their uncertainties. I: Bayesian statistical framework. *Journal of Engineering Mechanics*, 124(4):455–461, 1998. doi: 10.1061/(ASCE)0733-9399(1998)124:4(455). URL https://ascelibrary.org/doi/abs/10.1061/%28ASCE%290733-9399%281998%29124%3A4%28455%29.

[88] Lambros S. Katafygiotis and James L. Beck. Updating models and their uncertainties. II: Model identifiability. *Journal of Engineering Mechanics*, 124(4):463–467, 1998. doi: 10.1061/(ASCE)0733-9399(1998)124:4(463). URL https://ascelibrary.org/doi/abs/10.1061/%28ASCE%290733-9399%281998%29124%3A4%28463%29.

[89] Bence Kato and Gang Wang. *Ground Motion Simulation in an Urban Environment Considering Site-City Interaction: A Case Study of Kowloon Station, Hong Kong*. 08 2017.

[90] John T. Katsikadelis. *Boundary Elements: Theory and Applications*. Elsevier Science Ltd, Oxford, 2002. ISBN 978-0-08-044107-8. doi: https://doi.org/10.1016/B978-008044107-8/50003-1. URL http://www.sciencedirect.com/science/article/pii/B9780080441078500031.

[91] Marc Kham, Jean-François Semblat, Pierre-Yves Bard, and Patrick Dangla. Seismic site-city interaction: Main governing phenomena through simplified numerical models. *Bulletin of the Seismological Society of America*, 96(5): 1934, 2006. doi: 10.1785/0120050143. URL http://dx.doi.org/10.1785/0120050143.

[92] Chan G. Koh and Lin M. See. Identification and uncertainty estimation of structural parameters. *Journal of Engineering Mechanics*, 120(6):1219–1236, 1994.

[93] Ivan Kraus and D Džakić. Soil-structure interaction effects on seismic behaviour of reinforced concrete frames. pages 1–8. SE-50EEE, Skopje, Makedonija, April 2013.

[94] Sezgin Kucukcoban and Loukas F. Kallivokas. Mixed perfectly-matched-layers for direct transient analysis in 2d elastic heterogeneous media. *Computer Methods in Applied Mechanics and Engineering*, 200(1):57 – 76, 2011. ISSN 0045-7825. doi: https://doi.org/10.1016/j.cma.2010.07.013. URL http://www.sciencedirect.com/science/article/pii/S0045782510002252.

[95] Sezgin Kucukcoban and Loukas F. Kallivokas. A symmetric hybrid formulation for transient wave simulations in PML-truncated heterogeneous media. *Wave Motion*, 50(1):57–79, 2013.

[96] Danilo S. Kusanovic, Elnaz Seylabi, and Domniki Asimaki. Seismo-VLAB: An open-source finite element software for meso-scale simulations. *To be submitted to The Journal of Open Source Software*, 2020.

[97] Danilo S. Kusanovic, Elnaz Seylabi, Albert Kottke, and Domniki Asimaki. Seismo-VLAB: A parallel, object-oriented virtual lab for mesoscale wave propagation problems. In *The USSD Conference and Exhibition*, pages 97–104, Denver, USA, April 2020.

[98] Danilo S. Kusanovic, Elnaz Seylabi, Albert Kottke, and Domniki Asimaki. Seismo-VLAB: A parallel object-oriented platform for reliable nonlinear seismic wave propagation and soil-structure interaction simulation. *To be submitted to Computers and Geotechnics*, 2020.

[99] Danilo S. Kusanovic, Elnaz E. Seylabi, and Domniki Asimaki. Optimal implementation of frequency domain impedances in time domain simulations of building structures on embedded foundations, Feb 2020. URL engrxiv.org/fyw82.

[100] Henry Louis Langhaar. *Dimensional Analysis and Theory of Models*, volume 2. Wiley New York, 1951.

[101] Giovanni Lanzano, Emilio Bilotta, Gianpiero Russo, Francesco Silvestri, and SP Gopal Madabhushi. Centrifuge modeling of seismic loading on tunnels in sand. *Geotechnical Testing Journal*, 35(6):854–869, 2012.

[102] Kody Law, Andrew Stuart, and Konstantinos Zygalakis. *Data Assimilation: A Mathematical Introduction*. Texts in Applied Mathematics. Springer International Publishing, 2016. ISBN 9783319366876.

[103] LS-DYNA. LS-DYNA user's manual. *LS-DYNA, Livermore Software Technology Corporation, Livermore, CA, USA*, 4, 2013.

[104] Enrique J. Luco and Robert A. Westmann. Dynamic response of circular footings. *Journal of the Soil Mechanics and Foundations Division*, 97(4): 1381–1395, 1971.

[105] Enrique J. Luco and Robert A. Westmann. Dynamic response of a rigid footing bonded to an elastic half space. *Journal of Applied Mechanics*, 39 (4):527–534, 1972.

[106] John Lysmer, Roger L. Kuhlemeyer, Institute of Transportation Engineering., Traffic, Berkeley University of California, Soil Mechanics Laboratory., Bituminous Materials Research, and Geotechnical Engineering Group. *Finite dynamic model for infinite media*. Dept. of Civil Engineering, Univ. of California, Institute of Transportation and Traffic Engineering, Soil Mechanics Laboratory, Berkeley, Califiifornia, 1969.

[107] Jaroslav Mackerle. Object-oriented programming in fem and bem: A bibliography (1990-2003). *Advanced Engineering Software*, 35(6):325–336, June 2004. ISSN 0965-9978. doi: 10.1016/j.advengsoft.2004.04.006. URL http://dx.doi.org/10.1016/j.advengsoft.2004.04.006.

[108] Steffen Marburg. Six elements per wavelength: Is that enough? *Journal of Computational Acoustics*, 10(01):25–51, 2002. doi: 10.1142/S0218396X02001401. URL https://doi.org/10.1142/S0218396X02001401.

[109] MATLAB. *User's manual version 7.10.0 (R2010a)*. The MathWorks Inc., Natick, Massachusetts, 2010.

[110] MATLAB. *User's manual version 9.7 (R2019b)*. The MathWorks Inc., Natick, Massachusetts, 2018.

[111] Caleb W. McCormick. Msc/nastran user's manual. *MSR-39, The MacNeal Schwendler Corporation, Los Angeles, California*, 1981.

[112] F. McKenna. Opensees: A framework for earthquake engineering simulation. *Computing in Science Engineering*, 13(4):58–66, July 2011. ISSN 1558-366X. doi: 10.1109/MCSE.2011.66.

[113] Frank McKenna and Gregory L. Fenves. *An Object-Oriented Software Design for Parallel Structural Analysis*, pages 1–8. 2001. doi: 10.1061/40492(2000)30. URL https://ascelibrary.org/doi/abs/10.1061/40492%282000%2930.

[114] Frank McKenna, Gregory L. Fenves, Michael H. Scott, et al. Open system for earthquake engineering simulation. *University of California, Berkeley, CA*, 2000.

[115] Michele Meo and Giuseppe Zumpano. On the optimal sensor placement techniques for a bridge structure. *Engineering Structures*, 27:1488–1497, 8 2005. ISSN 0141-0296.

[116] George Mynolakis and George Gazetas. Seismic soil-structure interaction: Beneficial or detrimental? *Journal of Earthquake Engineering*, 4(3):277–301, 2000. doi: 10.1080/13632460009350372. URL https://doi.org/10.1080/13632460009350372.

[117] Nathan Mortimore Newmark et al. A method of computation for structural dynamics. American Society of Civil Engineers, 1959.

[118] Dean S. Oliver, Albert C. Reynolds, and Ning Liu. *Inverse Theory for Petroleum Reservoir Characterization and History Matching*. Cambridge University Press, 2008. doi: 10.1017/CBO9780511535642.

[119] Artur Pais and Eduardo Kausel. Approximate formulas for dynamic stiffnesses of rigid foundations. *Soil Dynamics and Earthquake Engineering*, 7 (4):213 – 227, 1988. ISSN 0267-7261. doi: https://doi.org/10.1016/S0267-7261(88)80005-8. URL http://www.sciencedirect.com/science/article/pii/S0267726188800058.

[120] Richard A. Parmelee, Seng-Lip Lee, and David S. Perelman. Seismic response of multiple-story structures on flexible foundations. *Bulletin of the Seismological Society of America*, 59(3):1061–1070, Jun 1969. ISSN 0037-1106. URL https://doi.org/.

[121] Fabian Pedregosa, Gaël Varoquaux, Alexandre Gramfort, Vincent Michel, Bertrand Thirion, Olivier Grisel, and et al Blondel, Mathieu. Scikit-learn: Machine learning in python. *Journal of Machine Learning Research*, 12: 2825–2830, 2011.

[122] Babak. Poursartip. *Topographic amplification of seismic motion*. University of Texas at Austin, ProQuest ID, 2017.

[123] Alfio Quarteroni, Riccardo Sacco, and Fausto Saleri. *Numerical Mathematics (Texts in Applied Mathematics)*. Springer-Verlag, Berlin, Heidelberg, 2006. ISBN 3540346589.

[124] Norman Ricker. The computation of output disturbances from amplifiers for true wavelet inputs. *Geophysics*, 10, 01 1945. doi: 10.1190/1.1437162.

[125] Anestis S. Veletsos and Damodaran V. Nair. Seismic interaction of structures on hysteretic foundations. *ASCE Journal of the Structural Division*, 101: 109–129, 01 1975.

[126] Logan Schwan, Claude Boutin, L.A. Padrón, Matthew S. Dietz, Pierre-Yves Bard, and Colin Taylor. Site-city interaction: Theoretical, numerical and experimental crossed-analysis. *Geophysical Journal International*, 205(2): 1006–1031, 2016. doi: 10.1093/gji/ggw049. URL http://dx.doi.org/10.1093/gji/ggw049.

[127] Michael H. Scott and Gregory L. Fenves. Plastic hinge integration methods for force-based beam–column elements. *Journal of Structural Engineering*, 132(2):244–252, 2006.

[128] U.D.H. Security and Federal Emergency Management Agency. *Improvement of Nonlinear Static Seismic Analysis Procedures: Fema 440*. Createspace Independent Pub, 2013. ISBN 9781484019436. URL https://books.google.com/books?id=jAimngEACAAJ.

[129] Jean-François Semblat, Marc Kham, and Pierre-Yves Bard. Seismic-wave propagation in alluvial basins and influence of site-city interaction. *Bulletin of the Seismological Society of America*, 98(6):2665, 2008. doi: 10.1785/0120080093. URL http://dx.doi.org/10.1785/0120080093.

[130] Julian Seward, Nicholas Nethercote, and Josef Weidendorfer. *Valgrind 3.3 - Advanced Debugging and Profiling for GNU/Linux Applications*. Network Theory Ltd., 2008. ISBN 0954612051.

[131] Elnaz E. Seylabi, Chanseok Jeong, and Ertugrul Taciroglu. On numerical computation of impedance functions for rigid soil-structure interfaces embedded in heterogeneous half-spaces. *Computers and Geotechnics*, 72:15 – 27, 2016. ISSN 0266-352X. doi: https://doi.org/10.1016/j.compgeo.2015.11.001. URL http://www.sciencedirect.com/science/article/pii/S0266352X15002189.

[132] Elnaz Esmaeilzadeh Seylabi. *Reduced order modeling of soil structure interaction problems*. UCLA, ProQuest ID, 2016.

[133] Valeria Simoncini and Daniel B. Szyld. Flexible inner-outer Krylov subspace methods. *SIAM Journal on Numerical Analysis*, 40(6):2219–2239, 2002.

[134] Valeria Simoncini and Daniel B. Szyld. Recent computational developments in Krylov subspace methods for linear systems. *Numerical Linear Algebra with Applications*, 14(1):1–59, 2007.

[135] Andrew W. Smyth, Sami F. Masri, Anastasios G. Chassiakos, and Thomas K. Caughey. On-line parametric identification of MDOF nonlinear hysteretic systems. *Journal of Engineering Mechanics*, 125(2):133–142, 1999. doi: 10.1061/(ASCE)0733-9399(1999)125:2(133).

[136] Enrico Spacone, Filip C. Filippou, and Fabio F. Taucer. Fibre beam–column model for non-linear analysis of r/c frames: Part II. Applications. *Earthquake Engineering & Structural Dynamics*, 25(7):727–742, 1996. doi: 10.1002/(SICI)1096-9845(199607)25:7<727::AID-EQE577>3.0.CO;2-O. URL https://onlinelibrary.wiley.com/doi/abs/10.1002/%28SICI%291096-9845%28199607%2925%3A7%3C727%3A%3AAID-EQE577%3E3.0.CO%3B2-O.

[137] Alexander Stepanov and Meng Lee. *The standard template library*, volume 1501. Hewlett Packard Laboratories 1501 Page Mill Road, Palo Alto, CA 94304, 1995.

[138] Jonathan Stewart, C.B. Crouse, Tara C. Hutchinson, Bret Lizundia, Farzad Naeim, and Farhang Ostadan. Soil-structure interaction for building structures. *Grant/Contract Reports (NISTGCR) - 12-917-21.*, National Institute of Standards and Technology, U.S. Department of Commerce: Gaithersburg, MD. (13-09-2012), 2012.

[139] Jonathan P. Stewart, Gregory L. Fenves, and Raymond B. Seed. Seismic soil-structure interaction in buildings. I: Analytical methods. *Journal of Geotechnical and Geoenvironmental Engineering*, 125(1):26–37, 1999. doi: 10.1061/(ASCE)1090-0241(1999)125:1(26). URL https://ascelibrary.org/doi/abs/10.1061/%28ASCE%291090-0241%281999%29125%3A1%2826%29.

[140] Jonathan P. Stewart, Raymond B. Seed, and Gregory L. Fenves. Seismic soil-structure interaction in buildings. II: Empirical findings. *Journal of Geotechnical and Geoenvironmental Engineering*, 125(1):38–48, 1999. doi: 10.1061/(ASCE)1090-0241(1999)125:1(38). URL https://ascelibrary.org/doi/abs/10.1061/%28ASCE%291090-0241%281999%29125%3A1%2838%29.

[141] Gilbert Strang and George J. Fix. *An analysis of the finite element method*, volume 212. Prentice-hall Englewood Cliffs, NJ, 1973.

[142] John C. Strikwerda. *Finite Difference Schemes and Partial Differential Equations*. Wadsworth Publ. Co., Belmont, CA, USA, 1989. ISBN 0-534-09984-X.

[143] Bjarne Stroustrup. *The C++ Programming Language*. Addison-Wesley Professional, 4th edition, 2013. ISBN 0321563840, 9780321563842.

[144] Ricardo Taborda and Jacobo Bielak. Large-scale earthquake simulation: Computational seismology and complex engineering systems. *Computing in Science Engineering*, 13(4):14–27, July 2011. doi: 10.1109/MCSE.2011.19.

[145] Ricardo Taborda and Jacobo Bielak. Ground-motion simulation and validation of the 2008 chino hills, california, earthquake. *Bulletin of the Seismological Society of America*, 103(1):131, 2013. doi: 10.1785/0120110325. URL http://dx.doi.org/10.1785/0120110325.

[146] Ricardo Taborda and Jacobo Bielak. Ground-motion simulation and validation of the 2008 chino hills, california, earthquake using different velocity models. *Bulletin of the Seismological Society of America*, 104(4): 1876–1898, 07 2014. ISSN 0037-1106. doi: 10.1785/0120130266. URL https://doi.org/10.1785/0120130266.

[147] Fabio Taucer, Enrico Spacone, and Filip C Filippou. *A fiber beam-column element for seismic response analysis of reinforced concrete structures*. University of California at Berkeley, 1991.

[148] James William Thomas. *Numerical partial differential equations: finite difference methods*, volume 22. Springer Science & Business Media, 2013.

[149] Romeo Tomeo, Antonio Bilotta, Dimitris Pitilakis, and Emidio Nigro. Soil-structure interaction effects on the seismic performances of reinforced concrete moment resisting frames. *Procedia Engineering*, 199:230 – 235, 2017. ISSN 1877-7058. doi: https://doi.org/10.1016/j.proeng.2017.09.006. URL http://www.sciencedirect.com/science/article/pii/S1877705817333969. X International Conference on Structural Dynamics, EURODYN 2017.

[150] Rabin Tuladhar, Takeshi Maki, and Hiroshi Mutsuyoshi. Cyclic behavior of laterally loaded concrete piles embedded into cohesive soil. *Earthquake Engineering & Structural Dynamics*, 37(1):43–59, 2008.

[151] Gwendolyn W. van der Linden, Abbas Emami-Naeini, Robert L. Kosut, H. Sedarat, and Jerome P. Lynch. Optimal sensor placement for health monitoring of civil structures. In *Proceedings of the 2011 American Control Conference*, pages 3116–3121, June 2011. doi: 10.1109/ACC.2011.5991121.

[152] Guido Van Rossum and Fred L. Drake. *Python 3 Reference Manual*. CreateSpace, Paramount, CA, 2009. ISBN 1441412697, 9781441412690.

[153] Polynikis Vazouras, Spyros A. Karamanos, and Panos Dakoulas. Finite element analysis of buried steel pipelines under strike-slip fault displacements. *Soil Dynamics and Earthquake Engineering*, 30(11):1361–1376, 2010.

[154] Anestis S. Veletsos and Jethro W. Meek. Dynamic behaviour of building-foundation systems. *Earthquake Engineering & Structural Dynamics*, 3 (2):121–138, 1974. doi: 10.1002/eqe.4290030203. URL https://onlinelibrary.wiley.com/doi/abs/10.1002/eqe.4290030203.

[155] Chang Y. Wang and Robert B. Herrmann. A Numerical Study Of P-, SV-, And SH-Wave Generation In A Plane Layered Medium. *Bulletin of the Seismological Society of America*, 70(4):1015–1036, 1980.

[156] Armand Wirgin and Pierre-Yves Bard. Effects of buildings on the duration and amplitude of ground motion in Mexico City. *Bulletin of the Seismological Society of America*, 86(3):914, 1996. URL http://dx.doi.org/.

[157] John P. Wolf. *Dynamic soil-structure interaction*. Prentice-Hall international series in civil engineering and engineering mechanics. Prentice-Hall, 1985. ISBN 9780132215657. URL https://books.google.com/books?id=0ORRAAAAMAAJ.

[158] John P. Wolf. Soil-structure-interaction analysis in time domain. *Nuclear Engineering and Design*, 111(3):381 – 393, 1989. ISSN 0029-5493. doi: https://doi.org/10.1016/0029-5493(89)90249-5. URL http://www.sciencedirect.com/science/article/pii/0029549389902495.

[159] John P. Wolf and Pius Obernhuber. Non-linear soil-structure-interaction analysis using dynamic stiffness or flexibility of soil in the time domain. *Earthquake Engineering & Structural Dynamics*, 13(2):195–212, 1985. doi: 10.1002/eqe.4290130205. URL https://onlinelibrary.wiley.com/doi/abs/10.1002/eqe.4290130205.

[160] Wenyang Zhang, Elnaz E. Seylabi, and Ertugrul Taciroglu. An ABAQUS toolbox for soil-structure interaction analysis. *Computers and Geotechnics*, 114:103143, 2019. ISSN 0266-352X. doi: https://doi.org/10.1016/j.compgeo.2019.103143. URL http://www.sciencedirect.com/science/article/pii/S0266352X19302071.

[161] Lupei Zhu and Luis A. Rivera. A note on the dynamic and static displacements from a point source in multilayered media. *Geophysical Journal International*, 148(3):619–627, 2002.

INDEX

A

Absorbing Boundary Condition, 40, 48

Assembly Operator, 19

B

Background Problem, 37

Berkeley earthquake, 121, 134

Body force, 16

Building Model

- Dimensionless flexible-base frequency, 110
- First modal parameters, 110, 129
- Southern California, 129

C

Cauchy Stress Theorem, 53

Chino-Hills earthquake, 121, 134

Class Files

- Algorithm definition, 20
- Assembler definition, 19
- Element definition, 18
- Integrator definition, 20
- LinearSystem definition, 20
- Load definition, 14
- Material definition, 15
- Node definition, 14
- QuadratureRule definition, 18

Continuum Form for Perfectly Matched Layer, 40

Courant-Friedrichs-Lewy condition, 60

D

Dimensional Analysis

- Dimensionless group, 102
- Dimensionless group correlation, 116
- Dimensionless group definition, 100
- Pearson's correlation, 117
- Physical parameters, 100

Direct Modeling Method

Absorbing boundaries conditions, 109, 130
Courant-Friedrichs-Lewy condition, 60, 130
Domain reduction method, 130
Problem definition, 108, 128
Divergence Theorem, 55
Domain Decomposition, 24
Domain Reduction Method
Application example, 46
Background model, 37
Effective force, 39
Equation of motion, 39
Formulation using perfectly matched layer, 43
Problem definition, 36

E

Earthquake
Berkeley, 121, 134
Chino-Hills, 121, 134
Northridge, 121, 134
Eigen c++ Template library, 24
EnKI-FEM Framework for Soil-Structure Interaction Problem, 89
Ensemble Kalman Inversion
Algorithm stopping criteria, 89, 114, 133
Artificial data, 86
Augmented states, 86
Covariance matrix, 87, 114
Invariant subspace property, 90
Kalman gain, 86
Observation vector, 85
Particle mean, 87, 114
Particle update, 87, 113, 133
Problem definition, 85, 113, 132
Sequential algorithm, 87
Equation Of Motion
Domain reduction method, 39
Fixed base building, 71
Hybrid formulation for wave propagation, 45
Soil-structure interaction, 74
Error definition, 78, 118

Example
Absorbing boundary condition, 48
Domain reduction method, 46
EnKI-FEM applied to SSI, 94
EnKI-FEM framework performance, 91
Reduced order model validation, 78
Seismo-VLAB's scalability, 29
Soil-structure interaction of building, 61

F

Finite Element Analysis
Applied forces, 13
Displacement field, 13
Element force vector, 18
Element mass matrix, 18
Element stiffness matrix, 18
Equilibrium equations, 15
Force vector, 16
Isoparametric elements, 16
Mass matrix, 15
Material constitutive law, 13
Numerical integration, 18
Principle of virtual work, 14
Problem definition, 12
Spatial discretization, 59
Stiffness matrix, 15
Strain vector, 13
Stress vector, 13
Temporal discretization, 59
Flexible-Base Frequency
Dimensionless frequency mapping, 114
Random forest, 114
Soil impedance algorithm, 117
Test distribution, 115
Time history performance, 120, 122, 123, 135
Training distribution, 115
Foundation Damping Matrix, 69
Foundation Input Motion
Method of analysis, 107

Normalized soil functions, 107
Transfer functions definition, 106
Foundation Stiffness Matrix, 69

G

Guyan Reduction, 70, 71

H

Hooke's Law, 53
Hybrid formulation for wave propagation
Equation of motion, 45
External force vector, 46
Semi-discrete form, 45
The governing equation, 44

I

Improvement Factor, 119
Isoparametric Transformation, 17

J

Jacobian Matrix, 17

K

Kinematic Constraint
Enforce rigid diaphragm behavior, 58
Solid to structural element connection, 58

L

Lax-Milgram Theorem, 56
Load Imbalance, 24

M

Memory Leaks, 29
Memory Usage, 33
Metis, 24
MUltifrontal Massively Parallel sparse direct Solver (MUMPS), 25

N

Next Generation Reduced Order Models, 5
NIST
Flexible-base frequency performance, 119
Frequency independent iterative procedure, 4

Period elongation, 3
Time history performance, 120
Zero-phase transfer functions, 4
Nonlinear Incremental Form, 19
Northridge earthquake, 121, 134
Numerical integration, 18

O

Object Oriented Analysis
Algorithm class, 20
Analysis class, 20
Assembler class, 19
Element class, 18
Integrator class, 20
LinearSystem class, 20
Load class, 14
Material class, 15
Node class, 14
QuadratureRule class, 18
OpenMPI, 24
Operator
Element assembly, 19
Constraint enforcement, 19

P

Perfectly Matched Layer
Coordinate stretching tensors, 41
Formulation using domain reduction method, 43
Problem definition, 40
Semi-discrete form, 42
Stress-history tensor, 41
Wave equation, 41
Period Elongation, 76
Point force, 16
Portable and Extensible Toolkit for Scientific computation (PETSc), 25
Principle of Virtual Work, 14

R

Radiation Damping, 77
Reduce Order Model

Equation of Motion for fixed base building, 71
Foundation Damping Matrix, 69
Foundation Stiffness Matrix, 69
Shallow foundation model, 67
Static condensation for building structures, 70
Reduced Order Model
Equation of motion for soil-structure interaction, 74, 112, 132
Foundation-input-motion force, 113
Free-field-motion force, 132
Lumped impedance components, 132
Problem definition, 111, 131

S

Scattered Displacement Field, 44, 54
Seismo-VLAB
Class interaction diagram, 23
Classes files, 21
Coding style, 26
Direct solver performance, 31
Eigen C++ Template Library, 24
External packages, 24
Iterative solver performance, 31
Multi-core performance, 30
MUMPS, 25
Parallel structure, 23
PETSc, 25
Program structure, 22
Single core performance, 29
Seismo-VLAB's solver performance, 30
Shallow foundation modeling, 67
Shape Function, 14
Soil Impedance
Dimensionless frequency mapping, 114
Matrix form, 103
Method of analysis, 103
Nonlinear curve fitting, 133
Normalized soil functions, 105
Problem definition, 102
Soil-Structure Interaction

Continuum formulation, 52
Dimensionless group, 102
Direct method, 108, 128
Direct method definition, 2
Force vector, 57
Mass matrix, 57
NIST procedure, 3
Numerical considerations, 57
Physical parameters, 100
Problem formulation, 52
Reduced order model, 111, 131
Semi-discrete form, 56
Stiffness matrix, 57
Strong formulation, 55
Substructure method definition, 2
Weak formulation, 56
Southern California
Period elongation map, 139
Radiation damping map, 139
Urban-scale effects map, 140
Static condensation method, 70
Strain-Displacement Matrix, 15
Strong Form of the Soil-Structure Interaction Problem, 55
Synthetic seismogram, 48, 49, 64

T

Test Function Space, 55
The Forward Model, 83
The Inverse Problem, 85
Traction force, 16
Transformation Operator, 19

W

Weak Form of the Soil-Structure Interaction Problem, 56